# SEA ICE COVER DEFORMATION ON THE LOCAL SCALE AND MESOSCALE AND ITS RELATIONSHIP TO ATMOSPHERE-OCEAN PROCESSES

**Yevgeny Aksenov**

Scott Polar Research Institute, University of Cambridge

Churchill College

**This dissertation is submitted for the degree of Doctor of Philosophy**



**2002**

of

or
ur
its
n
q
a
su
w

*To my wife and my parents*

# Summary

This thesis is concerned with the study of sea ice cover deformation caused by the processes in the atmosphere and ocean. Only a modest number of studies has addressed the cross-scale analysis of the ice deformation. The aim of the present research has two foci: to investigate the variability of ice deformations and identify mechanisms responsible for their generation, and to explore the relationships of the ice deformation in the range of spatial scales. Two types of ice, the multi-year pack ice in the central Arctic and the seasonal ice in the northern Baltic Sea, are studied. The research includes a field experiment, observation analysis and modelling.

Stresses in the ice generated by non-uniform drift of ice, ocean waves, and ice deformation due to variations in the ambient air temperature are considered. To separate thermal and motion induced deformation on the floe scale a thermo-mechanical non-linear viscous-elastic model has been developed. The results from these simulations are compared with the observations from the field experiment. To study the aggregate behaviour of the ice cover the mesoscale deformations are analysed along with the local ice strain. The continuum anisotropic and granular ice models are employed to simulate the highly inhomogeneous spatial structure of the deformation fields observed. The wave emission due to ice failure is also investigated. A comparison of field observations and laboratory tests in an ice tank and asymptotic analysis allow us to identify mechanisms of the wave emission at frequencies between 0.2 Hz and 1.0 Hz. The scaling formalism for the ice deformation and stress is suggested.

The results of the data analysis and modelling have converged into a coherent scheme describing the spatial and temporal variability of the sea ice cover deformation from the local scale through the single floe scale to the mesoscale.

# Acknowledgements

Firstly, I would like to thank my supervisor Prof. Peter Wadhams (SPRI) for his help, valuable advice and guidance, and for the use of the strain data collected during the SIMI experiment.

I am grateful to all my colleagues who worked on the ICE STATE project for their support, in particular, Prof. Matti Leppäranta (University of Helsinki), Prof. Kaj Riska and Dr. Jukka Tuhkuri (Helsinki University of Technology).

I would like to thank Drs. Jackie Richter-Menge and Bruce Elder from CRREL for the opportunity to use the ice stress data collected during the SIMI experiment, and Drs. James E. Overland and Sigrid Salo (Pacific Marine Laboratory NOAA) for the ice mesoscale deformation dataset. I am grateful to Drs. Max Coon (North West Research Association), Devinder Sodhi (CRREL) and Prof. John Dempsey (Clarkson University) for fruitful discussions during their stay in Cambridge, and to Profs. Benoit Mandelbrot (Yale) and Jean Feder (University of Oslo) for their enthusiasm in discussing the theory of fractals and its application to the geophysics of sea ice.

Finally, I would like to thank Prof. William D. Hibler III (International Arctic Research Center) for his advice, and the Frontier Research Program for the opportunity to do part of this research in the stimulating scientific environment of the International Arctic Research Center, Fairbanks.

This PhD project was supported by EC MAST-III Grant, contract No CT95-0006.

# Preface

The thesis consists of an introduction, seven chapters and an appendix. The Introduction begins from the historical excursus and gives an overall description of the research aims and methods. It also addresses the novelty of the research undertaken and makes notes on its practical value. Chapter 1 is a general introduction to the phenomenon of sea ice, its thermophysical and mechanical properties. Chapter 2 discusses sea ice on the geophysical scale, introduces a classification of sea ice cover deformation, and also discusses the causes of the different types of deformation events. Chapters 3, 4 and 5 are dedicated to the field measurements of the ice deformation and internal stresses including their analysis. Chapter 6 summarises the observations and modelling results. Chapter 7 offers the closure of the discussion and speculates about plausible directions in future research.

The dissertation represents my own work and conforms to the accepted standards of citation in those instances in which I have availed myself of the works of others. The dissertation does not exceed the regulations on length and has not been submitted to any other university or institution for any degree, diploma, or similar qualification.

Yevgeny Aksenov
Cambridge
February 2002

# Contents

# Introduction

## Historical snapshot

The research discussed in this thesis is devoted to the study of a natural phenomenon which has significantly affected human history - polar sea ice. From the end of the last Ice Age and the retreat of the great continental ice sheets, humans started to explore the northern regions of the planet and met an unknown phenomenon – frozen sea. The native people first, followed by European seal and whale hunters, explorers and scientists, began to investigate this unusual and hostile arctic environment. The extreme conditions forced them to learn how to survive in the frozen seas. The increasing complication of scientific expeditions required more careful planning and began a new branch of science: Polar Studies was born at the turn of the century. Starting as centres to prepare expeditions or as observatories the first institutions studying polar regions appeared practically at the same time in St. Petersburg (Arctic and Antarctic Research Institute, 1920) and Cambridge (Scott Polar Research Institute, 1920) and several years later in Norway (Norsk Polarinstitutt, 1933). In this manner the gathering, accumulation and analysis of the scientific facts obtained from the expeditions started to be more regular. The new branch of science from the beginning of its life was a blend of geography, physics, oceanography, meteorology, shipbuilding, logistics, zoology, even anthropology and medicine. Politics and the struggle to achieve access to new natural resources led to the fast development of the Russian North in the 1930s-1960s and the Alaskan coast in the 1970s-1980s. The unprecedented conquest of the Antarctic, comparable only to space exploration, lasted nearly a century and involved practically all the world with Britain, Russia and the United States putting the greatest efforts into their scientific programmes. Recent research in Antarctica shows less political influence in the scientific planning and a new era of international scientific co-operation has begun. Advanced technologies such as satellite imagery, numerical modelling and acoustic mapping took leading roles in the research strategy, bringing professionals from physics, engineering and computing into the field. On the other hand, many phenomena on the large geophysical scale have been brought to the attention of the scientists who study processes on the smaller, laboratory scale. For example, it is becoming more and more common for solid state physicists or crystallographers to be involved in the analysis of ice fracture, competing with an engineering approach to these problems. Many similar examples can be found in the field of polar biology, chemistry or the

study of the atmosphere. The most recent attempts to understand the mechanisms of climate change in the Arctic inherited the same approach. Therefore it seems to be natural that being born as a multi-disciplinary research field, Polar Science continues to unite the interests and efforts of scientists from various disciplines, an approach which is necessitated by the nature of the subject under the study.

## Purpose, motivation and importance of the research

The purpose of the present research is to investigate the dynamics of sea ice cover under natural forcing, to study the spatial and temporal variability of the ice deformation and internal stress fields, and to identify the processes responsible for the generation of the specific signatures in these fields. In particular the study is focused on the interaction of ice dynamics and deformation on a geophysical scale with the mechanical behaviour of ice as a material on smaller scales (local scale, size of the ice floe scale, floe assemblage scale). The research is motivated by two major problems in the geophysics of sea ice. The first so-called "scaling problem" attracted the attention of sea ice mechanics researchers and petroleum engineers who worked on the design of the offshore oil rigs for the Arctic in the 1970s. To investigate the ice loads on an oil platform or artificial island field measurements were conducted on several artificial structures in the Beaufort Sea. Unexpectedly the experiments showed that the maximal ice loads measured during ice fracture in the field were about 10-100 times less than those observed in the laboratory (Sanderson, 1988). In general, large areas of ice exhibit a tendency to fail more easily under the load than smaller ones. This effect was called the "scaling effect" and is represented by the curve known as "Sanderson curve" (Sanderson, 1988). J. Dempsey also proved the existence of scaling effects during his experiments on fracturing of large (up to 80 m) ice samples (Dempsey and Adamson, 1995; Dempsey, 1996). In spite of many attempts to prove or disprove (Dempsey and Palmer, 1999; Palmer, 1991; Sodhi, 2001) the scaling hypothesis, it still is one of the most controversial issues in ice mechanics. The effect raises a fundamental question, whether a sea ice cover can be treated as the same material as ice on the laboratory scale or whether it is a new material with different properties. For instance, ice strength, which obviously should depend only on the thermodynamic state of ice, its crystallographic structure and type of loading, varies with the size of the sample. This phenomenon affects the dynamical behaviour of a sea ice cover and

leads to a second fundamental problem, which could be described as a "modelling scaling problem".

Before introducing the problem it is worth describing in brief the history of sea ice numerical modelling. In the late 1950s – early 1960s because of the development of computers a major breakthrough in numerical modelling of the atmosphere and ocean occurred (Bryan, 1969). The arctic sea ice cover also began to attract the attention of ocean modellers, and several successful sea ice models were developed at that time. The early models treated sea ice cover as a viscous continuum (Campbell, 1965), or as an inviscid, incompressible (Rothrock, 1973) or cavitating (Nikiforov et. al., 1970) fluid with shear viscosity (Doronin, 1970). The later studies brought into life the idea that a sea ice cover exhibits the properties of a plastic granular material similar to sands, gravel, clays and fragmented rocks (Bratchie, 1984; Coon et. al., 1974; Overland et al., 1998; Tremblay and Mysak, 1997). The similarity is especially remarkable when an ice cover is failing under shear deformation. Another approach to sea ice modelling considering the ice cover as a continuous medium with viscous-plastic behaviour was developed by Hibler (1979 and 1980). The general idea was that even local sea ice deformation appeared to be plastic in nature, so its time or space averaging leads to viscous strain-stress relationships (Hibler, 1977). Another group of researchers suggested an elastic-plastic constitutive law to describe ice deformation (Coon, 1980; Pritchard, 1975). The "continuum" approach was extensively developed during the last two decades by a number of modellers. It became increasingly sophisticated and included the effects of different thicknesses of ice (Flato and Hibler, 1995), and even anisotropy of ice leads (Hibler and Schulson, 2000). An extreme tendency in sea ice modelling, both in terms of detailed simulation and of computer time expenditures, is to model a sea ice cover as a set of interacting particles floating on the ocean surface. This so-called "Discrete Element Modelling" method (DEM) came from engineering and was adapted for mesoscale simulation of ice dynamics (Frederking and Sayed, 1993; Hopkins, 1996) and modelling of ice ridge formation (Hopkins et al., 1999). These models simulate quite realistically the deformation patterns of ice cover on scales between 100 m and 10 km. Instead of the explicitly introduced yield curve the DEM use the description of floe interaction to obtain a plasticity limit. The only drawback of the method is that it requires parameterisation of the floe-floe interaction including cohesion, which is usually unknown on the majority of scales except the laboratory scale.

Despite its many successful applications the approach reveals fundamental flaws in our understanding of the mechanical behaviour of the sea ice on the geophysical scales. The models based either on a continuum approach or discrete element modelling have a set of tuning parameters such as ice viscosity, strength, elasticity modulus, friction coefficient, etc. On the one hand because the simulated material is actually saline ice and can be reproduced in laboratory conditions or just taken as a sample from the ice floe it should be possible to derive these parameters from laboratory testing such as loading, crushing, bending, towing of ice blocks upon each other, etc. On the other hand the tuning parameters of the models should be within the range of values that gives model results consistent with the observations, for example ice drift, thickness, deformation, etc. If one tries to derive the ice parameters from these two approaches one finds that some of them differ by a factor of 100 or more. For example, the ice strength of a small size ice sample (about 10 cm) is of the order of tens of MPa, which is about 100-500 times higher than that usually introduced into the visco-plastic type model, of about 25-50 KPa (Hibler and Tucker, 1977; Mellor 1986; Sanderson, 1988). Young's modulus of ice derived in the laboratory conditions again is about 100 times higher than for its model analogue; 1–10 GPa (Mellor, 1986) compared to 10–25 kPa (Hunke and Dukowitcz, 1997). To change the resolution of the model, say, by a factor of two one must change ice strength or another ice mechanical parameter to get sensible results. Again, similarly to the Sanderson curve these results inevitably lead to the following questions. What kind of material are we trying to simulate on the geophysical scale? Is it the same sea ice as we can study in the laboratory? If yes, why are its mechanical properties so different from those we derive from small-scale mechanical tests? Despite the fact that the discrepancy leads to these very fundamental questions its nature has never been fully understood. Besides its fundamental importance the scaling effect in the modelling has very important practical feedback. When the sea ice models try to resolve sea ice dynamics with higher and higher resolution they meet the problem that the parameterisation of the ice mechanical properties should be altered as well. Therefore besides the scaling effect observed in the experiments, there is, in a sense, a similar effect in the models which can be called a "modelling scaling problem".

The research in this thesis aims to answer these questions and give a physical explanation based on available observations. The results obtained from models will also be considered. Some of the questions can be answered only qualitatively partly because of the limited

[illegible]

[illegible]

[illegible]

observations available, and partly because the observational task was bulky and difficult. We studied a large but limited area of the ice-covered ocean: mostly the Beaufort Sea, partly the central Arctic, with an excursion to a northern part of the Baltic Sea, where we performed a field experiment. Nevertheless the results can be expanded with some caution for other ice-covered areas.

Before turning to the discussion of methods it is worth answering the questions: why it is so important to know about the structure of ice deformation fields? For what practical reason should we study geophysical ice dynamics including the scaling effect? There are several important reasons to do this. First of all it is important to make a prognosis of natural conditions in the ice-covered seas. Such prediction is vital for navigation, and for offshore gas and oil exploration. The sea ice is a very hazardous environmental phenomenon; it generates loads which can break a cargo ship in a two or seriously damage an off-shore oil rig. For example, during the elaboration of the North Sea Route Programme the sea ice conditions were considered as a major risk in estimation of the ship damage and the main cause of delays (Brigham, 1991). The exploitation of oil fields in the Beaufort Sea clearly demonstrated that the loads on a structure from the floating pack ice should be taken into account in its design, which led to the establishment of a new branch of mechanical engineering (Sanderson, 1988). There were many cases when onshore movement of sea ice had destroyed coastal structures, broken underwater pipelines and caused significant damage to the environment. On the other hand the role of the sea ice is not purely a destructive one. Like any natural phenomenon it can be hostile for human beings but it also plays a positive role at the same time. The polar sea ice cover is a key component in the Earth's climate system, which regulates the balance of fresh and salty water in the world ocean, the production of deep ocean water via deep convection and through its intricate thermodynamics maintains negative feedback to climate oscillations. The latter helps the climate system to adjust to fluctuations in the thermal forcing. Sea ice dynamics is responsible for fresh and salty water production, and redistribution of these types of water in the ocean through the following scenario. The motion of ice cover due to ocean currents and atmospheric forcing produces open water areas (coastal polynyas and leads) which, in their turn, freeze up and eject brine into the ocean. Later the nearly fresh ice will drift to a different region and melt there (Aagaard and Carmack, 1994). There is recent evidence that the existence of deep convection in the North Atlantic and therefore the stability of the contemporary thermohaline circulation in the world ocean are dependent on the

[illegible]

[illegible]

[illegible]

presence or absence of the Arctic sea ice cover. (Rahmstorf and Ganopolski, 1999; Wood et al., 1999). One can summarise by saying that sea ice is a very important component of the environment, and that the prediction of sea ice dynamics and thermodynamics is extremely important to the solution of vital engineering and environmental problems.

## Description of the methods and nature of the results

Our research was focused on an analysis of the spatio-temporal structure of sea ice cover deformation and stresses on a variety of scales: from the local scale (order of metres and dozens of metres), through the ice floe scale (~ 100 m -10 km) up to the mesoscale (~ 10 - 50 km) and regional scale (~ 50 - 500 km). Indeed the temporal range also had to be wide: from tens of seconds to months. It might appear that the range is too ambitious; however it is the only way to study cross-scale relationships for the ice deformation. Because even the large scale deformation process creeps slowly with a typical deformation rate of about $10^{-8}$ $s^{-1}$, the ice fracturing occurs locally very rapidly and leads to very high deformation rates of order $10^{-3}s^{-1}$ (for example across an active lead). A reasonable approach was to split the deformation signal into components with respect to the different type of deformation processes, analyse them separately and, later combine them into a coherent picture. In this research two basic types of deformation process were considered closely: thermally-induced deformation, deformation caused by ice non-uniform drift and deformation occurring due to ice fracture on both the ice floe scale and mesoscale. Other deformation processes such as deformation due to atmospheric turbulence and ocean waves were analysed in order to exclude their signatures from the observed fields. In other words, the research was pointed at an understanding of how the drifting ice deforms and fails under dynamical forcing. Despite the fact that attention has been mostly focused on the shear deformation and lead formation some analysis of the classical processes of pressure ridge formation has been performed as well. Attention was also paid to the oscillations which accompany ice fracture, ridging and lead shearing observed in the field (Aksenov and Wadhams, 1999; Smirnov et al., 1993).

The study included field experiments, theoretical analysis and modelling. Because of the wide spatial and temporal range of the analysed phenomena it was intended to use different types of deformation data and as many as possible. As the first step the *in situ* time series of

[illegible]

[illegible]

## Description of the methods and [illegible]

[illegible]

[illegible]

ice deformation data gathered during recent field experiments were processed and analysed. We mainly based the research on the analysis of the observations from two field experiments, SIMI and ZIP-97. Two types of ice cover, the multi-year pack ice in the central Arctic (Beaufort Sea and Arctic Ocean) and thin seasonal ice in the northern Baltic Sea, were studied. During the analysis the deformation signatures of the different processes, namely non-uniform ice drift, inertial oscillations, surface (swell and tidal) and internal ocean waves, turbulent atmospheric pressure fluctuations and ice expansion/contraction due to ambient temperature variations, were identified with reasonable certainty employing models of different complexity. Obviously not all of the processes could be identified, and therefore some ambiguity exists. A thermal-mechanical non-linear viscous-elastic model was employed to separate thermal and motion-induced deformation. The statistics of the local deformation and stresses were analysed. In the next stage the time series of the spatial deformation fields derived from drifting buoys and satellite observations were combined with the time series of the local deformations with the aim of investigating the cross-scale spatial and temporal variability of sea ice cover deformation. *In situ* observation of the local ice deformation and stresses of an ice floe were compared and stress – strain curves were drawn and analysed. A new process that is responsible for the generation of short period ice deformation in the Arctic pack ice was discovered and analysed: emission of an elastic wave by the tip of the opening crack. The statistics of the observed mesoscale deformation and stress fields were compared with those on the local scale. All these results are new and described for the first time. Data from large-scale laboratory deformation experiments in an ice tank of the Helsinki University of Technology were also used. Several methods were employed to perform the analysis, such as correlation and spectral analyses, affine fractal analysis, range-over-standard analysis and cross-scale analysis. On the assumption of the similarity of large and small-scale fracture processes, calculations of the mesoscale ice stresses were performed from satellite imagery (SAR, AVHRR) and aerial photography with the help of simplified ice fracture models. Results from complex numerical models, i.e. a visco-plastic model with dilatation (Tremblay and Mysak, 1997), and a visco-plastic anisotropic model (Hibler and Schulson, 2000) were used to estimate spatial variability of the ice deformation and stress fields. As a last stage all results of the analyses and modelling were assembled into a coherent scheme of the ice deformation, which describes ice deformation and internal force behaviour on a wide range of spatial and temporal scales. The research has demonstrated that there is an intricate but steady relationship between the ice deformation and stresses on the different scales. This relationship was found to be consistent with the observations and model results.

# Chapter 1. Sea ice as a material

This Chapter describes ice as a natural material which has anomalous properties compared with the majority of materials found in nature. Attention will be focused on the mechanical properties of sea ice, however its thermophysics will be also reviewed as far as it dictates the mechanical behaviour.

## 1.1 Geophysical sea ice

Sea ice represents the overwhelming majority of the floating ice in the polar oceans except for icebergs and ice shelves. In the Arctic sea ice certainly dominates despite the presence of icebergs and some fresh ice of river origin. There are several ways to describe a sea ice cover. According to the widely accepted World Meteorological Organisation classification the main characteristics (descriptors) of sea ice cover are its thickness, age, concentration, how severely it is fragmented and also its deformed state (percentage of ridged and level ice). Amongst ice characteristics there are others which describe the stage of ice melting, whether it is drifting or is anchored in the shallow water, how deep is the snow on the ice, etc. (WMO, 1970). Here only descriptors which are factors of the prime influence on the ice deformation and fracture are considered.

Geographically sea ice in the Arctic can be subdivided into the Pack Ice Zone, Seasonal Ice Zone, Marginal Ice Zones and fast ice (Fig. 1.1). Pack ice is the multiyear compact ice located in the central Canadian Basin and Beaufort Sea. In the Arctic Ocean the Seasonal Ice Zone can be found along the Siberian and Alaskan coasts and consists of young and first year ice. Marginal Ice Zones (MIZ) are usually attributed to the northern Greenland and Barents Seas. In the MIZ the ocean swell breaks large floes and severely fragmented ice dominates. Pancake ice is widely present for instance in the Greenland Sea (Wadhams, 1986). The fast ice is the stationary ice connected to the shoreline and sometimes grounded on the shallows. As a rule fast ice disappears in the summer except in the Canadian Arctic and some places near the Siberian coast. The size of each of these zones is about 500-2000 km long.

Thickness of the first year ice which has been thickened due to pure thermal growth without piling up, i.e. level ice (Fig. 1.2a) varies between 30 cm and 2.5 m depending on the

season. Ice thinner than 30 cm is usually attributed to young ice forms. The intact ice sheet is called "nilas". Ice which is formed from frazil ice (ice crystals suspended within the surface water) in the marginal ice zone, consists of small floes of specific shape. It is called "pancake ice".

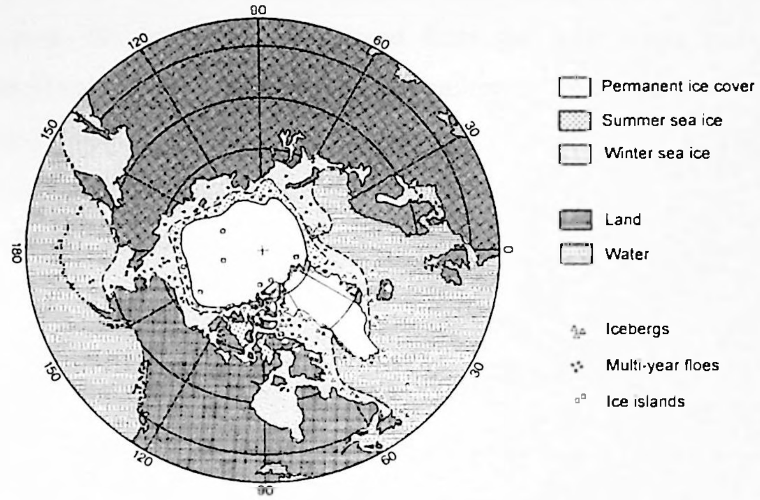


**Figure 1.1.** Sea ice in the Northern Hemisphere.

Multiyear ice thickness usually ranges from 2.2 up to 5-7 m for level ice (Maykut and Untersteiner, 1971) but can be up to 10-12 m (Cherepanov, 1964; Walker and Wadhams, 1979). Ridge building dramatically increases ice thickness (Fig. 1.2b). Ridged first year ice is usually about 2.5–4 m thick. Multiyear ice keels can be up to 47 m deep (Wadhams, 1998). Being affected by melting cycles and ridge building the upper surface of multiyear ice is much more uneven than that of first year ice. It consists of hummocks, old ridges transformed due to ablation, and surface depressions which appear because of the formation of melt ponds.

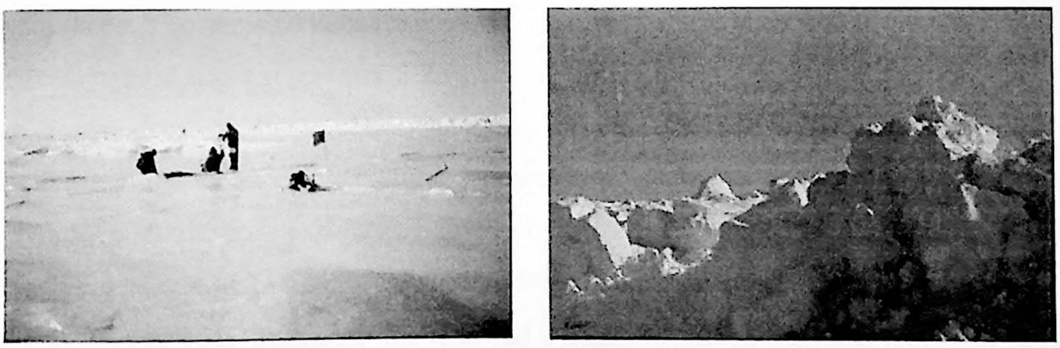

a b

**Figure 1.2.** Mature sea ice: (a) – level first year ice, Bay of Bothnia and (b) – multiyear ridge, central Arctic (photographs by author).

It is not only ice area or thickness, which is changing with the season; ice salinity and structure and, therefore the thermophysical and mechanical properties of ice cover are changing as well. Firstly because of the desalination processes multiyear ice is much fresher than first year ice. Secondly multiyear ice affected by several melting/freezing cycles incorporates a wider variety of crystal structures than first year ice. Besides granular and columnar structures, the prismatic ice formed from the melt water and also significant amounts of infiltration ice were observed in the multiyear ice (Schwarzacher, 1959; Weeks and Ackley, 1986). However, the annual ice structure "layering" which one could expect to find was observed in only limited cases (about 2 percent according to Schwarzacher, 1959). This fact gives the insight that only very small amounts of ice escape morphological changes due to deformation.

The temporal variability of sea ice in the Arctic is an endless subject, including regional and inter-annual, decadal and centennial variations. One who wishes to explore it in detail should address himself to the bibliography described above.

## 1.2 Ice crystal structure. Mechanisms of ice formation and growth

Ice and water have exceptional properties and thanks to them the present state of the Earth and the existence of life itself became possible. Only ordinary ice, hexagonal polymorph of ice $I_h$ (Hobbs, 1974) will be discussed here as it is the most widespread natural type of ice on the Earth (Weeks and Ackley, 1986). The main unusual property of ordinary ice is that its density is less than that of water (its melt). Such "lightening" because of freezing causes the ice to stay afloat on the water surface and prevents it from sinking into the melt, as most solids do. This unusual behaviour of ice is extremely important on the geophysical scale: it prevents natural water reservoirs from freezing up completely during the winter. The effect of the density decrease due to phase change along with other ice properties can be explained on the basis of the ice atomic structure. The water molecule has one oxygen atom bonded to two hydrogen atoms, with a distance between hydrogen and oxygen atoms of about 0.096 nm and an atomic angle of 104.6° (Wettlaufer, 1998). Such a structure leaves the water molecule with a positive electric charge on one side and a negative one on the other side. The negative charge of each water molecule forms a hydrogen bond with the positive charge (hydrogen) of its neighbouring molecule. When the temperature of water drops beyond the freezing point

[illegible]

the strength of the hydrogen bonds increases and the molecules form the crystal lattice of ice. In this arrangement each oxygen atom is surrounded by four other oxygen atoms. Together they form a tetrahedron with a distance between oxygen atoms of 0.276 nm (Bragg, 1922; Fletcher, 1970). This tetrahedral coordination leads to a crystal structure with a hexagonal symmetry, which has oxygen atoms located near a series of parallel planes. The position of the hydrogen atoms in the hydrogen bond is disordered but they obey the so-called Bernal-Fowler rule. According to this rule each oxygen atom is tetrahedrally surrounded by four hydrogen atoms; each of them in their turn is shared with the oxygen atom of a neighbouring molecule, making only "half" of the hydrogen atom belong to the oxygen atom. Protons (hydrogen atoms) are located at distances of 0.101 nm and 0.17 nm from the nearest oxygen atoms and the atomic angle of the ice molecule is 109.3°.

The crystallographic period along the *c*-axis is 0.737 nm, whereas that along the basal plane axis $a_3$ is 0.452 nm (Kamb, 1973; Hobbs, 1974). Such loose packing results in a lower density of ice, but on melting some of the hydrogen bonds are broken, allowing single water molecules to fill the voids in the crystal lattice, and the density of the melt increases. It is known that remains of an ice-like crystal lattice also exist in the liquid water. This could be the possible cause of altering its thermodynamic properties (Yershov, 1998).

The crystal structure of ice has several important consequences. The first is that ice can be much more easily fractured along the parallel planes which contain oxygen atoms – i.e. the basal plane (perpendicular to the axis of principal hexagonal symmetry or *c*-axis), while fracture along the other directions requires more energy. The second consequence is that because of the strict symmetry in the positions of the oxygen atoms and rather disordered positions of the hydrogen atoms the latter can cause different type of defects in the ice crystal structure. For example, it results in the so–called ionic defects, D- and L- defects. The crystal structure of ice compared to the amorphous distribution of water molecules results in about a four times higher thermal conductivity (2.22 W $m^{-1}$ $K^{-1}$, at 0°C), twice as high thermal diffusivity and lower heat capacity than those for water. Heat capacity for water and ice at 0°C are 75.3 $mol^{-1}$ $K^{-1}$ and 37.7 J $mol^{-1}$ $K^{-1}$ respectively (Nazintsev et al., 1988; Yen, 1981). The ice crystal structure also dictates how ice grows. Because more energy can be extracted from the system by attaching water molecules along the basal planes (perpendicular to *c*-axis),

[illegible]

[illegible]

[illegible]

[illegible]

ice crystal tends to grow along the basal planes, following the so-called Bravais law (Macklin and Ryan, 1966; Weeks and Ackley, 1986).

The formation of sea ice under "natural conditions", i.e. at the water–air open interface, with cooling from the top, and under normal atmospheric pressure will be considered from now on. It will include both the formation of sea ice in nature (*geophysical* sea ice) and sea ice produced in the laboratory but under the conditions close to those that exist in nature (*laboratory* or *artificial* sea ice). Two classifications of sea ice are based on the type of ice formation process, and on the shape of ice *polycrystals* and orientation of their *c*-axes.

Before the discussion starts it is necessary to clarify the terminology. The term *monocrystal*, or simply *crystal* will be used to stress that the ice crystal structure is highly periodic except for defects in the atomic lattice, whereas polycrystal includes monocrystals with co-directed c-axes, separated by inclusions of salt and other matter. These inclusion are not implanted into the ice crystal lattice but rather form zones which mark the borders for monocrystals. The term "ice grains" will be used only for the monocrystals of *granular ice,* whereas *platelets* will be used for monocrystals of *fibre ice* and *prismatic ice.*

One of the widely used classifications describes how the ice crystals are "assembled" together forming the macrostructure of ice. According to Cherepanov there are three types of ice macrostructure: granular ice, prismatic ice, and fibre ice (Cherepanov, 1976). Granular ice consists of monocrystals of pure ice (grains) with randomly three-dimensionally oriented *c*-axes. Ice of the granular structure is formed in the bulk of the turbulent water layer in the presence of free-floating ice crystals or solid particles which serve as centres of initial nucleation (for example *frazil* ice forms in such manner). The typical grain size is about 0.1 cm with a range between 0.05 and 2.0 cm (Weeks, 1998). Unlike granular ice both fibre and prismatic sea ice have ice monocrystals with the parallel directions of *c*-axis clustered together within a polycrystal. The monocrystals (ice platelets) inside such a cluster are evenly spaced and parallel. The clusters are separated by "sutures", filled with salt in the liquid and solid phase. For water with a salinity of less than 24.7 psu the freezing temperature is lower than the temperature of maximum density. Therefore if there is no turbulence immediately beneath the ice the water temperature is horizontally homogeneous with a large gradient downwards. The presence of an already formed ice layer supplies enough nucleation centres the crystal tends to grow along the basal planes, following the so-called Bernal and Fowler and Ryan, 1990; Weeks and Ackley, 1986).

The formation of sea ice under "natural conditions", i.e. at the water–air ocean interface, with cooling from the top, and under normal atmospheric pressure will be considered from now on. It will include both the formation of sea ice (natural sea ice) and sea ice produced in the laboratory but under the conditions close to those that exist in nature (laboratory or artificial sea ice). Two classifications of sea ice are based on the type of ice formation process and on the shape of ice crystals and orientation of their c-axes.

and prevents water from supercooling. In these conditions the growth of ice crystals with nearly vertically aligned *c*-axes is beneficial and as a result after the geometrical selection only ice crystals with a horizontal basal plane will survive. This leads to the formation of the prismatic ice structure (Fig. 1.3a). Due to horizontal orientation of the preferable direction of ice growth the vertical growth rate of prismatic ice is very low. Because prismatic ice can be formed only under special conditions (absence of convection in the upper water column and its low salinity) it is rare in nature. Prismatic ice structures have been found in the cores of second and multi-year ice and can be attributed to the autumn freezing up of the under ice melt water layer which had been formed during summer ice melting. A different crystal structure emerges when ice is formed from seawater with salinity greater than 24.7 psu. In this case the cooling of the water surface increases water density before it reaches freezing point and thus convection starts. As the result ice crystals grow faster in the vertical direction and much faster than crystals of the prismatic ice. Geometrical selection supports crystals with a horizontally oriented *c*-axis and forms fibre ice structure (Fig. 1.3b) (Weeks, 1998). Each polycrystal of fibre ice has horizontal dimensions of the order of a centimetre and a vertical dimension of several centimetres. At present there is not much information concerning the size of prismatic ice polycrystals; however, the available data show that their horizontal size is of the order of centimetres (Nazintsev et al., 1988).

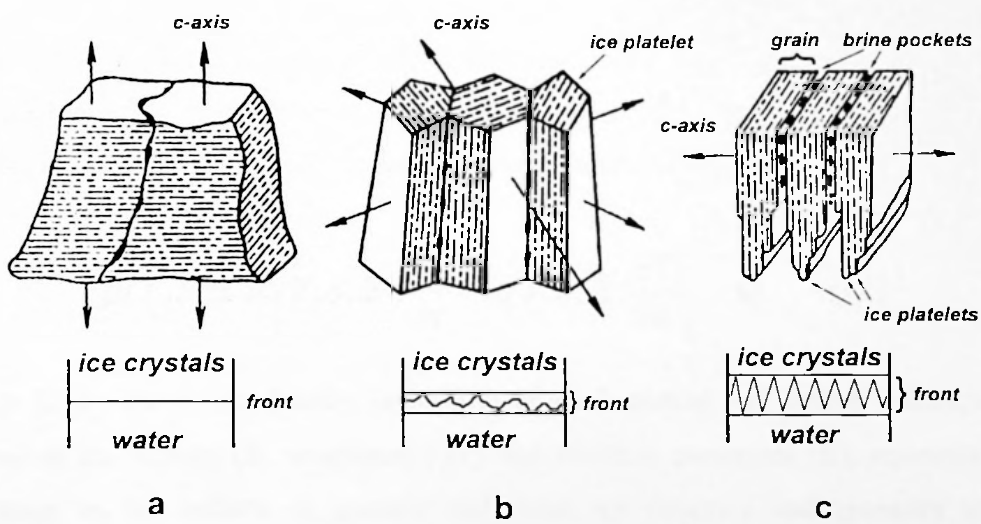


**Figure 1.3.** Structure of ice growth. (a) – prismatic ice, (b) – fibre ice, (c) – entrapment of brine by dendritic interface (after Nazintsev et al., 1988).

The formation of sea ice under natural conditions starts in the same way as fresh water ice formation. The first crystals appear in the form of minute spheres which grown further into

circular discs and under the morphological Fujioka–Sekerka instability develop into hexagonal dendritic stars (Arakawa and Higuchi, 1954; Weeks and Ackley, 1986). Needle-like crystal forms also are extremely common for the initial stages of fresh water freezing, but rather rare for sea ice formation (Arakawa and Higuchi, 1954). The needle-like crystals grow from the inclined discs due to supercooling of the surface water layer. In seawater significant supercooling does not appear because of the convective mixing and discs develop into stellar dendrites instead of needle crystals[1]. The stellar ice crystals grow until they overlap each other and freeze together forming a continuous thin ice "skim" on the surface of the calm seawater. Both discs and stellar dendrites have *c*-axes perpendicular to the plane of growth, i.e. basal plane parallel to their larger dimension. In calm water the crystals of ice are usually oriented in the plane of the water surface but in reality because of water turbulence they are often inclined and have a *c*-axis deflected from the vertical. Finally when initial forms of ice freeze up together they form a granular type of ice. The water turbulence allows ice crystals to develop not only on the water surface but also inside the water column, up to 1 m depth, i.e. frazil ice.

Once the intact ice layer on the sea surface has been formed the mechanism of ice crystallisation due to local constitutional supercooling is replaced by the mechanism of ice growth from the bottom surface of the ice skim. The ice crystallisation front advances downward into the water at a rate which is determined entirely by the heat fluxes towards the solid-liquid interface, latent heat of ice formation and its effective thermal conductivity (eq. 1.1). This is known as a classical "Stefan Problem" (Stefan, 1890).

$$\rho(T,S,\Xi)L(T,S,\Xi)\frac{\partial h}{\partial \tau} = \lambda(T,S,\Xi)\left.\frac{\partial T}{\partial z}\right|_{\varsigma} - \Phi \qquad (1.1)$$

where $\rho$, $L$, $\lambda$ – are the ice density, latent heat of ice formation and thermal conductivity as functions of ice salinity ($S$), temperature ($T$) and structure parameter ($\Xi$), representing the dependence on the volume of gaseous inclusions, ice structure and geometry of brine inclusions (Schwerdtfeger, 1963); $\frac{\partial h}{\partial \tau}$ – rate of ice growth; $\varsigma$ – position of the front of crystallisation; $\Phi$ – heat flux from the solute towards the front of the crystallisation.

[1] the needle-like crystals might appear in the sea water with a salinity < 24.7 psu.

[illegible]

[illegible]

$$[illegible]$$

[illegible]

[illegible]

Equation (1.1) demonstrates a rather simplified approach to the ice growth problem, where the solid-liquid interface is a planar one and a phase transition happens immediately after the water reaches freezing temperature. It can be used to calculate an ice thickness increment on the scale order of tens of centimetres or larger, i.e. larger than the typical size of ice crystals. However, on the microscale ice usually advances into the melt as a rather complicated dendrite-like surface. According to Nazintsev et al. (1988) the shape of the advancing interface is controlled by the orientation of the basal planes of growing crystals. Prismatic ice produces a rather smooth front of crystallisation, whereas fibre ice has a non-planar crystallisation front, leaving salt between dendrite fingers of pure ice. The latter leads to the massive entrapment of liquid salt and air bubbles into the ice when the crystal interface advances into the melt (Weeks and Ackley, 1986). Another important mechanism which may be responsible for the non-planar development of the ice growth interface should be mentioned here. This mechanism is the loss of interface stability and the formation of a very porous two-phase (solid and melt) ice layer between melt and solid ice, the so-called "mushy layer" (Huppert, 1990; Wettlaufer, 1998; Worster, 1992). Mushy layers have only been observed in laboratory experiments on ice crystallisation, and evidence of whether this layer exists in sea ice under natural conditions is not yet available (Fig. 1.6, page 20). The discussion of this phenomenon is beyond the framework of the current overview, however it is worth emphasising that the extremely high porosity of the mushy layer and therefore its high salinity can be important for the formation of brine channels and salt migration mechanisms (Wettlaufer et al., 1997; Wettlaufer, 1998).

Ice crystals grow faster in the vertical direction. Therefore, if conditions allow, the crystal grows vertically along its basal plane and competes with neighbours. After a while this process will leave only crystals with a horizontally oriented optical axis. The zone where re-orientation of the ice crystals is completed is called the *transition layer* after Perey and Pounder (1958). It is usually located in the top 5–10 cm of the ice sheet (Fig. 1.4). If sea ice grows thick enough a *columnar zone* beneath the transition layer is formed. The transition layer commonly disappears due to re-crystallisation and the columnar zone usually dominates the whole thickness of the ice sheet after some time[2]. The columnar zone in ice is associated

[2] Because only a limited number of ice cores are available the exact partitioning between columnar and transition zones and also volumes of the fibre and granular ice are not well known. For the Arctic figures vary between 0% and 40% for the granular ice (up to 70 % for the young ice in the leads) and between 20% and 95% for the fibre ice, whereas for the Antarctic they are between 5% and 99% for the granular ice and between 1% and 99% for the columnar ice (Weeks, 1998).

with the well pronounced crystal structure elongated parallel to the direction of the principal heat flux with the ice crystals becoming larger when they are closer to the lower surface (Fig. 1.4). The columnar zone consists of fibre ice which is also often called the *"columnar"* ice (Weeks, 1998). In this zone the ice crystals have their *c*-axes aligned to the horizontal plane with the azimuthal angles uniformly distributed between 0 and 90 degrees (Weeks and Ackley, 1986). The randomness in the horizontal orientation of the *c*-axes disappears when the presence of any type of anisotropic condition affects ice growth. For example, there is some evidence that the direction of the *c*-axis is correlated with the direction of main currents in the region (Cherepanov, 1971; Weeks and Gow, 1980). A discussion of the possible causes for *c*-axis anisotropy can be found in Weeks (1998). Thin ice which is forming in a lead also tends to have its *c*-axis aligned with the sides of the lead (Weeks and Ackley, 1986). Inside the columnar zone the skeleton layer is the lowermost region where the ice growth occurs can be identified (Fig. 1.4). This zone has very high salinity and porosity and, similar to the mushy layer, can be considered as a double-phase solid-liquid region which houses the intricate dendritic interface inside.

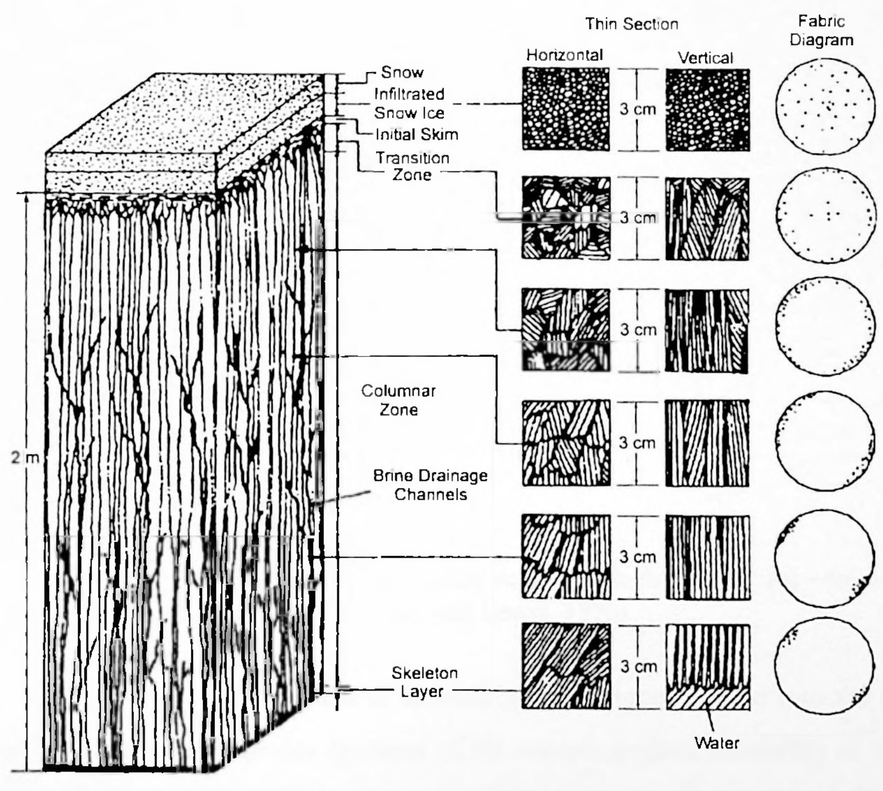


**Figure 1.4.** A sketch of the vertical structure of congelation ice (after Schwarz and Weeks, 1977).

Two important processes occur when sea ice grows under natural conditions. The first one is the migration and evolution of brine content and its redistribution in the bulk of the sea ice. This process affects the thermophysical and mechanical properties of sea ice, therefore it is essential to consider it closely (Weeks and Ackley, 1986). The second process is the coarsening of ice crystals. It also can be significant for the ice mechanical properties such as ice failure strength or elastic modulus (section 1.4, this Chapter).

The evolution of brine within sea ice is a complex process. Ice accretion on the bottom surface together with ablation on the upper surface moves the early formed ice upwards, replacing older ice with newly formed ice and causes a transfer of entrapped liquid, solid salt and gases towards the upper ice surface (Maykut and Untersteiner, 1971). The upward motion of salt competes with the following salt migration mechanisms: brine pocket thermal migration, brine expulsion, gravity drainage and flushing. Each of these mechanisms has different effects on the redistribution of the salt in the bulk of ice and also their intensity may vary from season to season.

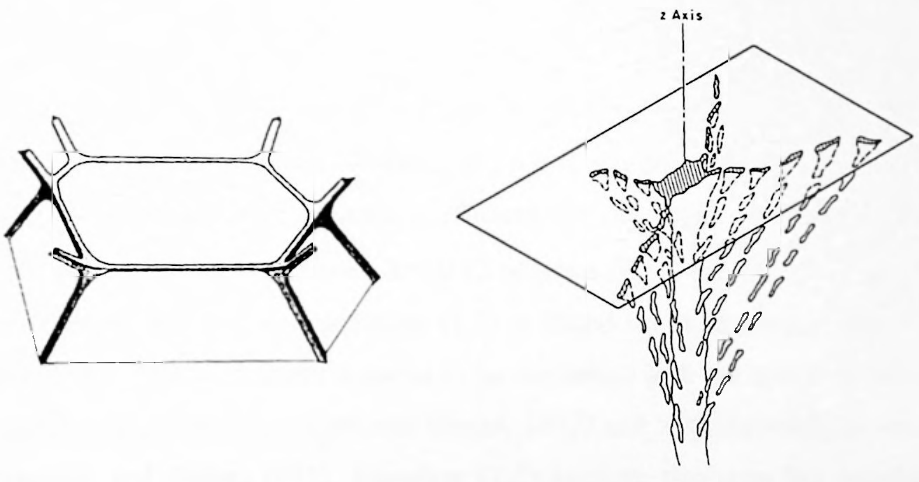


a b

**Figure 1.5.** A schematic drawing of the brine housing structures in the sea ice. (a) – vein-node system (after Nye, 1992); (b) – brine channel (after Lake and Lewis, 1970).

While solid-liquid interface advances the salt becomes incorporated into the ice between platelets and between the ice grains because of the morphological instability of the interface (Wettlaufer, 1998). Later, when ice crystals grow, brine becomes isolated from the liquid bulk in the form of brine pockets. Nye also suggested that at temperatures near the melting point liquid water may be present in ice solely due to the effect of the curvature depression of

melting point (Nye, 1992). Water resides in microscopic channels (veins) (size of 10-100 μm) at the vicinity of four-grain junctions (nodes). Therefore the liquid including brine can migrate through the ice volume via this network (Fig. 1.5a). This mechanism may be important but only in the narrow (and moving) region near the ice-water interface. At present experiments can neither confirm nor refute the presence of the liquid phase at the grain boundary (Mader, 1992). In addition liquid salt may be present in areas of internal melt, so-called Tyndall figures associated with air bubbles (Wettlaufer, 1998).

The amount of salt initially incorporated into sea ice during the formation is well described by the Burton-Primm-Slichter law on the assumption that the amount of salt incorporated into the solid is lower than in the solution and the growing interface remains stable (Cox and Weeks, 1975):

$$ln\left(\frac{1}{k}-1\right)=ln\left(\frac{1}{k_0}-1\right)-\frac{\delta v}{D} \qquad (1.2)$$

where, $v$ – is the velocity of the advancing interface; $k = S_s/S_l$ – is the ratio between salinity of the solid and liquid at the growing interface; $k_0$ – is $k$ at $v$ =0; δ – is a boundary layer thickness; and $D$ – is an effective transfer coefficient for the solute. At present the best estimates for the parameters are as follows: $k$ = 0.12 whereas $\delta/D = 4.2 \cdot 10^4$ s/cm (Weeks and Ackley, 1986). Despite the fact that equation (1.2) is based on assumptions valid for the inclusion of salt only in the solid phase it seems to be consistent with the results of laboratory experiments performed on NaCl ice (Cox and Weeks, 1975) and with the study of sea ice in the Arctic (Nakawo and Sinha, 1981). Equation (1.2) predicts that near the interface ice salinity is 9 psu for a growth rate of about 2 cm/day (typical growth rate of the thin ice), whereas for a growth rate about 0.1 cm/day (growth rate of the first-year ice) the ice salinity is about 5 psu. These numbers are reasonably close to the ice salinity observed in the field.

As the ice grows, its upper surface rises above sea level to maintain the hydrostatic equilibrium. It produces an increase in the pressure inside the interconnected brine system, driving the brine downward out of the ice (Eide and Martin, 1975). This mechanism of ice desalination is known as *gravity drainage*. Another process contributes to the ice desalination

while ice grows. When ice moves upward the brine becomes colder and therefore denser. It initiates convection within the ice sheet (Weeks, 1998).

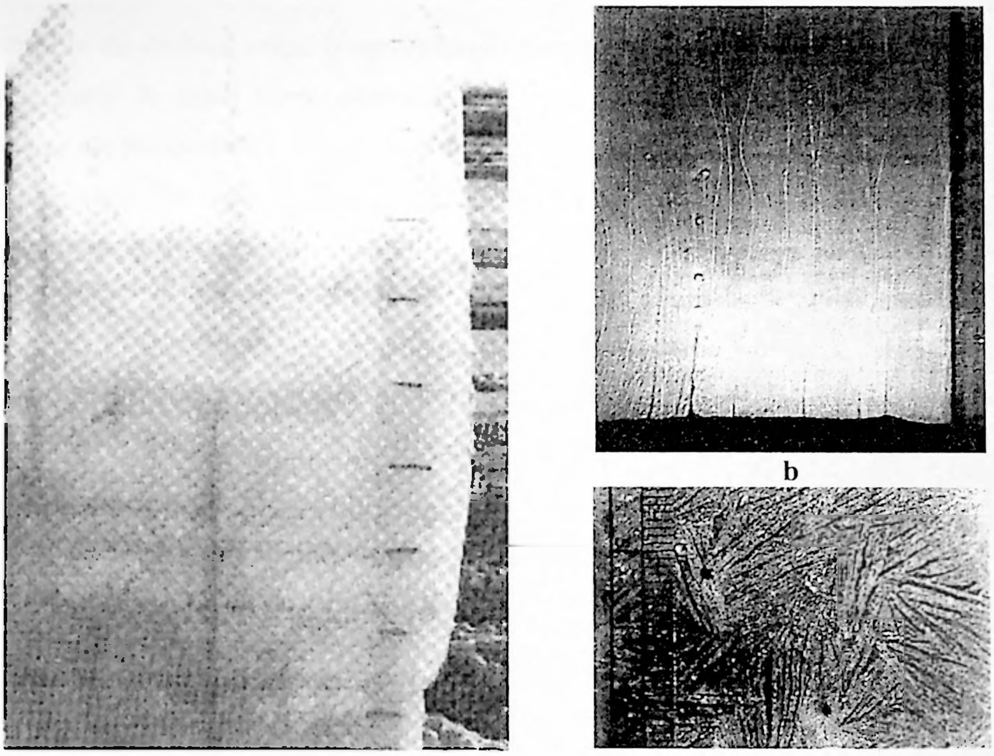

a c

b

**Figure 1.6.** Brine drainage channels. (a) – Barrow, Alaska (from Weeks, 1998); (b, c) – formation of channel-like structures inside mushy layer; view from the side (b) and from the bottom (c) (from Wettlaufer et al., 1997).

An important feature of the gravity drainage mechanism is that it is a highly non-uniform phenomenon. In natural sea ice it occurs via so-called *brine drainage channels* (Figs.1.5b and 1.6a). These structures consist of a nearly vertical tubular central channel with a series of inclined radial smaller side branches. According to available observations a typical diameter of the central tube is about 1 cm with a range between 0.1 and 10 cm (Lake and Lewis, 1970). At present there are no rigorous experimental results demonstrating how a brine channel is initiated. They are thought to be developed by interconnecting of the smaller brine structures (brine pockets, veins, etc.) in an early stage of ice desalination. While the brine and seawater start to circulate inside the drainage system voids increase in diameter, interconnect into tubes, and, finally form a brine channel. The formation of the brine drainage channel may be initiated by the convective motion of brine in the liquid near the crystallisation front and inside the mushy layer. This further leads to the development of the *pre-channel* structures

leaving later only a few of them under a selection process (Fig. 1.6b,c) (Wettlaufer et al., 1997).

Prior to the melting stage, brine drainage channels rarely extend throughout the ice. When the ice starts to melt, more channels penetrate the ice cover completely, dramatically increasing ice permeability. *Flushing* as a specific type of gravity drainage takes place during the melt season. The melt water accumulated on the ice and in the upper ice layer provides the hydrostatic pressure needed to overcome capillary force in the brine channels. This, in its turn, results in melt water run off through the drainage channels into the ocean and quick desalination of ice (Weeks and Ackley, 1986). The permeability of the drainage channels increases when melt water flows through, and therefore the process has positive feedback. Darcy's Law can describe the flow of brine through the interconnected network. In the case when the buoyancy force is balanced by the viscosity the velocity of the gravity drainage flow can, according to Doronin and Kheysin (1975), be calculated by solving the following equations:

$$\frac{d\omega_{br}}{dt} = g\left(1 - \frac{\rho_{a/w}}{\rho_{br}}\right) - \frac{\mu_{br}\omega_{br}}{\pi r^2} \tag{1.3a}$$

while the ice salinity changes according to:

$$\frac{\partial s}{\partial t} = -\omega_{br}\frac{\partial s}{\partial z} \tag{1.3b}$$

Here, $g$ – is the gravitational acceleration; $\omega_{br}$ - drainage velocity; $\mu_{br}$ – brine viscosity; $r$ – brine channel radius; $t$ and $z$ – time and vertical co-ordinate; $\rho_{br}$ - brine density. Density of air $\rho_a$ or water $\rho_w$ is used in formula (1.3a) depending on whether the point under consideration is above or below the water line.

Typical rates of salt expulsion from the ice due to gravity drainage and flushing are about $1.4\cdot10^{-1}$ kg· m$^{-3}$· a$^{-1}$ and $5\cdot10^{-1}$ kg· m$^{-3}$· a$^{-1}$ respectively. Some areas of ice are not included in the drainage network even during the melt season, so the salinity distribution in such areas is preserved for a long time (Fig. 1.7).

[illegible]

[illegible]

[illegible]

[illegible]

$$[illegible]$$

[illegible]

[illegible]

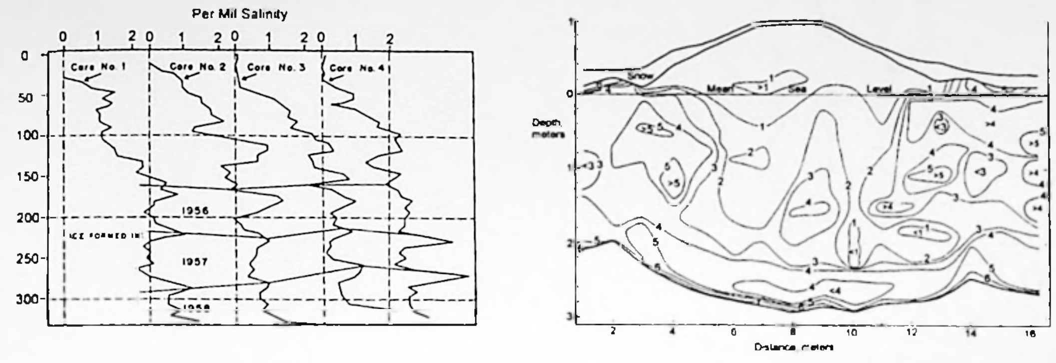


a

b

**Figure 1.7.** Salinity profiles. (a) – of multi-year ice floe (from Schwarzacher, 1959), (b) – of hummocked area of a multi-year ice floe (from Cox and Weeks, 1975). Salinity for the both pictures is given in ppt (psu).

The brine distribution within the ice sheet has important features. The vertical salinity profiles in first year ice exhibit two maxima at the top and at the bottom with the lower values near the middle. The first maximum is created by the entrapment of solid salt at the top cold layers of ice, while the second one is the result of brine migration. The average salinity of ice decreases as it becomes thicker. An example of salinity evolution for first year ice during its growth is shown in Fig. 1.8a. There is a strong relationship between ice salinity and its thickness, which can be approximated by a piece-wise linear function with the break point near the thickness of 30 cm (Fig. 1.8b). Multiyear ice is much less saline than first year because after the melting season starts ice loses the majority of its salt. The salinity of the multiyear ice basically increases with depth (Figs. 1.7a). The salinity field becomes even more non-homogeneous for ridged or hummocked ice. The numerous voids within ice ridges are filled with seawater which will create higher salinity zones when ice consolidates (Fig. 1.7b).

There is very limited information about metamorphic changes which ice undergoes with its ageing. Coarsening of ice crystals (Weeks uses the term *retexturing,* Weeks, 1998) happens when ice is highly desalinated and is at or near the melting point. The effect leads to a "rounding" of grain boundaries and elimination of the platelet structure, a similar process to that which occurs in metals (Weeks, 1998).

[illegible]

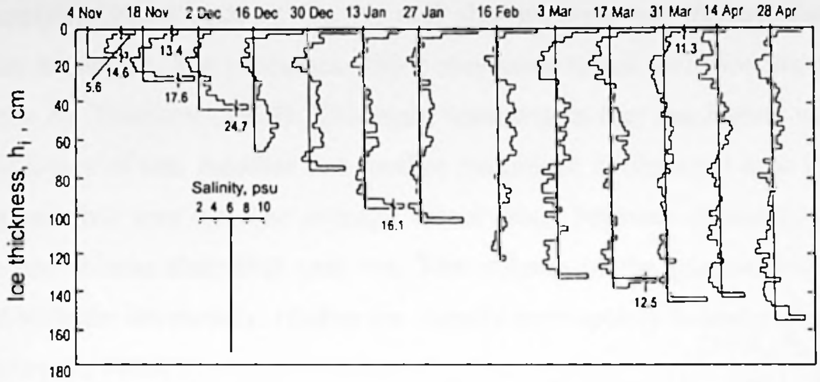


a

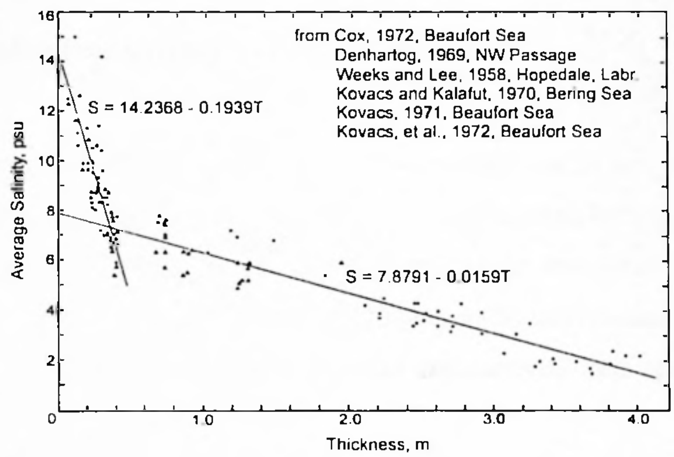


b

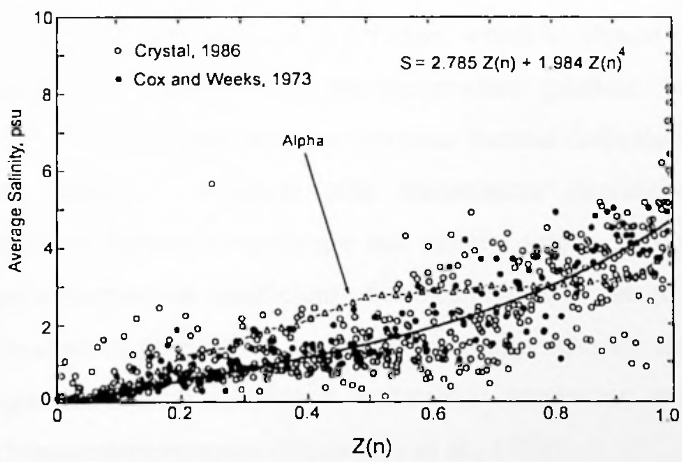


c

**Figure 1.8.** (a) – sea ice salinity profiles for Eclipse Sound, winter 1977-78 (from Nakawo and Sinha, 1981), (b) – average sea ice salinities as a function of ice thickness for first year ice (from Cox and Weeks, 1974), (c) – as in (b) but for multiyear ice (from Weeks, 1998). For multiyear ice normalised depth Z(n) was used.

Atmospheric gases such as $O_2$, $N_2$ and also methane are incorporated into the ice as bubble-like inclusions. The processes which may leads to gas inclusion are described in detail for example by Tsurikov (1979). The main tendency is that the higher values occur in the uppermost layers of ice. Another but smaller maximum is observed near the lower layer for the young and first year ice. The average values range between 10 and 20 ppt. Multiyear ice has more gas volume than first year ice. The volume of the gaseous inclusions is linearly correlated with the ice density. Higher ice density corresponds to lower volume of inclusions (Nazintsev et al., 1988).

## 1.3 Thermophysical properties of sea ice

This section gives an overview of the thermophysics of sea ice on the small scale. Thermophysical properties of sea ice affect its deformation behaviour mainly through the mechanism of thermal expansion (Chapters 2 and 4). In this sense the key thermophysical characteristics of sea ice are the thermal expansion coefficient (sometimes ice density is used instead of the expansion coefficient), thermal conductivity and specific heat (Weeks and Ackley, 1986).

Most materials have an expansion coefficient which is almost constant or at least one which is monotonically dependent on the temperature gradient. Sea ice as a composite material (pure ice plus brine) demonstrates intricate thermal deformation: in certain ranges of temperature and salinity it expands with temperature decreasing (positive expansion coefficient) whereas in certain temperature and salinity ranges it contracts with temperature decreasing (negative expansion coefficient). Such behaviour is caused by the different thermal expansion coefficients of pure ice polycrystals and brine, also by changes in the amount of brine with temperature. Pure ice has a volumetric expansion coefficient monotonically increasing with temperature increase (Nazintsev et al., 1988):

$$b_v = 158 + 0.54 \cdot t \qquad \text{for } -30\,^{\circ}\mathrm{C} < t < 0\,^{\circ}\mathrm{C} \qquad (1.4)$$

where: $b_v$ – is the volumetric expansion coefficient [$\mu$strain·$^{\circ}$C$^{-1}$]; $t$ – temperature [°C].

Equation (1.4) gives a typical value of the volumetric expansion coefficient of about 130 - 160 μstrain·[°C]$^{-1}$. For a single crystal of pure ice, the coefficient of linear expansion varies slightly with direction relatively to the crystallographic axes. The maximal difference does not exceed 2 percent (Mellor, 1986).

Whereas salt crystals occupy an insignificantly small volume in the sea ice and therefore do not affect the thermal expansion process, the dissolved salt contributes significantly to the thermal deformation. There are two competing processes: when temperature decreases pure ice contracts according to equation (1.4); at the same time due to the phase changes part of the brine becomes ice which can lead to the expansion of the sample. According to Doronin and Kheysin (1975) the total change in the volume of sea ice due to pure ice expansion and phase changes is:

$$b_{si}=1/V_o\, dV/dT+s(V-Vw)dS_p/dT/V_oS_p(S_p-s) \qquad (1.5)$$

where, $V_o$ – is the initial volume of sea ice sample [cm$^3$]; $V_w$ – is the volume of liquid phase [cm$^3$]; $s$ and $S_p$ – are the salinity of ice and salinity of brine in the ice [psu]; $T$ – is the ice temperature [°C].

Because the ice thermal expansion depends on the local ice temperature and salinity it also depends indirectly on the thermal conductivity and specific heat.

The specific heat of sea ice $c_{si}$ is the total heat required to raise the temperature of its constituents by one degree plus heat gained in the phase transitions. The latter results in the anomalously large specific heat of sea ice, up to several dozens of kJ kg$^{-1}$ K$^{-1}$ (Yen, 1981). The important feature is that the specific heat curve exhibits a discontinuity related to the deposition of the $NaCl_4 \cdot 2H_2O$ complex in the solid phase at the temperature –22.9°C. Except for the discontinuity the heat capacity rapidly increases with temperature increase. Pounder (1965) gave an expression for the temperature range of 0.°C to -22.9°C which is based on Schwerdtfeger (1963) parameterisation and is believed to be more accurate than the latter (eq. 1.6).

$$c_{si} = -\frac{s}{\alpha T^2} \cdot L_i + \frac{s}{\alpha T} \cdot (c_w - c_i) + c_i \cdot (1 - s) \quad (1.6)$$

where, $c_i$, $c_w$ – are the specific heats for pure ice and water, [J kg$^{-1}$ °C$^{-1}$]; $L_i$ – is the latent heats of pure ice fusion, [J kg$^{-1}$]; $T$, $s$ – are the sea ice temperature and salinity, [°C] and [psu]; $\alpha = -1.848 \cdot 10^{-2}$ [°C$^{-1}$].

The thermal conductivity of sea ice $\lambda_{si}$ is dictated by its phase composition and also spatial arrangement of the its phase components. A number of formulae were developed for this parameter, but for the present study the simple and the most practical one suggested by Untersteiner (1961) is in use (eq. 1.7).

$$\lambda_{si} = 2.03 + \frac{s \cdot 0.107}{T} \quad (1.7)$$

where, $\lambda_{si}$ – is the thermal conductivity [W m$^{-1}$ °C$^{-1}$]; $T$, $s$ – are the sea ice temperature and salinity, [°C] and [psu].

The thermal diffusivity of sea ice ($k_{si}$) depends on its thermal conductivity ($\lambda_{si}$), density ($\rho_{si}$) and specific heat ($c_{si}$):

$$k_{si} = \frac{\lambda_{si}}{c_{si} \rho_{si}} \quad (1.8)$$

Since during the formation of sea ice the phase change is continuous there is no "true" value for the latent heat of fusion, however the latent heat of ice formation $L_{si}$ is a useful concept and can be calculated following Pounder (1965):

$$L_{si} = L_i \cdot (1 - \sigma - \sigma / S_p) \quad (1.9)$$

where, $L_i$ – is the latent heats of pure ice fusion.

## 1.4 Mechanical properties of sea ice

Ice (fresh water ice or sea ice) displays complicated mechanical properties, because in nature it exists at a temperature rather close to the melting point. When deformed at high strain rate or when the load is brief ice behaves as an elastic material. However under sustained load ice experiences a large irreversible inelastic strain. The relationship between stress and strain rate is non-linear under creep conditions. For fresh water ice, mechanical properties are function of its temperature, porosity, grain structure, as well as of strain or stress rate (Mellor, 1986). All these dependencies remain important for saline ice; salinity, volume of brine and geometry of pores start to play their role as well.

Since ice is a visco-elastic material at the temperatures and strain rates which are the characteristics of the conventional mechanical experiments, the slope of the stress–strain rate curve does not give an accurate estimate of the elastic modulus $E$ (Mellor, 1986). The high frequency vibrational techniques involving propagation of small-amplitude pulses allow us to derive the true elastic modulus more precisely. For polycrystalline ice of low porosity $E$ varies between 9 and 9.5 GPa for the temperature range from –5°C to –10°C (Sinha, 1978). Surprisingly the temperature does not affect the true elastic modulus significantly, but porosity does. The modulus increases from about 10 MPa up to 10 GPa with a porosity increase from 0.2 to 0.9 (Mellor, 1986).

For the elastic analysis the effective elastic modulus $E'$ is often employed. Several approaches to parameterise the effective elastic modulus exist. The parameterisation suggested by Cox (1984) (eq. 1.10a) and one developed by Lewis (1993) (eq. 1.10b) are widely in use. Both formulae work for temperatures between –40°C and –5°C and give a range for the modulus somewhat between 1 and 10 GPa.

$$E'(T,p)=4.0\cdot 10^{9}\cdot(1-7.5472\cdot p)\times(1-0.012\cdot T) \qquad (1.10a)$$

$$\begin{aligned} E'(\dot{s},T,p)=&\varpi\cdot log(\dot{s}+3)+3.5\cdot 10^{9}\times \\ &\times(1-7.5472\cdot p)\cdot(1-0.0714\cdot T) \end{aligned} \qquad (1.10b)$$

where, $\dot{s}$ – is the strain rate; $\varpi$ = 0.1 – slope [$GPa\cdot log(\dot{s})$]; $p$ – ice porosity.

## 2.4 Mechanical properties of sea ice

[illegible]

[illegible]

[illegible]

$$[illegible]$$

[illegible]

Values of Poisson's ratio $\nu$ for sea ice are poorly known. However, they are thought to decrease with temperature and brine volume (Weeks and Assur, 1967). The value of $\nu$ for low porosity for both saline and fresh ice is about the same 0.33±0.03 (Mellor, 1986).

Since $\nu$ does not vary much, the bulk $K$ and shear $G$ moduli, and the flexural rigidity $L$ are fairly constant as well and can be derived from elastic modulus (eq. 1.11). When the effective elastic modulus is employed the effective Poisson's ratio $\nu'$ should be used as well. Following the discussion that can be found in Mellor (1986) and in Lewis and Richter-Menge (1998) $\nu'$ varies between 0.33 and 0.5.

$$K = E/(3 \cdot (1 - 2 \cdot \nu)) = E \tag{1.11a}$$

$$G = E/(2 \cdot (1 + \nu)) = 0.375 \cdot E \tag{1.11b}$$

$$L = E \cdot h^3/(12 \cdot (1 - \nu^2)) \tag{1.11c}$$

where, $h$ – is the thickness of the ice plate [m].

The next four characteristics are very important for ice fracture. Uniaxial compressive strength $\sigma_c$ is the maximal stress which can be developed under compression specified strain rate. It depends on ice structure, strain rate, and temperature. For strain rates lower than $10^{-3}$ the strength increases as strain rate to about the one-third power, whereas for the higher rates it increases as that to about the one-fourth power (eq. 1.12) (Mellor, 1986).

$$\sigma_c = \left( \frac{\dot{s} \cdot f(T)}{A} \right)^{1/n} \tag{1.12}$$

where, $n$=3 for $\dot{s}$ <$10^{-3}$ [$s^{-1}$], and $n$=4 for $\dot{s}$ ≥$10^{-3}$ [$s^{-1}$].

At low strain rates where ice creep is the dominant deformation process the temperature dependence of the strength $\sigma_c$ is characterised by an Arrhenius equation. In this assumption compressive strength can be derived from equation (1.13).

$$\sigma_c = \left[ exp\left( \frac{Q(T,\Xi)}{R \cdot T} \right) \cdot \frac{\gamma(T,\Xi)}{A(T,\Xi)} \right]^{1/3} \tag{1.13}$$

where, $R$ = 8.314 – is the universal gas constant [J·mol$^{-1}$·K$^{-1}$]; A and Q – are the creep parameter and the activation energy. For granular ice and for temperature below –8°C, A = 4.1· $10^8$ [MPa·s$^{-1}$] and Q = 120 [kJ·mol$^{-1}$]; for the temperature above –8°C A = 7.8· $10^{16}$ [MPa·s$^{-1}$] and Q = 78 [kJ·mol$^{-1}$]. For columnar ice A = 3.5· $10^6$ [MPa·s$^{-1}$] and Q = 65 [kJ·mol$^{-1}$] (Sanderson, 1988); $\Xi$ – is the ice structure parameter discussed earlier.

Because the deformation process is almost purely elastic at high strain rates one can expect only a weak dependence of $\sigma_c$ on temperature, in much the same way as the true elastic modulus varies. The effect of porosity on the uniaxial compressive strength $\sigma_c$ is the following. As porosity increases from 0.019 to 0.128 the strength decreases by a factor of approximately 0.6 (Mellor, 1986).

The uniaxial tensile strength of an ice sample $\sigma_t$ is probably the most important characteristic for geophysical scale ice mechanics because it is thought to be the main control parameter for the formation of cracks and leads in the ice cover (Weeks, 1998). At very low salinity rates, where the main deformation mechanisms are flow and recrystallisation there is no significant difference between $\sigma_c$ and $\sigma_t$. However, when the strain rate exceeds $10^{-6}$ [s$^{-1}$] and quasi-brittle fracture tends to occur, the tensile strength deviates from the compressive one, being about four times lower the former (Mellor, 1986). Once brittle fracture reaches its steady state there appears to be very little drift in $\sigma_t$, whereas compressive strength continues to increase with the strain rate. There is very little sensitivity of $\sigma_t$ to temperature in the quasi-brittle mode. The variation of $\sigma_t$ with porosity in freshwater ice indicates a consistent increase of strength by a factor of 0.8 with a porosity increase from 0.019 to 0.128, thus $\sigma_t$ is less sensitive to porosity than $\sigma_c$. For saline ice Lewis (1998) gave the approximation (eq. 1.14) based on laboratory measurements (Dykins, 1970).

$$\begin{aligned} \sigma_t(T,s) = &-348.9 \cdot 10^3 + 19.8 \cdot 10^3 \cdot T + \\ &+17.9 \cdot 10^3 \cdot s - 0.9 \cdot 10^3 \cdot T \cdot s \end{aligned} \tag{1.14}$$

Flexure of an ice plate or beam induces lateral strains in the interior, which have opposite signs above and below the so-called neutral bending surface. If a plate or beam bends upwards the stress above the neutral surface is tensile whereas the one below is compressive. Because as the rule $\sigma_c > \sigma_t$ under flexure failure ice tends to break in the area of tensile strain, therefore $\sigma_t$ controls much of the ice cracking during the initial stage of the ridge formation. Flexural strength $\sigma_{ft}$ is thought to be sensitive to the rate of loading $\dot{\sigma}$, however the nature of this relationship is not well defined. The dependence of $\sigma_{ft}$ on temperature has been studied extensively and manifests an overall increase of strength from 0.5 MPa to 2.5 MPa as the temperature drops from –5°C to –40°C. The strength increase can be described in terms of the reduction of the volume of brine $v_b$ (Timco and O'Brien, 1994) (eq. 1.15).

$$\sigma_{ft} = 1.76 \cdot exp\left(-5.88 \cdot (v_b)^{1/2}\right) \qquad (1.15)$$

The fracture toughness is used to describe yield strength of the flawed material, and concerns the opening of a crack in Mode I (Mellor, 1986). The process is characterised by the critical stress intensity factor $K_{Ic}$ which is related to the overall tensile failure ice stress in the following manner:

$$K_{Ic} = \sigma_t \cdot (\pi \cdot c)^{1/2} \qquad (1.16)$$

where, $c$ – is the half-length of the crack. If the crack is extended through the whole ice thickess, $c$ would be then half of the horizontal size of the crack. The studies show that $K_{Ic}$ decreases with increasing strain rate or rate of load varying between 20 [kPa·m$^{1/2}$] and 130 [kPa·m$^{1/2}$]. However for low rates it appears to be independent from the rate. This happens because at the low strain rates creep tends to reduce stress concentration at the tip of the crack (Lewis, 1998). There is strong evidence that $K_{Ic}$ decreases with temperature increase. For low strain rates the critical stress intensity factor increases by a factor of about two as the temperature drops from –5°C to –40°C (Mellor, 1986).

Summarising this section the following notes should be made. The first one concerns the creep behaviour of ice. Despite the fact that the section dealt primarily with the elastic characteristics of ice, the visco-elastic (creep) behaviour has been considered as well. Different parameterisations for the ice creep itself are discussed in Chapter 4 in more detail.

[illegible]

[illegible]

[illegible]

[illegible]

[illegible]

The second note addresses the dependence of the ice mechanical properties on the size of the sample, so-called "size effect". On the one hand the experiments demonstrate that the ice characteristics such fracture toughness of ice, as flexural, tensile and compressive strength of ice varies as the volume of the stressed material increases, i.e. size of the specimen (Dempsey, 1996; Dempsey and Palmer, 1999; Mellor, 1986; Weeks, 1998). For example, the relatively low level of the stresses in the interior of an ice floe observed *in situ* is evidence that the overall strength of the floe is much less than the tensile strength of a specimen from this floe (Lewis et al., 1994). On the other hand the absence of a size effect was found in brittle crushing of ice (Sodhi, 2001). The question as to whether this effect has a physical basis or is only an artefact of the experimental techniques is still open and requires further study.

# Chapter 2. Sea ice deformation and mechanics on the small and geophysical scales

This chapter describes the main type of sea ice deformations and the mechanisms of their generation. We discuss phenomena which occur on a wide range of spatial scales and have different durations.

## 2.1 Ice as a geophysical material. How it differs from "small-scale" ice

Bearing in mind that the purpose of this chapter is to give an overview of ice deformation on a variety of spatial and temporal scales, it is necessary to answer the question: what is the difference (if there is) between the mechanical properties of geophysical sea ice and the ice which is usually tested in the laboratory? For instance, we cut a sample from an ice floe during a field experiment and carefully preserve its salinity, structure and temperature until we can run the mechanical test. Then we test the sample and measure, say, its tensile strength. Is this tensile strength obtained from the test equal to the overall tensile strength of the ice floe? In other words, is an ice floe made from the same "material" as the small ice sample?

## 2.2 Natural scales of geophysical sea ice

Another important topic will be brought to the reader's attention in this section. As opposed to ice in the laboratory, geophysical ice happens to be involved in the processes which occur on a wide range of spatial scales and have duration from several milliseconds to several decades. Even if we restrict our task and study ice deformation and failure during only one season in a confined region, we are obliged to consider processes ranging on a spatial scale from several centimetres to several hundred of centimetres, and on a temporal scale from several seconds up to several months. It is not only the widely ranged spatial and temporal variability which makes the study of geophysical ice so complicated. It is also the manner in which these scales interact.

Let us explain this point. Sea ice literally "lies" between the atmosphere and ocean. Being a *geophysical phenomenon,* it is affected by the atmosphere and ocean, which, in turn, act on different temporal and spatial scales. Thus, the dynamic response of sea ice and as the result the ice morphological features presumably should have several *natural scales*. For sea ice cover, these features are: zones with ice of similar compactness, thickness and similar deformation state, systems of leads, coastal wind-generated polynyas, floe aggregates, shear zones, pressure ridges and cracks, ice vortices in the MIZ, etc. We need to stress here that the scale of external forcing can be different from that of the ice response. For example, large scale wind fluctuations due to passing cyclones in the range 500-1000 km and duration 5-10 days produce a lead network of about 500 km size, which can be preserved for much longer periods (up to 400 days).

**a**

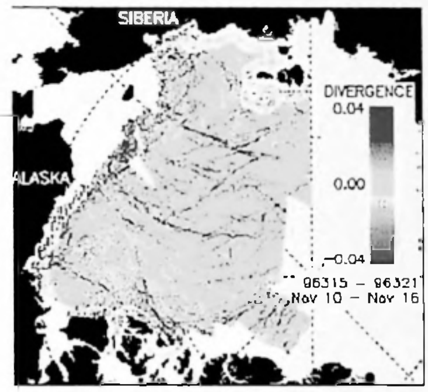


**b**

**Figure 2.1.** Examples of cracks (a) and leads (b) in the sea ice cover (negative divergence exposes active leads; data is processed by RGPS, Jet Propulsion Laboratory).

Because the maximal thickness of sea ice does not exceed 60 m (maximal draft of ice keels), on scales from kilometres and larger it can be considered as a very thin "plate" or "film" floating on the ocean surface. This plate or film behaves as a viscous liquid with a transition to plastic failure when stress exceeds some limit (Coon, 1980; Hibler, 1977 and 1979). Exhibiting "liquid-type" motion on the large scales and for a long period sea ice reacts as a nearly rigid body with a plasticity limit for shorter periods and smaller spatial scales. Strictly speaking the plate is not intact, it has "holes" and "cracks" inside, and during the warm season the ice cover is rather loose when ice floes are not connected together. Closely packed clusters of cracks in sea ice cover are called "leads". They can be easily seen on aerial photos and satellite pictures (Fig. 2.1a,b). Recent observations from satellites demonstrate that the main deformation of the ice cover occurs along the leads (Overland et al., 1995, 1998).

The principal dynamical and thermal forces act on the sea ice cover from the atmosphere (wind, atmospheric turbulence, sensible and latent atmospheric fluxes), through the atmosphere (short wave solar radiation and long wave re-emission) and from the ocean (currents, mesoscale eddies, ocean turbulence, surface elevation, tidal currents, ocean inertial oscillations, waves, etc.). In addition, drifting ice is affected by Coriolis force and interacts with the coast. Each of these forces has own spectrum, but the integral response of the sea ice cover to the external forcing is extremely non-linear. Under the multi-scale input the sea ice cover generates its own spectrum which, except for inertial and tidal peaks, can be approximated by a power law piece-wise function with a high degree of accuracy (Leppäranta and Hibler, 1987; Aksenov, 1999b). We will return to a discussion of the spectrum of ice motion in Chapters 4 and 5, but in the framework of the present section the following important fact should be stated. There is quite consistent evidence that if we consider ice motion during a long period (say, between several days and several months) both sea ice deformation and motion spectra do not show any significant peak except tidal and inertial oscillations, which are, strictly speaking, features of the ocean spectrum (Aksenov and Pozdnyshev, 1995; Aksenov, 1999b,c; McPhee, 1974). This does not imply that other periodic ice motions such as ocean swell, internal waves or oscillations caused by the ridge building and rafting process, etc. are not present. They are present, but, due to their episodic character, they are completely overwhelmed by the persistent aperiodic signals of a large amplitude (Fig. 4.16, Chapter 4). In most cases sea ice motion does not have an energetic spectral peak near the mesoscale eddy frequency, which is seen in the ocean spectrum. The only significant long period variation is the seasonal one. This makes it difficult to introduce any physically based temporal scale for a period longer than a day and shorter than a season. There is an exception to this rule. If ice moves near the coast or through a channel with some "quasi-periodical" boundaries it would possibly show a periodic component in its Lagrangian motion. An example of such motion will be discussed in Chapter 7. If we analyse ice motion on the shorter temporal scale the most pronounced is the long period ocean swell, of about 30 sec period, therefore it can be chosen as a short period scale.

A similar but at the same time different difficulty appears when one tries to introduce the spatial scales of sea ice processes. On the one hand large scales are quite obvious: size of the basin, sea, bay, etc. On the other hand small scale features such as size of crystal, brine channel or microcrack allow us to introduce physically justified small scales (Curtin, 1991).

However, between these two scales nothing is really certain. Thorndike (1986) introduced spatial correlation for the drift of ice pack over scales of order of 100 km. Hypothetically this spatial scale is initiated by the cyclonic weather systems in the Arctic. Borodachev (1974), Marko and Thompson (1977) and Timokhov and Kheysin (1987) have discussed the spatial periodicity of the leads in the winter ice pack, which is thought to be about 100 km. On the other hand, upward sonar ice thickness profiling in the central Arctic (Wadhams et al., 1992), differential ice pack motion analysis performed with the help of the RADARSAT Geophysical Processor System (RGPS) (Kwok, 2001) together with floe size distribution analysis from AVHRR (Lindsay and Rothrock, 1995) did not show any inherited physical scale order of 100 km. Both ice deformation/motion and ice floe size distributions are power law type distributions without any well pronounced preferred scale. Some researchers have been using the so-called *single floe scale*, meaning under this term the size of a single ice floe (Overland, et al., 1998; Richter-Menge and Elder, 1998). However, despite being physically well justified, this approach gives us too wide a range, nearly three orders of magnitude (the smallest floe can be about 10 m whereas the giant ice floes have a size of about 10 km). Another candidate for the physical scale is the ice thickness. It definitely plays a role in out-of-plane ice deformation, including ridge building, and can therefore be considered as a natural scale for these processes (Parmerter and Coon, 1972). However, its influence on the larger scale in-plane ice deformation is rather weak. Moreover, recent experiments and modelling studies have demonstrated that the ice thickness is not the only parameter which controls ice deformation. For example, the transition between ridging and rafting modes is also controlled by the small scale roughness of ice surfaces (Tuhkuri, et al., 1999), and this requires introducing another scale, ice roughness, which is at least an order of magnitude smaller than ice thickness. An additional problem is the sea ice cover anisotropy. Most of ice deformation structures such as ridges, leads, or different types of cracks have one of their dimensions about two to four orders of magnitude larger than another. For example, the width of a large lead is about 1-10 km whereas its length can vary between 100 and 1000 km (Fig. 2.1b). Similar proportions are observed for ridges. With a typical width between 1 and 100 m they may extend up to 75 km in length (Timokhov and Kheysin, 1987). Therefore ice deformation structures do not belong to a single scale.

In contrast to ice deformation there are very little data about spatial distribution of the internal stresses within the ice cover. Nevertheless, the limited observations (Richter-Menge

and Elder, 1998; Richter-Menge et al., in press) and simulation results (Hibler and Schulson, 2000) suggest that ice stresses exhibit significant anisotropy on the floe scale and larger, which again makes it difficult to assess spatial scale. The internal ice stress field will be discussed in detail in Chapter 7. Because the ice structure evolves with the season it has different spatial scales through the year (Borodachev et al., 1981). Therefore there are no physically well defined spatial scales for ice.

However, for now, for the sake of convenience we will use a hierarchy of scales suggested by Overland et al. (1995) and will come back to this discussion again in Chapter 7. Table 2.1 is based on the scale subdivision presented in this paper, with some alterations. We have added a single value characterising the magnitude of the scale. Besides, we have excluded the stress and strain rate magnitudes due to the uncertainty of their estimation. The table summarises the hierarchy of scales in the dynamics of sea ice. It is stressed here that this scheme should not be considered absolutely rigorous, as the processes governing different scales tend to overlap and produce very intricate signatures in ice behaviour. Nevertheless, we believe that the scheme reflects important aspects of sea ice dynamics. Let us describe the spatial variation in the geophysical sea ice cover starting from the largest scale.

Large-scale forces, such as near surface winds, mean ocean currents, and also ice melting and freezing redistribute sea ice within the basin in a non-uniform manner and form its large scale variability. On the basin scale sea ice forms distinguishable zones of different ice concentration and thickness size of about 500-2000 km. The ice deformation under wind action results in the lead network, shear zones, and large scale floe assemblages. Large leads can cut through the ice cover of the Arctic Ocean for 100-1000 km with spacing of 30-100 km (Lindsay and Rothrock, 1995; Overland, 1998). It is difficult to attribute a single temporal scale to all of these zones. For example, the seasonal ice obviously lives not more than one year, whereas the multiyear pack ice has a typical age from 2 to 10 years. Figures between one year and 10 years seem to be a reasonable approximation for this temporal scale.

**Table 2.1.** Hypothetical scale hierarchy for sea ice dynamics (adapted from Overland et al., 1995).

| Scale: Dynamical processes and correspondent observed features | | Range of scales Overland et al., 1995: Spatial | Range of scales Overland et al., 1995: Temporal | Estimation of scale: Spatial [m] | Estimation of scale: Temporal [sec] |
|---|---|---|---|---|---|
| **Large scale** | | | | | |
| Basin scale ice motion | large scale variations in ice thickness and concentration, large leads and polynyas | $500\text{-}2\cdot10^3$ km | 1-10 years | $10^6$ | $1\cdot10^8$ |
| **Regional scale** | | | | | |
| Regional scale ice motion and deformation | ice massifs, leads and polynyas | 100 km | 100-500 days | $10^5$ | $1.58\cdot10^7$ |
| **Mesoscale scale** | | | | | |
| Mesoscale scale ice motion and deformation | floe assemblage, giant floes, leads and polynyas | 10 km | 10-100 days | $10^4$ | $3.98\cdot10^6$ |
| **Floe scale** | | | | | |
| Floe scale Ridge building and rafting | floe, lead, ridges, finger rafts, cracks | 1 km | 1-10 days | $10^3$ | $3.98\cdot10^5$ |
| **Local scale** | | | | | |
| Local scale Motion induced and thermal cracking, buckling | small floes, ice blocks, cracks, morphological features | 1-100 m | <1 day | $10^1$ | $1.0\cdot10^4$ |
| **Microscale** | | | | | |
| Microscale cracking | microcracks (wing and comb cracks, etc.) | 1 cm-1 m | <1 day | $10^{-1}$ | $1.0\cdot10^1$ |

The next scale down is the regional scale. On the regional scale sea ice cover responds to both large-scale variability in the wind and current patterns and synoptic scale fluctuations in their field. On this scale one can again find ice zones with different concentration and thickness. The interaction of drifting ice with the shore also generates lead systems, floe aggregates and shear zones, and the formation of coastal polynyas and pressure ridge zones. A typical size of these features is about 10-200 km and their temporal scale is about 100-500 days.

[illegible]

[illegible]

| | | | | | |
|---|---|---|---|---|---|
| [illegible] | [illegible] | [illegible] | [illegible] | [illegible] | [illegible] |

[illegible]

The principal causes of the sea ice redistribution on the mesoscale are again the wind and current-induced sea ice drift and also interaction between ice massifs and the coast. Mesoscale ocean currents do not produce distinguishable ice features, except for ice vortices in the MIZ[1]. Vortices in the range of 10 to 50 km were first discovered in the Greenland and Barents Seas (Johannessen et al., 1994). Mesoscale structures have a life expectancy from several weeks up to several months. Tidal and inertial oscillations for ice covered seas generate semi-diurnal ice deformation waves. Because tidal deformation is dramatically enhanced near the shore it can be associated with a mesoscale deformation. While the ice deformation due to tides is noticeable only near the coast, the inertially generated ice deformations can became significant in the inhomogeneous ice cover (Leppäranta and Hibler, 1987). It is difficult to assess the scale of deformation anomaly due to inertial oscillations, but it is somewhat close to the size of mesoscale eddies.

Now let us consider the both scale of the single ice floe and local scale. Several processes are involved in the deforming of ice on these scales. The prime one is the floe-floe interaction (on the large scale it is parameterised as an internal ice force). Horizontal loading of the floe from the sides leads to deforming of the ice floe and ultimately to cracking, finger-rafting or ridge-building. Scales of the solitary ridges and ridged/rafted areas, ice floes, leads and cracks have approximately the same order of magnitude of about 1000 m. They are formed during sequences of single events, each with a duration between minutes and hours. Some of these features (ridges) are practically permanent for the whole winter, while others last for a period of several days (leads). Deformation of ice due to thermal expansion is the second important mechanism. The deformation is restricted by the borders of the single floe and does not affect other floes. Thermal strain produce cracks with a length from several metres to several hundreds of metres, which develop in minutes to hours but might survive for several weeks (Lewis, 1998). Different types of processes generate cyclic deformation of the ice floe. For example, surface and internal ocean waves are responsible for the generation of periodic ice deformations with a spatial periodicity in the range of 600 to 1000 m for both types of waves, and a period of 20-30 sec and 20-40 min for surface and internal waves respectively (Czipott et al., 1991; Wadhams, 1986).

[1] There is some evidence of the effect of eddies on the ice concentration in the Canadian Arctic (Zhang et al., 1999).

On the microscale ice deformation processes result in the appearance of micro-cracks with a size of 1-100 cm (Weeks and Ackley, 1986). The micro-cracks are fully developed in milliseconds.

Finally, two points should be noted at the end of this section. Firstly, the boundaries between the scales are rather fuzzy. On the one hand some of the processes tend to happen over several spatial and temporal scales (for example formation of leads). On the other hand some of the processes in one spatial scaling range manifest themselves in other temporal scales. For example tidal and inertial oscillations produce mesoscale anomalies, with a lifetime of no more than one day. Secondly, we should distinguish between the actual duration of the deformation process and the lifetime of the morphological signature that it leaves on the sea ice. Let us consider for instance ridge building. The duration of active ridge formation is about an hour, but the signature of the process (deformed ice cover) could survive for a year or longer. We believe that in terms of energy redistribution the duration of the process itself should be considered in the first instance.

## 2.3 Sea ice deformation caused by natural forces. Interaction between sea ice cover, atmosphere and ocean

This section gives a description of the natural processes responsible for the generation of ice deformations. Four main mechanisms can be identified as responsible for ice stress generation: non-uniform ice drift, swell, tidal and internal ocean waves, turbulent atmospheric pressure fluctuations, and ice expansion/contraction due to ambient temperature variations. The intensity of each mechanism varies with season, weather conditions and region of ocean.

### 2.3.1 Non-uniform ice drift

Non-uniform ice drift is the basic reason for the alteration of sea ice cover bottom and upper surface topography. The primary force which causes ice drift is the surface wind shear stress. The non-uniformity of ice drift due to wind forcing, shore interaction, or inertial oscillations of ice drift and surface ocean currents result in ice cover deformation and failure: cracking, ridging/rafting, appearance of shear zones and leads (Fig. 2.2). The deformations

initiated by those processes are basically temporarily aperiodic (except inertial), and well correlated with wind. The inertial oscillations have a period of about 12 hours (McPhee, 1978 and 1984). For certain conditions the ice failure and shear motion processes can produce periodic oscillatory deformations with high frequencies from 0.2 Hz up to 4 Hz (Aksenov and Wadhams, 1999; Czipott and Podney, 1989; Martin and Drucker, 1991; Smirnov et al., 1993; Wadhams and Wells, 1995).

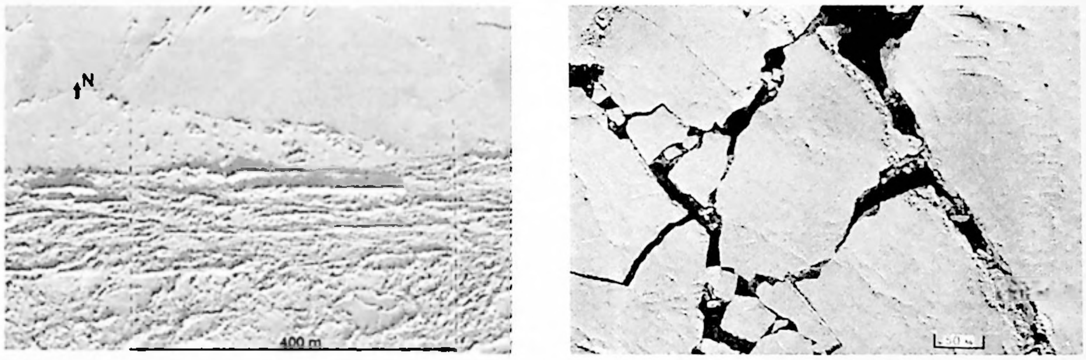


a b

**Figure 2.2.** Deformations of sea ice. Coastal shear zone in Beaufort Sea (a). Leads in first-year ice due to intensive deformation, central Arctic (b) (Borodachev et al., 1994).

### 2.3.2 Atmosphere turbulence and resonant waves

The resonant vibration of the ice cover under surface wind fluctuations tends to produce oscillations with periods of about 10 sec (Squire et al., 1995), and 13–20 sec (Nagurny et al., 1994). Long 30-60 sec period waves, called *infragravity waves* by analogy with the similar waves in the open ocean, have been observed in ice-covered seas (Menemenlis et al., 1995). They cannot be generated by wind. Presumably they also have a resonant character (Bogorodsky and Smirnov, 1982).

### 2.3.3 Ocean waves

Ocean waves are a major source of cyclic ice deformations. They were observed during field experiments in both pack ice and marginal ice zones (Czipott and Podney, 1989; Squire et al., 1995; Wadhams, 1986). The amplitude of swell-generated deformation is sufficient to break the ice sheet in the marginal zone (Wadhams, 1986). In general, surface waves with a period less than 10 sec are attenuated quickly and therefore are noticeable only near the ice

edge. Long period waves of about 20–30 sec period can travel significant distances through the ice zone and are observed as far as 500 km from the open sea (Wadhams, 1986). Ocean internal waves also leave a signature in the deformation record despite the fact that their amplitude is small (Czipott et al., 1991). Tidal deformations can reach significant amplitude in the compact ice areas in the coastal regions with significant tidal currents. Change of the sea level due to tides or storm surges can also produce intensive local stresses due to ice compaction and dilatation (Kowalik and Matthews, 1982). For most ice-covered seas the period of tidal deformations is close to the inertial period (10-12 hrs), because of the high latitude.

### 2.3.4 Thermally-induced deformation

Results of experiments show that thermal loading can achieve a significant level of amplitude and cause ice cracking and failure (Fig. 2.3), (Tucker and Perovich, 1992; Lewis et al., 1994).

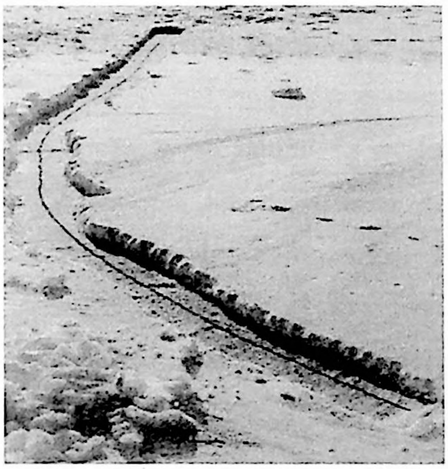

**Figure 2.3.** A thermal crack (cleared from snow) in first-year ice in Resolute Bay, March 1992. The length of the crack is about 10 m, and its depth is roughly 15 cm (after Lewis et al., 1994).

The cause of thermal deformation is the process of expansion/contraction of the body due to temperature variations. Sea ice as a composite material (ice plus salt water) depends on temperature and salinity and has both types of deformation behaviour: it expands and contracts with decrease in temperature (positive and negative expansion coefficients respectively). Such behaviour is caused by the difference between the thermal deformations of pure polycrystalline ice and salt water in the brine pockets. As the sea ice cover is mainly

[illegible]

[illegible]

[illegible]



[illegible]

[illegible]

heating/cooling from above, the nonuniformity of sea ice deformations at different depths causes stress variation with ice depth, and can even cause stresses of different sign. This complex loading also leads to non-planar deformations and complicated relations between strain and stresses.

## 2.4 Classification of the deformation

In this section, in addition to classification of ice deformation by the type of natural process responsible for their generation, we describe the classification of the ice deformation field according to: type of temporal variability (periodic–aperiodic), spatial configuration (in-plane–3-D), and temporal and spatial scales (micro–local–meso–large scale). The relationship between the classifications is also considered.

### 2.4.1 Periodic and aperiodic deformation

Tidal and inertial oscillations of ice cover motion and thermally-induced deformations have a periodic nature related to the diurnal cycle. Ocean surface and internal waves also make a cyclic impact on the ice cover. Wind forcing as well as residual non-daily thermal deformations should be considered as aperiodic or, at least, as quasiperiodic events with a very long period. Thus, we can separate ice deformations into two major components: periodic (with a period from several hundreds of milliseconds to hours) and aperiodic (with a time of variation from days to months). Further, we will use the term *waves* referring to the periodic deformations. As one can see, the range of the wave period is very wide and also includes waves generated by different physical processes, so we intend to refine the classification of long-period and short-period waves.

### 2.4.2 Long and short period cyclic deformation

The principal difference between short and long-period waves is as follows. Waves with a period greater than 8-14 sec have a positive slope in the dispersion curve, i.e. the phase and group velocities increase as the wave period increases. For short waves with a period less than 8 sec, the slope of the dispersion curve is negative, so the velocities decrease as the period increases (Fig. 2.4). In other words, the short waves propagate as elastic because of the

significant influence of the ice cover, whereas the long waves are not influenced by the presence of ice and propagate as surface gravity waves. Attenuation of long waves is slight and they can propagate for long distances through the ice zone. They can be called a *background* component of the wave field in the ice zone. Short waves attenuate relatively quickly and can be considered as a *local component* of the wave field.

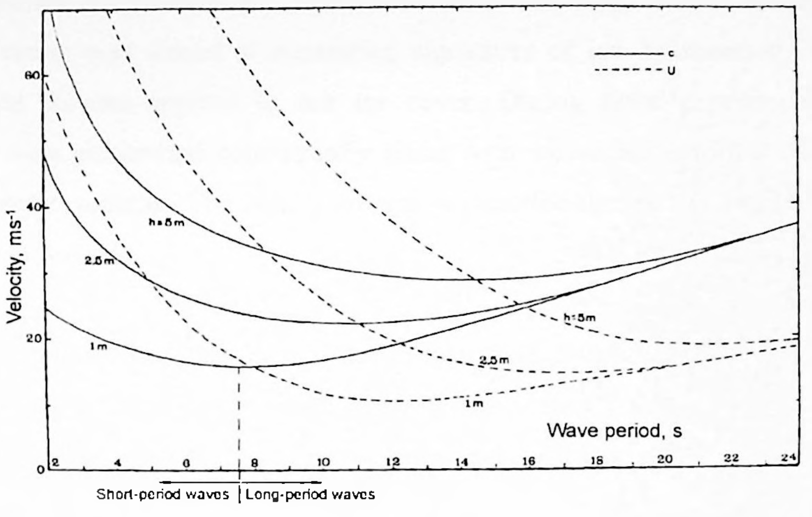


**Figure 2.4.** Dispersion relations for (c) phase and (U) group velocities of an ice-ocean coupled wave (after Wadhams, 1986).

### 2.4.3 In-plane and three dimensional deformation

The present view is that the ice deformations are basically *in-plane* deformations (Glen, 1970), which is true for the averaged large scale and mesoscale deformations. For level ice, local deformation is also in-plane, when ice failure, such as ridging, rafting, buckling or crack formation, does not appear in the vicinity of the observation site. For ice break-up events, the local stresses at different depths of ice are not equal (Tucker and Perovich, 1992). In addition, thermally-induced deformations and ice bending produce 3-D deformations and stresses, and at present, the question of whether local deformation and stresses can be approximated as in-plane tensors for the local scale is still open. Gravity waves can also produce bending, i.e. 3-D deformation.

# Chapter 3. Field experimental work
# Part I. Methods and Apparatus

The objectives of the experimental part of the research were to study the spatial and temporal variability of the ice deformation and stress fields on a local scale *in situ*. The analysis of the experimental results was aimed at separating signatures of ice deformation caused by the different natural forcing applied to sea ice cover. During these experiments the on-ice measurements were performed concurrently along with mesoscale deformation observations and satellite remote sensing. The final goal was to describe the ice deformation field on the local scale and mesoscale.

This chapter describes the ZIP-97 campaign first with the overview of the SIMI experiment following afterwards. First, however, the method for observing ice deformation and internal forces and a description of the existing measuring gauges are presented.

## 3.1 Sensors

Deformation of the ice cover, like the deformation of any body, can be determined by tracking the relative motion of the points of this body. The established way of doing it in the field is to attach a gauge rigidly to the ice surface and monitor how these gauges will elongate under the deformation. With the known length of gauge this will give the linear relative deformation - strain. As has been mentioned in Chapter 2, starting from the scale larger than 100-1000 m (the typical size of an ice floe), sea ice cover can be considered as a relatively thin plate. It deforms in the horizontal plane, besides the cases when it bends due to surface waves, thermal deformation or during ridge building. Therefore it is sufficient to measure horizontal components of the deformation tensor to derive the deformed state of the ice cover. The deformation here means the local deformation, i.e. area averaged deformation on a scale of $1\text{-}10^4$ m$^2$.

The earliest sensors developed to measure ice deformation were strainmeters, designed in the 1970s by the Department of Earth Sciences, University of Cambridge. The design was improved by the Cavendish Laboratory (Allan and Winsor, 1975; Goodman et al., 1975) and

the Scott Polar Research Institute (Moore and Wadhams, 1981). The SPRI strainmeter was a wire gauge 1 m long (Fig. 3.1). The strainmeter with 95 cm leg length was designed in two versions: the wire one and the rod one. The wire version of the strainmeter used invar wire

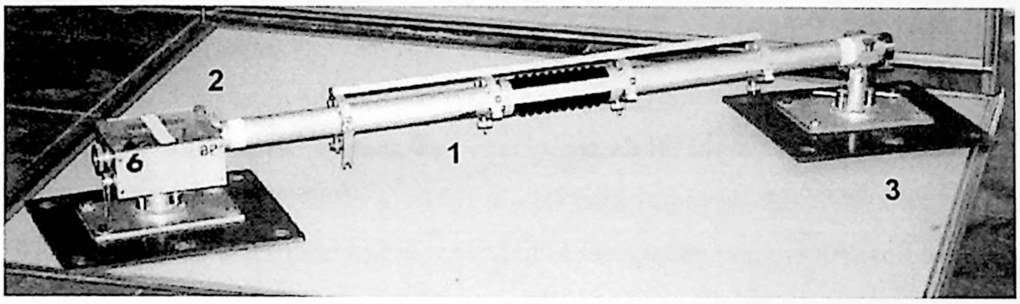


**Figure 3.1.** SPRI strain gauge, (1) – leg, (2) – end unit, (3) – fixing plate.

under tension and could give a resolution of $5\times10^{-8}$ strain. A stainless steel tube was used for the rod version which could discriminate only $5\times10^{-7}$ strain but was portable and simpler to install (Goodman, 1980; Sanderson, 1988). The disadvantage in employing steel was a high thermal expansion coefficient ($3\times10^{-2}K^{-1}$), but it was impossible to produce a robust Invar tube at that time. An improvement was made when the steel tube was replaced by hollow carbon fibre, which has carbon fibres oriented along the tube axis with the glass fibres bound around the tube circumferentially. The thermal expansion coefficient for this composite material is $1.5\times10^{-6}K^{-1}$ and it was used in the design of the *BP Sunbury strainmeter* and later *BP-Delta* gauges.

At present, the most advanced gauge, the *BP-Delta* strainmeter, was designed in the 1970s by *British Petroleum* to improve the measuring of the loads on artificial islands in the Beaufort Sea (Child and Duckworth, 1989; Duckworth and Westermann, 1989). The new strainmeter (Figs. 3.2 and 3.3a) has three legs with a fixed length of 0.30 m, set at an angle of 60° to one another as a single rosette, while the *BP Sunbury strainmeter* has one leg 0.95 m long. One end of each leg is directly attached to the ice when the other end is connected to a linear displacement transducer which, in turn, is rigidly mounted on the ice with the help of a ball joint, magnetic base system, and ice screws (Figs. 3.2b and 3.3b). This joint scheme was earlier implemented in the *BP Sunbury Strainmeter*. Instead of one-leg gauges a rosette strainmeter measures not only uniaxial strain, but provides all components of in-plane deformation tensor. As the ice deforms, the gauge length acts through a Linear Variable Differential Transformer (*LVDT*) which gives a corresponding electrical output (Child and the Scott Polar Research Institute (Mason and Washburn, 1963). The SPRI [illegible] was 1 m long (Fig. 3.1). The [illegible] 15 cm [illegible] sections, one with one end and the rod one. [illegible]



Figure 3.[illegible]

[illegible]

At present, the most advanced gauge, [illegible] was designed in the 1980s by [illegible] to improve the [illegible] (Chen and [illegible], 1988; [illegible]). The [illegible] (Figs. 3.2 and 3.3a) has three legs [illegible] of [illegible] to one another at a single [illegible], the end of each leg is [illegible] [illegible] [illegible] [illegible] [illegible]. [illegible] [illegible]

Duckworth, 1989). To expand the working range of the instrument without losing sensitivity it was fitted with a so-called "re-zeroing" device consisting of a feedback system, which activates a servomechanism when the linear displacement on a leg exceeds ±0.03 mm and returns the LVDT into its null position. This enables us to measure the maximal strain of $3 \cdot 10^{-2}$ with very high resolution. Because the LVDT gives practically "infinitely" high accuracy the gauge resolution depends only on the type of sampling electronic card, and the level of the overall electronic noise in the system. For example a 12-bit digital card allows us to resolve deformation of $3 \cdot 10^{-8}$ strain, while a 16-bit digital card improves the resolution up to $2 \cdot 10^{-9}$ strain. The level of the electronic noise generated in the system is more difficult to estimate. It depends on the particular sensor; even cross talking between sensor and other equipment

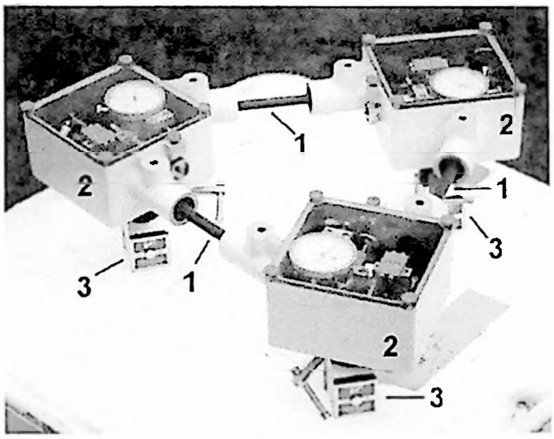


a

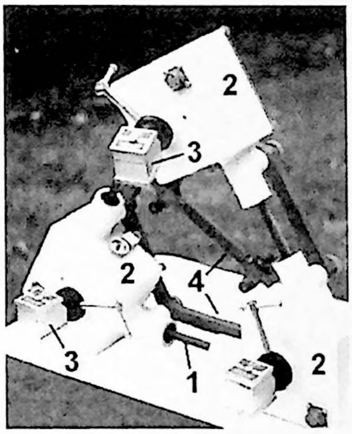


b

**Figure 3.2.** General view (a) and bottom view (b) of the BP-Delta strainmeter. (1) – hollow carbon tubes; (2) – end unit with LVDT transducer; re-zeroing motor and thermistor; (3) – ball joint and magnetic base system; (3) – holding frame.

could affect noise level significantly. During the sensor calibration estimates of the electronic noise level were conducted, and gave average values of $1 \cdot 10^{-8}$strain used in the field data analysis. This work will be described later in this chapter. Three electronic control circuits, one for each leg of the strainmeter, power the LVDT, the re-zero motor, and amplify the output signal. To avoid interference between amplifier boards each of them was mounted in a separate box (see Fig. 3.8, section 3.2 ). Additionally a thermistor was fitted into the gauge to control its temperature, which allows us to eliminate deformation of the transducer due to variation in the ambient temperature. Because of the presence of the rezeroing device in the

[illegible]



[illegible]

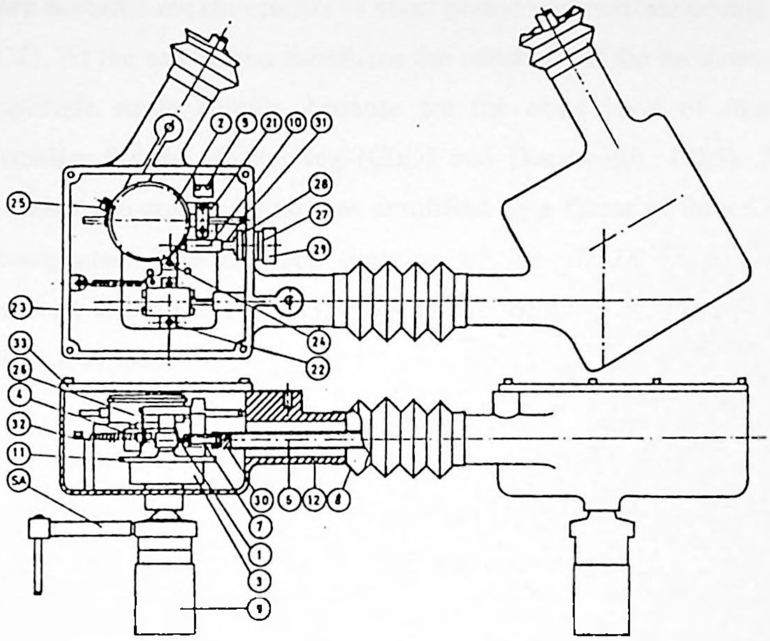

a

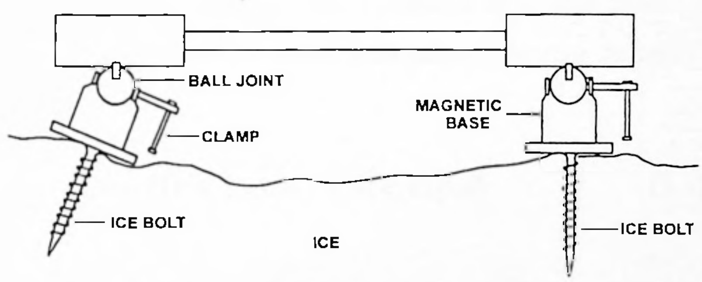


b

**Figure 3.3.** Detailed drawing of the BP-Delta strainmeter (a) and connection of the strainmeter to the ice surface (b) (after Child and Duckworth, 1989). Key: (1) – LVDT and core; (2) – dial test gauge; (3) – linear bolt slide; (4) – micromotor and gearbox; (5) – micro switch; (6) – carbon fibre tube; (7) – universal joint; (8) – bellows; (9) – magnetic base; (10) – flexible coupling; (12) – strainmeter table; (13) – jig and transit clamp; (14) – ball for clamp; (15) – clamp ring; (16) – ball half shell for clamp; (17) – ball base; (18) – clamp shaft; (19) – tommy bar (SA); (20) – tommy bar end; (21) – dial test gauge half shell; (22) – LVDT half shell; (23) – LVDT support; (24) – motor half shell; (25) – universal joint half shell; (26) – LVDT core support; (27) – PTFE washer; (28) – adjustment screw securing sleeve; (29) – adjustment knob; (30) – carbon fibre rod insert; (31) – adjustment thread; (32) – spring; (33) – corner box cover.

strainmeter the data was processed in order to delete artificial steps; this procedure will be discussed later. The shorter legs of the *BP-Delta* gauge compared to other gauges are beneficial for more accurate measurements of short period deformation events (Murphy et al., 1957; Squire 1978). At the same time it reduces the accuracy of the measurements of slowly varying low amplitude strain signals, because for the same level of strain the absolute deformation is smaller for the shorter leg (Child and Duckworth, 1989). To improve the accuracy of the sensor the output signal was amplified by a factor of three, compared to the *BP Sunbury strainmeter.* The detailed drawing of the *BP-Delta* strainmeter and the installation scheme are shown in Fig. 3.3, whereas the technical characteristics of the gauge are listed in Table A1, Appendix.

Despite the fact that strainmeters allow us to observe deformation it is very difficult to derive the actual local stresses from the deformation record. This happens because several factors play a role. The major problem of the strainmeter is that it measures only upper surface deformation. Any bending of the ice due to surface waves, an asymmetric lateral loading or thermal deformation causes non-uniform stress distribution with the depth and therefore wrong estimation of the stress from the strainmeter readings. The second difficulty is to relate strain and stress for different types of deformation process. For a cyclic loading with a period of order of several seconds or for rapid events such as ice cracking the strain-stress relationships are predominantly elastic with some *effective Young's Modulus* averaged through the ice thickness

$$\overline{E} = \int_{o}^{H} E[s(h,\tau), t(h,\tau), \Xi(h,\tau)] \cdot dh \qquad (3.1)$$

With the Young modulus $E$ being a function of ice salinity $s$, temperature $t$ and crystal structure $\Xi$ (i.e. granular, columnar) and therefore varying significantly with depth, information about ice temperature and salinity profiles, and structure becomes apparent. The metamorphoses of ice with seasonal change (variable $\tau$), especially brine drainage, could also obscure the picture. Therefore frequent coring of ice at all locations of the instruments is unavoidable. For slowly varying loads with a typical period of several hours the secondary creep overrules other deformation processes and the viscous flow law could be applied. This makes it again essential to know ice characteristics such as temperature, salinity, and creep-rate compliance. Sanderson (1988) suggested the inversion of the biaxial stress equations under secondary creep conditions, but made a remark that if primary creep occurs the stress

would be higher. However, the most complex strain-stress relationships appear due to rapidly fluctuating loads during, for example, the ridge formation process. These events could last from minutes to hours involving elastic as well as plastic failure and produce intricate signatures in the strain records (Aksenov, 1999c; Sanderson, 1988).

To measure ice stress another type of sensor, the stress-meter could be employed. Stress in any material can be measured only indirectly. For instance, stress can be derived from the deformation of the material itself (using strain gauges as was discussed before) or from that of an elastic body embedded in the medium. To measure ice stress the gauge is usually frozen inside the ice. When ice is under load and deforms, the transducer deforms as well. This deformation can be converted into stress using the known elastic modulus of the transducer and its inclusion factor. The latter is defined as the ratio of the undisturbed ice pressure to the pressure measured by sensor. Generally speaking there are two different types of stress sensors depending on the inclusion factor: so-called "soft" sensors with the overall effective elastic modulus of the transducer nearly equal to or less than surrounding ice, and "stiff" sensors with a elastic modulus much greater than that of ice. On one hand, a stiff sensor tends to overestimate the stress due to stress concentration near the sensor. If this concentration of stress is high it can result in the ice failure near the sensor and lead to measurement errors (Cox and Johnson, 1983). On the other hand, a soft sensor with the elastic modulus significantly lower than that of ice underestimates stress in the surrounding ice because most of the load is supported by ice but not by the sensor. Because the elastic modulus of ice varies from 0.5 to 10 GPa and depends on salinity, temperature, grain size, crystal orientation, and also on loading rate, it is a rather difficult task to develop a sensor which has a more or less constant inclusion factor as the ice properties vary. Here "ice" means the ice as a material, i.e. on the laboratory scale of about 10 cm – 1m, ice cover or geophysical ice will be referred to an ice on the geophysical scale. The possible causes of measurement errors also can be as follows: localised plastic yield around the sensor, differential thermal expansion between ice and gauge, and localised failure of ice around the sensors because of the overloading. It was shown that two particular types of sensors, thin wide sensors with the modulus closer to that of ice and a stiff cylindrical sensor, are not affected by these problems (Templeton, 1979). The main benefit emerging from the use of the soft sensor is to obtain an inclusion factor closer to one. In this case the gauge does not disturb much the stress field near the sensor. On the other hand stiff sensors enable us to measure the high frequency component of the ice

stress which is a great advantage when the inclusion coefficient is well-defined (Cox and Johnson, 1983; Croasdale and Frederking, 1987).

A variety of instruments employed to measure ice stress in the field is described in Croasdale and Frederking (1987) and summarised in Table 3.1. The CRREL biaxial stress gauge used in the SIMI experiment is discussed in more detail.

**Table 3.1.** Ice stress sensors.

| Type of sensor/Manufacturer | Construction | Basis principle of measurements |
|---|---|---|
| IOL (soft sensor)/ESSO Resources, Canada. | Thin, wide double sandwich of aluminium plates (0.79x122x122 cm) with elastomeric core. | Sensor measures changes in electrical capacitance between metal plates due to deformation. |
| UAG (uniaxial sensor)/University of Alaska, USA. | Aluminium cylinder (diameter 2.54 cm diameter, length 7.62 cm). | Gauge uses 4 strain gauges connected in a bridge to read tension and compression and provide temperature compensation. |
| EPR(soft sensor)/Exxon Production, Canada. | Thin, wide aluminium panel (1.1x45 cm). | Sensor uses strain gauges to measure ice pressures normal to the panel. |
| Earth Pressure Cells (pressure sensor). | Two sealed steel plates (20x30x1 cm) filled with hydraulic fluid pressurised by $CO_2$ gas. | Sensor measures pressure of fluid to monitor pressure in the ice. |
| NRC (soft sensor)/National Research Council of Canada. | Thin aluminium tube (outside diameter 5.0 cm, length 10 cm). | Gauge uses 3 strain gauges bonded to the inside to measure circumferential strain. |
| OSI (stiff sensor)/Oceanographic Services Inc. | Steel stiff cylinder (outer diameter 2.86 cm, wall thickness 0.79 cm, length 57.0 cm). | Sensor monitors radial deformation of the cylinder with a vibration wire. |
| CRREL gauge (stiff sensor). | Steel stiff cylinder (diameter 5.7 cm, length 20.3 cm). | Gauge measures radial deformation of the cylinder. |
| Photo-elastic sensor. | – | Stress is determined from iso-chromatic fringe patterns. |

The biaxial ice stress sensor (CRREL) consists of a stiff steel cylinder. It is 20.3 cm long, 5.7 cm in diameter and it has a wall thickness of 1.6 cm (Fig. 3.4c). Principal ice stresses normal to the axis of the gauge are determined by measuring the radial deformation of the cylinder wall in three directions. This is accomplished by the use of vibration wire technology advanced by an IRAD Gauge. The tensioned wires are set 120° from each other across the cylinder diameter. The diametral deformation of the gauge in these directions is determined

[illegible]

[illegible]

[illegible]

[illegible]

by plucking each wire with a magnet/coil assembly and measuring the resonant frequency of the vibrating wires.

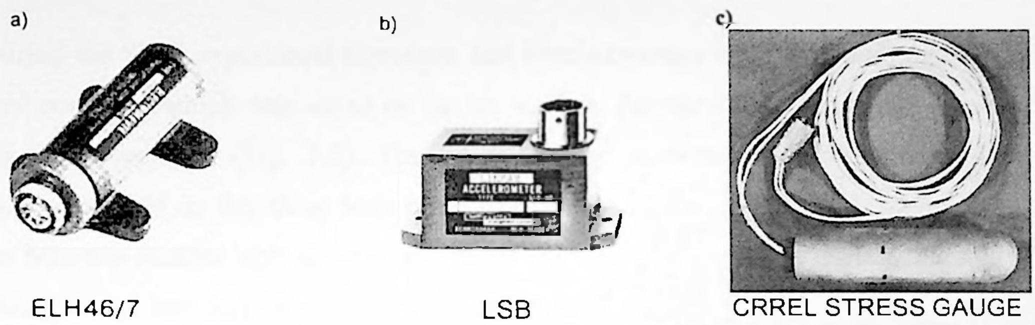


**Figure 3.4** Tiltmeter ELH-46/47 (a), linear accelerometer LSB (b) and CRREL stress gauge (c). (c) – (from Cox and Johnson, 1983).

A thermistor is also placed inside the cylinder to measure the gauge temperature. Both ends of the sensor are sealed to protect the wires and electronics from moisture. The sensor was fabricated by IRD Gauge, Lebanon, N.H., USA. The gauge usually is deployed at a 30-50 cm depth in the ice sheet. The basic characteristics of the CRREL sensor are the following. Linear temperature relation: 5kPa/°C. Resolution - 20kPa. Maximal stress is up to 2.5 MPa (Table A2, Appendix). The CRREL stress sensor was employed to measure local stress during the SIMI experiment.

In support of the deformation measurements the local acceleration and tilt of the ice cover are usually observed by orthogonally mounted "liquid" tiltmeters and three axis inertial accelerometers. The core of an ELH-46/47 tiltmeter sensor produced by TILT Measurements Ltd. (Fig. 3.4a) is a closed bent glass tube - ***vial*** containing a bubble of gas, an electrically conducting liquid and electrodes to make external electrical contact. At any time, the bubble settles at the highest point in the tube. As the vial tilts, the relative position of the bubble to the electrodes changes. This change is converted into an electrical signal and gives an angle of tilt ("Description of Tiltmeter transducers", 1985).

The LSB linear accelerometers (Fig. 3.4b) (Schaevitz Eng. Corp.) are based on the closed loop balance system. Unbalanced motion of a pendulous mass due to oscillation of the accelerometer is detected by a position sensor, the output signal of which is applied to the torque motor through an electronic amplifier. The motor restores the pendulum to the position

before acceleration. The current through the motor is accurately proportional to the input acceleration ("Linear and angular servo accelerometers", 1982). The parameters of instrumentation can be found in Tables A3 and A4, Appendix.

During the SIMI experiment tiltmeters and accelerometers were mounted together inside a special container which was set up on the ice surface. For the ZIP-97 campaign a new set of sensors was developed (Fig. 3.5). The tiltmeters and accelerometers along with a digital compass were built on the same base plate fixed using screws to the ice. It made more stiff contact between sensors and ice and prevented the rocking of sensors during ridging. Three adjustable screws and lock-bolt allowed us to maintain the level position of the sensors even when the surface of an ice floe was not horizontal (Fig. 3.5a).

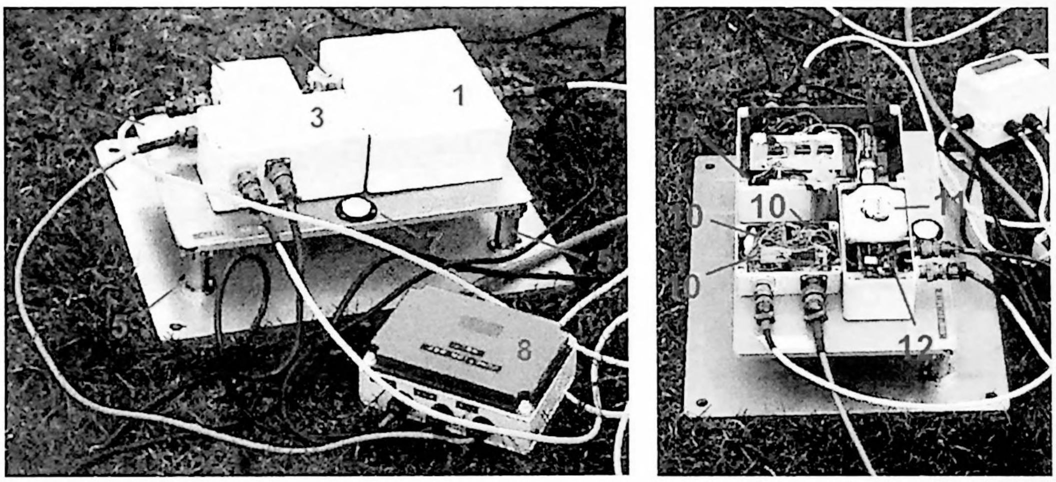


a b

**Figure 3.5.** Base plate with the tiltmeters, accelerometers and digital compass; (a) – general view, (b) – electronics. *1* - tiltmeter housing box; 2 – accelerometer housing box, 3 – digital compass housing box; 4 – lower and upper bases; 5 – adjustable screws; 6- lock-bolt; 7 – level; 8 – signal junction box; 9 – tiltmeter; 10 – accelerometer; 11 – compass; 12 – GPS.

[illegible]

[illegible]

[illegible]





[illegible]

## 3.2 Calibration

The calibration of BP-strainmeters is based on the method developed by British Petroleum (Child and Duckworth, 1989; Westerman and Duckworth, 1984), and it uses the thermal expansion of a hollow triangular calibration jig with a given expansion coefficient. A strainmeter is clamped to the steel plates of the jig, and heated/cooled water is pumped through the calibration jig causing the expansion/contraction of the jig to be measured by the strainmeter. The water temperature was carefully controlled by a thermostat bath. A thermally insulated box (Figs. 3.6 and 3.7a) avoids the cooling of the jig by ambient air.

The author performed the calibration of 12 strainmeters before the fieldwork. Two gauges were destroyed during ice deformation events, thus we were able to calibrate only the remaining set of gauges. For each strainmeter several calibration "runs" were made. Each run included several observations and started as a rule from a temperature of about 20°C with a further temperature increase up to about 40°C followed by a cooling down phase. During the observation output signal from each strainmeter leg ($S^i_j$) along with the temperature of the leg of the calibration jig ($T^i_j$), thermal bath temperature and room temperature were measured. Readings of the strainmeter output were taken with the help of Signal Centre software with an accuracy of ±0.001 volt, whereas the temperature of the calibration jig and thermal bath temperature were measured by a Toshiba thermistor (accuracy ±0.01 °C). Room temperature was monitored by a *Grant Electronics* thermometer with accuracy ±0.1°C. Equation (3.2) shows the relationships to derive the calibration coefficients.

After the correction of the strainmeter output signal for the board gain $g_{board}$ and computer gain $g_{computer}$ (eq. 3.2a) the calibration curve $V^i_j=f(T^i_j)$ was obtained (Fig. 3.7b). The slope of the calibration curve for each strainmeter leg $p^i$ was estimated with the help of the Least Squares Fit method (eq. 3.2a). For each calibration run following equations (3.2b,c) calibration coefficients $k^i_{high,low}$ for the high and low amplification for each strainmeter leg were calculated. In contrast to the installation used by Child and Duckworth (1989) we completely insulated the strain gauge along with the calibration jig from the ambient air. This was aimed at better controlling the thermal deformation of the strainmeter arms. Therefore, the correction of the strainmeter deformation signal for the known thermal expansion of its

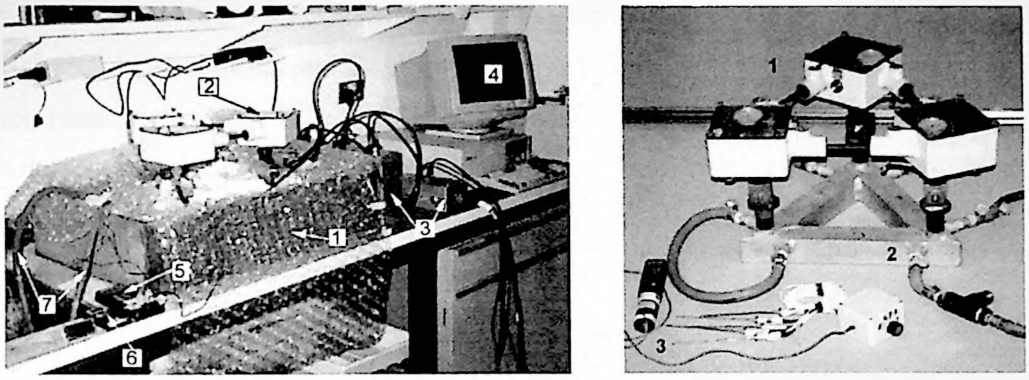


a b

**Figure 3.6.** Thermal calibration of the BP-Delta strainmeter. (a) – general view of the calibration set-up (thermostat bath is on the left outside of the frame). (1) - thermo-insulated box with calibration jig; (2) - strainmeter; (3) - amplifiers; (4) - recording computer; (5) - thermistor to measure temperature of the calibration jig arms; (6) - air and water temperature probe; (7) - water tubes. (b) – view of the sensor attached to the calibration jig. (1) – strainmeter; (2) - calibration jig; (3) – thermal probe.

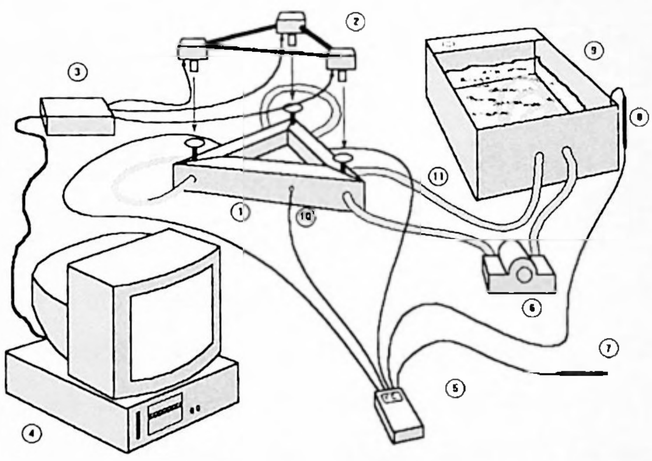


a

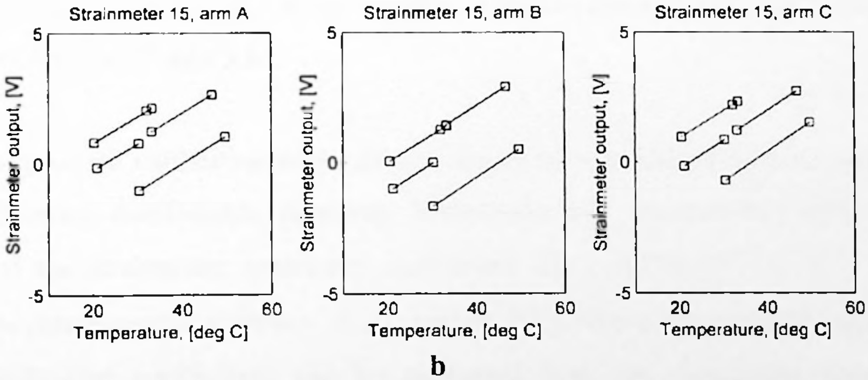


b

**Figure 3.7.** Thermal calibration layout (a) and an example of the calibration curve for the strain gauge N° 15 (b). 1- hollow calibration jig; 2- strainmeter; 3 - amplifier; 4 - recording computer; 5 - thermistor; 6 - water pump; 7 - room temperature probe; 8 - water temperature probe; 9 - thermostat bath; 10 – jig arm temperature probe; 11 - water tubes.

legs was carried out (eq. 3.2b). We used a thermal expansion coefficient of the gauge equal to $2.33\cdot10^{-6}$ [°C$^{-1}$] (Westerman and Duckworth, 1984). Finally the set of calibration coefficients for each strainmeter gauge $k_{high,low}$ *[A,B,C]* was calculated as averages from the series of the calibration runs (eqs. 3.2d,e) with the standard deviation given by equation (3.2e). In spite of being very time-consuming (it took from one to three days to calibrate a single gauge) the above thermal calibration method has an advantage over the mechanical one, as there is no stick-slip error, achieving a good accuracy.

$$p^i = LSM\{T_j^i, V_j^i\}, \qquad V_j^i = S_j^i/(g_{board}\cdot g_{computer}), \qquad i=1,N,\ j=1,M \tag{3.2a}$$

$$k^i_{low}[A,B,C] = \frac{E[A,B,C]}{p^i[A,B,C]\cdot L[A,B,C]} + \frac{K_{thermal\,expansion}}{p^i[A,B,C]}, \qquad i=1,N \tag{3.2b}$$

$$k^i_{high}[A,B,C] = k^i_{low}[A,B,C]/G[A,B,C], \qquad i=1,N \tag{3.2c}$$

$$k_{high,low}[A,B,C] = Mean\{k^i_{high,low}[A,B,C]\} = \frac{1}{N}\sum_{i=1}^{N} k^i_{high,low}[A,B,C] \tag{3.2d}$$

$$Std\{k_{high,low}[A,B,C]\} = \frac{1}{N}\sqrt{\sum_{i=1}^{N}\left(k^i_{high,low}[A,B,C] - k_{high,low}[A,B,C]\right)^2} \tag{3.2e}$$

where, $S^i_j$ , $T^i_j$ – are the output signal from the strainmeter arm and temperature of the strainmeter arm; $V^i_j$ – is the output signal corrected for board and computer gains; $p^i$ – is the slope of the calibration curve calculated with the help of the Least Squares Method (LSM); $k^i_{high,low}$ *[A,B,C]* – is the calibration coefficient for each arm of the strainmeter [m/m/volt] obtained from the single calibration run; $k_{high,low}$ *[A,B,C]* – is the averaged calibration coefficient from the series of the calibration runs [m/m/volt]; $i=1,N$ – is the number of the calibration "runs", and $j=1,M$ – is the number of observations in each calibration "run". For the other notation see Table 3.2.

The original BP calibration tables do not supply us with the information about the errors of the calibration coefficients, however, Westerman and Duckworth (1984) obtained the accuracy of the strainmeter sensitivity coefficient $\Delta\alpha = \pm0.03\cdot10^{-6}$ [m·°C$^{-1}$] relative to a temperature measurement accuracy of $\Delta T = \pm0.01$ [°C]. The corresponding maximal error in the BP calibration coefficients can be estimated from the elementary theory of errors described in detail in the majority of the textbooks on observational analysis.

**Table 3.2.** Strainmeter parameters.

| Parameter | Notation | Units | Value |
|---|---|---|---|
| Output signal from the strainmeter arm | $S'_i$ | [volts] | variable |
| Board gain | $g_{board}$ | [n/d] | 1 |
| Computer gain | $g_{computer}$ | [n/d] | 1 |
| Output signal in corrected for the gains | $V'_i$ | [volts] | variable |
| Minimal change in the output signal from the strainmeter arm | $V_\delta [A,B,C]\|_{min}$ | | variable |
| Maximal error in output signal measurements | $\Delta V_\delta [A,B,C]\|_{max}$ | [volts] | $1\cdot10^{-3}$ |
| Temperature of the strainmeter arm | $T'_i$ | [°C] | variable |
| Maximal temperature change of the strainmeter arm | $T_\delta [A,B,C]\|_{max}$ | [°C] | variable |
| Maximal error in temperature measurements | $\Delta T_\delta [A,B,C]\|_{max}$ | [°C] | $1\cdot10^{-2}$ |
| Slope of the calibration curve | $p^i$ | [volt·°C$^{-1}$] | variable |
| Minimal value of the calibration curve slope | $p[A,B,C]\|_{min}$ | [volt·°C$^{-1}$] | variable |
| Maximal error of the calibration curve slope from current calibration | $\Delta p[A,B,C]\|_{max}$ | [volt·°C$^{-1}$] | $6\cdot10^{-3}$ |
| Minimal value of the calibration curve slope from BP calibration | $p_{BP}[A,B,C]\|_{min}$ | [volt·°C$^{-1}$] | variable |
| Maximal error of the calibration curve slope from BP calibration | $\Delta p_{BP} [A,B,C]\|_{max}$ | [volt·°C$^{-1}$] | variable $1\cdot10^{-4}$ |
| Thermal expansion of the jig arms | $E[A,B,C]$ | [m·°C$^{-1}$] | variable |
| Maximal thermal expansion coefficients of the jig arms | $E[A,B,C]\|_{max}$ | [m·°C$^{-1}$] | variable |
| Maximal error in the thermal expansion coefficients of the jig arms | $\Delta E[A,B,C]\|_{max}$ | [m·°C$^{-1}$] | $5\cdot10^{-10}$ |
| Length of the corresponding strainmeter arm | $L[A,B,C]$ | [m] | 0.3 |
| Error in the strainmeter arm length measur. | $\Delta L[A,B,C]$ | [m] | $1\cdot10^{-6}$ |
| High/low gain ratio for the strainmeter amplifiers | $G[A,B,C]$ | [n/d] | variable |
| Minimal high/low gain ratio for the strainmeter amplifiers | $G[A,B,C]\|_{min}$ | [n/d] | 10.18 |
| Maximal error estimate of the minimal high/low gain ratio for the strainmeter amplifiers | $\Delta G[A,B,C]\|_{max}$ | [n/d] | $5\cdot10^{-3}$ |
| Thermal expansion of the strainmeter arm | $K_{thermal\ expansion}$ | [m·m$^{-1}$·°C$^{-1}$] | $2.33\cdot10^{-6}$ |
| Error in the expansion coefficient | $\Delta K_{thermal\ expansion}$ | [m·m$^{-1}$·°C$^{-1}$] | $5\cdot10^{-9}$ |
| Maximal strainmeter sensitivity | $\alpha$ | [m·°C$^{-1}$] | $6.86\cdot10^{-6}$ |
| Maximal error of the strainmeter sensitivity | $\Delta\alpha$ | [m·°C$^{-1}$] | $3\cdot10^{-8}$ |
| Maximal strainmeter calibration coefficient | $k_{high,low}\|_{BP}$ | [m·m$^{-1}$·volt$^{-1}$] | variable |
| Maximal error of the strainmeter calibration coefficient from BP calibration | $\Delta k^i_{high,low}\|_{BP}$ | [m·m$^{-1}$·volt$^{-1}$] | variable |
| Maximal relative error of the strainmeter calibration coefficient for BP calibration | $\varepsilon k_{high,low}\|_{BP}$ | [%] | variable |
| Calibration coefficient for each arm of the strainmeter | $k^i_{high,low} [A,B,C]$ | [m·m$^{-1}$·volt$^{-1}$] | variable |
| Averaged calibration coefficient for each arm of the strainmeter | $k_{high,low} [A,B,C]$ | [m·m$^{-1}$·volt$^{-1}$] | variable |
| Maximal error of the strainmeter calibration coefficient from current calibration | $\Delta k^i_{high,low}\|_{max}$, | [m·m$^{-1}$·volt$^{-1}$] | variable |
| Maximal relative error of the strainmeter calibration coefficient for current calibration | $\varepsilon k_{high,low}\|_{max}$ | [%] | variable |

Following equations (3.3a-d) we derived the accuracy of the calibration coefficients as $\Delta k_{low}|_{BP}$ =±1.47·10$^{-6}$ [volt$^{-1}$] for the low and $\Delta k_{high}|_{BP}$ =±1.59·10$^{-7}$ [volt$^{-1}$] and for high amplification (gain) respectively. However, based on the same principles our estimates for the errors in the calibration coefficients (eqs. 3.3f-h) are somewhat higher: $\Delta k_{low}|_{\max}$ =±1.65·10$^{-5}$ [volt$^{-1}$] and $\Delta k_{high}|_{\max}$ =±1.64·10$^{-6}$ [volt$^{-1}$] for the low and high gains respectively. We believed that such relatively higher errors were caused by the fact that we were not able to perform many calibration "runs" for each strain gauge and therefore the dispersion of the values of the calibration curve slope was rather high. However, even in this case the maximal relative error of the coefficients $\varepsilon k_{high,low}|_{max}$ did not exceed 7.6 percent comparing to maximal error $\varepsilon k'_{high,low}|_{BP}$ of about 0.7 percent in BP calibration (eqs. 3.3c,e and 3.3g,i and Table T11, Tables: Calibration coefficients).

Three errors, namely "BP estimates" ($\Delta k_{high}|_{BP}$, $\Delta k_{low}|_{BP}$), error estimates from the current calibration ($\Delta k_{high}|_{\max}$), $\Delta k_{low}|_{\max}$), and the maximal standard deviation of the calibration coefficient $Std\{k_{high,low}\}|_{\max}$ equal to 1.17·10$^{-6}$ [volt$^{-1}$] and 1.18·10$^{-5}$ [volt$^{-1}$] respectively (eq. 3.2c) were calculated. Because both sets of errors ($\Delta k_{high}|_{\max}$), $\Delta k_{low}|_{\max}$) and $Std\{k_{high,low}\}|_{\max}$ were affected by the high dispersion of the calibration curve slope we chose the BP estimates as the maximal error estimates for the strainmeter calibration coefficients. It gives us the values of $\Delta k_{low}|_{BP}$ =±1.47·10$^{-6}$ [volt$^{-1}$] and $\Delta k_{high}|_{BP}$ =±1.59·10$^{-7}$ [volt$^{-1}$] for the low and high gains, and the relative maximal errors for the calibration coefficient $\varepsilon k_{high,low}^{\max}$ were estimated as 0.7 percent. Finally, the accuracy of the deformation measurements can be derived in a similar manner using error estimates for the calibration coefficients (see next section).

Results of the calibration calculations are presented in Tables T1-T9 (Tables: Calibration coefficients). Comparison of the results of the calibration with those done by BP (Westerman and Duckworth, 1984) showed a statistically insignificant difference between mean values (Table T10, Tables: Calibration coefficients). However, the calibration coefficients derived from the mechanical calibration method (Duckworth, personal communication, 1995) were about 20 percent lower than those from the thermal calibration method. Stick-slip error induced by the method of the mechanical calibration is thought to be the reason for such a difference (Duckworth, personal communication, 1995). On the basis of the comparison the

$$k_{low}\big|_{BP} = \frac{\alpha}{p_{BP}[A,B,C]\big|_{min} \cdot L[A,B,C]} \tag{3.3a}$$

$$\Delta k_{low}\big|_{BP} = \frac{\Delta\alpha}{p_{BP}[A,B,C]\big|_{min} \cdot L[A,B,C]} + \tag{3.3b}$$

$$+\frac{\alpha\big|_{max} \cdot \Delta p_{BP}[A,B,C]\big|_{max}}{p_{BP}[A,B,C]\big|_{min}^{2} \cdot L[A,B,C]} + \frac{\alpha\big|_{max} \cdot \Delta L[A,B,C]}{p_{BP}[A,B,C]\big|_{min} \cdot L[A,B,C]^{2}}$$

$$\varepsilon k_{low}\big|_{BP} = \frac{\Delta\alpha}{\alpha\big|_{min}} + \frac{\Delta p_{BP}[A,B,C]\big|_{max}}{p_{BP}[A,B,C]\big|_{min}} + \frac{\Delta L[A,B,C]}{L[A,B,C]} \tag{3.3c}$$

$$\Delta k_{high}\big|_{BP} = \frac{\Delta k_{low}\big|_{BP}}{G[A,B,C]\big|_{min}} + \frac{\Delta G[A,B,C]\big|_{max} \cdot k_{low}\big|_{BP}}{G[A,B,C]^{2}\big|_{min}} \tag{3.3d}$$

$$\varepsilon k_{high}\big|_{BP} = \frac{\Delta k_{low}\big|_{BP}}{k_{low}\big|_{BP}} + \frac{\Delta G[A,B,C]\big|_{max}}{G[A,B,C]\big|_{min}} \tag{3.3e}$$

$$\Delta k_{low}\big|_{max} = \frac{\Delta E[A,B,C]\big|_{max}}{p[A,B,C]\big|_{min} \cdot L[A,B,C]} + \frac{\Delta p[A,B,C]\big|_{max} \cdot E[A,B,C]\big|_{max}}{p[A,B,C]^{2}\big|_{min} \cdot L[A,B,C]} + \tag{3.3f}$$

$$+\frac{\Delta L[A,B,C] \cdot E[A,B,C]\big|_{max}}{p[A,B,C]\big|_{min} \cdot L[A,B,C]^{2}} + \frac{\Delta K_{thermal\,expansion}}{p[A,B,C]\big|_{min}} + \frac{\Delta p[A,B,C]\big|_{max} \cdot K_{thermal\,expansion}}{p[A,B,C]^{2}\big|_{min}}$$

$$\varepsilon k_{low}\big|_{max} = \frac{\Delta p[A,B,C]\big|_{max}}{p[A,B,C]\big|_{min}} + \frac{\Delta L[A,B,C]}{L[A,B,C]} + \tag{3.3g}$$

$$+\frac{\Delta E[A,B,C]\big|_{max} + \Delta K_{thermal\,expansion} \cdot L[A,B,C] + \Delta L[A,B,C] \cdot K_{thermal\,expansion}}{E[A,B,C]\big|_{min} + L[A,B,C] \cdot K_{thermal\,expansion}}$$

$$\Delta k_{high}\big|_{max} = \frac{\Delta k_{low}\big|_{max}}{G[A,B,C]\big|_{min}} + \frac{\Delta G[A,B,C]\big|_{max} \cdot k_{low}\big|_{max}}{G[A,B,C]^{2}\big|_{min}} \tag{3.3h}$$

$$\varepsilon k_{high}\big|_{max} = \frac{\Delta k_{low}\big|_{max}}{k_{low}\big|_{min}} + \frac{\Delta G[A,B,C]\big|_{max}}{G[A,B,C]\big|_{min}} \tag{3.3i}$$

**Notation:** $T_\delta\,[A,B,C]\,|_{max}$ and $V_\delta\,[A,B,C]\,|_{min}$ – are the maximal temperature change of the strainmeter arm and the minimal change in the correspondent output signal from the strainmeter arm; $\Delta T_\delta\,[A,B,C]\,|_{max}$ and $\Delta V_\delta\,[A,B,C]\,|_{max}$ – are the estimates of the maximal error; $\alpha$ – is the maximal strainmeter sensitivity and $\Delta\alpha$ – is the maximal error of the strainmeter sensitivity following Westerman and Duckworth (Westerman and Duckworth, 1984); $k_{high,low}\,|_{BP}$ – is the maximal value of the strainmeter calibration coefficient [m/m/volt] for high and low gains; $\Delta k^{j}_{high,low}\,|_{max}$, $\Delta k^{j}_{high,low}\,|_{BP}$ – are the estimates of the maximal error of the strainmeter calibration coefficient [m/m/volt] for the present calibration and for calibration carried out by BP. Other notations are shown in Table 3.2.

original calibration coefficients obtained by the manufacturer (Westerman and Duckworth, 1984) were chosen with confidence limits derived from the current calibration. The calibration coefficients for the gauges, used for the data processing for the SIMI and ZIP-97 experiments are shown in Tables T12 and T13, Tables: Calibration coefficients).

In order to detect the lowest measurable strain, a set of noise tests was performed. The set up for the tests was the same as for calibration, however the jig was maintained at a constant temperature all the time. Random fluctuation in the strainmeter signal for the given constant length of the jig was taken as a noise level in the gauge chain. From these experiments we adopted a noise level of about $1 \cdot 10^{-8}$ [$m \cdot m^{-1}$] for a 12-bit digital card.

The calibration of the tiltmeters was performed with the help of the base with variable tilt angle (D. Crane, personal communication). The results of the calibration are listed in Table T14, Tables: Calibration coefficients). For the accelerometers, as their characteristics are very stable, the calibration made by the manufacturer was used (Table T15, Tables: Calibration coefficients).

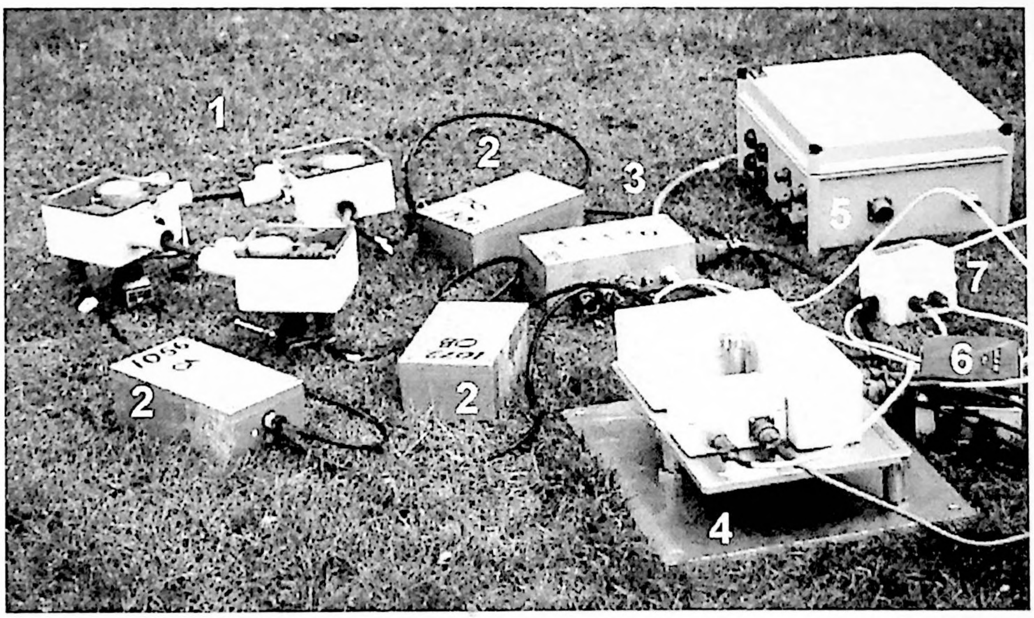


**Figure 3.8.** The set of sensors to measure the local ice deformation and motion. BP-Delta strainmeter (1) together with the electronic circuit boxes (2) and indicating box (3); (4) – base plate with tiltmeters and accelerometers, (5) – recording computer, (6) – signal junction box, (7) – power junction box.

## 3.3 Data recording and processing

The analogue data from the sensors were transmitted via cables or a VHF telemetry system, amplified, processed by anti-alias analogue filters, digitised and recorded on a logger system (Fig. 3.9). Two logging systems a SQUIRREL Logger (Grant Electronics) and a waterproof computer developed at SPRI, were used to store the data (Figs. 3.8 and 3.10). A detachable monitor allowed us to control the data logging and downloading in fair weather conditions while for unmanned recording it is detached and the computer is fully waterproof. The recording on the computer employed MS Windows-based *Signal Centre Software* (developed by Signal Centre Inc.). The data were recorded as non-stop segments of several hours with short breaks in between for data downloading, stored in binary form and further converted to ASCII codes.

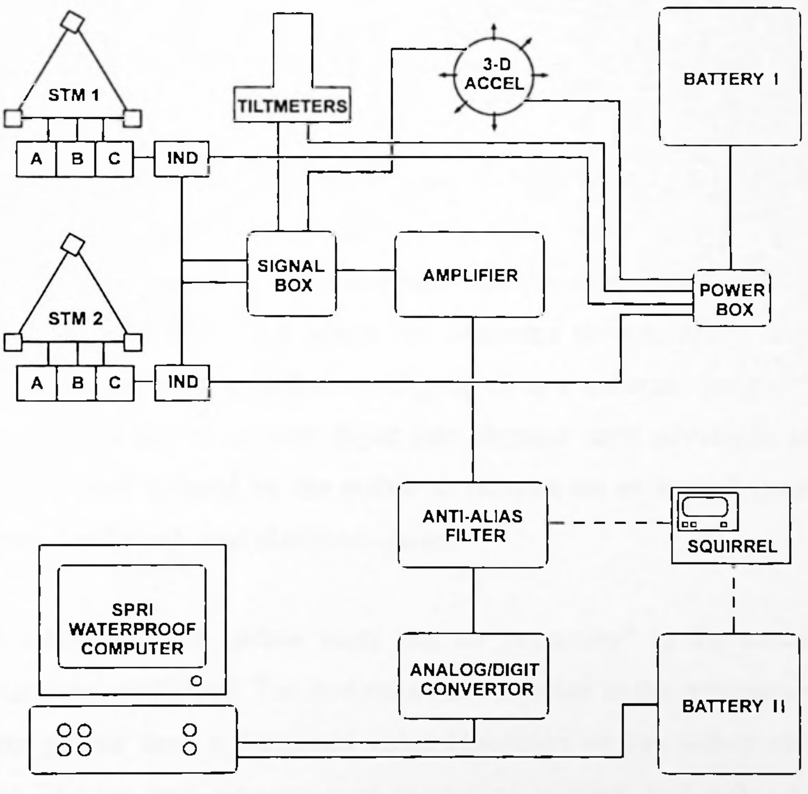


**Figure 3.9.** Schematic for two data logging systems: SQUIRREL (dashed lines show the SQUIRREL logger connection) and Signal Centre. Key: STM 1,2 – strainmeters; A,B,C – strainmeter electronic circuit boxes; IND – strainmeter indicator boxes; 3-D ACCEL – accelerometers to measure three-dimensional acceleration; SIGNAL BOX – signal junction boxes; POWER BOX – power junction boxes.

Data processing includes data digitising procedure, conversion and so-called *"de-glitching"* correction procedure of the strain data (schematic is shown in Fig. 3.11a). These three stages are denoted as processes P1, P2, and P3 in Fig. 3.11a. While computer logging produces a digital signal (S2, Fig. 3.11a), the SQUIRREL logger stores data in analogue form (S1, Fig. 3.11a), which requires additional processing. The program *sqtrans* supplied by Grant

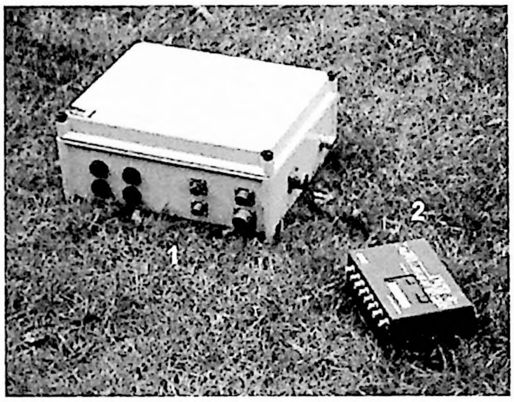


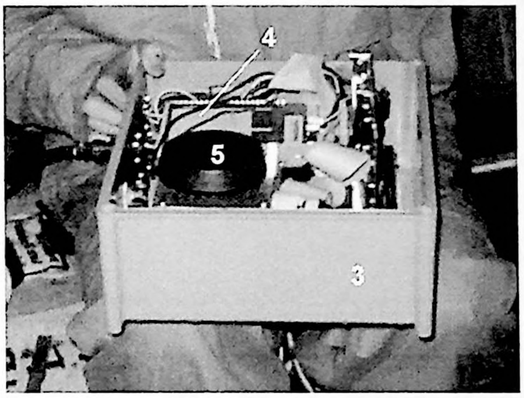


**Figure 3.10.** Data loggers. General view (a) and electronics of the recording computer (b). (1) – recording computer; (2) – SQUIRREL Logger (Grant Electronics); (3) – carbon-reinforced waterproofed computer box; (4) – hard-disk; (5) – GPS antenna.

Electronics was used to digitise the data in this case. In both cases when we used either the SQUIRREL logger or the *Signal Centre* software the data format required conversion into ASCII form with further re-sampling and conversion into physical units (S3, Fig. 3.11a). The program *sqtrans* produces ASCII files which are subjected to re-sampling and calibration procedures. To process the data recorded via *Signal Centre* software programs to convert binary data to into ASCII and to convert digits into physical units developed at SPRI were employed. The latter were updated by the author to process set of several instruments with different calibration coefficients and electronic gains.

To de-glitch strain data, i.e. delete steps due to "rezeroing" in the strain record, the following procedure was employed. The raw record is subjected to the programs which detect artificial step data greater than a permitted value (modified by the author versions of the SPRI's programs). The program removes such re-zeroing glitches, and makes a second pass through the data set to remove glitches introduced by "re-zero overshoots". This permits identification of the artificial steps in the record, and allows the correction procedure to be applied without any data loss (Craze, 1995). Figure 3.11 shows the schematic of the

[illegible]

[illegible]



[illegible]

[illegible]

[illegible]

processing and gives an example of the strainmeter data processing, while equations (3.4) describe the stages of the data processing for all types of sensors.

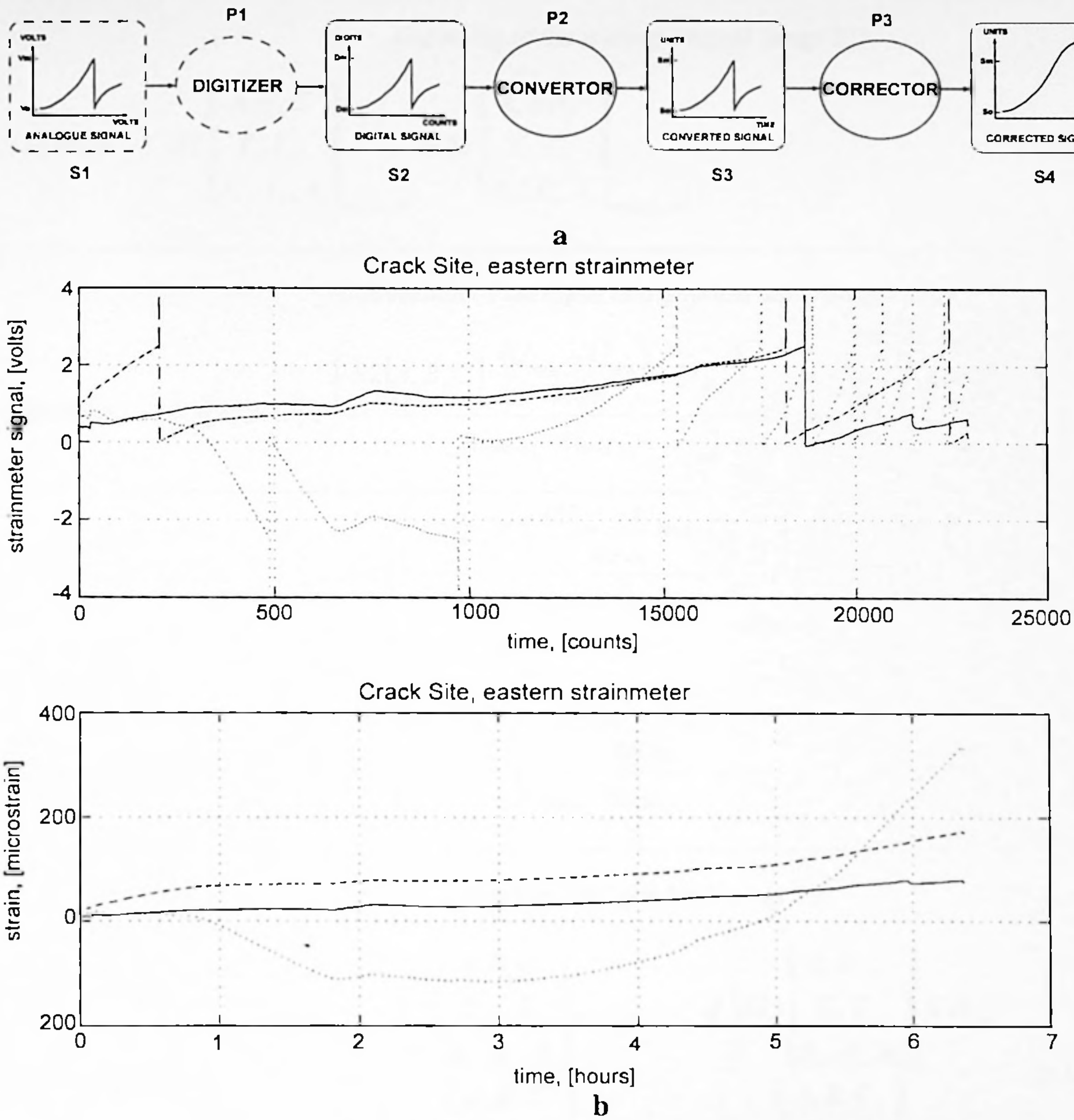


**Figure 3.11.** Schematic of the data processing (a); an example of the raw and processed strainmeter record (b). S1, S2, S3, S4 – are the stages of the signal processing. P1, P2, P3 – are digitising, conversion, and correction procedures.

The error in the measurements depends on the level of the output signal therefore it varies with time (Fig. 3.12). Nevertheless, using the error estimates of the calibration coefficients (section 3.2) we were able to derive the maximal total error of the strain measurements from equations (3.5a,b) tilt measurements from equations (3.5c,d) and 3-D acceleration measurements from equations (3.5e,f). These formulas were obtained in the same manner as

| Sensors | Stage of processing | |
|---|---|---|
| | Digitising of the analogue signal (stage P1) | |
| all sensors | $S2\begin{bmatrix} A,B,C \\ T_1,T_2 \\ A_x,A_y,A_z \end{bmatrix}_{n=1,2,\dots N} = S1\begin{bmatrix} A,B,C \\ T_1,T_2 \\ A_x,A_y,A_z \end{bmatrix}_{t=t1,t2,\dots tN}$ | (3.4a) |
| | Conversion of the digits into physical units (stage P2) | |
| strainmeter | $S3[A,B,C]=\dfrac{\left(S2[A,B,C]\cdot\dfrac{(U_{max}-U_{min})}{4096}+U_{min}\right)}{g_{computer}\cdot g_{board}}\cdot k_{high}[A,B,C]$ | (3.4b) |
| tiltmeter | $S3[T_1,T_2]=\arctan\left(\dfrac{\left(S2[T_1,T_2]\cdot\dfrac{(U_{max}-U_{min})}{4096}+U_{min}\right)}{g_{computer}\cdot g_{board}}\cdot\alpha_{46/47}+\beta_{46/47}\right)$ | (3.4c) |
| accelerometer | $S3[A_x,A_y,A_z]=\dfrac{\left(S2[A_x,B_y,C_z]\cdot\dfrac{(U_{max}-U_{min})}{4096}+U_{min}\right)}{g_{computer}\cdot g_{board}}\cdot\gamma_{xyz}[A_x,A_y,A_z]$ | (3.4d) |
| | Correction for "glitches" (stage P3) | |
| strainmeter | $S4\begin{bmatrix} A,B,C \\ T_1,\ T_2 \\ A_x,A_y,A_z \end{bmatrix}=\begin{cases} S3\begin{bmatrix} A,B,C \\ T_1,\ T_2 \\ A_x,A_y,A_z \end{bmatrix}, & if \left\vert\delta S3\begin{bmatrix} A,B,C \\ T_1,T_2 \\ A_x,A_y,A_z \end{bmatrix}\right\vert \le \delta S_{lim} \\ S3\begin{bmatrix} A,B,C \\ T_1,T_2 \\ A_x,A_y,A_z \end{bmatrix}+\delta S_{lim}, & if \left\vert\delta S3\begin{bmatrix} A,B,C \\ T_1,T_2 \\ A_x,A_y,A_z \end{bmatrix}\right\vert > \delta S_{lim} \end{cases}$ | (3.4e) |

**Notation:** $S3[A,B,C][T_1,T_2][A_x,A_y,A_z]$ and $S4[A,B,C][T_1,T_2][A_x,A_y,A_z]$ – is the output signals in digits from strainmeters, tiltmeters or accelerometers, and their values in [m·m$^{-1}$], [radians], and [m·s$^{-2}$] respectively; $U_{max}$, $U_{min}$ – maximal and minimal output signal [volt]; 4096=$2^{12}$ – number of digits in the signal range for the 12-bit card; $\alpha_{46/47}$ – slope of the calibration curve for the tiltmeters *ELH-46* and *ELH-47*, equal to 105.61·$10^{-3}$ [volt$^{-1}$] and 10.561·$10^{-3}$ [volt$^{-1}$]; $\beta_{46/47}$ =-0.37204·$10^{-3}$ [volt$^{-1}$] – offset for the tiltmeter calibration curve; $\Upsilon_{xyz}$ = 3.8011 [m·s$^{-2}$·volt$^{-1}$] – accelerometer calibration coefficient; $\delta S3[A,B,C;T_1,T_2;A_x,A_y,A_z]$ – difference between two neighbouring values of the digital signal; $\delta S3_{lim}$ – empirically derived maximal allowed difference between two neighbouring values of the digital signal; *t1,t2,...tN* – time when digital samples were taken; *n=1,2,...N* – discreet sample number. For other notations see Table 3.2.

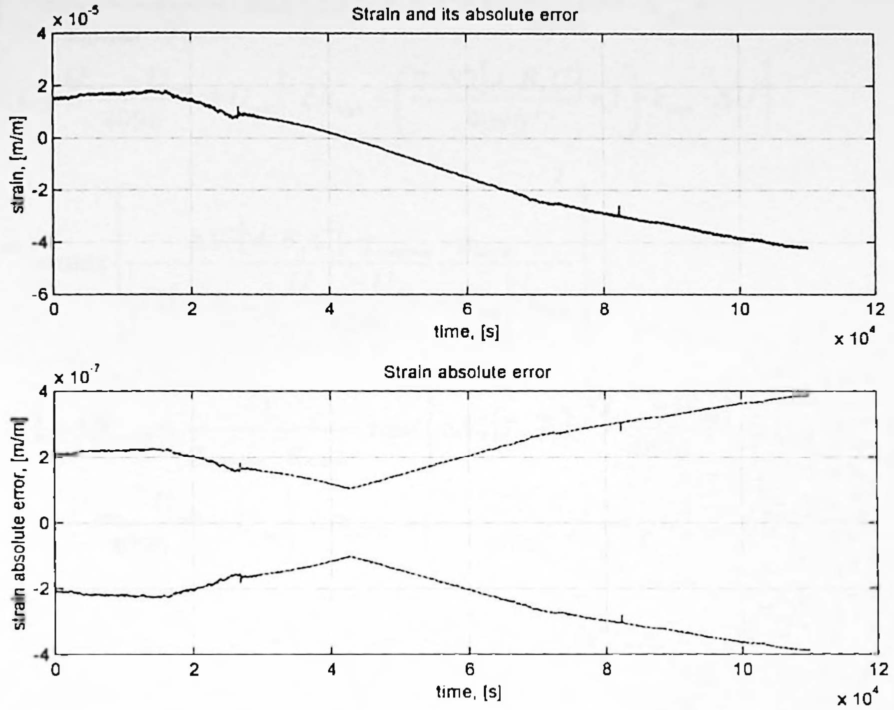


**Figure 3.12.** An example of the absolute error estimates for the strain measurements.

were equations (3.3). The relationships for the tiltmeters were obtained with the help of Taylor expansion on the assumption of a small tilt of the floe. Equations (3.5) give the maximal error of deformation measurements of about $9.3 \cdot 10^{-7}$ [m·m$^{-1}$] for the level of the signal of about 10 volts and signal accuracy $\pm 1$ digit. The corresponding deformation is about $1.18 \cdot 10^{-4}$ [m·m$^{-1}$], therefore the relative error does not exceed 0.8 percent. We believe that this level of accuracy is more realistic than the error of strain measurements of $3 \cdot 10^{-8}$ [m·m$^{-1}$] acknowledged by Duckworth and Westerman (1989). Their estimate is based on the resolution of the sensor used along with a 12-bit digitising card, and does not take into account errors in calibration coefficient and output signal. For the level of the output signal of about 3.5 volts the level of the tilt is about $1.5 \cdot 10^{-3}$ [radians] (ELH-46), or $2.0 \cdot 10^{-4}$ [radians] (ELH-47). For this level of the signal the accuracy of the tilt measurements is of about $1.05 \cdot 10^{-5}$ [radians] (0.7 percent) for an ELH-46 sensor, and $1.15 \cdot 10^{-6}$ [radians] (0.6 percent) for an ELH-47 sensor. The accuracy of the acceleration measurements is about $1.2 \cdot 10^{-4}$ [m·s$^{-2}$] for the level of acceleration of about $5.9 \cdot 10^{-3}$ [m·s$^{-2}$]. The relative error estimate for acceleration is about 2.1 percent.

[illegible]

$$\Delta S[3,4]^{strn} = \frac{1}{g_{computer}\cdot g_{board}}\cdot \max\left\{ \Delta S2[A,B,C]\cdot\frac{|U_{max}-U_{min}|}{4096}\cdot k_{high} + \left|S2[A,B,C]\cdot\frac{U_{max}-U_{min}}{4096}+U_{min}\right|\cdot\Delta k_{high} + \left(\frac{2\cdot S2[A,B,C]}{4096}+1\right)\cdot k_{high}\cdot\Delta U\right\} \tag{3.5a}$$

$$\varepsilon S[3,4]^{strn} = \max\left\{\frac{\Delta S3[A,B,C]\cdot g_{computer}\cdot g_{board}}{\left|\left|S2[A,B,C]\cdot\frac{U_{max}-U_{min}}{4096}+U_{min}\right|\cdot k_{high}\right|}\right\} \tag{3.5b}$$

$$\Delta S3[T_1,T_2] = \Delta\beta_{46/47} + \frac{1}{g_{computer}\cdot g_{board}}\cdot\max\left\{\Delta S2[T_1,T_2]\cdot\frac{|U_{max}-U_{min}|}{4096}\cdot\alpha_{46/47} + \left|S2[T_1,T_2]\cdot\frac{U_{max}-U_{min}}{4096}+U_{min}\right|\cdot\Delta\alpha_{46/47} + \left(\frac{2\cdot S2[T_1,T_2]}{4096}+1\right)\cdot\alpha_{46/47}\cdot\Delta U\right\} \tag{3.5c}$$

$$\varepsilon S[3,4]^{tilt} = \max\left\{\frac{\Delta S3[T_1,T_2]\cdot g_{computer}\cdot g_{board}}{\left|\left|S2[T_1,T_2]\cdot\frac{U_{max}-U_{min}}{4096}+U_{min}\right|\cdot\alpha_{46/47}+\beta_{46/47}\cdot g_{computer}\cdot g_{board}\right|}\right\} \tag{3.5d}$$

$$\Delta S[3,4]^{acc} = \frac{1}{g_{computer}\cdot g_{board}}\cdot\max\left\{\Delta S2[X,Y,Z]\cdot\frac{|U_{max}-U_{min}|}{4096}\cdot\gamma_{xyz} + \left|S2[X,Y,Z]\cdot\frac{U_{max}-U_{min}}{4096}+U_{min}\right|\cdot\Delta\gamma_{xyz} + \left(\frac{2\cdot S2[X,Y,Z]}{4096}+1\right)\cdot\gamma_{xyz}\cdot\Delta U\right\} \tag{3.5e}$$

$$\varepsilon S[3,4]^{acc} = \max\left\{\frac{\Delta S3[X,Y,Z]\cdot g_{computer}\cdot g_{board}}{\left|\left|S2[X,Y,Z]\cdot\frac{U_{max}-U_{min}}{4096}+U_{min}\right|\cdot\gamma_{xyz}\right|}\right\} \tag{3.5f}$$

**Notation:** $\Delta S4|_{max}$, $\varepsilon S4|_{max}$ – are the error estimates for the deformation measurements [m·m$^{-1}$], tilt measurements [radians], acceleration measurements [m·s$^{-2}$]; $\Delta U = 1\cdot10^{-3}$ [volts] – is the accuracy of the both maximal and minimal values of the output signals $U_{max}$ and $U_{min}$; $\Delta\alpha_{46} = 5\cdot10^{-6}$ [volt$^{-1}$], $\Delta\alpha_{47} = 5\cdot10^{-7}$ [volt$^{-1}$], $\Delta\beta_{46/47} = 5\cdot10^{-9}$ [volt$^{-1}$], $\Delta\Upsilon = 9.5\cdot10^{-3}$ [volt·g$^{-1}$] – error estimates for the tiltmeter and accelerometer calibration parameters. For other notations see Table 3.2.

When the output signal is close to zero the "small error assumption" is no longer valid, and the relative error can be large. To avoid this we have introduced the minimal measurable, so-called "blank" level of the signal. It was chosen as $\pm\Delta S4|_{max}$ for each type of sensor.

[illegible]

[illegible]

[illegible]

# Part II. Description of the experiments

In our study we relied mainly on two field experiments: the *Sea Ice Mechanics Initiative* (SIMI) Camp, Beaufort Sea, 1993-1994 and the *Zooming in Ice Physics* (ZIP–97) field campaign, spring 1997, Bay of Bothnia, Baltic Sea. The author took part in ZIP-97 himself. The processing and analysis of the data collected on SIMI by Dr. P. Wadhams et al. (Scott Polar Research Institute), Dr. J. Richter-Menge et al. (Cold Regions Research and Engineering Laboratory) and Dr. J. Overland et al. (Pacific Marine Environmental Laboratory) were largely the author's work as well. The initial results obtained from these field experiments were reported earlier (Aksenov, 1999a; Overland et al., 1998; Richter-Menge and Elder, 1998; Wadhams and Wells, 1995;), however, the first consistent analysis of the SIMI data has been performed by the author and presented in this thesis for the first time.

## 3.4 Zooming in Ice Physics Field Campaign

### 3.4.1 Overview of the campaign

The ZIP-97 field campaign was organised by the ICE STATE project and funded by European Marine Science and Technology Programme (MAST-III). The aim of the experiment was to study the mechanics of a sea ice cover on three spatial scales: basin-wide (order of hundred kilometres), intermediate (from several kilometres up to several tens of kilometres) and local (from several tens of metres up to hundreds of metres) scales. Sometimes the intermediate scale is called "mesoscale", due to the proximity of this scale to the Rossby scale in the ocean. The first objective was to observe ice drift and deformation on these scales, and investigate the relationship between ice deformation processes. The second objective was to measure thickness distribution and geometrical properties of the ice cover (including fragmentation of the ice cover, orientation of the shear zones and leads, size of ice blocks in ridges, etc.), and relate their evolution to ice deformation processes. The third was to study in detail ridging and rafting processes of the sea ice cover and to evaluate the different remote sensing techniques allowing us to measure morphological properties of ice and monitor its dynamics. The experiment was also designed to provide a comparison where

possible between ice deformations occurring in nature and those generated under laboratory conditions in the Large Scale Ice Tank at the Helsinki University of Technology.

Nine institutions from Finland, Great Britain, Iceland, Norway and Russia participated in the field campaign. The Department of Geophysics of the University of Helsinki (Prof. Matti Leppäranta) was in charge of the planning and organisation of the campaign. The observational programme consisted of observations of ice deformation and ice kinematics; measurements of the ice thickness and observations of ice morphology. The supporting information included meteorological observations, real time monitoring of ice conditions within the experimental area, current measurements within the near ice water boundary layer and observational programme on ice thermophysics. The latter incorporated ice temperature profiling along with ice salinity measurements and ice structure observations. Such an extensive observational programme required sophisticated planning and much logistical support and involved the use of light aircraft, helicopters, and a research ship. The operational centre of the campaign received satellite imagery and meteorological information from neighbouring weather stations in real time.

The experiment took place in March 1997 in the Bay of Bothnia (Fig. 3.13). The Bay of Bothnia is the most northern part of the Baltic Sea. It has an area of about 37 000 km$^2$ and lies within the region 63°N – 66°N and 20°E – 26°E. The bay is about 300 km long and about 80 km wide in its southern part and about 200 km wide in the northern part. The water depth varies between 5 and 147 m. There is a group of scattered islands in the north of the bay with Hailuoto Island (65°N, 24.7°E) being the largest amongst them. The water in the bay is relatively fresh with a salinity in the mixed layer of about 3–4 psu. The average depth of the halocline is between 40 and 50 m. As a rule sea ice appears every winter in the bay at the beginning of December and stays for more than six months. The bay is frequently covered by ice completely. The maximal ice thickness near the shore can reach 120 cm. However, ice ridging and multiple rafting are the main mechanisms responsible for the formation of thick ice. Winter storms can clear a large part of the bay, compressing the ice cover against the coast. This can increase the thickness of ridged ice up to 15 m. Grounded ridges and extensive piling up of ice against the shore are common phenomena in the eastern part of the basin. The wide land-fast ice zone in the eastern part of the bay is more stable than drifting ice. Its outer border follows the 50 m isobath and is partly anchored by grounded ridges on shoals. The

buffer zone between land-fast ice and drifting pack ice consists of severely fragmented ice and often the shear slip lines are formed in this zone. Typical maximal velocity of ice drift is about 10–30 cm/s, and in extreme cases can be as high as 50 cm/s (Haapala and Stipa, 1997). The fragmentation of ice cover varies significantly within the basin. The size of ice fragments can be as small as one metre (the size of ice rubble) and as large as several kilometres (the size of a large ice floe). The ice consists of granular and columnar types of ice with a typical salinity of about 0.5–1 psu (Cheng, 2001). Congelation is thought to be the dominant process of ice growth in the Baltic Sea, with the infiltrated type of ice contributing about 10–30 percent in total ice volume.

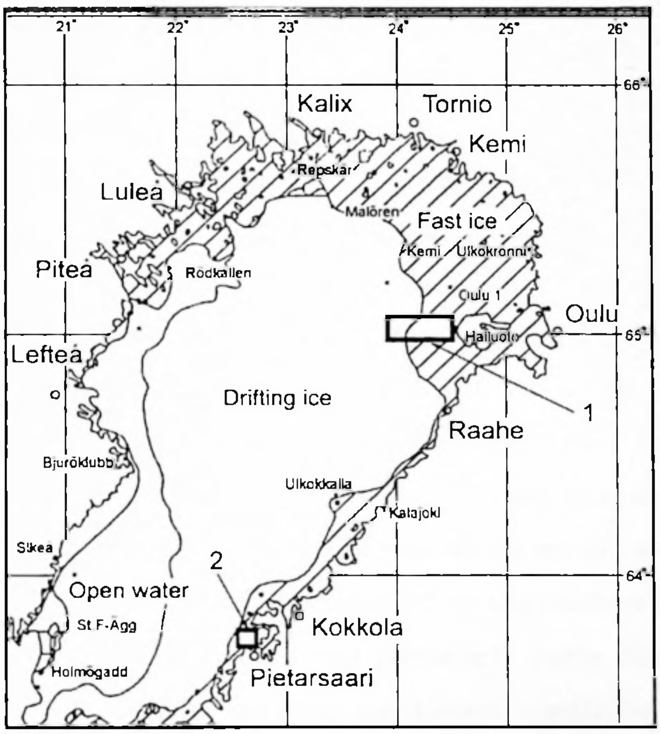


**Figure 3.13.** Location of the experimental sites in Bay of Bothnia; drifting ice edge and border of the fast ice are shown (17 March, 1997). 1 – experimental site in the vicinity of Hailuoto Island; 2 - R/V "Aranda".

Two separate experimental sites were chosen for the ZIP-95 field campaign (Fig. 3.13). The main site was established in the vicinity of Hailuoto Island, northern Bay of Bothnia (65°N, 24°E). The Perämeri research station of the University of Oulu, located on the western shore of Hailuoto Island, hosted the operational centre for the campaign. The station provided accommodation, workshops and informational support for the members of the field groups. To access the observational sites on the drifting ice of about 30 km offshore and to move the

equipment, helicopters were used on a daily basis. Several snowmobiles and a heavy terrain vehicle (HTV) were employed for travelling from the base to the sites on the fast ice. The second experimental site was located at the border of the fast ice near Kokkola (63.8°N, 22.6°E). The R/V "Aranda" was moored in the fast ice and served as a base for week-long observations (Fig. 3.13). The ship was also part of another extensive field programme carried out by the Finnish Institute of Marine Research.

### 3.4.2 Meteorological and ice conditions in the experimental area

Weather conditions during the experiment fell into two distinctive types. Between 4$^{th}$ and 14$^{th}$ March the westerly winds brought warm and moist air in the experimental area. The temperature during this period varied from –6°C to +3°C, with an average humidity of about 85 percent (Fig. 3.14b,c). The whole period was characterised by a series of depressions arriving from the west (Fig. 3.14c). Two severe storms came on 9$^{th}$ and 13$^{th}$ March from the west and northwest respectively (Fig. 3.13d). The averaged wind speed was about 10 m/s, whereas the average wind direction was somewhat close to 270°. A maximum 10-minute average wind speed of 19 m/s was recorded at the Marjaniemi weather station (Fig. 3.14a,d). However the wind speed in the gusts was much higher. The weather during the second period, 15$^{th}$ - 22$^{nd}$ March, was dominated by an anticyclone (Fig. 3.14c). During this the air was dry and cold, with temperatures between –13°C and –2°C and an average humidity of about 70 percent (Fig. 3.14b, c). Relatively low cloudiness during the day and night enhanced diurnal variation in the air temperature. The amplitude of the diurnal cycle reached 8°C (Fig. 3.14b). During this period the wind direction was particularly stable changing between 310° and 360°. In contrast to its direction the wind speed varied significantly (Fig. 3.14d). The wind speed fluctuated between 1m/s and 10 m/s during the calm period (15$^{th}$ –18$^{th}$ and 20$^{th}$ –22$^{nd}$ March). Strong winds with speed up to 17 m/s came from the north on 19$^{th}$ March (Fig. 3.14d).

In addition to the meteorological observations, scientists from the University of Helsinki and the University of Lapland carried out measurements of the incoming solar radiation (Fig. 3.15) and observations on ice-snow albedo along the calibration line. The pair of pyranometers LICOR SA-200, one pointed towards the sky to measure incident solar radiation and the other pointed down towards the ice surface to measure reflected part of the

[illegible]

[illegible]

[illegible]

[illegible]

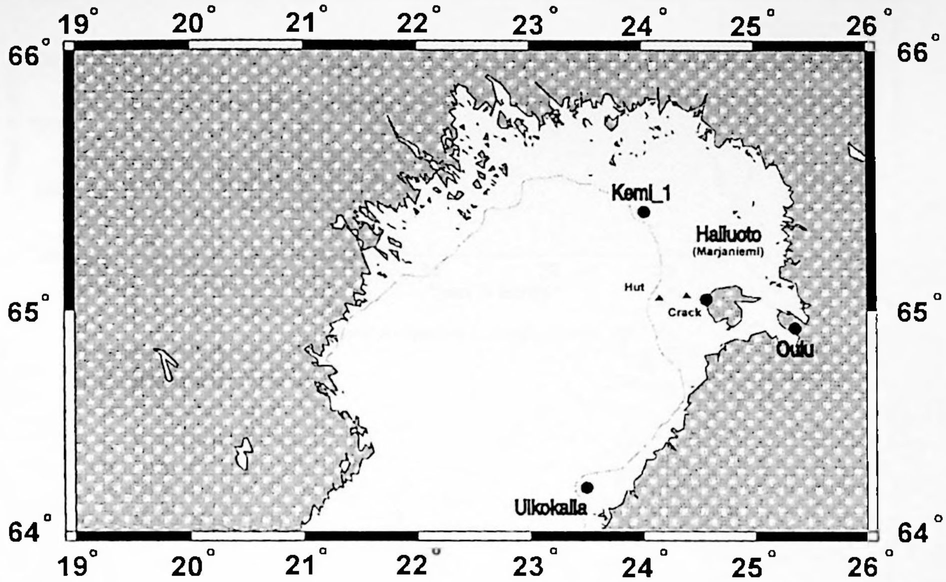


**a**

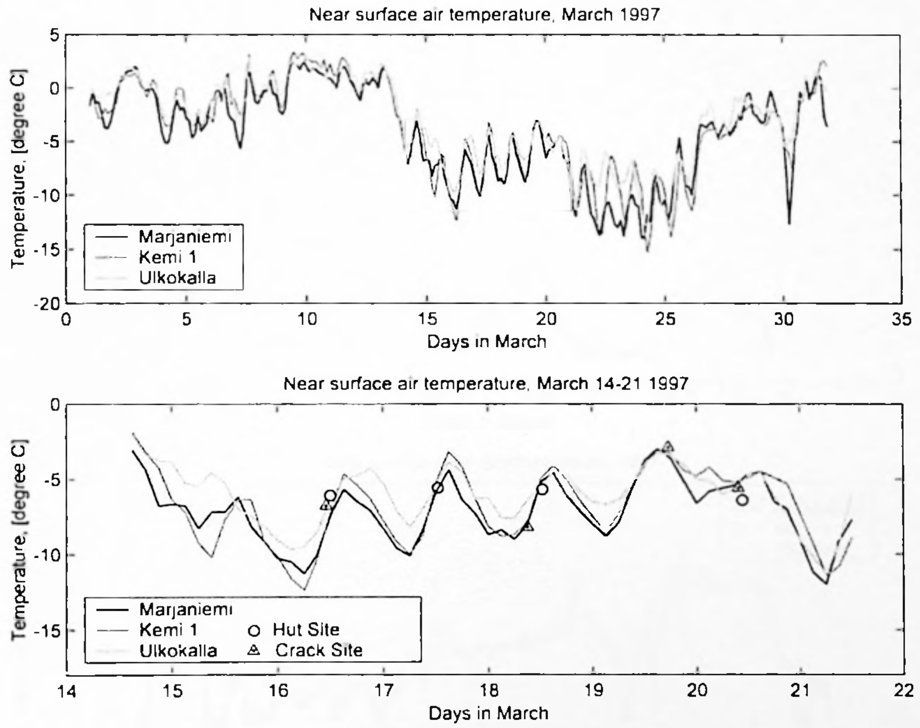


**b**

**Figure 3.14 a,b.** Meteorological observations during ZIP–97 experiment, 15 – 21 March, 1997. (a) – locations of the weather stations; (b) – near surface air temperature observed at the weather stations and at the experimental sites; (c) – near surface atmospheric pressure and air humidity observed at the weather stations; (d) – near surface wind speed and direction observed at the weather stations.

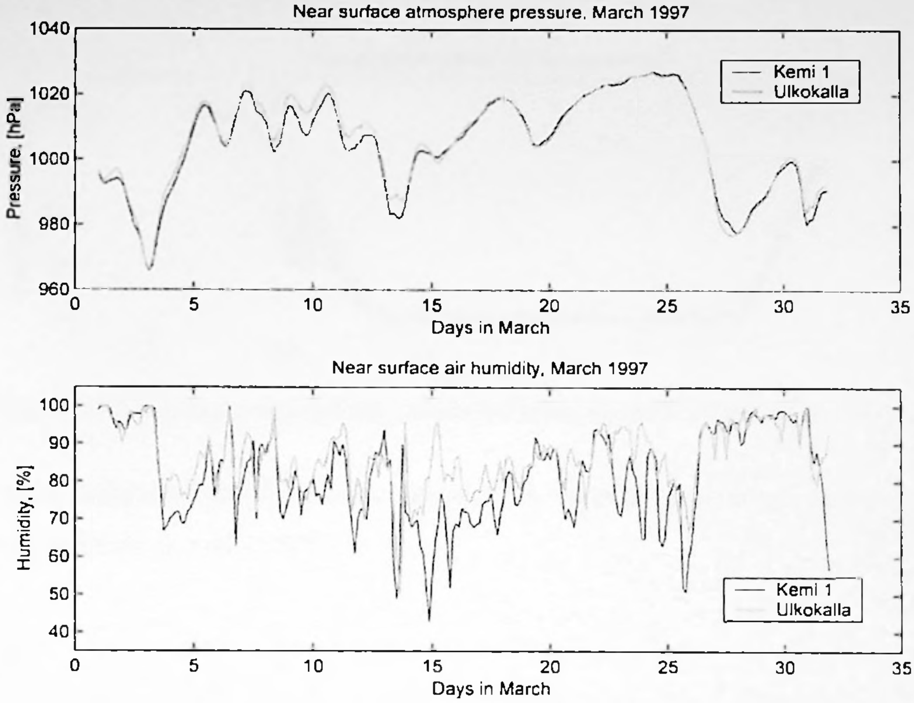


c

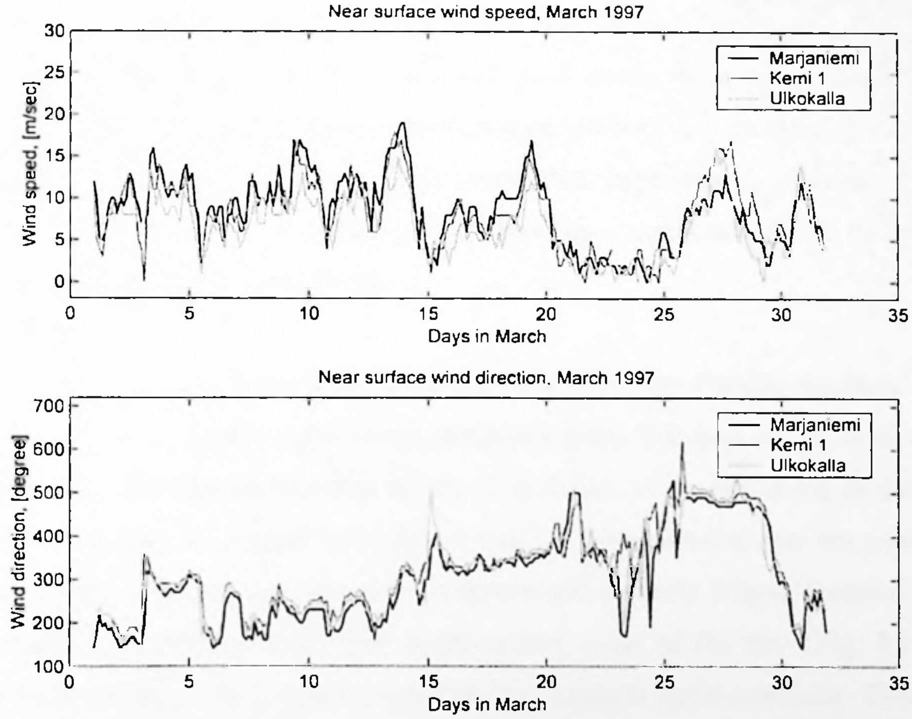


d

**Figure 3.14 c,d.** Meteorological observations during ZIP–97 experiment (continued), 15 – 21 March, 1997. (c) – near surface atmospheric pressure and air humidity observed at the weather stations; (d) – near surface wind speed and direction observed at the weather stations.

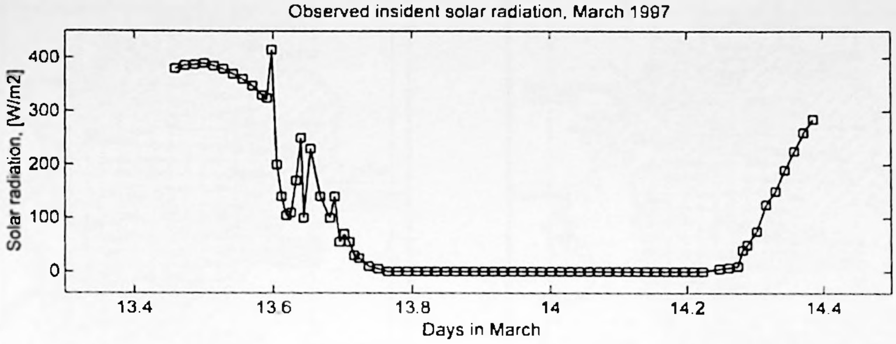


**Figure 3.15.** Incident solar radiation observed along the calibration line at stake 30.

radiation, were employed for these observations. The detailed description of the observations can be found in Herlevi et al. (1997).

The mild-winter 1996–1997 resulted in thinner ice formed in the Bay of Bothnia compared with an average year. The average thickness of the level land fast ice in March in the vicinity of Hailuoto Island was about 70 cm with a maximum value as high as 111 cm. On the other hand, unsettled and stormy weather in January, February and March 1997 forced ice to drift into the north-eastern Bay of Bothnia and led to severe ice deformation in the area of the experiment. A drilling programme carried out on drifting ice revealed extensive multi-layer rafting of the majority of the ice floes even when they visually seemed to be single-layered. The total thickness of the rafted ice was between 2 and 6 m with the thickness of the single-layered ice between 20 and 70 cm.

Ice conditions on the basin scale were monitored by the Finnish Institute of Marine Research. Sea ice charts of the region were produced every 3-4 days on the basis of satellite imagery, aerial reconnaissance and ship reports (Fig. 3.16). At the beginning of the campaign the bay was completely covered in ice with a lower ice concentration near the western shore. In the eastern part of the bay ice was more compact and severely ridged. Extensive land fast ice was formed along the northern and north-eastern coast of the bay (Fig. 3.16). On 6$^{th}$ March the south-south-westerly wind pushed the ice towards north-northeast. This led to the opening of a large lead in the western Bay of Bothnia and ice ridging near the eastern shore. During the next four days the wind force gradually increased moving ice farther towards the east of the basin. Cracks running in the southwest–northeast direction were formed in the middle of

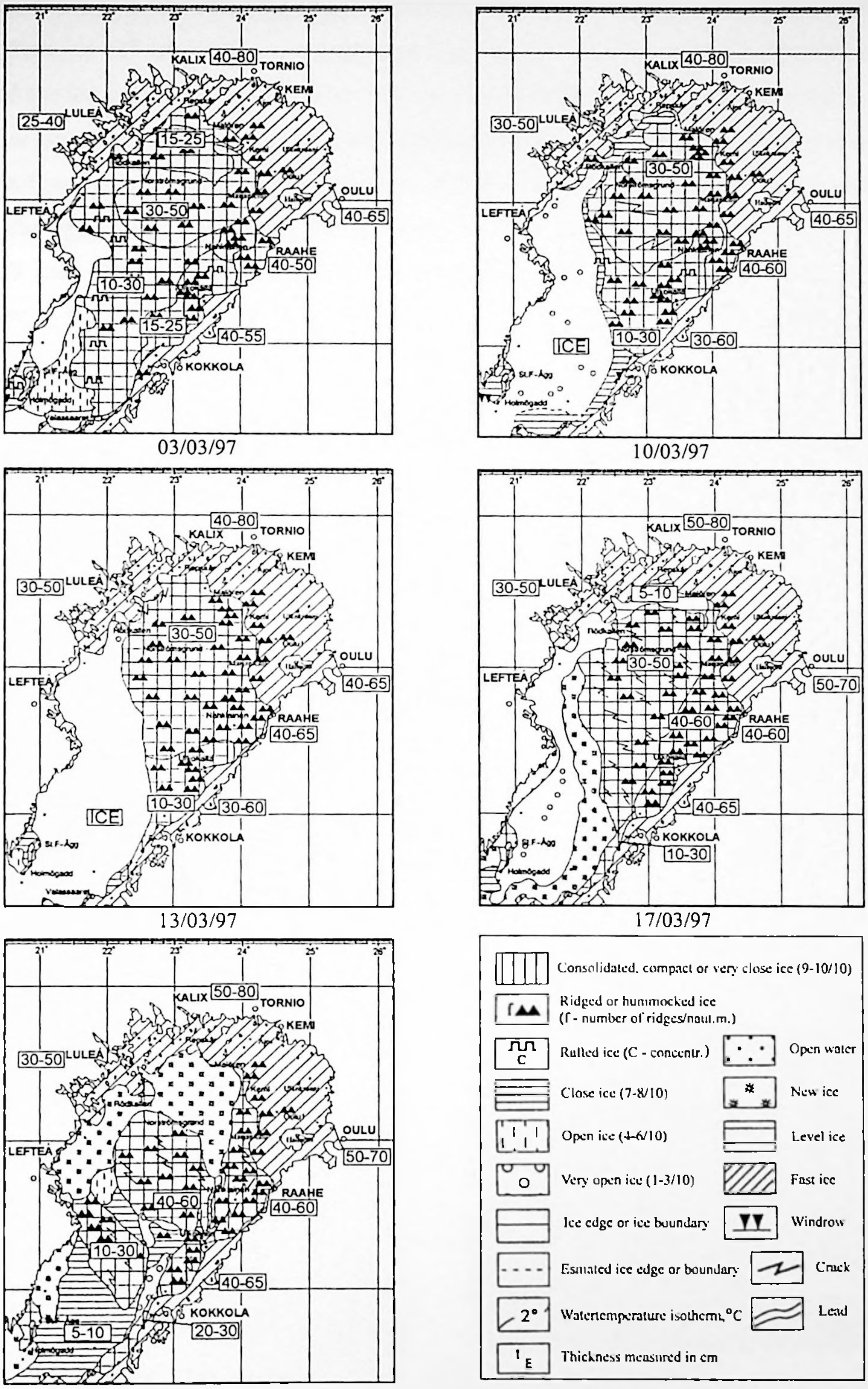


**Figure 3.16.** Ice conditions in the Bay of Bothnia in March, 1997 (ice charts produced by Finnish Institute of Marine Research).

the bay. Because of the relatively high air temperature the ice formation in the leads slowed down. Then on 13th March the wind changed to northeast increasing to gale force; this again changed the ice conditions in the basin. The old cracks in the drifting ice began closing down with new cracks opening in the northwest–southeast direction. Ice started to move to the south with a polynya forming in the northern part of the bay. Because of the cold air coming into the region the open water quickly began to freeze up. The new ice was observed even in the southern part of the bay. On the 14th the storm died out and in the next three days the moderate winds from the north had a very limited effect on ice conditions except that several north-south oriented slip lines were formed in the proximity of Hailuoto Island, until the next gale came on 18th March. The storm lasted for about two days and led to a dramatic ice drift to the south. The whole massif of ice pack in the northern part of the bay moved by about half degree to the south leaving only a narrow drifting ice band adjacent to the land fast ice (Fig. 3.16). On 21st March the wind dropped and the newly formed open water became quickly covered with young ice.

To carry out observations three observational sites, the *Hut Site*, *Crack Site*, *Southern Ridge Site*, were set up on the land fast ice, and another one, the *Central Buoy Site*, on the drifting ice near the Central GPS drifter (Figs. 3.17 and 3.19).

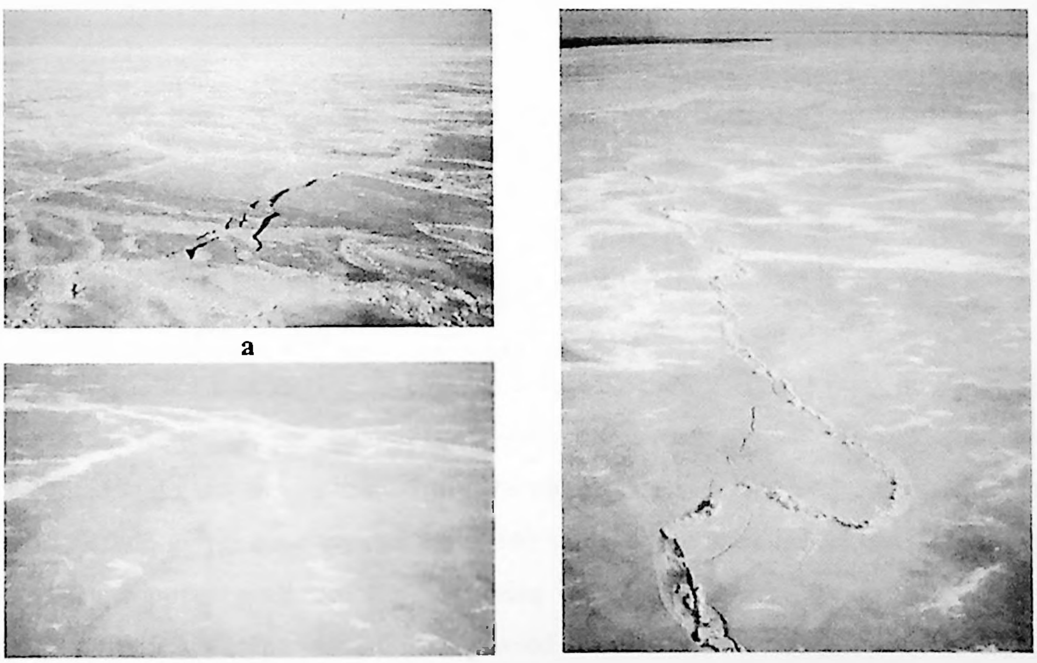


**Figure 3.17.** Aerial view of the ice conditions near Hailuoto Island during ZIP-97 experiment, Site 1, March, 1997, Bay of Bothnia. (a) – Central Buoy Site; (b) – Hut Site; (c) – Southern Ridge Site (photographs by author).

When the experiment began, ice at all observational sites appeared to be moderately deformed. Drifting ice in the vicinity of Hailuoto Island was ridged and rafted, however a significant area of the ice pack consisted of underformed single-layered ice floes (Fig. 3.17a). Land fast ice near the island was quite thick and grounded on the shoals at several places. This made it able to withstand deformation and therefore fast ice was weakly ridged until the end of the experiment (Figs. 3.17b,c, and 3.19b,c). At Site 2 located near Kokkola ice was even less deformed and almost completely grounded on the shallow water (Fig. 3.18). All observational sites on the land fast ice were set up on the level single-layered ice sheet with thin (about 2 cm or less) snow cover (Figs. 3.18b and 3.19b,c,d). The observational floe at the Central Buoy Site had a smooth upper surface but was severely rafted underneath. Maximal ice thickness in the ridge was up to 6 m (Fig. 3.31). Snow depth at this site was between 5 and 10 cm (Figs. 3.19a, 3.20 and 3.21).


a


b

**Figure 3.18.** Ice conditions near Kokkola during ZIP-97 experiment, Site 2, March, 1997, Bay of Bothnia. (a) – R/V "Aranda" moored in the fast ice; (b) – fast ice near Kokkola (photographs by author).

Storms on 9th, 13th and 19th March changed the ice conditions dramatically. The ridge building at the Central Buoy Site on 8th March was so extensive that it damaged the sensors and recording computer. During the ice pile-up the GPS buoy antenna, 2 m in height, was buried under the ice blocks (Fig. 3.20). Ice thickness measurements performed on drifting pack ice demonstrated the presence of heavy ice conditions in the region: 30-90 cm level thin ice was rafted and compressed in the ridges to about 5 m thickness by the north-east ice drift (Fig. 3.21a). The aerial observations exhibited significant variations of the ice deformation state and snow coverage. From the beginning of the experiment the snow cover melted gradually until 19th March, when a strong wind from the north brought a snowstorm. This caused the accumulation of a significant snow volume in the ridges. However, the snow cover on the large area of the level ice was blown away. The combination of thin ice, shallow water

[illegible]

[illegible]

[illegible]

[illegible]

[illegible]

and strong on-shore wind resulted in the building of grounded ridges up to 8 m high. Figure 3.21b portrays one of these ice structures. The ridge had an elliptical shape elongated in the SSW-NNE direction. The structure was about 8 m in height and had horizontal dimensions of about 70 × 20 m. The ice cover around the ridge seemed to be intact. However, the overall large-scale motion of the surrounding drifting ice moved the grounded ice to the shoal, piled it up and created the large open water area at the down-wind side of the ridge (Fig. 3.21b).

**Figure 3.19.** Observational sites near Hailuoto Island, Site 1, ZIP-97 experiment, March, 1997, Bay of Bothnia. (a) – Central Buoy Site; (b) –Hut Site, fast/rubble ice border is visible at the distance; (c) – Crack Site; (d) – "semi-circular" ice fragments near the Southern Ridge Site (photographs by author).

Changeable weather and intensive ice deformation created quite remarkable conditions for ice formation. Numerous examples of the consolidation of fragmented ice were observed in the field. One of them is shown in Fig. 3.22b. The photograph against the sunlight allows us to view the bits of brashed ice incorporated into the new ice. In turn, Figure 3.22a demonstrates an example of the infiltrated ice layers presumably formed during snowstorms along with ice freezing/melting events.

[illegible]

[illegible]



[illegible]

[illegible]

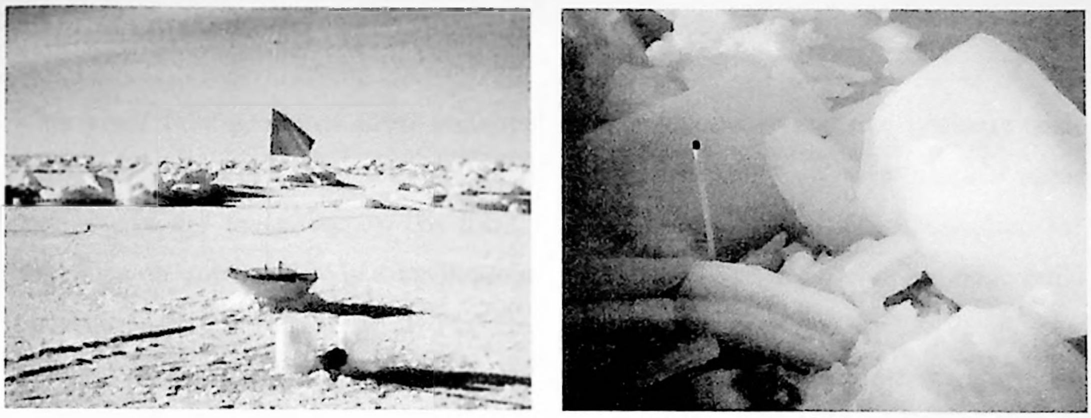

**Figure 3.20.** GPS drifter deployed at the Central Buoy Site by the University of Helsinki team. Photographs were taken by author on March 6 (left) and 15 (right), 1997. Central Buoy Site, Bay of Bothnia.

**Figure 3.21.** Ice deformations occurring as a result of the storm on 13 March. Ice ridges at the Central Buoy Site on March 15 (left) and large grounded ridge south-west of Hailuoto Island, aerial view (right). Bay of Bothnia (photographs by author).

**a** **b**

**Figure 3.22.** Ice near Hailuoto Island during ZIP-97 experiment. (a) – layers in ice, Central Buoy Site; (b) – refrozen bits of brashed ice, drifting ice south-west of the island.

### 3.4.3 Log of the experiment

The small field group of SPRI consisted of one researcher and two graduate students (including the author). The task of our group during the campaign was to measure deformation of the ice cover on the local scale and to compare this deformation to the deformations on intermediate and basin-wide scales. We hoped to observe the ridge building and measure local deformation related to this event. Also we expected to observe emission of short period (about 2-3 s ) elastic waves hypothetically related to ridge formation or possibly ice shear motion. As it will be evident later only part of these expectations were met.

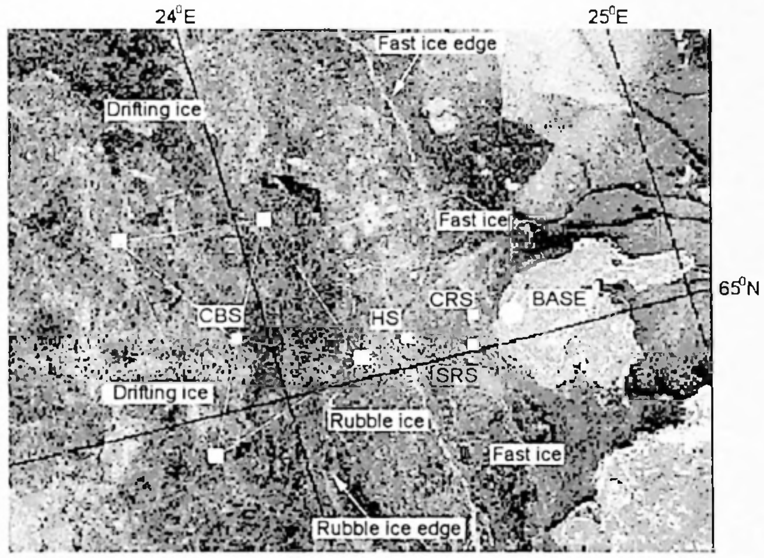


**Figure 3.23.** The scheme of observational sites overlaid ERS image (copyright ESA), Bay of Bothnia, in the vicinity of Hailuoto Island, March 1997. CBS-Central Buoy Site; HS-Hut Site; CRS-Crack Site; SRS-Southern Ridge Site.

The group arrived at the Perämeri Research Station on 4$^{th}$ March 1997. On 5$^{th}$ March the group flew to the Central Buoy Site, an ice floe inside the ice pack zone (Fig. 3.23) about 20 km offshore from Hailuoto Island. Here we installed a set of the deformation sensors including two strainmeters, two tiltmeters and three accelerometers (Fig. 3.24). We chose the "SPRI floe" next to the floe where the GPS-drifter and the Acoustic Doppler Current Profiler (ADCP) had been installed by the University of Helsinki. The SPRI's waterproof computer with two weeks' logging capacity was set up to record signal from the sensors. After setting up the instrumentation on the drifting ice and completing the ice thickness measurements of the floe our group went to Kokkola on 7$^{th}$ March 1997, where we boarded the Finnish

[illegible]

[illegible]



[illegible]

[illegible]

research vessel "Aranda" (Finnish Institute of Marine Research). After 12 hours of sailing the ship found a mooring site about 2 km from the fast ice edge onshore (Fig. 3.13). On this day University of Helsinki deployed all five ice drifters with Global Positioning System (GPS) at the main experimental site near Hailuoto Island and began to receive data on ice drift (Figs. 3.25 and 3.26). The first flight with an airborne Laser Profilometer in the northeastern Bay of Bothnia was accomplished.

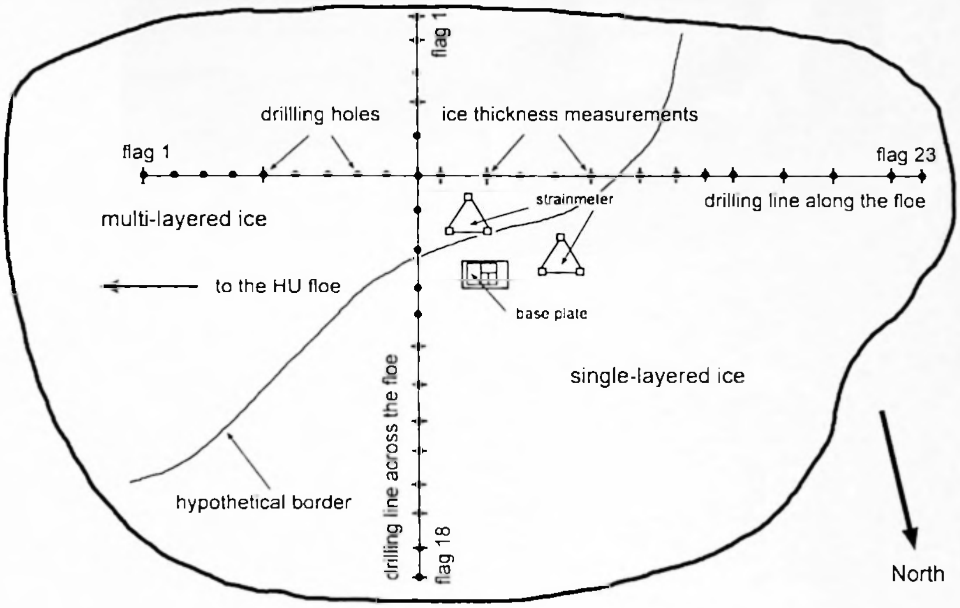


**Figure 3.24.** SPRI experimental floe at the Central Buoy Site. Drilling sections and schematic positions of the instruments are shown. The hypothetical border between single layered ice at the north-western part of the floe and multi-layered rafted ice at the south-eastern end of the floe is shown.

On the next day the research crew of the ship began the atmospheric observations while the SPRI group along with the team from the Helsinki University of Technology travelled by skidoo towards the drifting ice trying to find a suitable site for the observations. The Helsinki University of Technology team quickly discovered a curvilinear ridge to measure and started the work. However, ice conditions were not so favourable for the ice mechanics measurements for which the SPRI group was responsible. Because of the low water or, perhaps previous on-shore ice movement the majority of the land-fast and near-shore drifting ice was grounded on the shoals and completely stationary (Fig. 3.18). Farther offshore the drifting ice was afloat, but it was unreachable by skidoo because of a large coastal polynya. Under these circumstances the decision to abandon the ship was taken by the SPRI group on

a

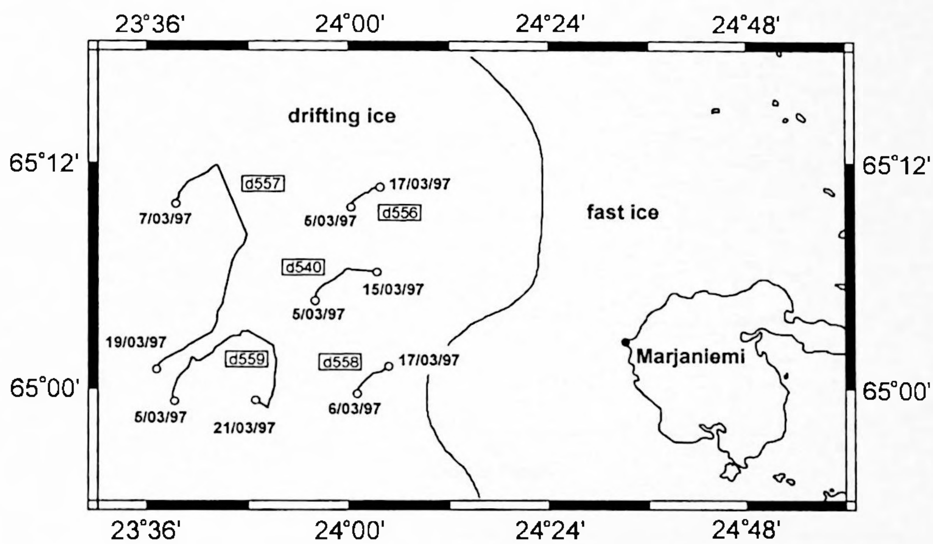


b

**Figure 3.25.** GPS drifters: general view (a) and trajectories (b). ZIP Experiment, Bay of Bothnia, March 5–21, 1997. Start and end of each trajectory are marked with hollow circle, whereas GPS buoy number (i.e. d557) is shown in a frame. (a) – photograph by author; (b) – from Tuhkuri et al., 1998.

the same day. Early morning of 9th March 1997 the equipment was loaded onto the skidoo trailer and after shuttling between the ship and the shore against 15 m/s wind the SPRI group headed towards Hailuoto Island by land. The team returned to the Perämeri research station on the same night.

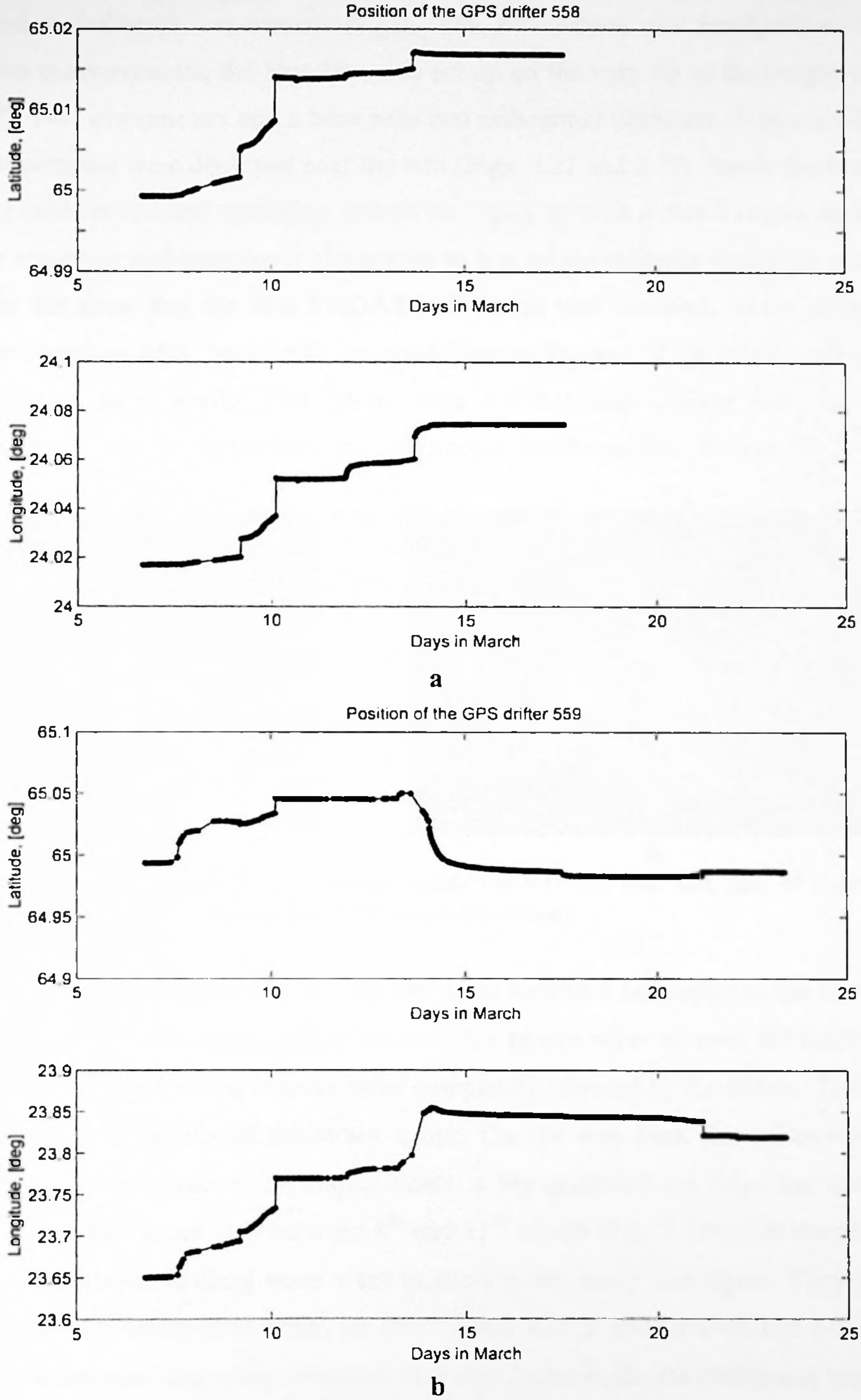


**Figure 3.26.** Time series of the positions of the drifters d558 (a) and d559 (b). ZIP Experiment, Bay of Bothnia, March 6–24, 1997. Black circles – actual observations; black line – linear interpolation between observations (courtesy of Dr. Zhanhai Zhang).

On the next day the other members of the field campaign arrived at the Perämeri research station and a full-scale experiment began. On 10$^{th}$ March the headquarters for local deformation measurements, the Hut Site, was set up on the very tip of the tongue of fast ice (Fig. 3.23). Two strainmeters and a base with two orthogonal tiltmeters, 3-axis accelerometer and digital compass were deployed near the tent (Figs. 3.27 and 3.28). Inside the tent a water-proof PC-based control and recording system was spun up with a diesel engine to supply the power for computer and transducer electronics to test an autonomous recording system (Fig. 3.27b). On the same day the first RADARSAT image was received, which allowed us to familiarise ourselves with "real time" ice conditions in the area of the experiment and in the Bay of Bothnia as a whole. The 10-km long ice thickness drilling line, the so-called "calibration line", was set up between the Marjaniemi lighthouse and the Hut Site (Fig. 3.29).

a b

**Figure 3.27.** Sensors (a) and recording centre inside the tent (b). Hut Site, Bay of Bothnia. Strain gauges are covered by protecting boxes (photographs by author).

On 11$^{th}$ March the University of Helsinki team flew in a helicopter to the Central Buoy Site and discovered massive ridging of the site. Ice blocks were all over the site (Figs. 3.20 and 3.21a). Local deformation sensors were completely covered by ice rubble. The team was able to recover only pieces of the strain gauge. On the way back they discovered further convincing evidence of recent ice displacement: a big grounded ice ridge had been formed south of the Hut Site some time between 8$^{th}$ and 11$^{th}$ March (Fig. 3.21b). On the next day the University of Helsinki drilling team went to the Central Buoy Site again. They performed drilling of the "University of Helsinki ice floe" where ADCP and GPS-drifters were installed. The SPRI's waterproof recording computer was also found in the ice rubble and brought back to the base. The carbon-reinforced computer box was damaged and water leaked inside leaving little chance for the record to be recovered. The author, being responsible for the data processing, managed to decode part of the record; however it appeared that the sensors close

[illegible]

[illegible]

[illegible]

[illegible]

[illegible]

to the ridge had been damaged first, therefore only a flat signal was recorded. From the length of the record we estimated that ridging event occurred on 8th March. The base plate with the set of tiltmeters and accelerometers was never recovered from the rubble.

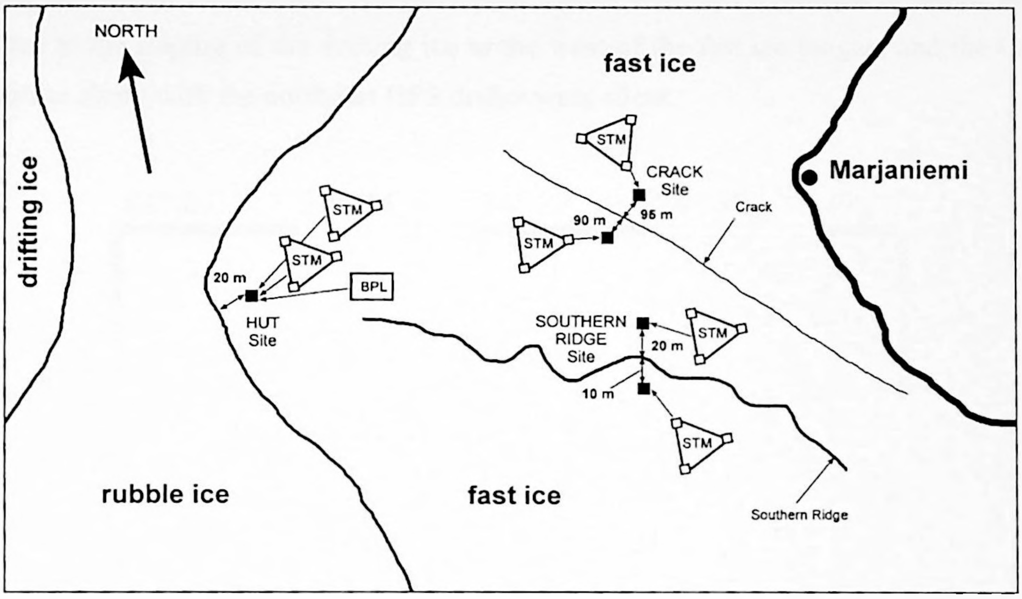


**Figure 3.28.** Scheme of SPRI experimental sites near Hailuoto Island. Distance at the vicinity of the sites (given in metres) are on a different scale compared to the overall size of the experimental area, which is about 20 km long and 10 km wide. Key: STM – strainmeter; BPL – base plate with tiltmeters and accelerometers; black squares mark the location of the sites.

On 12th March the team from the University of Lapland together with the University of Oulu group performed mapping of the ice thickness in the experimental area with the help of an airborne radar system. On the same day a team from the Thule Institute employed Ground Penetrating Radar (GPR) to measure ice thickness along the calibration line and verified the results against the measurements obtained by drilling.

A storm came next day from the northwest direction. The fast ice tongue near the island was subjected to significant deformation that resulted in the formation of a small ridge right across the calibration line.

On 14th March the SPRI team continued to record deformation at the Hut Site. Two thermistor chains to measure internal ice temperature on different horizons were set up at the Hut Site. The first chain was located about 20 m from the tent towards the rubble field, while

the second one was about 40 m from the tent to the south. The second set of thermistor chains was installed at the second observational site, the Crack Site. The site was chosen on the fast ice at a distance of about 5 km from the Marjaniemi lighthouse. The western chain was installed 31.5 m to the west of the partially frozen crack, while the eastern chain was set up 33 m to the east of the same crack. All thermistor chains were left overnight to freeze in. The storm led to the ridging of the drifting ice to the west of the fast ice tongue, and the Central GPS-drifter along with the northeast GPS drifter went silent.

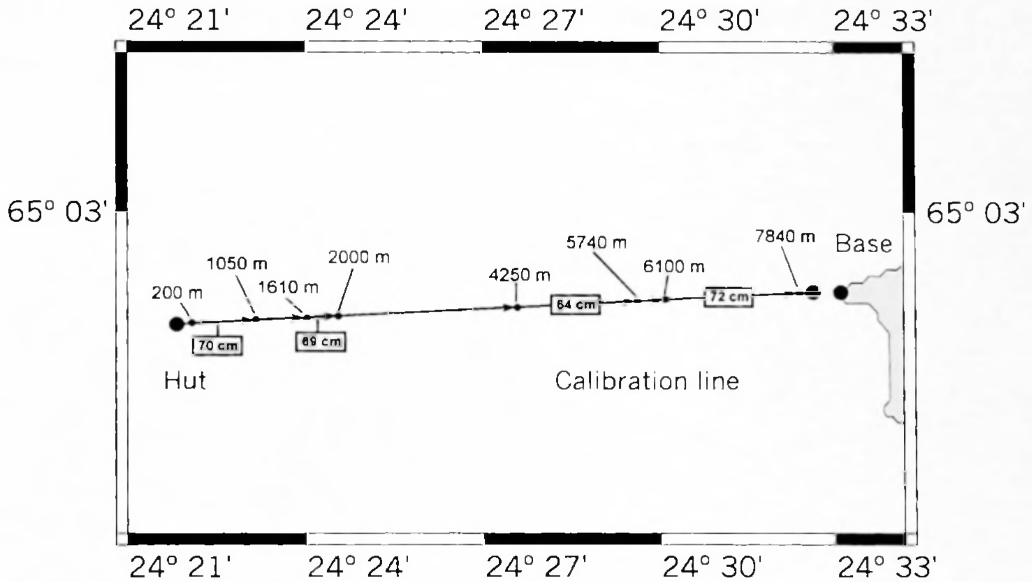


**Figure 3.29.** Mean ice thickness between Marjaniemi Harbour and the Hut Site along the calibration line. Averaging was inside sections. Beginning and end of those are marked as the distance in metres from the hut. Thickness is shown in centimetres.

Several attempts to find the drifters were undertaken. The search succeeded on 15th March, when the University of Helsinki team together with the author spotted the Central GPS-drifter from the air. Later the team landed at the site and found it buried under 2 m of ice rubble (Fig. 3.20b). At noon the second site for the local deformation measurements at the Crack Site was set up (Fig. 3.28). Two sets of strainmeters were installed on opposite sides of a partially frozen crack 185 m apart from each other. The first reading from the new set of instruments along with temperature data from all thermistors were taken.

The Helsinki University of Technology team arrived at the Marjaniemi site after successfully finishing their drilling programme near Kokkola and began to drill the ice ridge in the ice rubble area on 16th March. The SPRI group continued to record deformation at two

observational sites. The author successfully decoded the first ice deformation records from the Hut and Crack Sites. The University of Helsinki team started drilling the grounded ridges near Marjaniemi Harbour.

On 17th March, while the observations at the Hut and Crack Sites were continuing the author with another member of the group went by skidoo to visit a large grounded ridge to the south of the calibration line discovered by the University of Helsinki team on 11th March. The second goal of the trip was to find a possible observational site for additional deformation measurements. The reconnaissance succeeded. Travelling to the south-east from the Hut Site we found a suitable place for the strainmeter installation, close to a newly formed ice pressure ridge (Fig. 3.28). There were fresh polynyas in the proximity of the ridge, therefore there was a high probability that deformation would develop at this site. It was decided to install the instruments at this site. After travelling for about 20 km on the fast and severely fragmented drifting ice we reached the destination of our journey: the large grounded ridge about 8 m high (Fig. 3.21b).

On 18th March we continued to record the deformations at the Hut and Crack Sites. In addition two strainmeters were installed at the third observational site chosen on the day before. Strainmeters were set up at a distance from the new ridge of 20 m to the north and 10 m to the south. The new site was called the Southern Ridge Site. When the team were leaving the wind shifted to the west and increased. During the night a severe snowstorm developed.

On next day the storm continued. The SPRI team made two unsuccessful attempts to reach the observational sites by skidoo. The visibility was less than 20 m and the installations were not found. Only when the wind decreased were we able to reach the Southern Ridge Site, collect the logger and dismantle sensors. The snow drift was so strong that when we opened the boxes with instruments we found them filled with fine snow, however it did not affect the measurements. The Hut Site was unreachable all day.

The field campaign started to wind down on 20th March. During the next two days the SPRI team recorded the deformation at the Crack Site. Ice temperature profiling was done on the 20th at both the Hut and Crack Sites. The deformation sensors were recovered successfully from all sites. However, the thermistor chains were frozen into the ice and could not be

recovered. The team packed their equipment and left Hailuoto Island for Helsinki on 22 March 1997.

### 3.4.4 Observations

The observational programme of the SPRI group included the monitoring of local ice deformations, measurements of ice and snow thickness at all observational sites, and vertical profiling of the ice temperature (Table 3.3). The program was tied up to the observations on mesoscale ice deformation carried out with the help of GPS drifters by the University of Helsinki. Episodic measurements of the snow surface and near surface air temperatures were conducted as well.

**Table 3.3.** Coordinates of the observational sites, ice thickness and strainmeter orientations.

| Site | Latitude Longitude | Directions of arms, [degree] | | | Ice thickness [m] |
|---|---|---|---|---|---|
| | | A | B | C | |
| Central Buoy | 65°04,71′N $^{GPS1}$ | 210°[17] | 150°[17] | 270°[17] | 3.99 |
| | 23°56,149′E $^{GPS1}$ | 270°[4] | 210°[4] | 150°[4] | |
| Hut | 65°02,38′N $^{GPS2}$ | 100°[20] | 220°[20] | 340°[20] | 1.00 |
| | 24°22,12′E $^{GPS2}$ | 100°[28] | 220°[28] | 340°[28] | |
| Crack | 65°02,40′N $^{GPS2}$ | 225°[1] | 165°[1] | 105°[1] | 0.98 |
| | 24°28,61′E $^{GPS2}$ | 70°[2] | 10°[2] | 310°[2] | 0.98 |
| Southern Ridge | 65°01′ N $^{CALC}$ | 300°[28] | 240°[28] | 180°[28] | 0.95 |
| | 24°28′ E $^{CALC}$ | 300°[11] | 240°[11] | 180°[11] | 0.90 |

Note: All angles are positive in the clockwise direction; strainmeter number is listed in the brackets;
GPS1 - Position observed using GPS on March 5, 1997, (drifting ice);
GPS2 - Position observed using GPS, (fast ice);
CALC - Position calculated with the help of triangulation, (fast ice).

[illegible]

[illegible]

[illegible]

[illegible]

| | | | | | |
|---|---|---|---|---|---|
| [illegible] | [illegible] | [illegible] | [illegible] | [illegible] | [illegible] |

[illegible]

**Table 3.4.** Observations on local ice deformation during ZIP-97 experiment.

| Start of record | Stop of record | Site | Sensors | Sampling frequency |
|---|---|---|---|---|
| 06.03.1997<br>12.40 | 08.03.1997*<br>12.17 | Central Buoy | 2 strainmeters<br>3 accelerometers<br>2 tiltmeters | 10 Hz |
| 11.03.1997<br>15.13 | 11.03.1997<br>17.35 | Hut | 2 strainmeters<br>3 accelerometers<br>2 tiltmeters | 10 Hz |
| 15.03.1997<br>11:42:00 | 15.03.1997<br>18:04:33 | Crack | 2 strainmeters | 1 Hz |
| 15.03.1997<br>20:53:00 | 16.03.1997<br>04:57:57 | Crack | 2 strainmeters | 1 Hz |
| 16.03.1997<br>10:56:17 | 16.03.1997<br>17:00:00 | Crack | 2 strainmeters | 1 Hz |
| 16.03.1997<br>20:45:00 | 17.03.1997<br>04:49:57 | Crack | 2 strainmeters | 1 Hz |
| 17.03.1997<br>11:40:57 | 17.03.1997<br>18:05:00 | Crack | 2 strainmeters | 1 Hz |
| 17.03.1997<br>21:12:00 | 18.03.1997<br>05:16:57 | Crack | 2 strainmeters | 1 Hz |
| 18.03.1997<br>11:29:00 | 18.03.1997<br>14:45:36 | Hut | 1 strainmeter | 1 Hz |
| 18.03.1997<br>17:46:00 | 19.03.1997<br>01:50:57 | Southern Ridge | 2 strainmeters | 1 Hz |
| 19.03.1997<br>17:30:00 | 20.03.1997<br>01:34:57 | Crack | 2 strainmeters | 1 Hz |
| 20.03.1997<br>12:00:00 | 20.03.1997<br>20:02:45 | Crack | 2 strainmeters | 1 Hz |
| 20.03.1997<br>21:00:00 | 21.03.1997<br>05:30:00 | Crack | 2 strainmeters | 1 Hz |

**Note:** Local time (Helsinki); *- date and time were calculated, sensors were destroyed early by ridge building.

[illegible]

| [illegible] | [illegible] | [illegible] | [illegible] | [illegible] |
|---|---|---|---|---|
| [illegible] | [illegible] | [illegible] | [illegible] | [illegible] |
| [illegible] | [illegible] | [illegible] | [illegible] | [illegible] |
| [illegible] | [illegible] | [illegible] | [illegible] | [illegible] |
| [illegible] | [illegible] | [illegible] | [illegible] | [illegible] |
| [illegible] | [illegible] | [illegible] | [illegible] | [illegible] |
| [illegible] | [illegible] | [illegible] | [illegible] | [illegible] |
| [illegible] | [illegible] | [illegible] | [illegible] | [illegible] |
| [illegible] | [illegible] | [illegible] | [illegible] | [illegible] |
| [illegible] | [illegible] | [illegible] | [illegible] | [illegible] |
| [illegible] | [illegible] | [illegible] | [illegible] | [illegible] |
| [illegible] | [illegible] | [illegible] | [illegible] | [illegible] |
| [illegible] | [illegible] | [illegible] | [illegible] | [illegible] |
| [illegible] | [illegible] | [illegible] | [illegible] | [illegible] |

[illegible]

The local deformation of ice cover was monitored at 4 sites, Central Buoy, Hut, Crack, and Southern Ridge located 20 km, 9 km, 5 km and 7 km from the Marjaniemi lighthouse respectively (Figs. 3.23 and 3.28). The heave/tilt and BP-Delta strain gauges were installed on the fast and drifting ice (Figs. 3.24 and 3.28). Coordinates of the experimental sites, strainmeters orientation and ice thickness at the location of gauges are listed in Table 3.3. In total we monitored local ice deformation for about two weeks. The observational periods were as follows: March $6^{th}$ –$11^{th}$, March $15^{th}$ –$18^{th}$, and March $19^{th}$ – $21^{st}$. Most of the time the data were recorded at a sampling rate of 1 Hz in segments of about 8 hours with breaks for 2-3 hours (Table 3.4).

Records from all sensors (strainmeters, accelerometers and titlmeters) were processed according to the scheme described in section 3.3, this chapter. Each record was digitised and converted into physical units according to the calibration. Signals from strainmeter were also corrected in order to delete artificial steps due to re-zeroing. In addition the correction for the thermal drift of the sensors was applied. Thermistors frozen into the ice allowed us to eliminate such deformation of each transducer due to variation in the ambient temperature.

We assessed the quality of the strain records at the Crack, Hut and Southern Ridge Sites as good, while the data from the Buoy Site were unreliable due to damage to the sensors during the intensive ridging at the experimental site discussed earlier. The Mohr's Circle rule was applied to transform the deformation of three strainmeters arms into the principal components of the strain tensor. Figure 3.30 gives an example of the local deformation record from the sensors deployed at the Crack and Southern Ridge Sites. The signal recorded at the Crack Site shows a well pronounced thermally induced ice strain (see below) whereas the deformation at the Southern Ridge Site is clearly related to the event of ice failure.

Experience in observing local ice deformation and stress demonstrates significant spatial variability of these fields presumably related to the local inhomogeneity of the ice thickness (Richter-Menge and Elder, 1998; Tucker and Perovich, 1992). Therefore, the SPRI group decided to carry out an extensive programme of ice thickness measurement at all observational

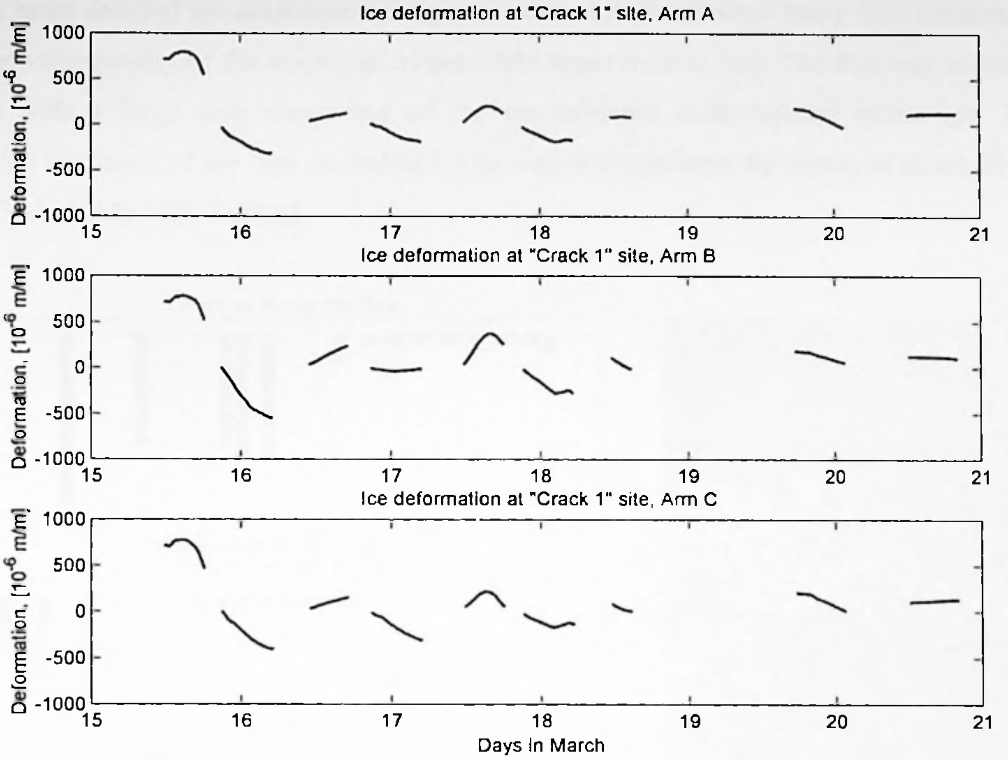


**a**

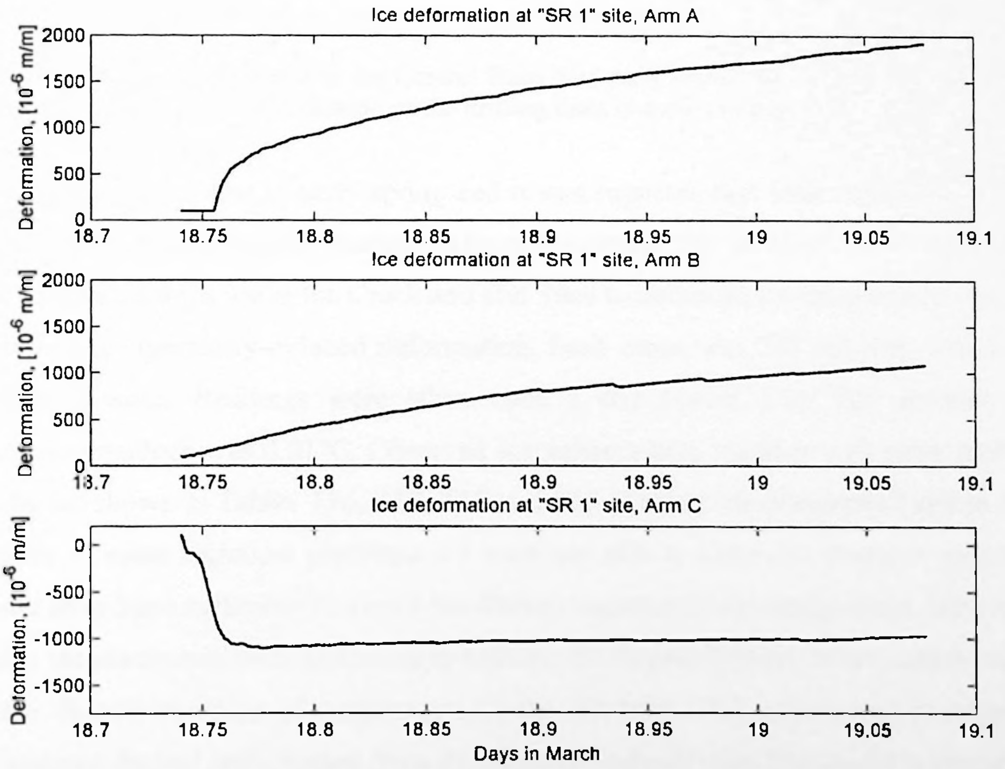


**b**

**Figure 3.30.** Local ice deformation from (a) Crack 1 and (b) Southern Ridge.

sites. The most detailed ice thickness survey was carried at the Central Buoy Site because of the high inhomogeneity of the thickness of the SPRI experimental floe. The floe was severely deformed with a large area consisting of the consolidated multi-layered rafted ice. The maximal ice thickness of the floe exceeded 5.5 m with a single layer thickness of about 20-30 cm (Fig. 3.31, Table T22, Tables).

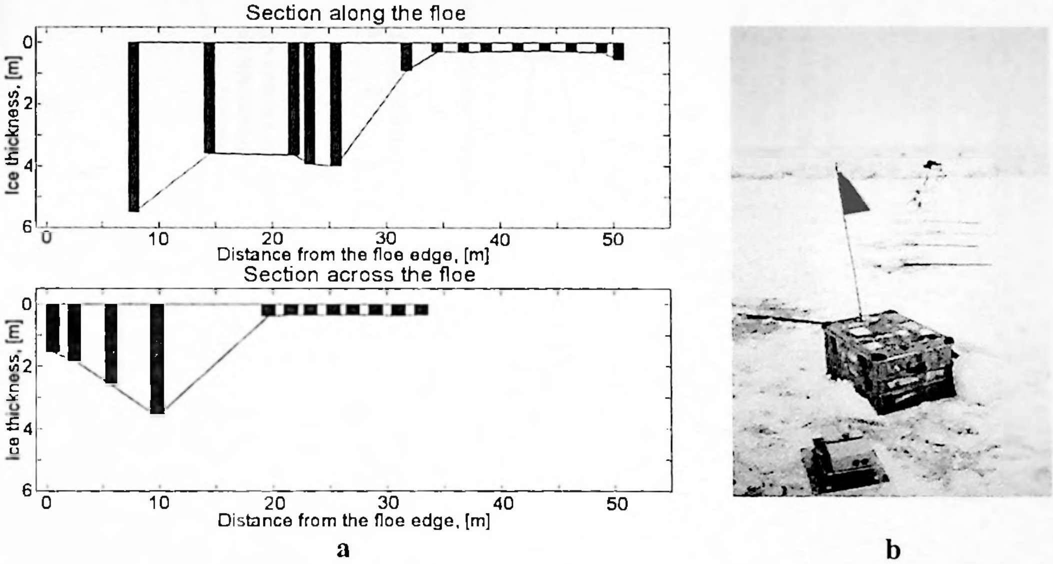


**Figure 3.31.** Profiles of ice thickness at the Central Buoy Site on 6 March (a); drilling line along the floe (b). Bars show measurements. Location of the drilling lines is shown in Fig. 3.24.

The campaign took place in early spring and it was expected that solar irradiation of the ice surface would generate diurnal thermal deformation inside the ice sheet. Four thermistor chains were frozen into the ice at the Crack and Hut Sites to obtain an ice temperature vertical profile and monitor thermally-induced deformation. Each chain was 230 cm long with a 10 cm sampling distance. Readings were taken once a day (Table 3.5). The accuracy of temperature observations was 0.01°C. Observed ice temperatures together with snow surface temperatures are shown in Tables T16, T17, T18 and T19 (Tables: Measurements) and in Fig. 3.32. Because of some logistical problems we were not able to carry out frequent sampling which would have been sufficient to record the diurnal variation in the temperature. However, our available measurements were sufficient to validate the thermodynamic model employed to calculate the diurnal variation of temperature in the ice bulk. This allowed us to separate thermally-induced diurnal deformation from dynamically induced one. The model is presented in Chapter 4.

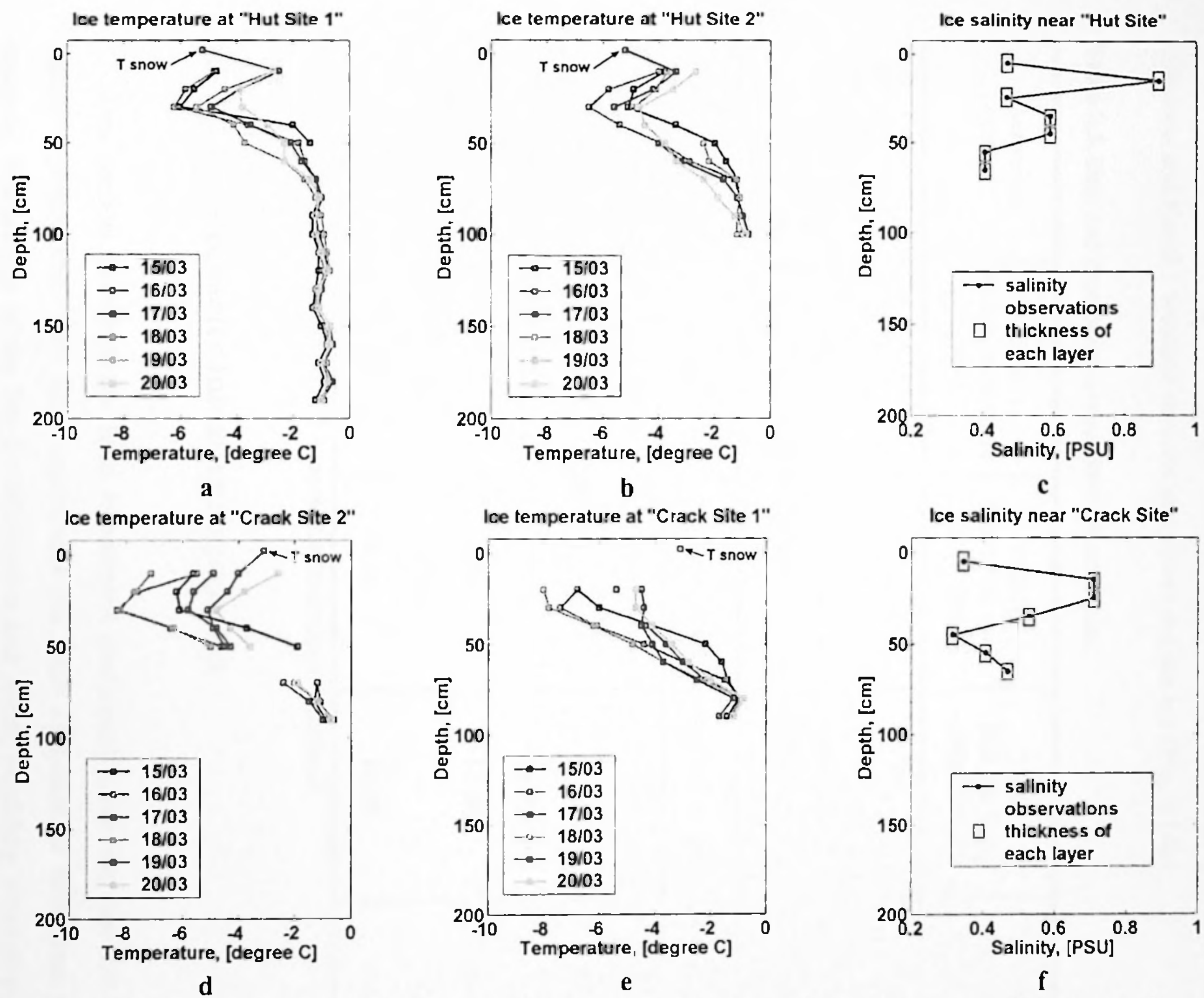


**Figure 3.32.** Ice temperature and salinity profiles at the Hut and Crack Sites. Salinity data were supplied by Dr. Jari Haapala.

Ice salinity data from the coring were kindly supplied by Dr. Jari Haapala and were used to calculation ice mechanical properties (Fig. 3.32). In addition we carried out measurements of the near surface air temperatures to compare local temperature conditions to the observations made at the nearest weather stations. This comparison demonstrated that the near surface temperature regime was practically the same in the vicinity of the Marjaniemi, Ulkokala and Kemi 1 weather stations and above the sea ice (Fig. 3.14b).

**Table 3.3.** Date and time of ice temperature observations.

| Thermistor Location | TMR-1 Crack, near shore (No 1) | TMR-2 Crack, far from shore (No 2) | TMR-3 Hut, far from ridge (No 2) | TMR-4 Hut, near ridge (No 1) |
|---|---|---|---|---|
| Ice thickness at the site, [m] | 0.98 | 0.98 | 1.0 | 2.0 |
| Sensor deployed on | 15.03.97, 10:10 | 15.03.97, 10:15 | 14.03.97, 16:00 | 14.03.97, 16:00 |
| Date and time of temperature sampling | | | | |
| 15.03.97 | 10:55 | 11:10 | 12:52 | 12:45 |
| 16.03.97 | 11:00 | 11:10 | 11:50 | 11:57 |
| 17.03.97 | 18:00 | ~18:00 | 12:19 | 12:30 |
| 18.03.97 | 9:00 | 8:50 | 12:30 | 12:20 |
| 19.03.97 | 17:28 | 17:26 | — | — |
| 20.03.97 | 9:40 | 9:30 | 10:30 | 10:38 |

**Note:** Local time (Helsinki); No 1, 2 - number of thermistor in logbook.

## 3.5 Sea Ice Mechanics Initiative Experiment

This section describes the field experiment performed under the Sea Ice Mechanics Initiative programme. This field experiment has been discussed in numerous papers (for example, Proceedings of the Sea Ice Mechanics and Arctic Modeling Workshop, 1995, and Journal of Geophysical Research, 103(C10), 1998). Therefore, only a brief description of the experiment is given in this section with an emphasis on the present research.

### 3.5.1 Overview of the experiment

Similarly to the ICE STATE field campaign the objectives of the SIMI experiment were to study deformations and dynamics of the Arctic pack ice on several spatial scales using accurate instrumentation, such as GPS and ARGOS buoys, stress and strain transducers and acoustic equipment. However, in contrast to the ICE STATE campaign the SIMI experiment was less focused on the relationship between ice dynamics and morphology, but included extensive small-scale ice mechanical tests performed *in situ* in the ice camp. Only one Synthetic Aperture Radar (SAR) satellite ERS-1 was available at that time, hence this limited the cross analysis of the ice dynamics from different observational platforms (Overland et al., 1998). The SIMI experiment lasted significantly longer than the ICE STATE field programme and covered the ice formation season as well as period of the maximal ice extent.

A camp was established on a multi-year ice floe in the Beaufort Sea 250 nautical miles north of the Alaskan coast (75°N, 142°W) and was occupied from late September 1993 until April 1994. During this period the camp drifted approximately 140 nautical miles to the west (74°N, 155°W). From the end of December 1993 until the beginning of March 1994 the camp was left unmanned, however the majority of equipment was designed to run autonomously and data collection continued throughout this period as well. With the help of Global Positioning System (GPS) and ARGOS system the position of the experimental floe was monitored through the whole year from September 1993 until October 1994. Over this period the floe was entrained into the Beaufort Gyre and nearly completed a loop in a clockwise direction with a total drift of about 500 nautical miles (Fig. 3.33).

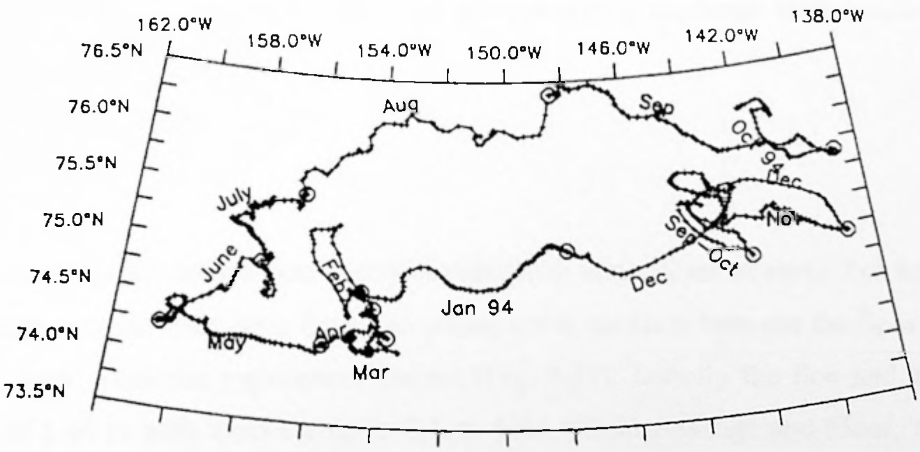


**Figure 3.33.** Daily positions of SIMI camp from autumn 1993 until autumn 1994 (after Overland et al., 1998).

[illegible]

[illegible]



[illegible]

In autumn 1993 the ice conditions in the Alaskan sector of the Beaufort Sea were extremely mild. The ice extent was minimal in relation to the previous 20 years (Overland et al., 1998). In September, when camp was set up, the ice edge was about 120 – 180 nautical miles from the coast, leaving a large part of the sea ice-free. The position of the camp was about 60 nautical miles from the ice edge in the interior of the ice zone with average concentration of 90-100 percent and a concentration of the multiyear ice of about 80 percent (Fig. 3.34a). While the cold season progressed the sea extended towards the coast, and the sea became completely ice covered with only few coastal polynyas remaining by January 1994. The multiyear ice edge also moved to the south and was found at about 100 – 120 nautical miles from the coast on 28$^{th}$ January (Fig. 3.34b). The mean thickness of the level first year ice in the vicinity of the camp reached 2 m whereas the first year ice in the southern part of the sea was thinner, only about 70 – 120 cm thick. Several deformation events in the vicinity of the camp were visually observed during its manned stage. One of these events occurred as early as in September 1993. The lead adjacent to the experimental floe began to close and a ridge formed from the thin ice (Fig. 3.35).

Over the course of the experiment the daily averaged air temperature in the vicinity of the camp was above -20°C only on a few occasions; quite often the temperature went below -35°C. The exception was late September and early October 1993 when the air was generally warmer and the temperature varied between -5°C and -17°C (Richter-Menge and Elder, 1998; Wells et al., 1995). The autumn and winter months were characterised by a series of depressions. They brought strong winds with speeds often up to 20 m/s into the area of the experiment. Winds in March and April 1994 were generally moderate with speeds below 10 m/s (Overland et al., 1998).

### 3.5.2 Observations

The experimental ice floe was nearly circular with dimensions of about 3×3 km and was surrounded by several multi-year floes; the young ice in the leads between the floes was about 15-30 cm thick when the experiment started (Fig. 3.35). Initially the floe had an average thickness of 1.44 m with level ice up to 2.1 m thick (Richter-Menge and Elder, 1998). The upper surface of the floe was relatively flat and had very few small ice sails. However the mapping of the floe thickness demonstrated that the floe was not uniform: the large area of

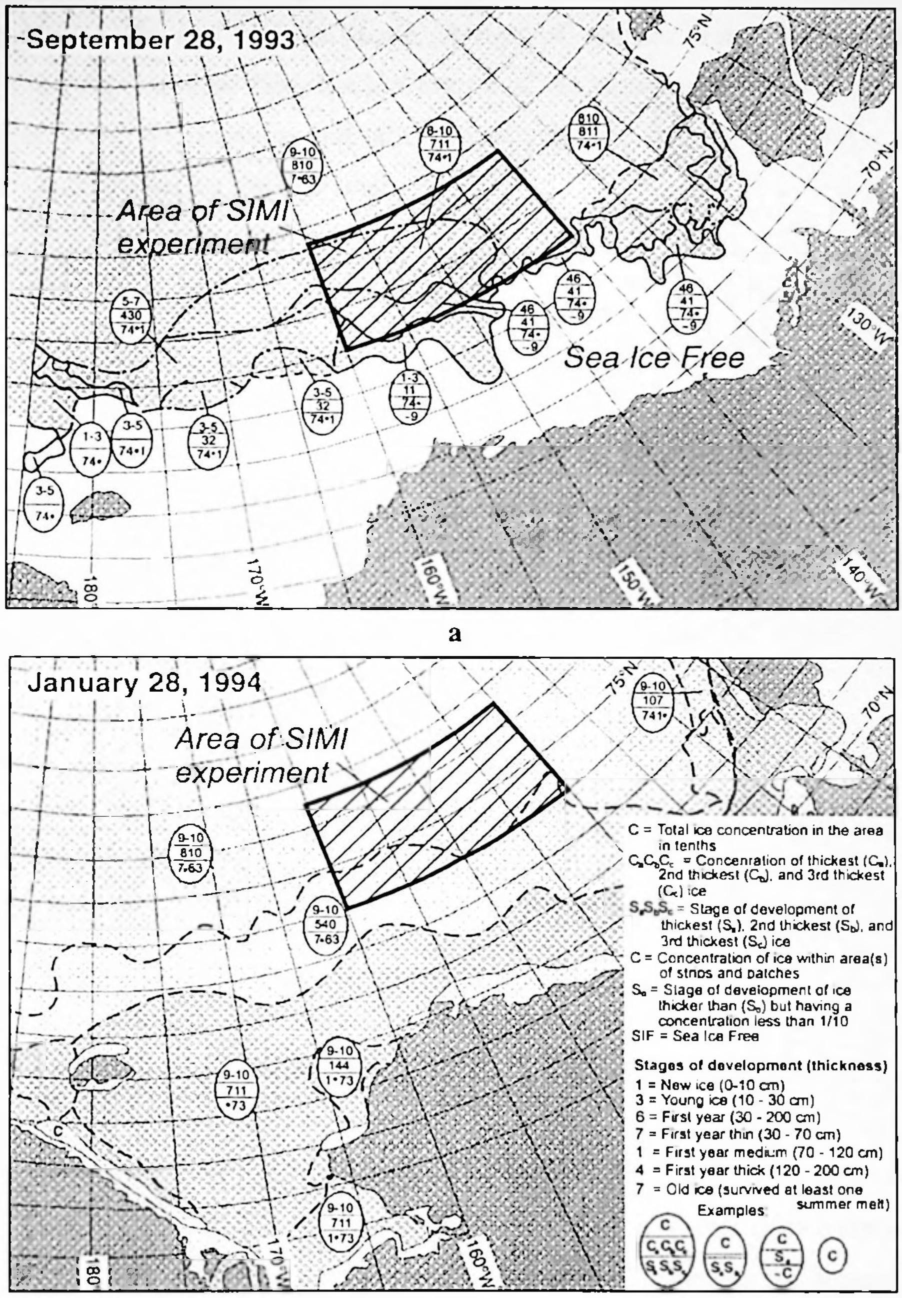


**Figure 3.34.** Ice conditions in the vicinity of SIMI camp (a) in September 1993 and (b) in January 1994 (after Overland et al., 1998).

the level first year ice of about 1 m thick extended for about 1500 m from the floe edge inside the floe interior. The ice drilling also revealed the presence of ice keels up to 4 m deep in the central part of the floe (Richter-Menge and Elder, 1998).

During the SIMI experiment ice deformations were monitored *in situ* on two spatial scales: the local scale and regional scale. Arrays of sensors were installed at different locations of the experimental floe. Such a layout of the experiment allowed us not only to observe local scale deformation but also investigate the spatial variability of the ice deformations and stresses on the floe scale.

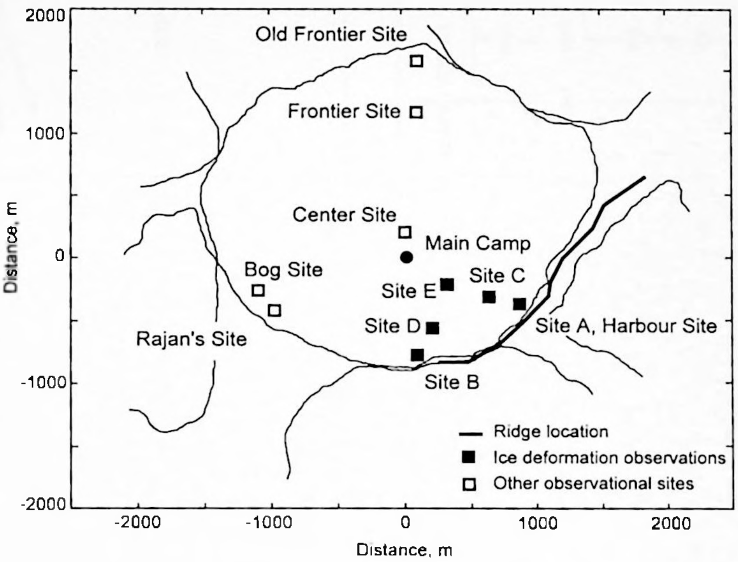


**Figure 3.35.** Layout of sensors on experimental floe. A, B, C, D and E - sites of deformations measurement. Harbour, Center, Bog, Frontier, Old Frontier - sites of CRREL stress gauges. Thick solid line shows location of ridge formed in September 1993.

A team from SPRI led by P. Wadhams monitored local deformation of the ice cover and its motion with the help of tiltmeters, *BP-Delta* strainmeters, and three-axis inertial accelerometers. The sensors were deployed near the edges of the floe and in the floe interior. Figure 3.35 shows locations of the observational sites while Fig. 3.36 gives a layout of the sensors at sites A, B, C, D and F. The team carried out measurements in two stages. The first one started in September 1993 and ended in December 1993 whereas the second stage took place in April 1994. The first stage consisted of three observational periods: September 22$^{nd}$ – 29$^{th}$; September 30$^{th}$ – October 29$^{th}$, and November 1$^{st}$ – 28$^{th}$. The full-scale experiment took place during the third observational period with the most extensive observational programme on ice deformations, so the author will mainly address these observations in his research. The sampling frequency for the measurements of strain, acceleration and tilt varied between 1 and 3 Hz. Here we give examples of one tilt and one accelerometer record, experiment 13, 28$^{th}$

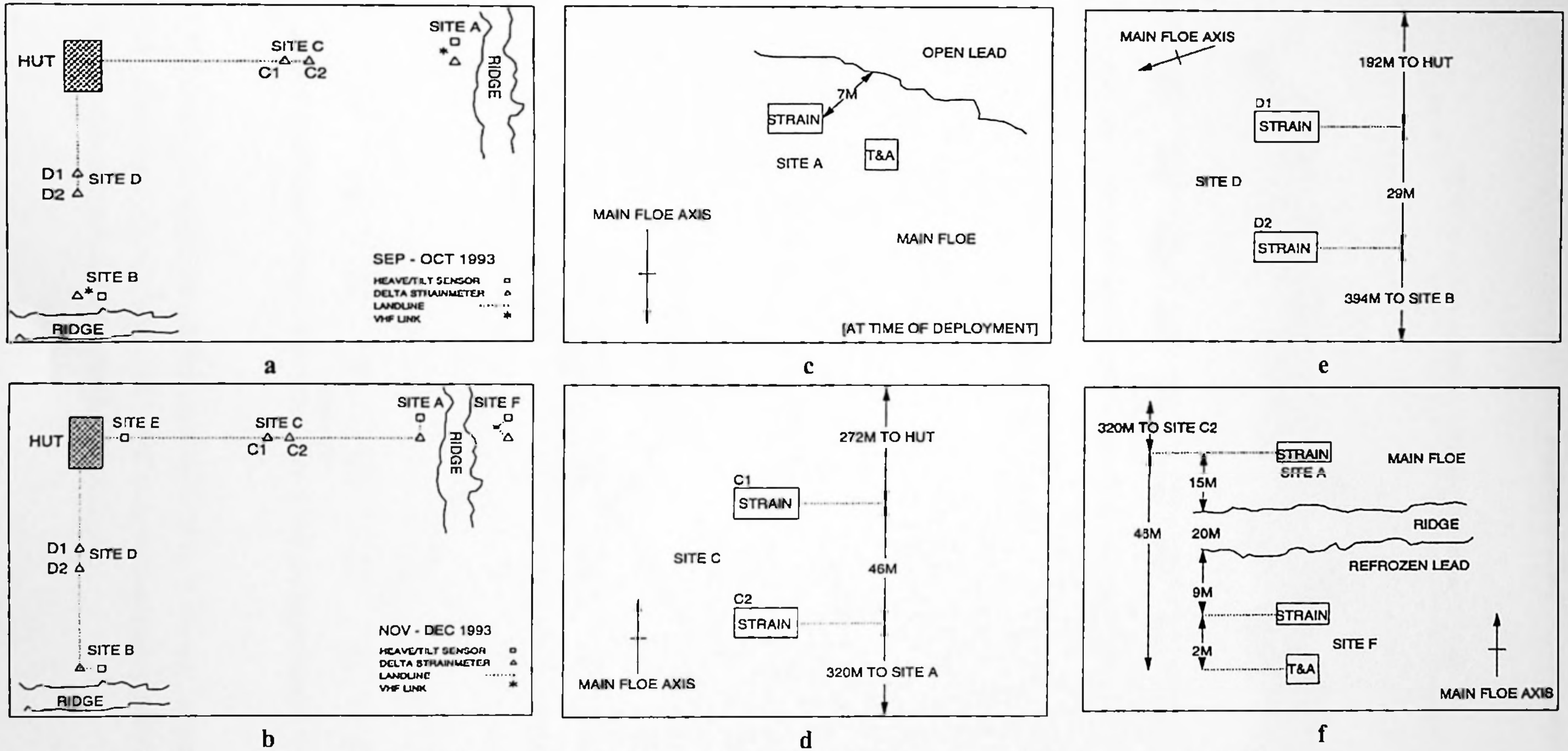


**Figure 3.36.** Location of SPRI experimental sites on the floe (a,b) and layout of sensors at experimental sites A, C, D and F (c-f).

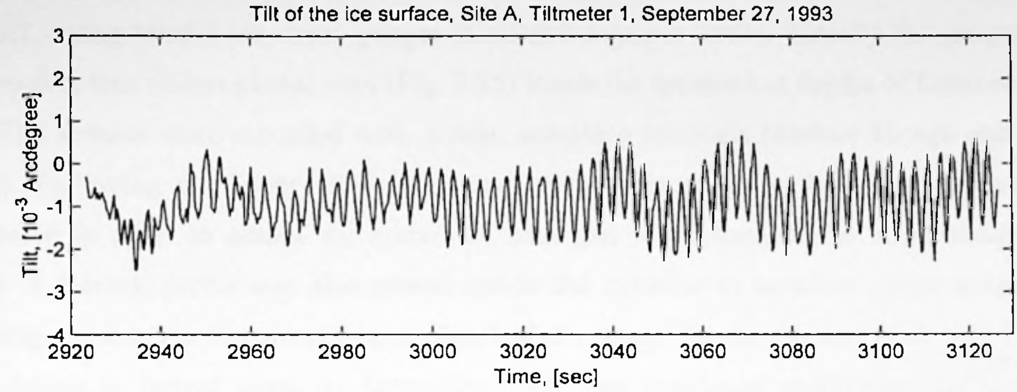


**Figure 3.37.** An example of the short period oscillations of the ice over. SIMI camp, Experiment 13, September 28, 1993.

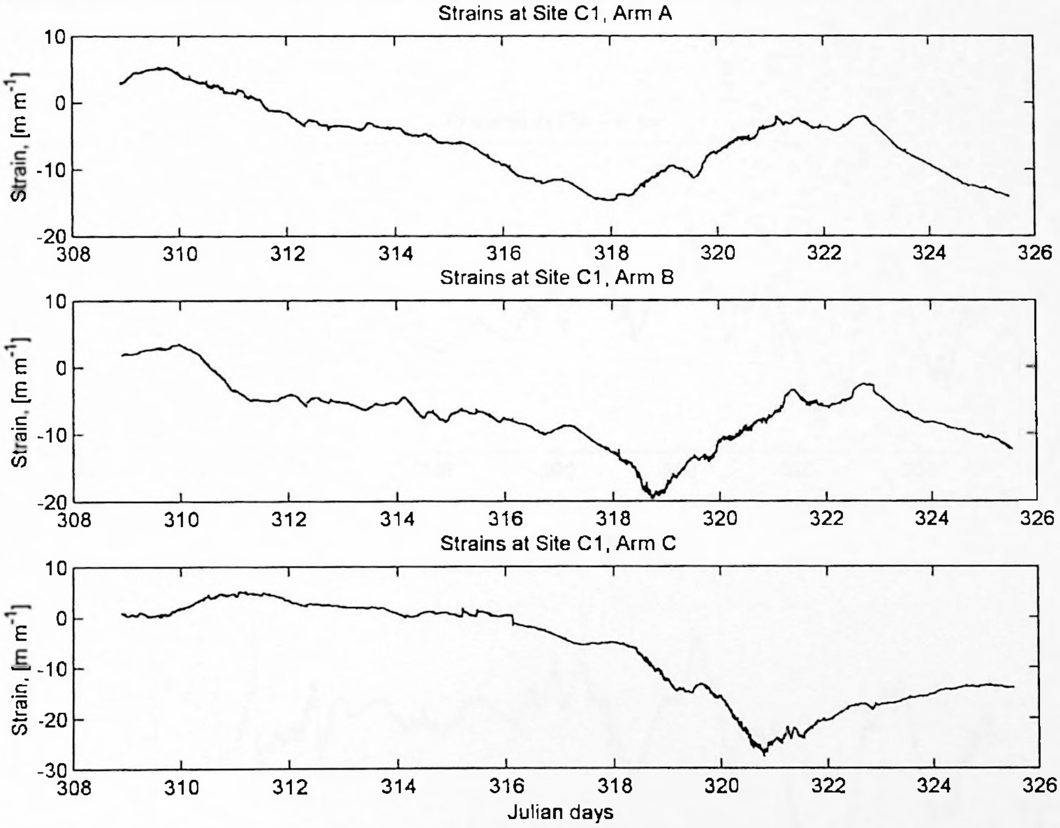


**Figure 3.38.** Local deformations (strains) observed at Site C1 of the experimental floe. SIMI camp, autumn/winter 1993.

September, 1993, which contain short period oscillations (Fig. 3.37) and an example of three one dimensional strains from Site C1 (Fig. 3.38). The complete data set is stored on the server at the Scott Polar Research Institute, University of Cambridge.

The local stresses in the ice were monitored during the SIMI experiment by staff from CRREL, using biaxial ice stress gauges (Cox and Johnson 1983). Initially the gauges were deployed at four observational sites (Fig. 3.35) inside the ice sheet at depths of between 20-98 cm. The stresses were recorded with 5 min. sampling intervals (Richter-Menge and Elder, 1998). Following the Mohr Circle rule the output signals from the stress gauges were processed in order to obtain the horizontal principal component of the stress tensor (Fig. 3.39). A thermal probe was also placed inside the cylinder to measure gauge temperature enabling an observer to correct output signal of the sensor for the thermal drift. The CRREL team began to record stress in September 1993 and continued monitoring for about six months. Because of an intense deformation event in November 1993 the so-called Bog Site was abandoned and the Frontier Site was relocated to a new position close to the floe centre (Fig. 3.35).

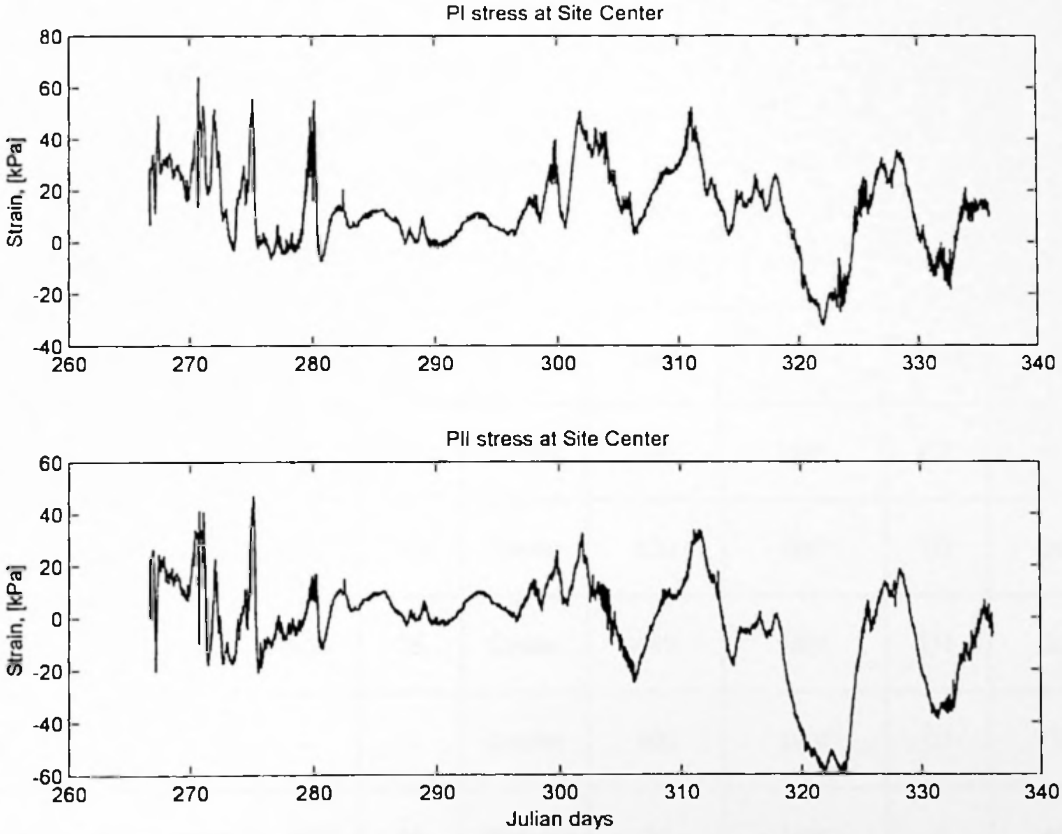


**Figure 3.39.** Principal components of the local stress observed at the Center Site of the experimental floe. SIMI camp, autumn/winter 1993.

Distances between the SPRI and CRREL observational sites as well as compass orientation of gauges are shown in Table 3.6. The complete description of the deformation and stress sensors is given in section 3.1 of this chapter. Details of the SPRI experimental

programme during the SIMI field experiment can also be found in Wadhams and Wells (1995), Wells et al. (1995), and Aksenov (1997).

Local strain and stress data along with regional scale deformations were the main data sets for the author's analysis. While the stress data were processed and kindly supplied by CRREL scientists, the record of local ice strain, tilt and acceleration required decoding and full processing before being suitable for the analysis. The author performed data processing according to the scheme described earlier in Chapter 3.

**Table 3.6.** Layout of the observational sites.

| Site | Orientation of arms* | | | Strain gauge No | Nearest stress gauge | | | Nearest strain gauge | |
|---|---|---|---|---|---|---|---|---|---|
| | A | B | C | | is at | Distance m | Wire 1 is oriented** | is at | Distance m |
| A | 280° | 220° | 160° | 30 | Harbour | 10 | 300° 01.05.00 | F | 44 |
| B | 130° | 70° | 10° | 8 | Harbour | 1100 | 180° | D2 | 394 |
| C1 | 130° | 70° | 10° | 5 | Center | 690 | 180° | C2 | 46 |
| C2 | 130° | 70° | 10° | 20 | Center | 736 | 180° | C1 | 46 |
| D1 | 180° | 120° | 60° | 17 | Center | 620 | 180° | D2 | 29 |
| D2 | 180° | 120° | 60° | 26 | Center | 649 | 180° | D1 | 29 |
| E | – | – | – | – | Center | 400 | 180° | C1 | 270 |
| F | 180° | 120° | 60° | 16 | Harbour | 54 | 180° | A | 44 |

**Note:** * - Clockwise from the north; ** - count clockwise from the north.

Regional ice deformations were monitored with the help of GPS and ARGOS drifters. Twelve drifters were deployed in the vicinity of the SIMI camp in late September 1993. The

buoys formed two arrays around the camp with initial diameters of about 10 and 20 km (Overland et al., 1998). Another GPS buoy was also installed near the centre of the experimental floe. All drifters were designed to use the same group of satellites for a given "fix" in order to reduce error in the positioning using GPS. ARGOS positions were also obtained to check GPS and fill the gaps if a period between GPS "fixes" exceeded 5 hours. The total accuracy of the positions of the drifters was between 3 and 20 m. Time series for 13 buoys were received by the author from the Pacific Marine Environmental Laboratory courtesy of Dr. J. Overland. The regional scale deformations were derived from differential motion of the ice drifters following the Differential Kinematic Parameter method (Crane and Wadhams, 1996; Wadhams et al., 1989). Examples of the distances and azimutal directions from the SIMI camp to the drifters are shown here (Figs. 3.40 and 3.41).

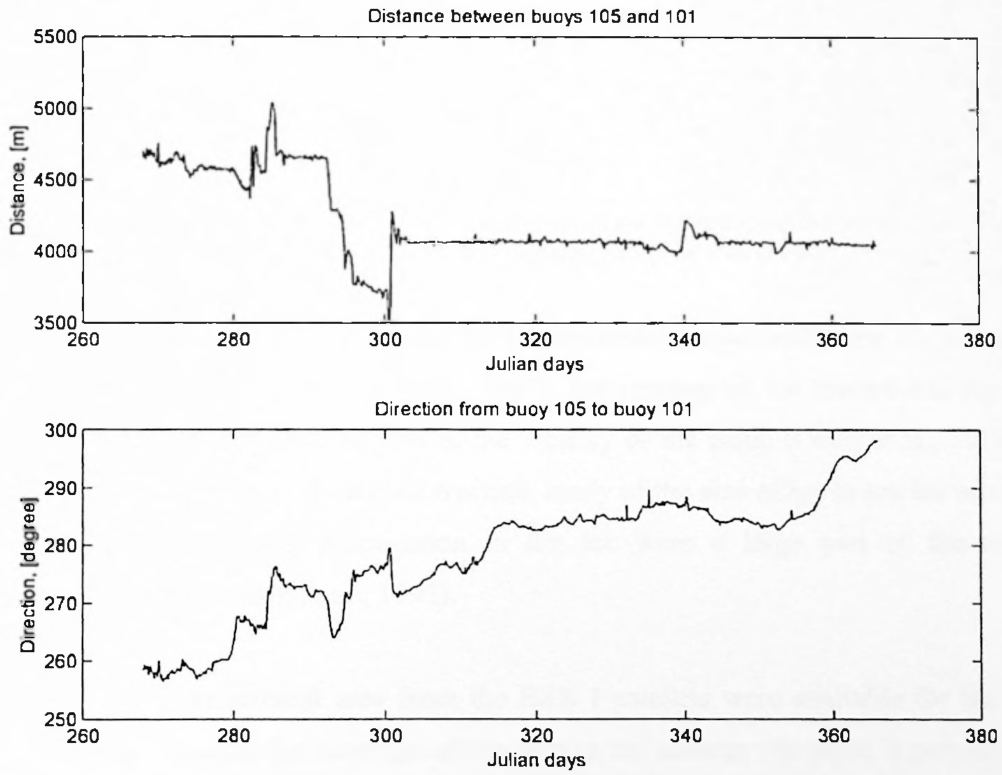


**Figure 3.40.** Above: distance between buoy 105 installed on the main experimental floe and buoy 101. Below: azimutal direction from buoy 105 towards buoy 101 (0 is true north).

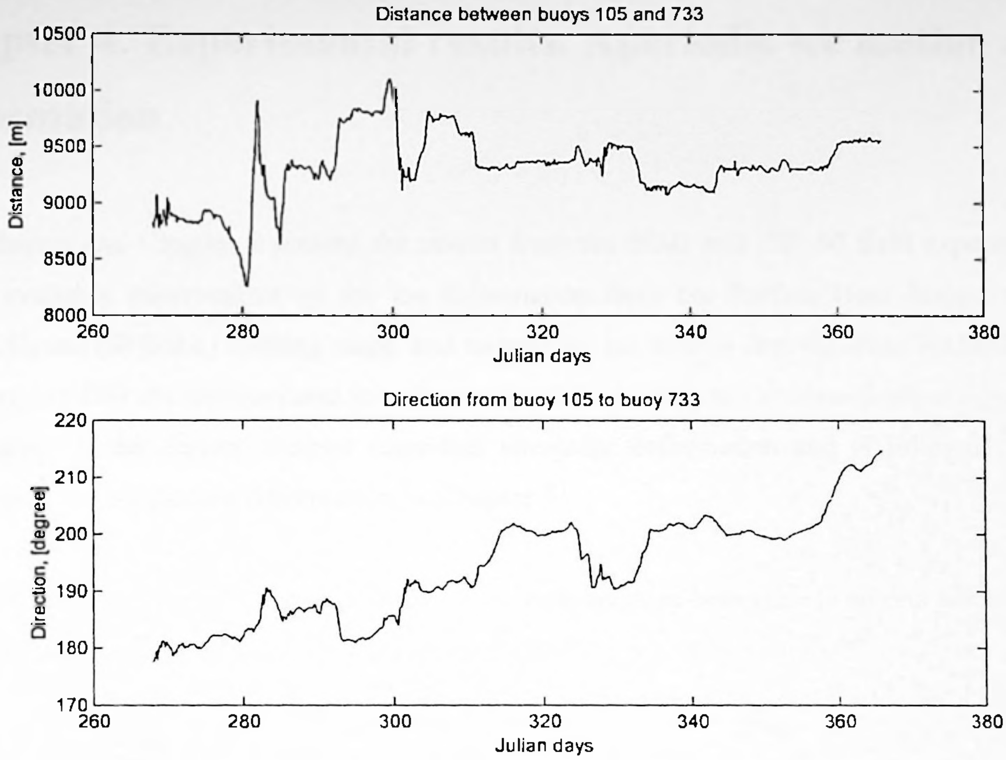


**Figure 3.41.** Above: distance between buoy 105 installed on the main experimental floe and buoy 733. Below: azimutal direction from the buoy 105 towards buoy 733 (0 is true north).

Additional data were collected during the experimental period, including ice salinity and temperature measurements (Perovich et al., 1997), information on ice mechanical properties (Adamson et al., 1995) and ice structure in the vicinity of the camp (Coon et al., 1995). The experiments on the large scale *in situ* ice fracture, study of the size effect in sea ice mechanics and monitoring of the crack propagation in the ice were a large part of the research programme as well (Adamson et al., 1995).

Images of the experimental area from the ERS 1 satellite were available for the spring stage of the camp. Because the coverage of the area in the autumn was poor, it proved to be a difficult task to take good images of the camp area. However, the author succeeded to obtain some regional deformation fields. The observations on local wind and air temperatures were carried out during the manned stages of the ice camp (Wells et al., 1995).

[illegible]

[illegible]

[illegible]

[illegible]

# Chapter 4. Experimental results. Aperiodic ice motion and deformation

This chapter and Chapter 5 present the results from the SIMI and ZIP–97 field experiments. Other available observations on the ice deformation from the Surface Heat Budget of the Arctic Ocean (SHEBA) drifting camp and mesoscale ice motion derived from RADARSAT imagery (RGPS) are incorporated into the analysis. According to the classification suggested in Chapter 2, the current chapter considers aperiodic deformation and is followed by an analysis of the oscillatory deformation in Chapter 5.

The discussion has two foci: a study of the relationships between ice strains and stresses on the floe scale and a cross-scale examination of the ice deformation. The essence of the cross-scale analysis is to compare the floe scale and mesoscale ice deformation caused by non-homogeneous ice drift, and also to estimate the level of the internal stresses achieved during the deformation events.

Because several processes affect the overall ice deformation the signal recorded by the sensors is rather complex. Therefore, the first task was to identify different types of the deformation processes and to isolate deformation signals related to them.

## 4.1 Thermally-induced deformation

The expansion of ice due to changes of the ambient air temperature leads to a substantial strain of the ice floe. Thermally induced stress can be as large as that generated during a deformation event (Tucker and Perovich, 1992); hence this type of ice deformation process ought to be considered of a prime importance. Strain records from the both SIMI and ZIP-97 field experiments show the presence of variability highly correlated to the fluctuations in the atmosphere temperature. To study the contribution of the thermally-induced deformation into the overall ice deformation a visco-elastic (creep) model was developed by the author.

### 4.1.1 The model for the thermal deformation

The model is based on the scheme suggested by Lewis (1993 and 1998) and has two principal components. The first component simulates ice thermodynamics whereas the second one, the mechanical model, calculates the deformation and stress in the ice interior from the temperature field obtained from the thermodynamic component of the model.

The thermodynamic component calculates the temperature of the ice or snow surface at the current time step from the balance of the six thermal fluxes on the surface (eq. 4.1). These fluxes are: the absorbed short wave radiation $Q_{swa}$; the incoming long wave radiation $Q_{lw}$; the long wave black body emission $Q_{lwe}$, the latent $Q_{lat}$ and sensible $Q_{sen}$ heat fluxes; the conductive heat flux from the ice or snow interior towards the surface $Q_{cond}$. In its turn the conductive flux is derived from the solution of the heat diffusion equation for the ice and snow interior. We assumed horizontally uniform thermal forcing. Therefore, the formulation of the problem is one–dimensional.

To obtain the diurnal cycle of the incoming short wave radiation the total solar insulation for the clear sky $Q_{si}$ was calculated from the local solar zenith angle for the specified day of the astronomical year, time of the day and latitude of the experimental site using Shine's formula (Shine, 1984). Parameterisation suggested by Laevastu (1960) was used to calculate the incoming short wave radiation for the cloudy sky (eqs. 4.1a-g). Finally, the short wave radiation absorbed by the snow-ice surface $Q_{swa}$ is equal to the product of the incoming short wave radiation and albedo factor (eq. 4.1c).

The incoming long wave radiation $Q_{lw}$ was obtained from the formula for the clear sky conditions developed by Idso and Jackson (1969) and modified by an empirical cloudiness factor (Marshunova, 1961) (eq. 4.2a). The long wave emission $Q_{lwe}$ was defined following the Stefan–Boltzmann law for black body radiation (eq. 4.2b). The fluxes of the latent $Q_{lat}$ and sensible $Q_{sen}$ heat were calculated using the equations from Parkinson and Washington (1979) and Doronin and Kheysin (1975) with the modification for the stability of the above ice air column from Meier et al. (1999) (eqs. 4.3a-c).

$$Q_{si} = \frac{S_0 \cdot cos^2(z)}{(cos(z)+1) \cdot e_a \cdot 10^{-5} + cos(z) + 0.046} \tag{4.1a}$$

$$Q_{sw} = Q_{si} \cdot (1 - 0.6 \cdot c^3) \tag{4.1b}$$

$$Q_{swa} = Q_{sw} \cdot (1 - a_{si}) \tag{4.1c}$$

$$cos(z) = sin(\phi) \cdot sin(\delta) + cos(\phi) \cdot cos(\delta) \cdot cos(\alpha_h) \tag{4.1d}$$

$$e_a = P_0 \cdot q_a / (0.622 + 0.378 \cdot q_a) \tag{4.1e}$$

$$\delta = 23.4° \cdot cos(172 - day) \cdot \pi / 180° \tag{4.1f}$$

$$\alpha_h = (12 - t_{sol}) \cdot \pi / 12 \tag{4.1g}$$

where, $S_0$ = 1353 [W·m$^{-2}$] – is the solar constant; $z$, $\phi$, $\delta$, , $\alpha_h$ – are the solar zenith angle, latitude, solar declination and hourly angle [rad]; *day* and $t_{sol}$ – are the day of the year and solar time; $e_a$ – is the near surface vapour pressure [Pa]; $c$ – is the cloudiness; $a_{si}$ – is the snow or ice albedo; $P_0$ = 1.013·10$^5$ – is the reference near surface atmosphere pressure [Pa].

$$\begin{aligned} Q_{lw} = & \left(1 - \frac{0.261}{exp\left(7.77 \cdot 10^{-4} \cdot (273 - T_a)^2\right)}\right) \times \\ & \times \sigma_{st} \cdot T_a^{\ 4} \cdot (1 + 0.275 \cdot c) \end{aligned} \tag{4.2a}$$

$$Q_{lw'} = \sigma_{st} \cdot T_{surf}^{\ \ 4} \tag{4.2b}$$

where, $T_a$ and $T_{surf}$ – are the near surface air temperature and snow-ice surface temperature in Kelvins; $\sigma_{st}$ = 5.673·10$^{-8}$ – Stefan-Boltzmann constant [W·m$^{-2}$·K$^{-1}$].

$$Q_{sen} = \rho_a \cdot C_a \cdot W \cdot C_T (T_a - T_0) \tag{4.3a}$$

$$Q_{lat} = \rho_a \cdot L_v \cdot W \cdot C_q (q_a - q_0) \tag{4.3b}$$

$$\begin{aligned} q_a - q_0 = & 3.8_a \cdot 10^{-3} \cdot exp(a \cdot T_a) \times \\ & \times [r - exp(a \cdot (T_0 - T_a))] \end{aligned} \tag{4.3c}$$

where, $T_a$, $T_0$, $q_a$, $q_0$, – are the air temperature and specific humidity at the 10 m height and at the air-ice interface [K]; $a$ = 0.086 [K$^{-1}$]; $W$ – is the wind speed at the 10 m height [m·s$^{-1}$]; ; $r$ – is the relative humidity at the 10 m height; $C_a$ – are the air density [kg·m$^{-3}$] and specific heat of air [J·kg$^{-1}$·K$^{-1}$]; $L_v$ – is the latent heat of vaporisation [J·kg$^{-1}$]; $C_q$ = 1.75·10$^{-3}$ and $C_t$ – are the latent and sensible heat transfer coefficients.

The transfer coefficient $C_t$ in equation (4.3a) depends on the stability of the air column and equals to the value of $0.66 \cdot 10^{-3}$ when $(T_a - T_0) > 0$, i.e. the column is stable, and to the value of $1.13 \cdot 10^{-3}$ when $(T_a - T_0) < 0$, i.e. the column is unstable.

$$Q^{snow}{}_{cond} = \lambda_s \cdot \left(T_{si} - T_{surf}\right) \tag{4.4a}$$

$$Q^{ice}{}_{cond} = \lambda_i \cdot \left.\frac{\partial T}{\partial z}\right|_{surf} \tag{4.4a}$$

where, $\lambda_s$, $\lambda_i$, – are the thermal conductivity of snow and ice; $T_{surf}$, $T_{si}$ – are the temperatures of the snow surface and at the snow-ice interface.

The conductive flux at the air interface is calculated for two cases: the snow covered ice $Q^{snow}{}_{cond}$ and the bare ice $Q^{ice}{}_{cond}$. During the both ZIP-97 and SIMI experiments the temperature profile in the snow bulk assumed to be linear because the snow cover was thin. In this assumption the flux is proportional to the temperature difference between snow-interface and upper snow surface (eq. 4.4a). For the bare surface conductive flux is computed from the temperature difference between the surface and the next ice layer (eq. 4.4b).

$$\rho_i \cdot C_i \cdot \frac{\partial T}{\partial t} = \lambda_i \cdot \frac{\partial^2 T}{\partial z^2} \tag{4.5a}$$

$$\left.T\right|_{z=0} = T_{surf}, \left.T\right|_{z=H} = T_{fr}, \left.T\right|_{t=0} = T_{init}(z) \tag{4.5b}$$

where, $\rho_i$, $C_i$ – are the density and specific heat of ice; $T_{surf}$, $T_{fr}$ – are the temperature of the upper ice surface and freezing point temperature; $T_{init}(z)$ – is the initial profile of the ice temperature; $t$, $z$ – are the time and the ice depth.

Equation (4.5a) describes the diffusion of heat in the ice bulk and can be solved for temperature $T(z,t)$ for the given boundary and initial conditions (4.5b). In the most general case parameters $\lambda_{is}$, $\rho_{is}$, $C_{is}$ are functions of the temperature, which makes the equation non-linear, however in the majority of practical cases the parameters can be taken as constants within a certain temperature range without significant effect on the solution.

The heat diffusion equation is solved with the help of finite difference method. The forward-marching explicit scheme was applied to calculate temperature in the snow-ice

interior $T_{is}$ and conductive flux towards the upper surface $Q_{cond}$. The conductive flux in the snow-ice interior depends on the surface temperature in the non-linear manner; hence the iterative procedure was applied on each time step to equilibrate the heat loss from the snow-ice surface to the flux from the interior. The sensitivity tests demonstrate that it is sufficient to perform 10 iterations to stabilise the temperature with the accuracy of about 0.2 °C.

The approach described above was used successfully to simulate ice thermodynamics in the Arctic over long periods (months and seasons), and to model the diurnal variations of the temperature in the ice interior in the northern Baltic (Parkinson and Washington, 1979; Meier et al., 1999; Cheng et al., 2001).

Additional features of the thermodynamic model are the special treatment of the upper surface melting and ice accretion at the bottom surface. In order to simplify the thermodynamic part the following assumption for the melting of the upper surface was made. If the temperature of the snow surface exceeds $T_{melt}$ = 0.1615°C one layer of snow melts and surface temperature is set to the value of $T_{melt}$. The snow continues to melt until it is gone completely, then the surface temperature of ice is set to $T_{melt}$. However the ice is not allowed to melt but its surface is kept at the melting temperature until the heat balance is such that cooling of the surface occurs. This scheme tends to simulate the fact that the melt water in spring stays on ice for some time serving as a heat reservoir and delays the melting of upper ice surface. The model does not simulate the accretion and melting at the ice bottom surface. It was assumed that on the one hand the period of the simulations is too short to introduce any significant ice accretion. On the other hand the ocean flux towards the ice is quite small (of about 1-2 $W \cdot m^{-2}$) and is balanced by the small conductive flux at the lower ice surface, so the melting at the ice bottom is negligible.

The mechanical part of the model calculates thermally-induced deformation and stress with the help of non-linear visco-elastic rheology so-called "Maxwell model" (eq. 4.6). This type of constitutive law considers ice behaving as an elastic as well as viscous (creeping) continuum in response to the load (Mellor, 1986). In most general three–dimensional cases the stress $\dot{\bar{\bar{\sigma}}}$ and strain $\dot{\bar{\bar{\varepsilon}}}$ rates are tensors, whereas the effective elastic modulus $E'$ becomes a tensor if ice anisotropy is taken into account (Mellor, 1986). The creep rate $\gamma$ is the

[illegible]

non-linear power–law–type function of stress tensor $\bar{\bar{\sigma}}$ and temperature $T$, and also depends on ice porosity, salinity and type of ice, i.e. granular or columnar (Sanderson, 1988).

$$\dot{\bar{\bar{\varepsilon}}}(\bar{x},t)=\frac{\dot{\bar{\bar{\sigma}}}(\bar{x},t)}{E'(\dot{s},T,\Xi)}+\gamma(\bar{\bar{\sigma}},T,\Xi) \tag{4.6}$$

where, $\dot{\bar{\bar{\sigma}}}$ and $\dot{\bar{\bar{\varepsilon}}}$ – are the tensors of the stress and strain rates; $\bar{\bar{\sigma}}$ – is the stress tensor; $E'$ – is the effective elastic modulus; $\bar{x}$, $t$ – are the spatial coordinate and time; $\dot{s}$, $T$, $\Xi$ – are the total strain rate, ice temperature and structure. The latter includes salinity, porosity and also takes into account whether ice is granular or columnar type.

In the present study we consider an isotropic horizontally homogeneous ice plate of thickness $H$, resting on the water. The plate is heated/cooled from above in a horizontally uniform manner due to variations in the atmosphere temperature and fluxes. In these conditions the thermo-mechanical response of the plate is also isotropic and horizontally uniform. Therefore, following Lewis (1993) the governing equation becomes one–dimensional (eq. 4.7a). These assumptions mean that we simulate deformation developing in the inner area of the floe, far enough from its edges. The stress observations demonstrate that over a distance greater than 100-200 m from the floe edge in the floe interior the isotropic component of the stress tensor largely dominates the shear component (Richter-Menge and Elder, 1998; Tucker and Perovich, 1992, also see discussion in section 4.2 of this chapter). A typical size of floe during these experiments was about 1000-2000 m. It makes the anisotropic boundary region to be order of 1 percent of the total floe area.

$$\dot{\sigma}(z,t)=E'(\dot{s},T,\Xi)\cdot\dot{s}(z,t) \tag{4.7a}$$

$$\dot{s}(z,t)=\dot{\varepsilon}_t(\dot{T})-\dot{\zeta}(\dot{\varepsilon}_t,\gamma,E')-\gamma(\sigma,T,\Xi) \tag{4.7b}$$

$$\dot{\varepsilon}_t(\dot{T})=\beta_T\cdot\dot{T}(z,t) \tag{4.7c}$$

where, $\dot{\varepsilon}_t$, $\dot{\zeta}$, $\gamma$ – are the rate of the thermo-elastic strain, strain rate due to floe bending, and creep rate; $\dot{s}$, $\sigma$, $\dot{\sigma}$ – are the total strain rate, stress and stress rate; $\beta_t$ – is coefficient of the ice thermal expansion [K$^{-1}$]; other notations are given earlier.

[illegible]

[illegible]

$$[illegible]$$

[illegible]

$$[illegible]$$

[illegible]

The first term on the right side of equation (4.7b) represents the thermo-deformation of the ice because of the temperature change. This component is purely elastic and depends on the rate of the temperature change and the ice thermal expansion coefficient (eq. 4.7c).

The term $\dot{\zeta}$ describes the reaction of the floe to the different deformation of ice layers due to vertical gradient of the temperature in ice. Let us consider this process in greater detail. Under the variation of the atmospheric conditions the temperature of the upper ice surface tends to vary as well. When surface temperature decreases/increases upper ice layers shrink/expand in phase with this variation. At the same time the lower ice layers are kept at the nearly constant temperature (close to the freezing temperature) and are shrinking and expanding less. The vertical gradient in the horizontal deformation makes the ice floe curl up or down and changes the balance between gravity and buoyancy force (hydrostatic balance) for the local point of the ice floe. The change in the hydrostatic balance opposes the bending of the floe, and if the floe is big enough (300 m in diameter or more) might completely eliminate the bending (Bogorodsky et al., 1972). As the upper layers of the large floe begin to shrink the lateral strain is transmitted towards lower layers making them shrink to some degree. As a rule the upper ice layers deform more than the lower ones. Because of that and because the floe is too large and can not bend the upper part of the ice bulk undergoes tension whereas the lower part experiences compression (Lewis, 1993 and 1998; Tucker and Perovich, 1992).

One should notice that if the floe can bend a larger strain in the upper ice layers is generated but the stress amplitude in the floe interior is reduced. Such an effect can be seen for example from the comparison between the time series of stress observed near the edge and in the central region of the same ice floe (Tucker and Perovich, 1992; and also section 4.2 of this chapter).

A formulation for the described process was suggested by Bogorodsky et al. (1972) on the assumption of pure elastic deformation and further extended by Lewis (1993 and 1995) for the visco-elastic deformation with lateral variation of ice strain because of the variable snow depth. The latest formulation also takes into account the impact of the existed flaws in the ice interior on the thermal stress (Lewis, 1998). For the aim of the current research we employed more simple formalism (eq. 4.8). The equation was derived from the formulation

[illegible]

[illegible]

[illegible]

[illegible]

[illegible]

[illegible]

suggested by Lewis (1998) with number of flaws equal to zero and with the uniform snow depth. The choice was made because on the one hand the number of flaws used in the original formula is unknown parameter, impossible to derive precisely for the real experimental site. On the other hand the snow depth during the both ZIP-97 and SIMI experiments was quite uniform on the large area of the experimental floe which eliminates the lateral variation of the strain rate term $\dot{\zeta}$.

$$\dot{\zeta}(\dot{\varepsilon}_t,\gamma,E')=\frac{\int_0^H E'(\dot{s},T,\Xi)\cdot\left(\dot{\varepsilon}_t(\dot{T})-\gamma(\sigma,T,\Xi)\right)\cdot dz}{\int_0^H E'(\dot{s},T,\Xi)\cdot dz} \qquad (4.8)$$

where, $H$ – is the thickness of ice; other notations are given earlier.

There is a number of formulae to parameterise the creep rate $\gamma$ of fresh water ice as well and saline ice. The majority of them use the power–law formulation with the parameters derived from the Arrhenius equation (Glen, 1955). The author tested two basic schemes: the formula suggested by Richter-Menge and Cox (1995) for saline ice and the parameterisation for the fresh water ice (Sanderson, 1988). The latter accounts for the type of ice: whether it is granular or columnar ice (eq. 4.9). This scheme was found to give better results for the fresher ice in the Baltic.

$$\gamma(\sigma,T,\Xi)=A(T,\Xi)\cdot exp\left(-\frac{Q(T,\Xi)}{R\cdot T}\right)\cdot\sigma^3(z,t) \qquad (4.9)$$

where, $R$ = 8.314 – is the universal gas constant [$J\cdot mol^{-1}\cdot K^{-1}$]; A and Q – are the creep parameter and the activation energy. For the granular ice and for the temperature below –8°C, A = $4.1\cdot 10^8$ [$MPa\cdot s^{-1}$] and Q = 120 [$kJ\cdot mol^{-1}$]; for the temperature above –8°C A = $7.8\cdot 10^{16}$ [$MPa\cdot s^{-1}$] and Q = 78 [$kJ\cdot mol^{-1}$]. For the columnar ice A = $3.5\cdot 10^6$ [$MPa\cdot s^{-1}$] and Q = 65 [$kJ\cdot mol^{-1}$] (Sanderson, 1988); other notations are given earlier.

It has been demonstrated that the effective elastic modulus of the both fresh water ice and saline ice being the function of its temperature and porosity also depends on the deformation rate (Lewis, 1993; Mellor, 1986). Two parameterisations, one for the fresh water ice (Cox, 1984) and the other for the saline ice (Lewis, 1993), were tested for the current model (eqs. 4.10a and 4.10b respectively). Both schemes reflect the fact that ice is more rigid when it is

[illegible]

[illegible]

[illegible]

[illegible]

[illegible]

colder and less rigid when it has a higher porosity. The formulae work for a wide range of temperatures: between –40°C and –5°C (Lewis, 1993). Mellor (1986) first recognised the fact that the value of the effective elastic modulus of the freshwater ice almost halves with the reduction of the strain rate from $10^{-3}$ [$s^{-1}$] to $10^{-8}$ [$s^{-1}$]. Lewis applied this idea to the saline ice. He also put the lower limit of 1 GPa on the value of the elastic modulus. We found that parameterisation suggested by Cox (1984) (eq. 4.10a) gives somewhat better results for the fresher ice in the Baltic (section 4.1.2).

$$E'(T,p) = 4.0 \cdot 10^9 \cdot (1 - 7.5472 \cdot p(z)) \times \\ \times (1 - 0.012 \cdot T(z,t)) \tag{4.10a}$$

$$E'(\dot{s},T,p) = \varpi \cdot log(\dot{s}(z,t) + 3) + 3.5 \cdot 10^9 \times \\ \times (1 - 7.5472 \cdot p(z)) \cdot (1 - 0.0714 \cdot T(z,t)) \tag{4.10b}$$

where, $\varpi$ = 0.1 – slope [$GPa \cdot log(\dot{s})$]; $p$ – ice porosity; other notations are given earlier.

For each time step the mechanical component of the model calculates the thermal deformation $\dot{\varepsilon}_t$ in the ice interior based on the ice temperature obtained from the thermodynamic model. The first guess for the creep rate $\gamma$ is determined from the stresses $\sigma$ from the previous time step except the first time level where we use initial values for the stresses. Then the first guess for the term $\dot{\zeta}$ is calculated from the new value of $\gamma$ and a total strain rate $\dot{s}$ is obtained. Finally the effective elastic modulus $E'$ and stress rate $\dot{\sigma}$ are determined. To converge to the solution the iterative process is used with three to four iterations per time step. When Lewis formalism is used to derive elastic modulus we put a limit of 1 GPa on the value of $E'$ and a limit of $10^{-24}$ [$s^{-1}$] on the strain rate $\dot{s}$ used in the calculation of the elastic modulus. However, the strain rate is not limited for the rest of the calculations.

The stability of the whole thermo-mechanic model is conditioned by the stability of the explicit scheme employed to solve the thermal diffusion equation:

$$\Delta t_{max} = \Delta z^2 \cdot \frac{\rho_{is} \cdot C_{is}}{2 \cdot \lambda_{is}} \tag{4.10c}$$

The variations in the initial conditions either for the temperature or stress do not affect the simulation results after two days. In contrast to the tests presented by Lewis (1993), the model

[illegible]

[illegible]

[illegible]

[illegible]

was sensitive to the choice of the creep parameterisation. We attribute this difference to the type of parameterisation scheme (Sanderson, 1988) used in our experiments and to the fact that the ice we simulated is significantly warmer than that modelled by Lewis. The use of the constant value for the effective elastic modulus (values of 1GPa, 3GPa, 4GPa, 5GPa, and 10GPa were tested) makes some difference compared to the use of equation (4.10). Lower values of the modulus enhance strain whereas the stress level is reduced.

### 4.1.2 Case study I: Zooming in Ice Physics field campaign

During the ZIP-97 field campaign the observations of the local deformation covered four distinctive periods: two quiet periods ($16^{th}$ –$18^{th}$ March and $20^{th}$ –$21^{st}$ March) when the wind was light and therefore the thermal forcing prevailed and two periods with strong winds ($14^{th}$ –$15^{th}$ March and $18^{th}$ –$19^{th}$ March). A high level of the solar insulation led to the development of a strong diurnal cycle in the air temperature and these oscillations controlled the ice deformation when the wind was light or moderate (Figs. 3.14 and 3.30, Chapter 3, Part II). Two intensive deformation events are present in the surface strain records (Fig. 3.30, Chapter 3, Part II). The aim of the present analysis is to simulate surface ice deformation under the thermal forcing and therefore to estimate the residual mechanically induced component in the strain record.

In the first instance the thermal deformation was calculated with the help of the simplest model (results are not shown). According to this model the uppermost ice layer deforms independently from the layers below, proportionally to the product of the ice linear expansion coefficient $\beta_t$ and atmospheric temperature $T_a$. This model is reasonably good for the thin ice and conditions when the ice (or snow) surface temperature is close to atmospheric, i.e. for the winter or for cloudy weather. Therefore, as was expected, the model did not explain all variations in the ice deformation record. The way forward was to apply a more sophisticated model.

On the second stage of the analysis the complex thermo-mechanical model described in the previous section was applied. The cloudiness, atmospheric temperature together with the humidity and winds observed at the meteorological stations near the experimental site were averaged. These fields forced the thermodynamic part of the model from above. The freezing point temperature of the seawater $T_{fr}$ was chosen as the boundary condition from below.

Using the formula suggested by Millero (1978) for the typical water salinity in the Baltic (about 5 psu) we arrived at the value of –0.26°C for the freezing temperature. For the mechanical simulations we assumed that the upper part of the ice consisted of granular ice whereas the lower part of columnar ice with the approximate ratio of 1:3. This assumption was based on the coring performed in the Baltic ice (Kawamura et al., 2001). The model was initialised with some typical ice temperature profile and the uniform vertical stress profile $\sigma$ = 10 kPa. The parameters used in the simulations are listed in Table 4.1.

**Table 4.1.** Parameters used in the simulations for Case I.

| Parameter | Notation | Units | Value |
|---|---|---|---|
| Thermal conductivity of ice | $\lambda_i$ | $[W \cdot m^{-1} \cdot K^{-1}]$ | 2.03 |
| Thermal conductivity of snow | $\lambda_s$ | $[W \cdot m^{-1} \cdot K^{-1}]$ | 0.24 |
| Density of ice | $\rho_i$ | $[kg \cdot m^{-3}]$ | 910.0 |
| Specific heat of ice | $C_i$ | $[m \cdot °C^{-1}]$ | 2093.0 |
| Freezing point temperature | $T_{fr}$ | [°C] | -0.26 |
| Thermal expansion coefficient for ice | $\beta_i$ | $[K^{-1}]$ | $5.1 \cdot 10^{-5}$ |
| Ice salinity | $S_i$ | [psu] | 0.35–0.90 |
| Water salinity | $S_w$ | [psu] | 4.9 |
| Ice porosity | $p$ | [n/d] | 0.1 |
| Universal gas constant | $R$ | $[J \cdot mol^{-1} \cdot K^{-1}]$ | 8.314 |
| Creep parameter for granular ice, $T_i$<–8°C | A | $[MPa \cdot s^{-1}]$ | $4.1 \cdot 10^{8}$ |
| Creep parameter for granular ice, $T_i$<–8°C | Q | $[kJ \cdot mol^{-1}]$ | 120 |
| Creep parameter for granular ice, $T_i$>–8°C | A | $[MPa \cdot s^{-1}]$ | $7.8 \cdot 10^{16}$ |
| Creep parameter for granular ice, $T_i$>–8°C | Q | $[kJ \cdot mol^{-1}]$ | 78 |
| Creep parameter for columnar ice | A | $[MPa \cdot s^{-1}]$ | $3.5 \cdot 10^{6}$ |
| Creep parameter for columnar ice | Q | $[kJ \cdot mol^{-1}]$ | 65 |
| Effective elastic modulus of ice | $E'$ | [Gpa] | 1–10 |
| Grid spacing | dz | [m] | $5 \cdot 10^{-2}$ |
| Time step | dt | [s] | 600 |
| Volume ratio between granular and columnar ice | μ | [n/d] | 0.44 |

Comparison between simulated ice thermodynamics and observations available demonstrated good agreement between them. Values for the simulated incoming short wave radiation and that observed during the ZIP-97 experiment (ZIP-97 Data report) correspond well (Fig. 4.1). The measured ice temperature at the surface and that in the interior are close to the simulated one. Figure 4.2 portrays the variations of the ice temperature in the interior as calculated in the model. One can see strong diurnal variations in the ice

[illegible]

| | |
|---|---|
| [illegible] | [illegible] |

[illegible]

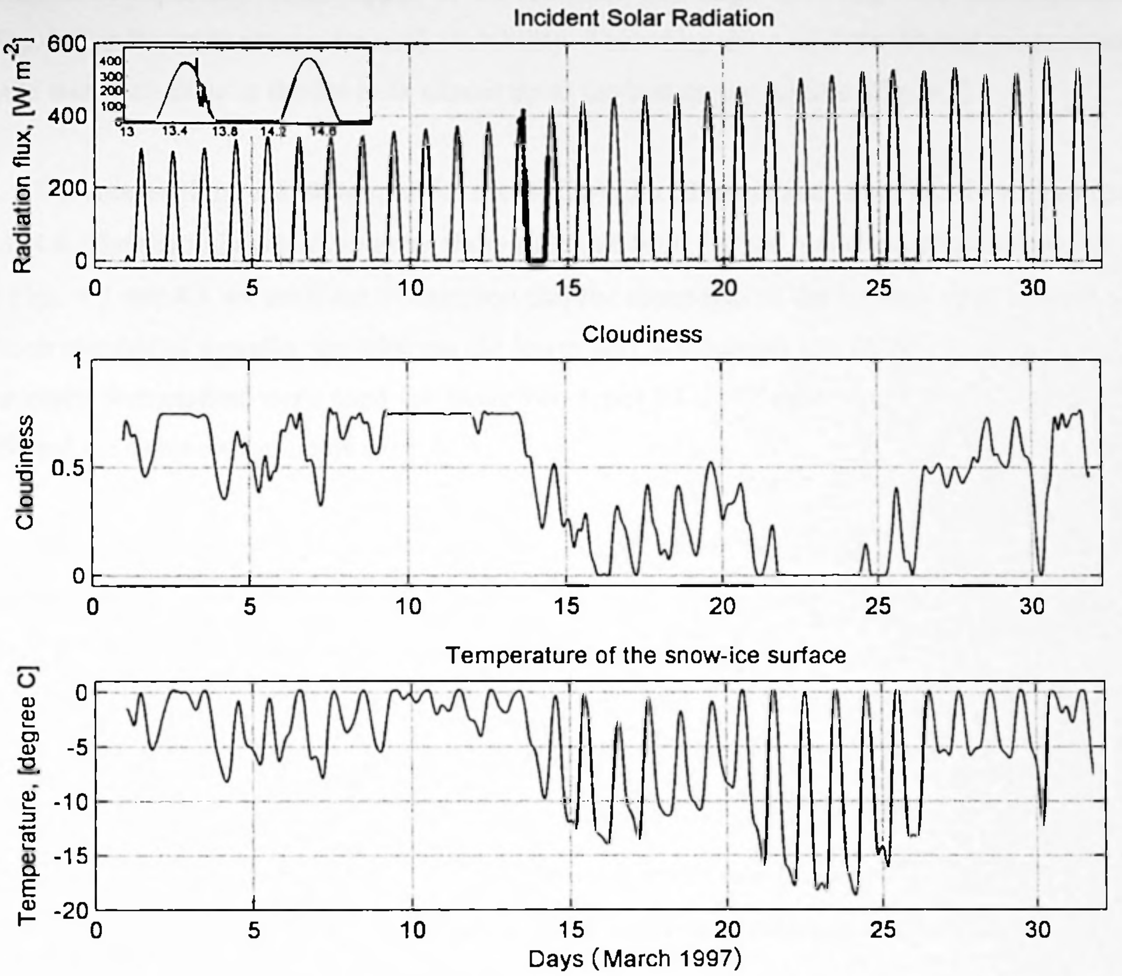


**Figure 4.1.** The results from the thermodynamic simulations: solar incident radiation; estimated cloudiness and temperature of snow-ice surface. For comparison the observed incoming short wave radiation is shown as black dots and also in the insert of the upper picture. March 1997, Bay of Bothnia, near Hailuoto Island.

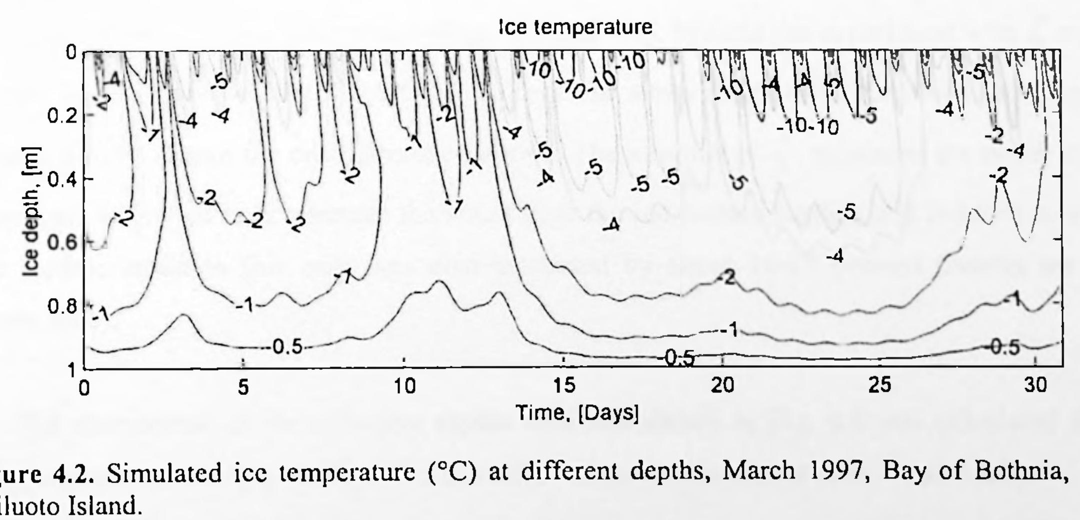


**Figure 4.2.** Simulated ice temperature (°C) at different depths, March 1997, Bay of Bothnia, near Hailuoto Island.

temperature especially in the upper of the ice bulk. The large incoming solar radiation flux (Fig. 4.1) is the main reason for such variability. According the model the diurnal temperature cycle was noticeable in the ice bulk almost up to the bottom ice surface (Fig. 4.2).

The results of the simulation of the thermally-induced stress and strain are shown in Figs. 4.3–4.9. The diurnal cycle dominates these fields as well. For the model experiments depicted in Figs. 4.3 and 4.4 we used the assumption that the upper part of the ice bulk up to a depth of 40 cm consists of granular ice whereas the lower part is columnar ice. Different parameters in the creep formulation were used for these two types of ice (Sanderson, 1988) and this fact affected the deformation fields (Fig. 4.3).

The extreme variability of the ice deformation occurs in the top 20 cm of the ice bulk as one can see from the figures. However the deformation was able to penetrate into the ice depth almost reaching its lower surface. The model experiments demonstrated that amplitude of the stress variation could reach 1 MPa at the surface with a variation of strain of about 200 microstrain (Figs. 4.3 and 4.6). The thermally-induced strain rate and the creep rate have approximately the same order of magnitude (Figs. 4.8 and 4.9). The term $\dot{\zeta}$ is an order of magnitude smaller (of about $10^{-8}$ [$s^{-1}$]) and the total strain rate is about $3 \cdot 10^{-8}$ [$s^{-1}$] (Figs. 4.3 and 4.7). Therefore the viscous deformation of ice has a large effect in reducing the strain rate that otherwise would have been very large.

The fact that the floe resists the bending leads to the redistribution of the lateral stress in the vertical: the stress in the upper ice part is reduced whereas the stress in the lower one is enhanced and has the opposite phase (Figs. 4.3 and 4.4). We ran the experiment with $\dot{\zeta}$ equal to zero, which corresponds to free floe bending. The stress distribution for such model layout is quite different from the case discussed above. The absence of $\dot{\zeta}$ enhanced the stress in the upper part of the ice bulk whereas the stress near the ice bottom surface was reduced to zero. The surface strain in this case was also increased by about 10-15 percent (results are not shown here).

The distribution of the effective elastic modulus shown in Fig. 4.4 was calculated from Cox parameterisation (eq. 4.10a). The modulus varies somewhat between 4 and 6 GPa

[illegible]

[illegible]

[illegible]

[illegible]

[illegible]

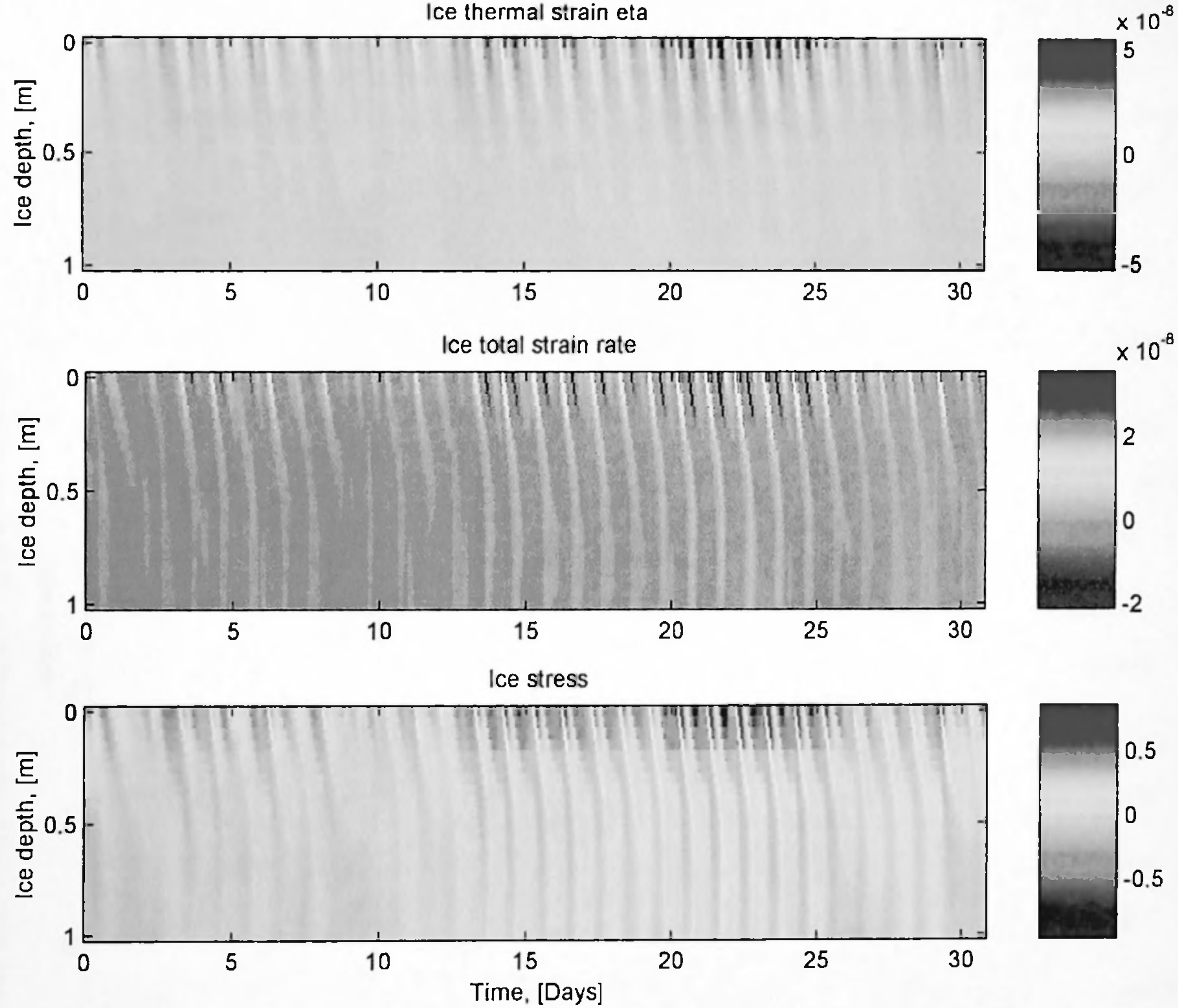


**Figure 4.3.** Simulated evolution of the ice internal stresses (MPa), strain and strain rate ($s^{-1}$) at different depths, March 1997, Bay of Bothnia.

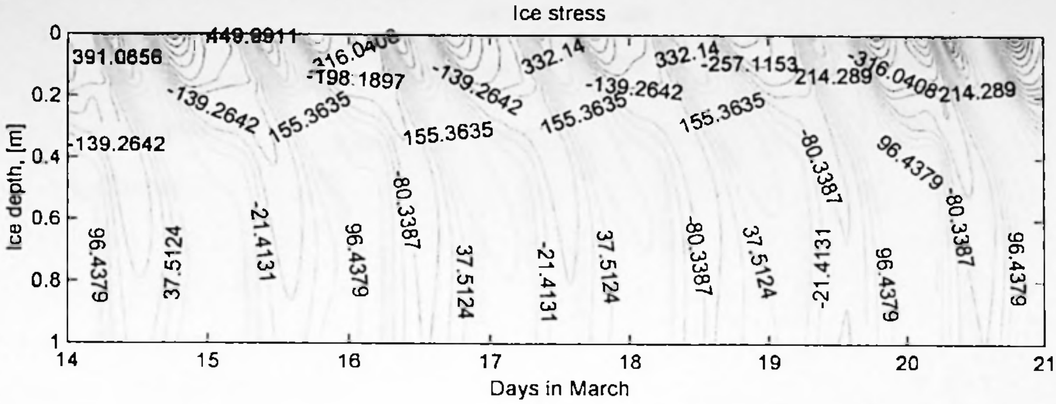


**Figure 4.4.** Simulated evolution of internal ice stresses (kPa) at different depths, March 1997, Bay of Bothnia, near Hailuoto Island.

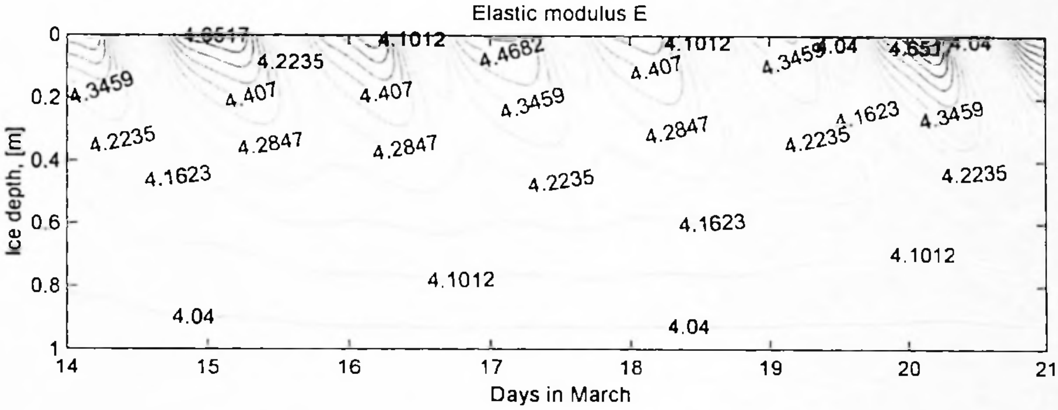


**Figure 4.5.** Simulated evolution of effective elastic ice modulus (GPa) at different depths, March 1997, Bay of Bothnia, near Hailuoto Island.

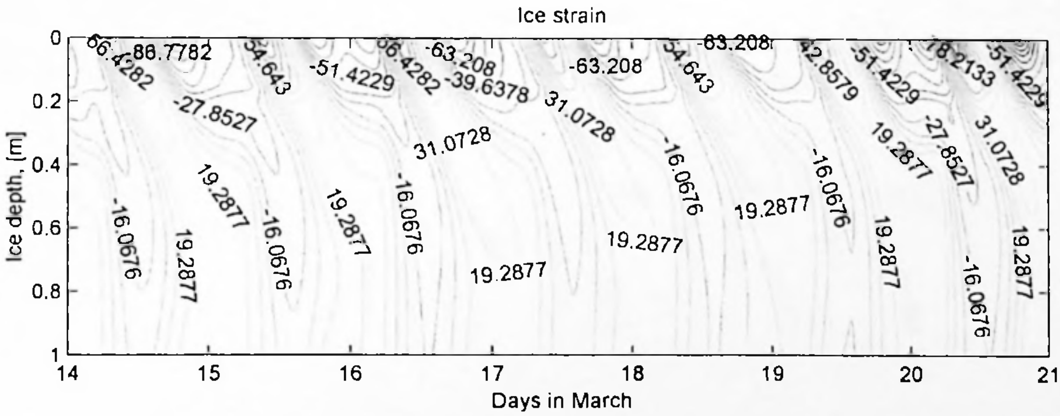


**Figure 4.6.** Simulated evolution of ice strain ($10^{-6}$) at different depths, March 1997, Bay of Bothnia, near Hailuoto Island.

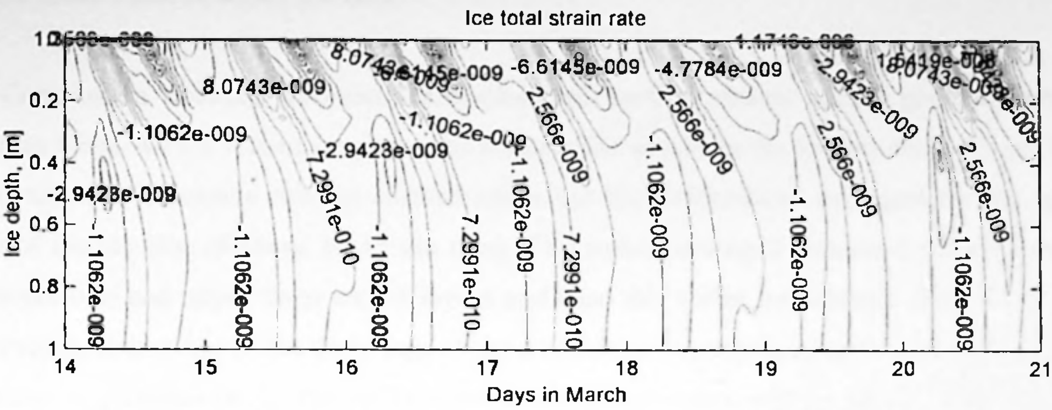


**Figure 4.7.** Simulated evolution of total ice strain rate ($s^{-1}$) at different depths, March 1997, Bay of Bothnia, near Hailuoto Island.

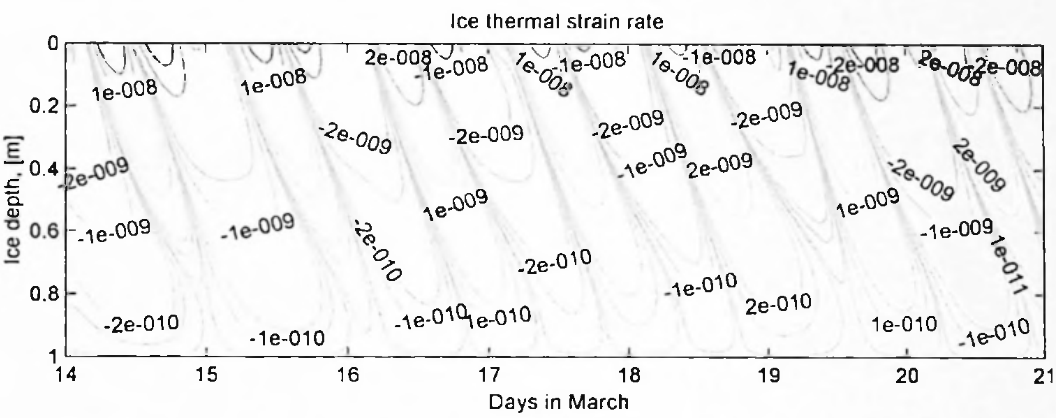


**Figure 4.8.** Simulated evolution of thermally induced ice strain rate ($s^{-1}$) at different depths, March 1997, Bay of Bothnia, near Hailuoto Island.

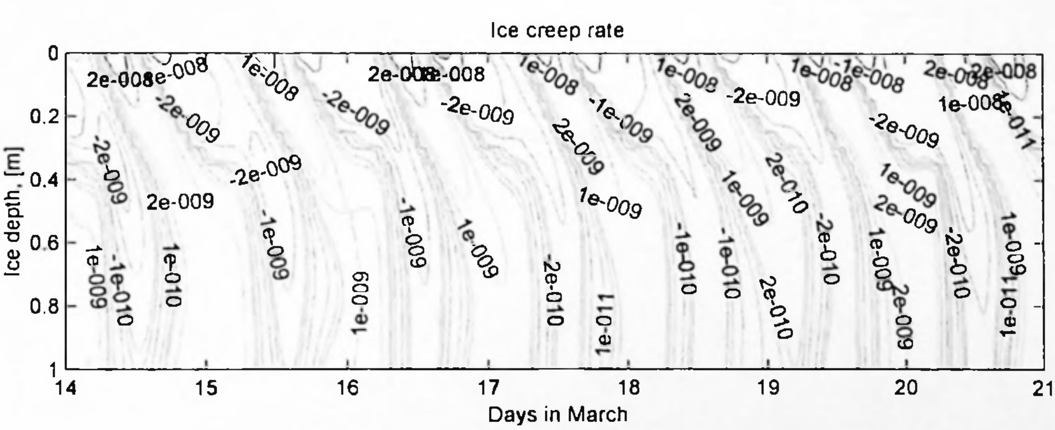


**Figure 4.9.** Simulate evolution of creep rate ($s^{-1}$) at different depths, March 1997, Bay of Bothnia, near Hailuoto Island.

with a mean value of about 4.4 GPa.

Comparison between simulated and observed surface strains shows good agreement between them. As ice screws employed to connect the sensor to the ice are about 15 cm long the strainmeter measures not the surface strain but the deformation averaged for the upper layer of the ice floe of about 10-15 cm deep. The author averaged simulated deformation of the upper two and upper three model layers and used this series for analysis (Fig. 4.10). The observed deformations of the three legs of the strainmeter were processed in order to calculate the isotropic component of the strain tensor; this component is shown in Fig. 4.10. Despite having gaps in the record the deformation observed with the help of strainmeters demonstrated the ability to capture the thermal deformation signal quite well. Deformation events occurring on 15$^{th}$ March and between 18$^{th}$ and 20$^{th}$ March had larger amplitudes compared to thermally-induced strain, so the signal can be reasonably easy split into thermo-mechanical deformation and just dynamically-induced events.

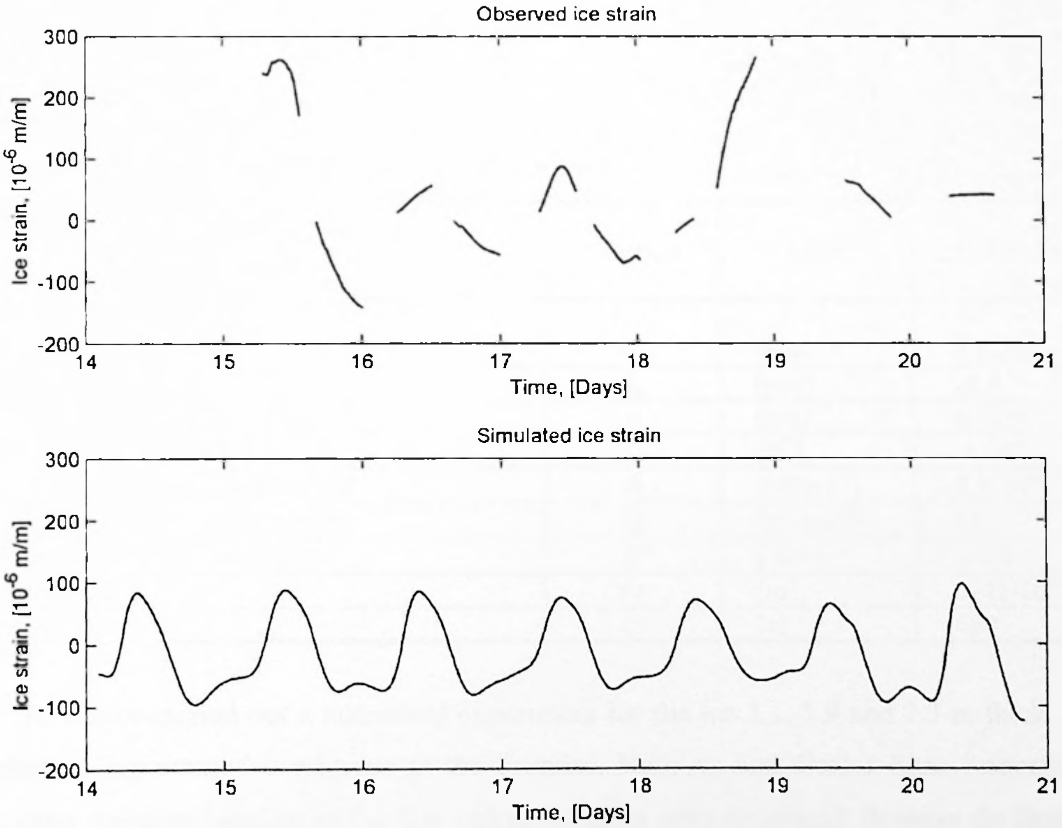


**Figure 4.10.** Observed isotropic part of local strain (top) along with simulated thermal strain (bottom) at the surface, March 1997, Bay of Bothnia, near Hailuoto Island. Simulated strain was averaged for three top model layers.

### 4.1.3 Case study II: Sea Ice Mechanics Initiative experiment

To investigate thermal deformation and stresses of the ice floe measured during the SIMI experiment the thermo-mechanical model was applied. The formulation of the model was essentially the same and the main difference between this version of the model and the version described earlier concerned parameterisation of the ice creep. In present simulations the creep law for the saline ice suggested by Sanderson (1988) was used (eq. 4.11). This parameterisation uses brine volume to introduce the effect of the ice salinity (eq. 4.11b).

$$\gamma(\sigma,T,\Xi)=A(T,\Xi)\cdot exp\left(-\frac{Q(T,\Xi)}{R\cdot T}\right)\cdot\sigma^{3}(z,t)\cdot\left(1-\sqrt{v_b/v_0}\right)^{-3} \quad (4.11a)$$

$$v_b=S\cdot 10^{-3}\cdot(0.53-49.2/T) \quad (4.11b)$$

where, $v_b$ and $v_0$ – are the brine volume for the saline and normalised constant, $v_0$ = 0.16 (Sanderson, 1988); A and Q – are the creep parameter and the activation energy. For the columnar saline ice A = $3.5\cdot 10^{6}$ [$MPa\cdot s^{-1}$] and Q = 65 [$kJ\cdot mol^{-1}$] (Sanderson, 1988); other notations are given earlier.

**Table 4.2.** Parameters used in the simulations for Case II.

| Parameter | Notation | Units | Value |
|---|---|---|---|
| Ice salinity | $S_i$ | [psu] | 0.1–6.0 |
| Water salinity | $S_w$ | [psu] | 28.4 |
| Ice porosity | $p$ | [n/d] | 0.1258 |
| Freezing point temperature | $T_{fr}$ | [°C] | -1.547 |
| Creep parameter for columnar ice | A | [$MPa\cdot s^{-1}$] | $3.5\cdot 10^{6}$ |
| Creep parameter for columnar ice | Q | [$kJ\cdot mol^{-1}$] | 65 |
| Effective elastic modulus of ice | $E'$ | [Gpa] | 1–10 |
| Grid spacing | dz | [m] | $5–11\cdot 10^{-2}$ |
| Time step | dt | [s] | 600 |

The author carried out a numerical experiment for the ice 1.1, 1.9 and 2.3 m thick. This simulations represented conditions at the Frontier, Harbour and Center Sites respectively. Two cases involved bending of the floe and no-bending were simulated. Because the floe was rather thick the no-bending case was under analysis. Parameters used for the simulation are listed in Table 4.2. The value for the upper surface seawater salinity was taken from CTD measurements carried out from the SIMI floe. The freezing temperature was calculated from

the formula suggested by Millero (1978) and checked against the CTD observations as well. The average porosity of the ice was taken $p$ equal to 0.1258 (Lewis and Richter-Menge, 1998).

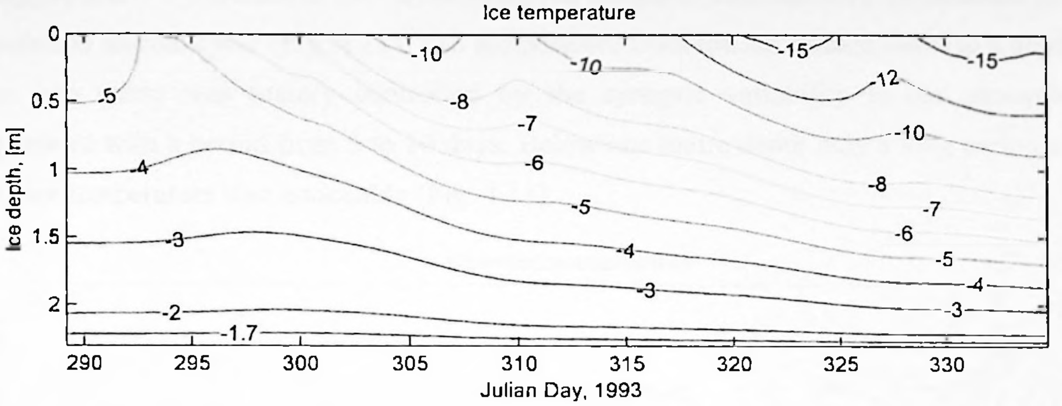


**Figure 4.11.** Simulated ice temperature (°C) at different depths for the Center Site, October–November 1993, Beaufort Sea, SIMI camp.

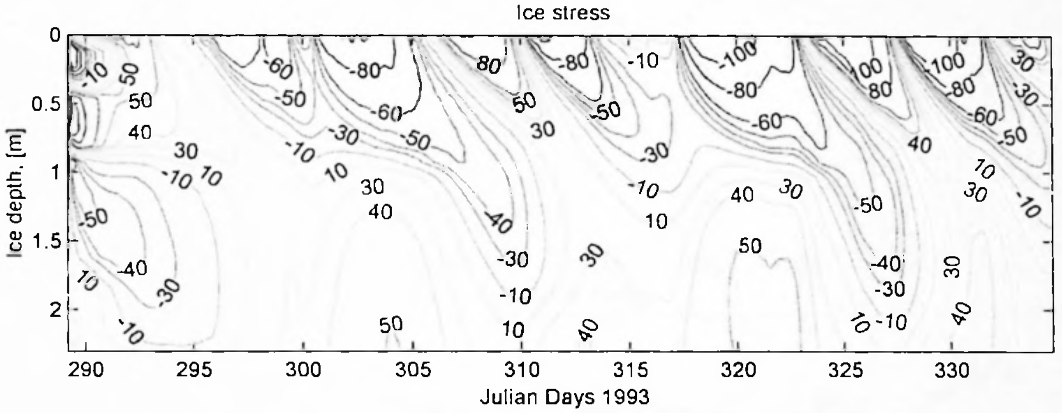


**Figure 4.12.** Simulate evolution of ice internal ice stresses (kPa) at different depths for the Center Site, October–November 1993, Beaufort Sea, SIMI camp.

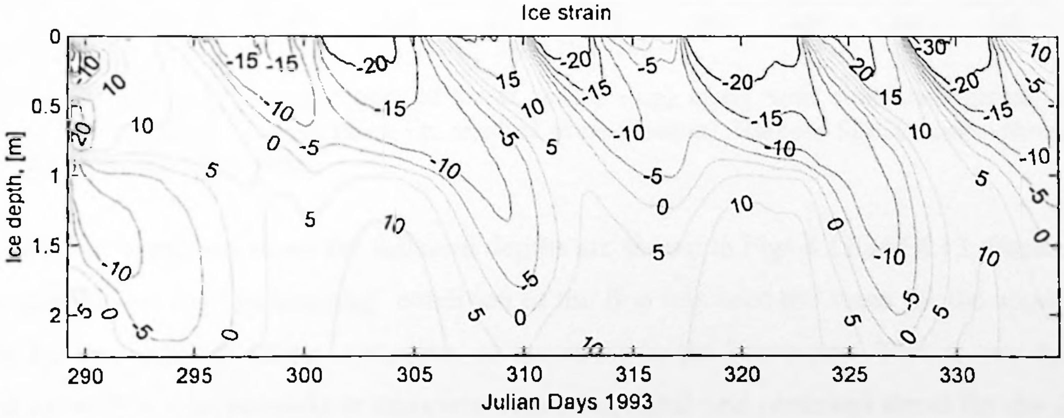


**Figure 4.13.** Simulated evolution of total ice strain ($10^{-6}$) at different depths for the Center Site, October–November 1993, Beaufort Sea, SIMI camp.

Simulated ice temperature was compared against observations made at different ice depths at the sites of stress sensors (Richter-Menge and Elder, 1998) and the author found that they were in satisfactory agreement. A comparison between temperature variations observed during the ZIP-97 experiment and those observed on SIMI demonstrated the absence of the pronounced diurnal cycle (Fig. 4.11). The temperature from the ice surface down to a depth of about one metre was mainly controlled by the synoptic variability in the atmospheric temperature with a period from 5 to 10 days. Below one metre depth only a long period trend in the ice temperature was noticeable (Fig. 4.11).

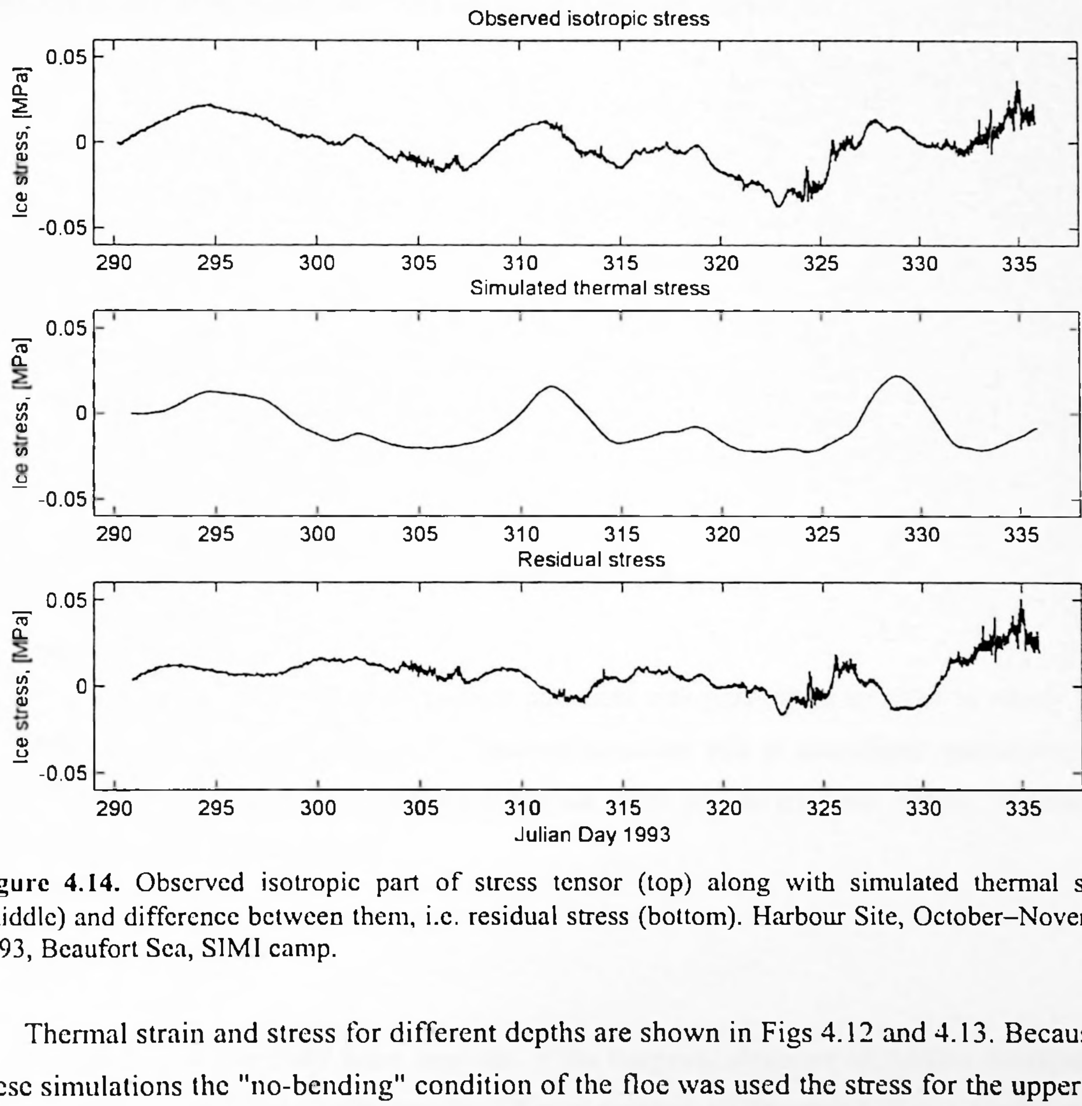


**Figure 4.14.** Observed isotropic part of stress tensor (top) along with simulated thermal stress (middle) and difference between them, i.e. residual stress (bottom). Harbour Site, October–November 1993, Beaufort Sea, SIMI camp.

Thermal strain and stress for different depths are shown in Figs 4.12 and 4.13. Because in these simulations the "no-bending" condition of the floe was used the stress for the upper part of an ice floe exhibits mirror symmetry to the stress in the lower part. This is true for the strain as well. It was possible to compare simulated stress and observed stress for the SIMI experiment. For all observational sites simulated thermal stress agreed reasonably with the

[illegible]

[illegible]



[illegible]

[illegible]

observed isotropic component of the stress tensor (eq. 4.12, next section). However, there is a certain difference between them (Fig. 4.14). One can see that thermal stress follows the isotropic stress quite closely until the magnitude of the former becomes excessively high (days 310-311, 327-328, Fig. 4.14). Then the magnitude of the isotropic stress drops sharply; sometimes it can be followed by stress oscillations. The author attributes this behaviour to the formation of thermal cracks in the upper part of the ice bulk. The residual stress varied between -10 and 10 kPa except for the period when some strong deformation events took place on days 332-336 (Fig. 4.14). The same analysis was applied to the deformation and stress measured at the Center Site and the results obtained support the above argument.

In conclusion it may be said that more complex models, for example with lateral variations of the ice thickness and snow depth, or with the explicit simulation of ice cracking, can be applied to get a more accurate result. Nevertheless even on the basis of the performed simulations we can state that the magnitude of the thermal deformations is about 5-10 times smaller ( $\sim 1\text{-}4 \cdot 10^{-4}$ strain) than the dynamically induced ones ( $\sim 1.5\text{-}3.5 \cdot 10^{-3}$ strain). These figures can be used for the estimation of the up-scaling effect. To analyse the variability of the laterally non-uniform stresses and deformation fields the three-dimensional model should be applied. One of the possible ways is to use a finite element model (FEM).

## 4.2 Heuristic analysis of the local stresses and strains

The analysis of SIMI ice deformation data sets was performed in order to obtain more information about ice deformation, its spectral structure and to investigate spatial/temporal variability of deformations and stresses in the ice cover caused by wind. Firstly, we consider the local ice stress observations.

### 4.2.1 Local ice stresses

The author performed the basic analysis of the temporal structure of stresses described by Richter-Menge and Elder (1998) but for different sections of the record. It was found that the major and minor principal stress components are characteristic of two types of variability: low frequency (order of days) and high frequency (order of hours) (Fig. 4.15).

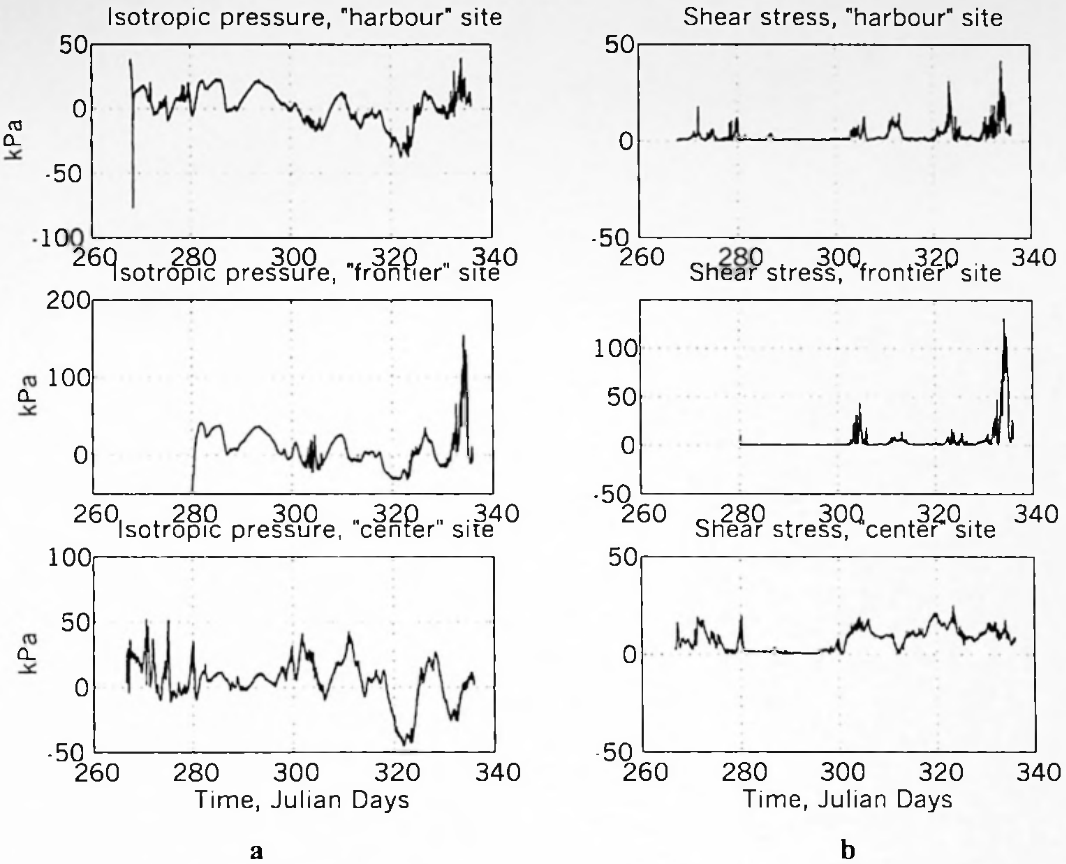


**Figure 4.15.** Isotropic pressure (a) and shear stresses (b) for the Harbour, Center and Frontier Sites, SIMI, West Camp, September-December 1993.

The major and minor components of the stress tensor as well as the pure compression $\Pi$ and the shear stresses $\Gamma$ were derived from the Mohr's Circle rule (eq. 4.12). We obtained the cross correlation matrixes for all stress tensor components for all observational sites. The calculations show that pure isotropic pressure at all sites has a lower correlation (correlation coefficient 0.79) than minor principal stress (correlation coefficient 0.93). The shear stresses at the different sites are correlated more strongly than major principal stress (Tables 4.3 and 4.4). The lowest correlation coefficient (0.10) was representative of the major stresses at the Frontier and Center Sites (Table 4.3). As a first approximation, the major stress component can be presented as the sum of the motion-induced and thermal deformation of an ice cover. Therefore, the motion-induced stress is equal to the shear stress derived from equation. The isotropic pressure contains both dynamic and thermal components.

$$\sigma_1 = -\tfrac{1}{3}[\varsigma_a + \varsigma_b + \varsigma_c] - \tfrac{2}{3}\sqrt{\varsigma_a^{\,2} + \varsigma_b^{\,2} + \varsigma_c^{\,2} - \varsigma_a \cdot \varsigma_b + \varsigma_a \cdot \varsigma_c - \varsigma_b \cdot \varsigma_c}$$

$$\sigma_2 = -\tfrac{1}{3}[\varsigma_a + \varsigma_b + \varsigma_c] + \tfrac{2}{3}\sqrt{\varsigma_a^{\,2} + \varsigma_b^{\,2} + \varsigma_c^{\,2} - \varsigma_a \cdot \varsigma_b + \varsigma_a \cdot \varsigma_c - \varsigma_b \cdot \varsigma_c}$$

$$\varphi = \tfrac{1}{2} arctg(\frac{\sqrt{3}}{2\varsigma_a - \varsigma_b - \varsigma_c}(\varsigma_c - \varsigma_b)) \qquad (4.12)$$

$$\Pi = \frac{\sigma_1 + \sigma_2}{2}$$

$$\Gamma = \frac{\sigma_1 - \sigma_2}{2}$$

where $\varsigma_a, \varsigma_b, \varsigma_c$ - given stresses on stress gauge arms, $\sigma_1$, $\sigma_2$ - major and minor principal stresses, $\varphi$ - direction of major stress, $\Pi$, $\Gamma$ - pressure and shear stress. The positive stress corresponds to the compression and clockwise shear.

The major stress varies significantly from the centre of the floe towards the edges. The minor stress is isotropic within an ice floe, correlating well with changes in the ice temperature (coefficient 0.8-0.9) and typical of a weak spatial variability. Stresses precede ice temperature variations by approximately 0.6 days, the same result was obtained by Richter-Menge and Elder (1998).

The correlation function calculated for stress components for pairs of sites revealed the existence of a time shift in the variations of minor stresses for all the sites (Fig. 4.16). The major stress component at the edges of the floe varies simultaneously. The shear stresses also change synchronously at edge sites as the isotropic pressure is delayed for about two hours at the Harbour Site with respect to the Frontier Site (Table 4.4). A comparison of time delay in isotropic pressure variations and thickness at the sites shows good agreement and it can be approximated by:

$$y = -0.193 \cdot \exp(h \cdot 1.34) + 3.34 \qquad (4.13)$$

where $h$ - mean ice thickness (m) at an observational site, $y$ - time delay (hours).

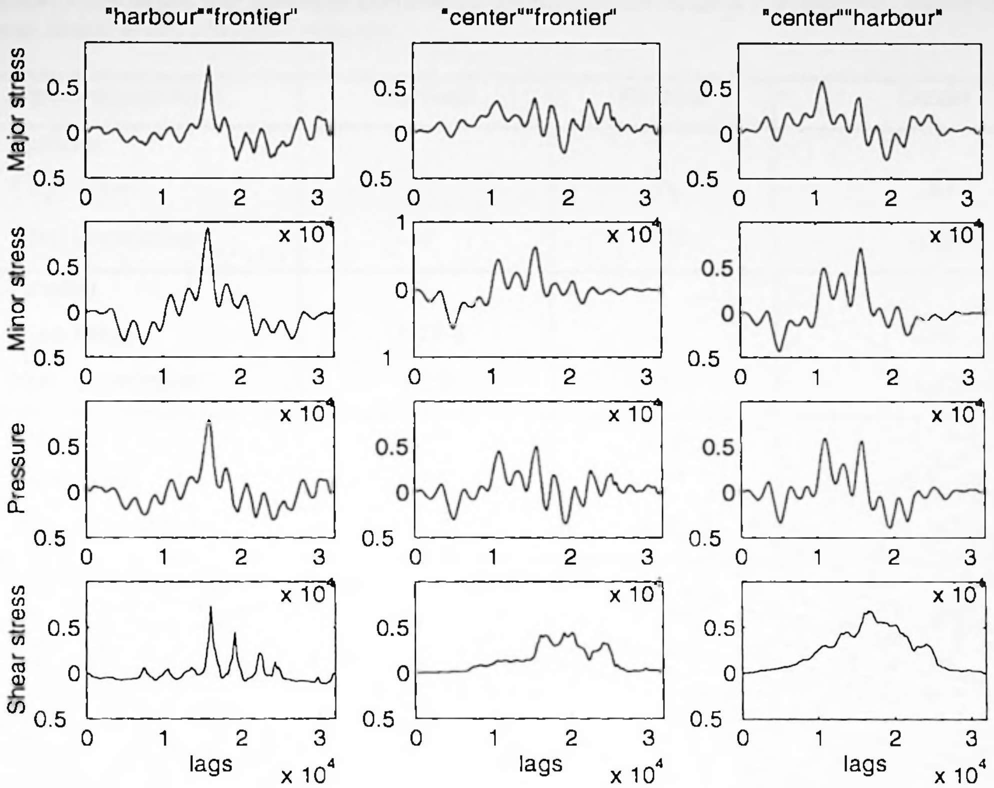


**Figure 4.16.** Cross correlation functions for stress tensor components for the Harbour, Center and Frontier Sites, SIMI, West Camp, September-December 1993.

**Table 4.3.** Time delay and maximal correlation coefficient for stresses components. Upper triangle is the minor stress, lower triangle - major stress.

| Observational sites | Harbour | Frontier | Center |
|---|---|---|---|
| Harbour | | | |
| Time delay | – | -2.75 h | -1.37 h |
| Max. correlation. | 1 | 0.93 | 0.71 |
| Frontier | | | |
| Time delay | 0 h | – | -5.5 h |
| Max. correlation | 0.74 | 1 | 0.70* |
| Center | | | |
| Time delay | –** | –** | – |
| Max. correlation | 0.28 | 0.10 | 1 |

* - The correlation function has several peaks; extreme coefficient 0.58 with delay 58 hrs.

** - time delay was not calculated because of low correlation.

**Table 4.4.** Time delay and maximal correlation coefficient for stresses components. Upper triangle is the shear stress, lower triangle - pressure.

| Observational sites | Harbour | Frontier | Center |
|---|---|---|---|
| Harbour | | | |
| Time delay | – | 0 h | _** |
| Max. correlation | 1 | 0.73 | 0.40 |
| Frontier | | | |
| Time delay | -2.23 h | – | _** |
| Max. correlation | 0.79 | 1 | 0.22 |
| Center | | | |
| Time delay | _** | _** | – |
| Max. correlation | 0.52 | 0.23 | 1 |

** - time delay was not calculated because of low correlation.

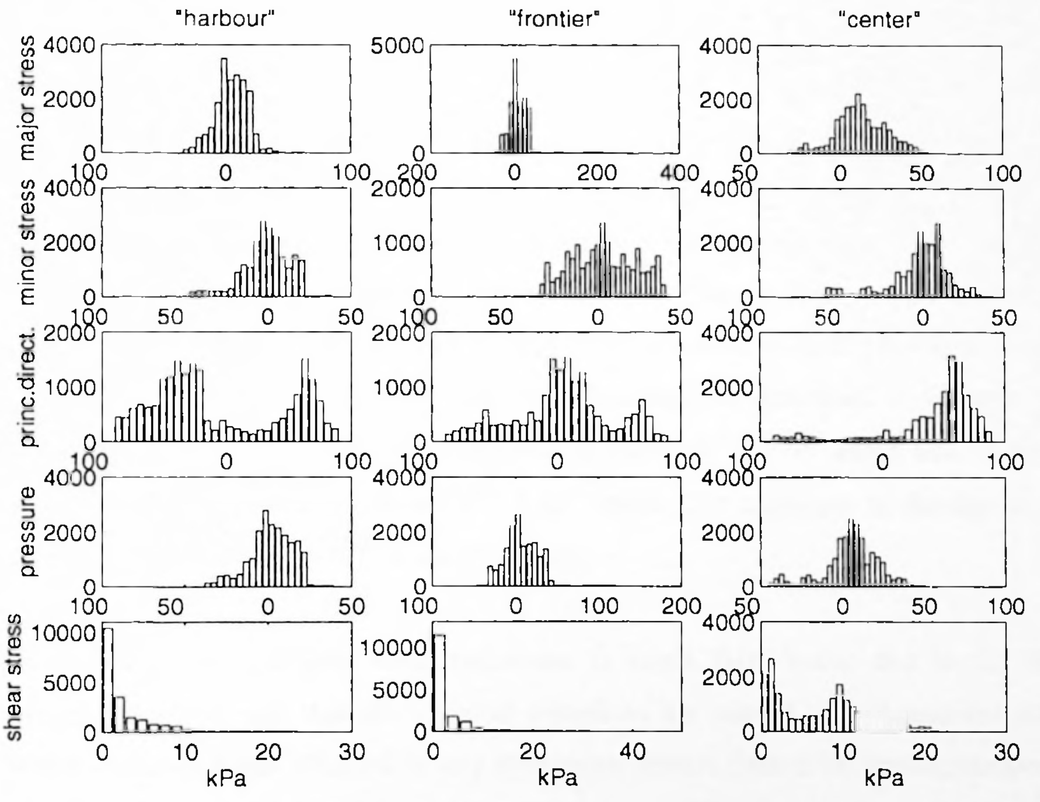


**Figure 4.17.** Histograms for stress tensor components for the Harbour, Center and Frontier Sites, SIMI, West Camp, September-December 1993.

Therefore, the dynamically-induced stresses occur synchronously at different points on the floe and thermal deformation is developed with time delays according to the following

[illegible]

[illegible]

[illegible]

[illegible]

rule: the thicker the ice, the sooner the thermal stress appears. In spite of the high correlation of stresses between the sites the correlation function shows the non-linear character of stress components relations.

The distribution functions of stress components differ significantly. For the shear stresses, the functions are exponential, and they appear Gaussian for the other components (Fig. 4.17). The distribution of principal direction is bimodal at edge sites and unimodal in the centre. The distribution function of the shear component at the edge of the floe preserves the exponential shape on time scales from thousands to hundreds of hours and can be approximated as:

$$log10[f(\sigma)]=a\cdot\sigma+b \qquad (4.14)$$

where, $f(\sigma)$ - shear stress distribution function, $a$ - slope of exponent, $b$ - intersection.

### 4.2.2 Local ice strain

To measure local ice deformation BP-strainmeters were employed at all five observational sites on the multi year floe (Chapter 3, Part II). Similar to the stress series the temporal variability of both principal strain exhibits the presence of long and short term components, roughly order of days and order of hours correspondingly. The variability of the shorter period order of seconds is also well pronounced, related to the presence of different waves in the area and deformation due to ice breaking and ridge building, as described in Chapter 5. The magnitude of the strains for long term variations is about $10^{-5}$ - $5\cdot10^{-4}$ strain and for the short period components it is smaller, about $10^{-6}$ - $5\cdot10^{-5}$ strain. The amplitude of the shorter period deformation is of about $10^{-7}$ - $10^{-6}$ strain (Fig. 4.18).

It is believed that the long term variations in strain field occur due to ice thermal expansion/contraction, and that short period variations are related with dynamical loads on ice. When ice cover is not affected by any dynamical impact (like drift, waves, compression) the spectrum has an exponential shape which presumably reflects thermal deformation. Dynamical deformation caused by flexural waves or ridge building process adds energy in the high frequency band from $10^{-2}$ - $10^{1}$ Hz (Fig. 5.2, Chapter 5).

[illegible]

[illegible]

[illegible]

[illegible]

[illegible]

[illegible]

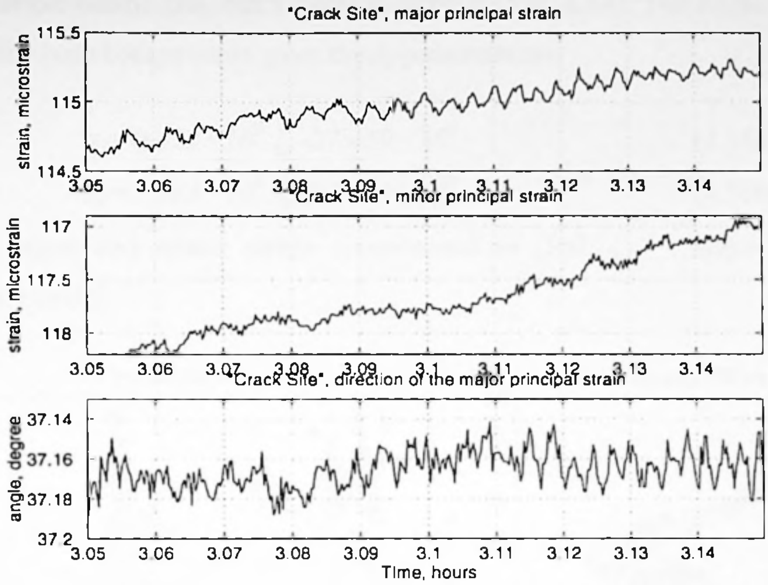


**Figure 4.18.** Short term variations in ice strain related to the ocean swell, eastern strainmeter, Crack Site, ZIP-97, March 1997.

Further analysis involved calculation of the principal strains as well as pure compressive and shear strains from the Mohr's circle:

$$e_1 = \tfrac{1}{3}[\varepsilon_a + \varepsilon_b + \varepsilon_c] + \tfrac{2}{3}\sqrt{\varepsilon_a^2 + \varepsilon_b^2 + \varepsilon_c^2 - \varepsilon_a \cdot \varepsilon_b + \varepsilon_a \cdot \varepsilon_c - \varepsilon_b \cdot \varepsilon_c}$$

$$e_2 = \tfrac{1}{3}[\varepsilon_a + \varepsilon_b + \varepsilon_c] - \tfrac{2}{3}\sqrt{\varepsilon_a^2 + \varepsilon_b^2 + \varepsilon_c^2 - \varepsilon_a \cdot \varepsilon_b + \varepsilon_a \cdot \varepsilon_c - \varepsilon_b \cdot \varepsilon_c}$$

$$\gamma = \tfrac{1}{2} arctg(\frac{\sqrt{3}}{2\varepsilon_a - \varepsilon_b - \varepsilon_c}(\varepsilon_c - \varepsilon_b)) \qquad (4.15)$$

$$P = \frac{e_1 + e_2}{2}$$

$$Sh = \frac{e_1 - e_2}{2}$$

where $\varepsilon_a, \varepsilon_b, \varepsilon_c$ - given strains on strainmeter arms, $e_1$, $e_2$ - major and minor principal strains, $\gamma$ - direction of major strain, $P$, $Sh$ - pure compressive and shear strains.

### 4.2.3 Strain-Stress relationship

The stresses observed at the Center Site and strain measured at Site C2 were used for this analysis. Examination of stress and strain records together shows that they are correlated with coefficients 0.78 and 0.89 for the major and minor components respectively and there is no time delay between them. However, for the major principal components the relationship does

[illegible]

[illegible]

[illegible]

[illegible]

[illegible]

[illegible]

[illegible]

[illegible]

[illegible]

not follow a simple elastic law, but exhibit hysteresis (Fig. 4.19). The linear least mean square fit calculated for both components gave the approximation:

$$\sigma_1 = 0.622 \cdot 10^9\, \zeta_1 - 27.459 \cdot 10^3 \qquad (4.16a)$$

$$\sigma_2 = 3.383 \cdot 10^9\, \zeta_2 - 53.854 \cdot 10^3 \qquad (4.16b)$$

where $\sigma_{1,2}$ - major and minor stress components in [Pa], $\zeta_{1,2}$ - major and minor strain components in [strain].

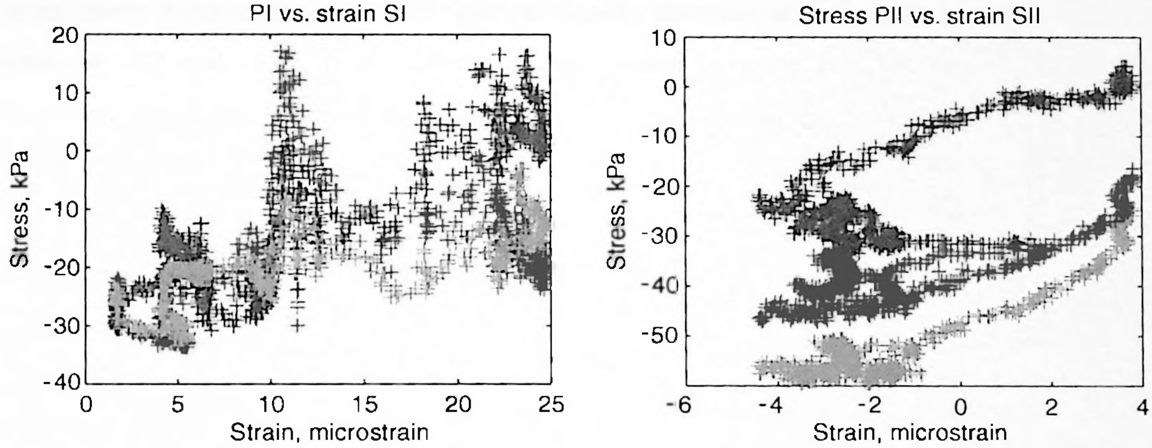


a b

**Figure 4.19.** Major principal stress – strain (a) and minor principal stress – strain (b) relations. Stresses were observed at the Center Site; strains – at Site C2 (green crosses). The relationships between strains observed at Site C2 and stresses at the Harbour (red) and Frontier (blue) Sites. SIMI, West Camp, September-December 1993.

Minor principal stresses and strains exhibit strong correlation possibly related to thermally-induced deformation of ice floes. The elastic modulus derived from equation (4.16b) is about 3.4 GPa which is close to the estimate obtained from equation (4.10). Major components have a positive correlation coefficient and the relations seem to be closer to the elastic type with effective Young's modulus of 0.6 GPa (Fig. 4.19). This figure is realistic even though it is close to the lower limit of modulus. The strain-stress curve for major components is continuous but have a significant non-linear shape probably related to the delayed response of stresses at the lower ice levels to the thermal deformation of upper ice levels. The relationships between strains observed at Site C2 and stresses at the Harbour (red) and Frontier (blue) Sites are shown for comparison. The hysteresis due to delayed response mentioned earlier is presented. Stresses and strain rates have significantly weaker correlation and no realistic linear approximation was obtained for their relation (not shown). It was not

[illegible]

[illegible]

[illegible]

possible to analyse the stress variations shorter than 10 minutes due to the low sampling rate, so we consider the stress and strain variability from several days to tens of minutes.

### 4.2.4 Spectra

The spectrum of ice deformations generated by non-uniform ice drift is of special interest. The slope of the spectrum characterises the ratio between stress fluctuations on different scales. There are no identifiable peaks in the local stress spectra, and all the tensor components demonstrate a smooth spectral density decrease with frequency (spectral slopes between -1.2 and -1.7). It is possible to distinguish between two spectral slopes with a transition frequency of about $2\times10^{-4}$ Hz for the shear component, $4\times10^{-4}$ Hz for the major principal component, and near $7\times10^{-4}$ Hz for the isotropic and minor principal components (Fig. 4.20). More detailed analysis shows that because the shear and major principal stress components, earlier attributed to motion-induced deformations, have higher dispersion for short periods, they are characteristic of a more gentle spectral slope than the thermally-induced minor principal stress and isotropic pressure (Table 4.5). Strain tensor components observed in the fast ice in the Bay of Bothnia showed much steeper spectra, with a slope of about -1.8 due to dominant thermally-induced deformations (Fig. 4.21).

**Table 4.5.** Approximation parameters for the spectrum of stress and strain tensor components. Approximation for the ice temperature spectrum is listed as well.

| Data | Slope | | | Intersect | | |
|---|---|---|---|---|---|---|
| | whole spectrum | long periods | short periods | whole spectrum | long periods | short periods |
| Shear | -1.159 | -1.666 | -0.849 | 4.695 | 0.047 | 6.878 |
| Isotropic component | -1.385 | -1.672 | -0.557 | 3.930 | 1.445 | 9.631 |
| Major principal stress component | -1.266 | -1.563 | -0.699 | 5.554 | 2.948 | 9.482 |
| Minor principal stress component | -1.535 | -1.760 | -0.559 | 2.427 | 0.489 | 9.149 |
| Major principal strain component | -1.793 | -1.927 | -0.825 | -3.451 | -3.833 | -2.421 |
| Minor principal strain component | -1.795 | -1.928 | -0.828 | -4.561 | -4.940 | -3.533 |
| Mesoscale deformation, dilatation | -1.519 | -1.903 | -0.389 | -16.571 | -20.799 | -6.020 |
| Ice temperature | -1.455 | -1.955 | -0.809 | -17.319 | -21.799 | -12.748 |

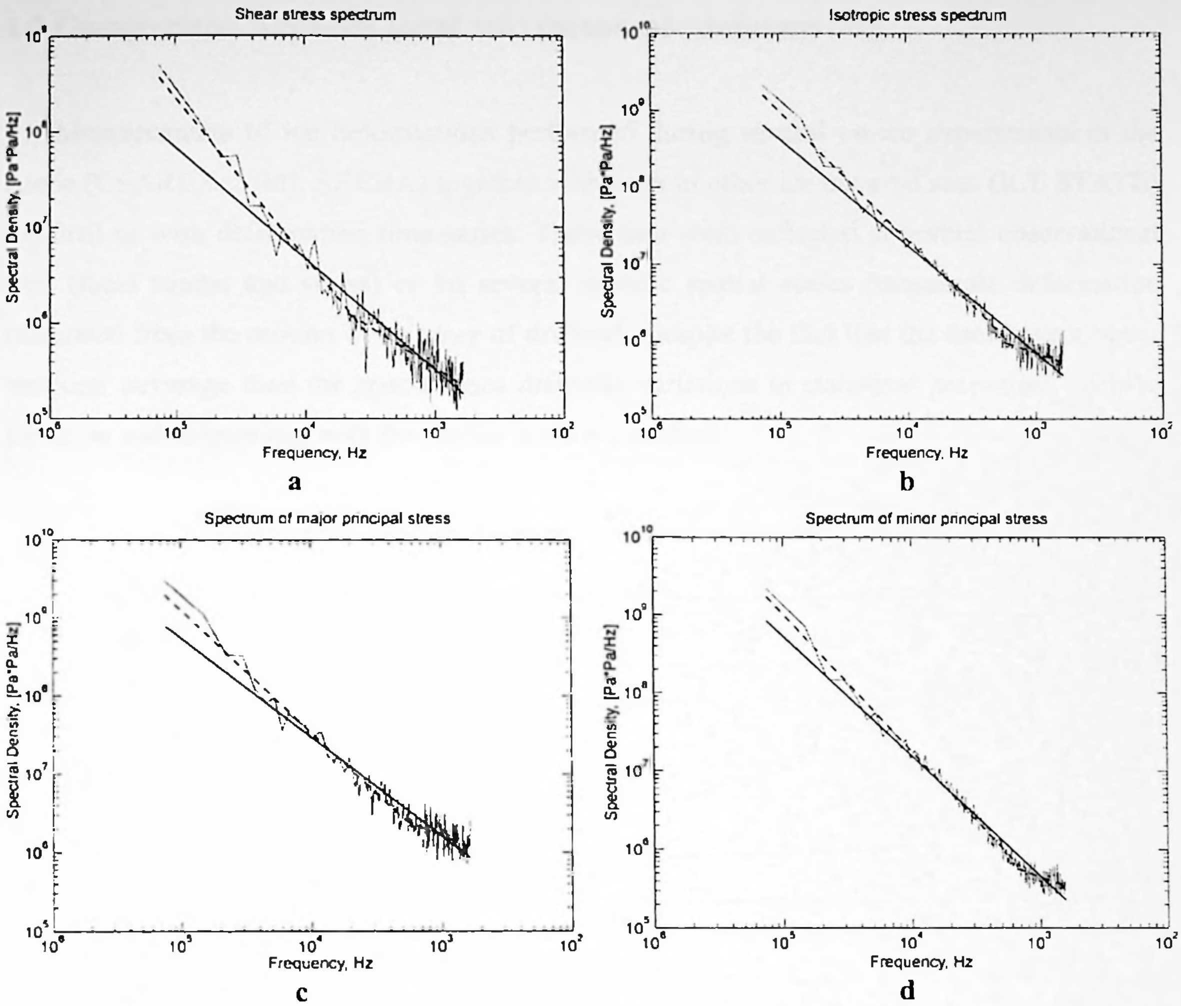


**Figure 4.20.** Spectrum of shear stress (a) and isotropic (b) component of stress tensor; and major (c) and minor (d) principal stresses. Best linear fits are shown. SIMI, West Camp, September-December 1993.

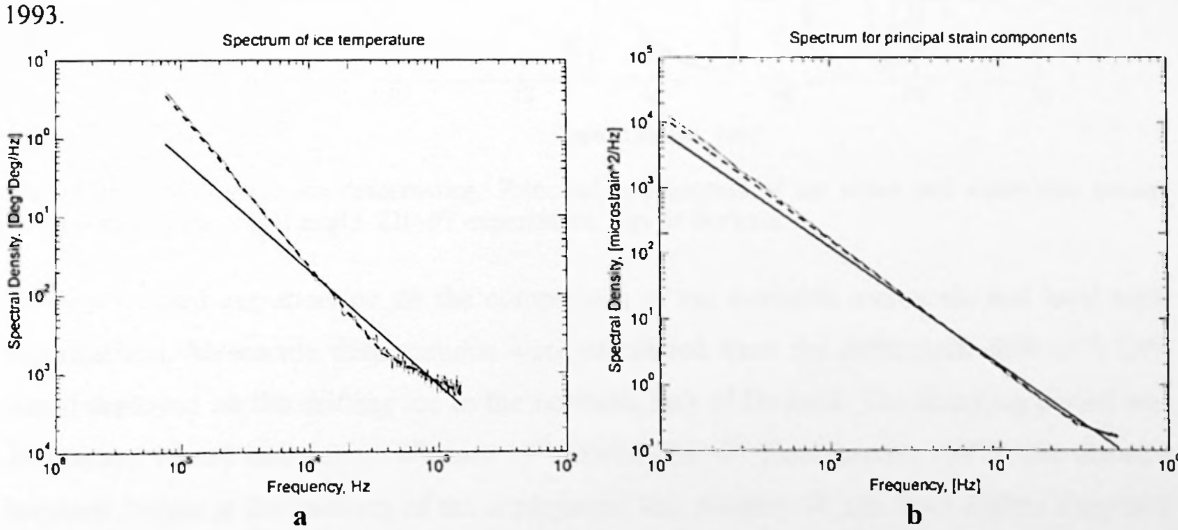


**Figure 4.21.** Spectrum of ice temperature (a) and major principal component of strain tensor (b). Best linear fits are shown. ZIP-97, Bay of Bothnia, March 1997.

## 4.3 Comparison between local and mesoscale deformation

Measurements of ice deformations performed during several on-ice experiments in the Arctic (CEAREX, SIMI, SHEBA) together with ones in other ice-covered seas (ICE STATE) supplied us with deformation time series. These data were collected at several observational sites (local strains and stress) or on several specific spatial scales (mesoscale deformation calculated from the motion of an array of drifters). Despite the fact that the data have a better temporal coverage than the spatial ones dramatic variations in statistical properties, such as the mean and dispersion, with the spatial scale are evident.

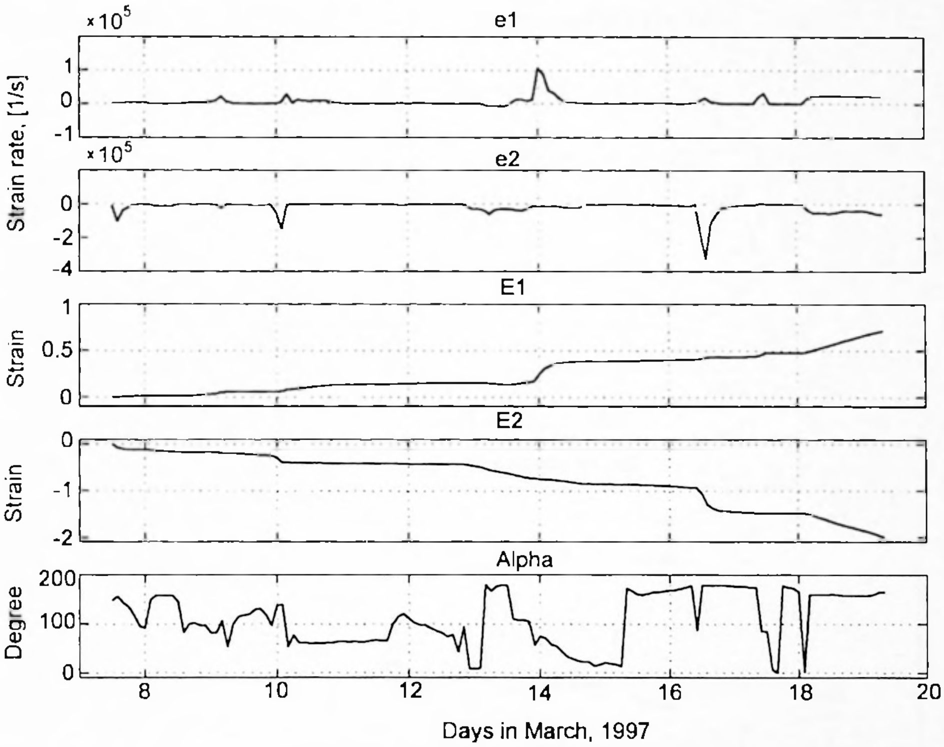


**Figure 4.22.** Mesoscale ice deformation. Principal components of the strain and strain rate tensors along with their principal angle. ZIP-97 experiment, Bay of Bothnia.

We focused our attention on the comparison of the available mesoscale and local scale deformations. Mesoscale deformations were calculated from the differential drift of 5 GPS buoys deployed on the drifting ice in the northern Bay of Bothnia. The sampling period was 10 min and record lasted from 8$^{th}$ until 19$^{th}$ March (ZIP-97 Data Report, 1997). The distance between drifters at the moment of the deployment was roughly 50 km. Two drifters happened to be in the zone of slow motion near the fast ice edge, while the rest was driven along the shore by a strong ice drift with velocities up to 50 cm/s. A slip line appeared about 10 km

westward from the fast ice edge and went right through the array. The deformation tensor components calculated from the relative displacement of buoy are presented in Fig. 4.22.

Both principal components of the mesoscale strain have similar variability: large periods with practically constant deformation are interrupted by rapid step-like changes. Such a character of the deformation is evidence of the plastic flow. The deformation series also resemble other series obtained in the Arctic (Overland et al., 1998). Following the analysis described in section 4.1 the thermal component was extracted from the strain record and the remaining motion-induced deformation was analysed. A comparison between mesoscale and local deformations measured simultaneously by *BP-Δ* gauges shows that in general they follow the same tendency. However there are two important features.

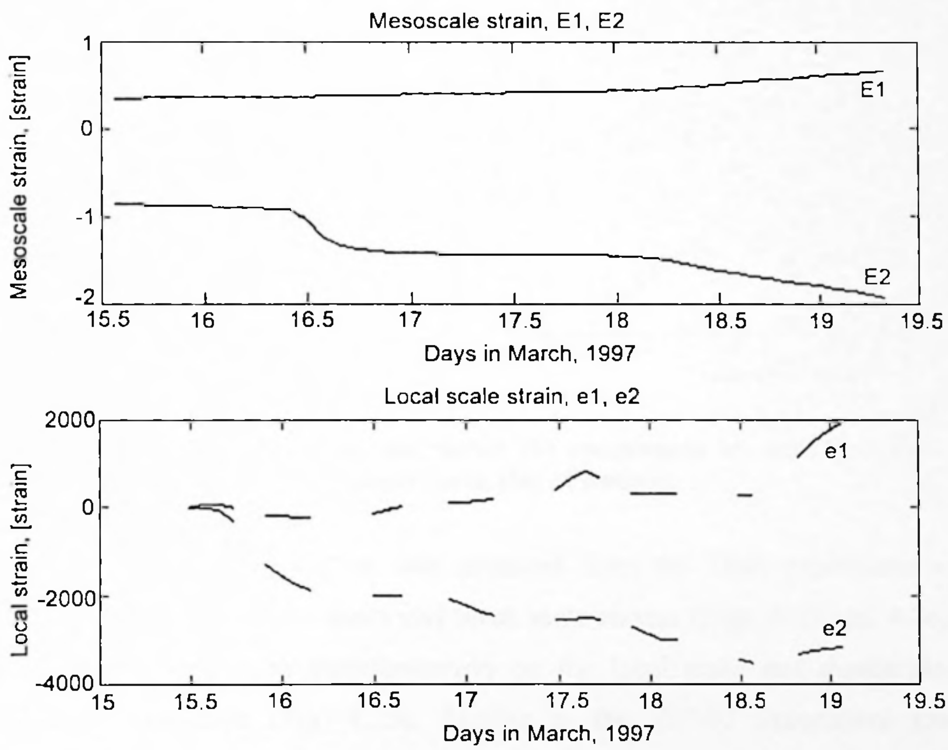


**Figure 4.23.** Mesoscale (top) and local scale (bottom) deformations. ZIP-97 experiment.

Firstly there are periods when deformations act almost simultaneously and periods when, with the constant local strain, the mesoscale strain varies significantly (Figs. 4.23 and 4.24). We relate this phenomenon with the fact that on the mesoscale ice drifts according the rules of the granular plastic flow. Besides the rearrangement of the pack ice produces stationary zones supporting the external load, in the same manner as "stress chains" act (see section 7.2.1, Chapter 7).

[illegible]



[illegible]

[illegible]

The second feature is that the levels of the mesoscale and local scale deformations differ by 3 orders of magnitude (Fig. 4.24 ). Again this important fact can be explained in term of ice pack "geometry". When the area surrounded by drifters deforms the main deformation occurs in localised zones such as leads, ridges or shear slip lines. The differential motion of buoys gives us the average deformation in the area that contains zones of high deformation as well as zones with a very little deformation (intact floes). A strain gauge measures deformation in the latter, so it never gives a high deformation associated with ice failure (probably nobody would try to put the sensor across an opening crack; it could help to measure high level local strain, but the result will be disastrous).

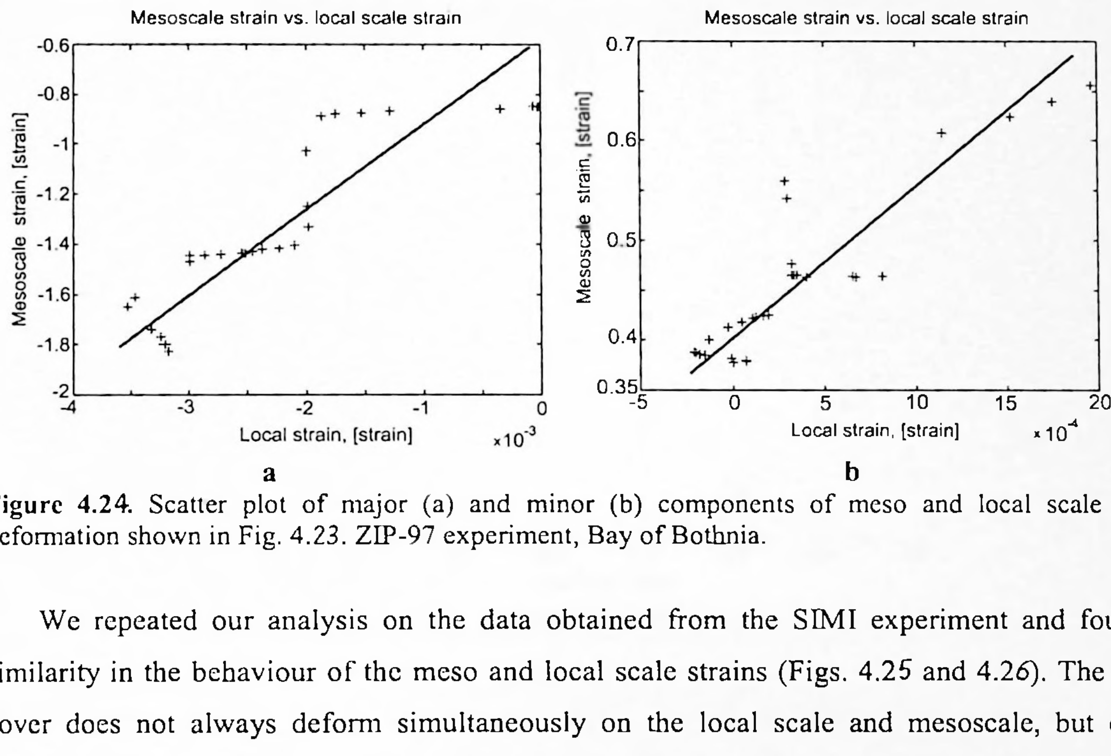


**Figure 4.24.** Scatter plot of major (a) and minor (b) components of meso and local scale ice deformation shown in Fig. 4.23. ZIP-97 experiment, Bay of Bothnia.

We repeated our analysis on the data obtained from the SIMI experiment and found similarity in the behaviour of the meso and local scale strains (Figs. 4.25 and 4.26). The ice cover does not always deform simultaneously on the local scale and mesoscale, but can exhibit lag in deformation (Fig. 4.25). Similar to the ZIP-97 experiment the average mesoscale deformation is 4 orders of magnitude larger than the average local strain (Fig 4.26b).

Generally speaking, the typical mesoscale deformation for a month-season time span is of order of a tenth up to several strain, while the local deformation never exceeds $10^{-2}$. The reason for this is quite obvious: mesoscale deformation as a rule includes deformation across open

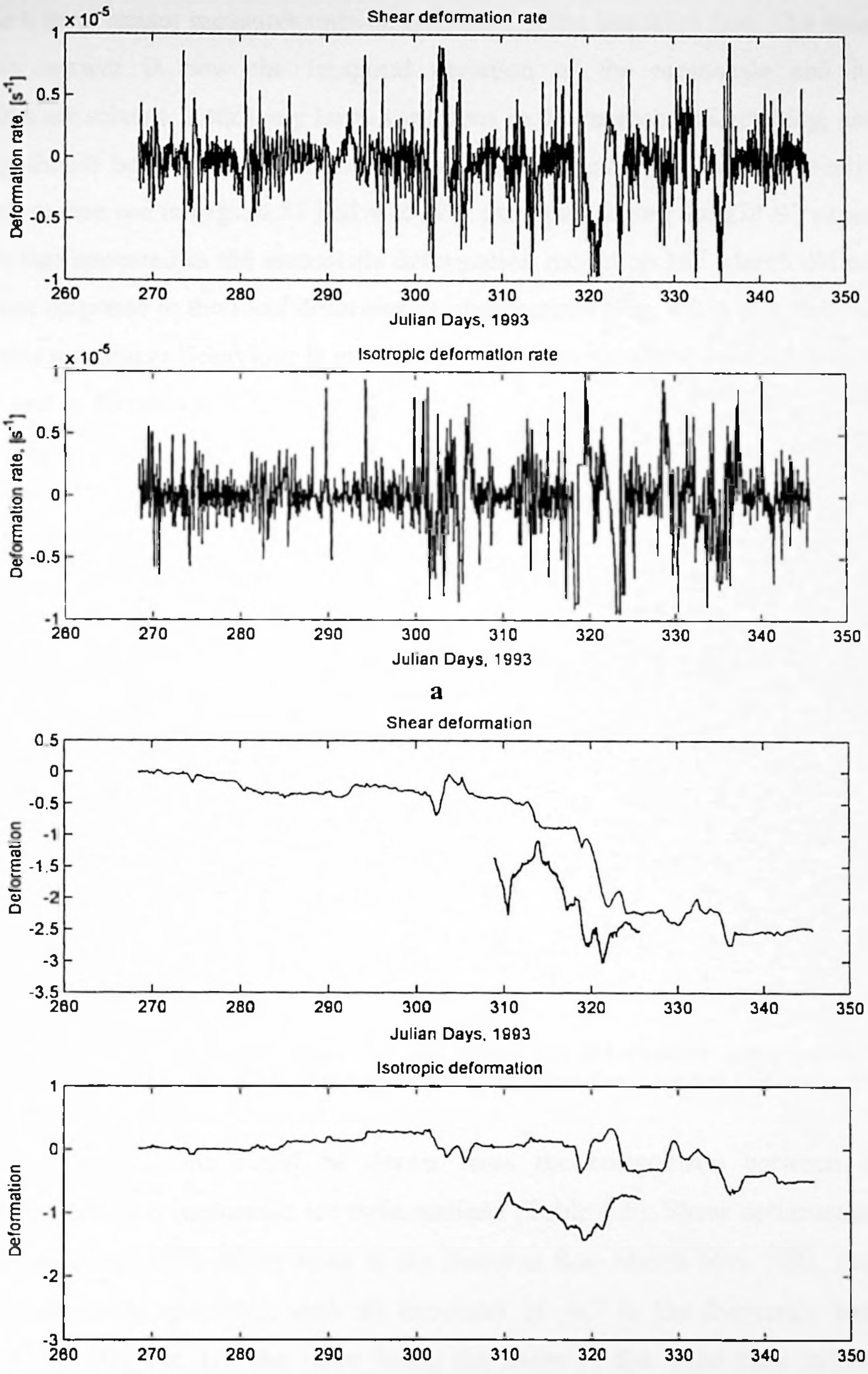


**Figure 4.25.** Rates of mesoscale deformation components (a). Components of mesoscale deformation (upper curves) and of local strains (lower curves) (b). For convenience local strains are multiplied by factor of $2 \cdot 10^4$. SIMI Fall Experiment, Beaufort Sea, October-December 1993.

leads while a local sensor measures only deformation of the intact ice floe. The more difficult question to answer is how the temporal variation of the mesoscale and local scale deformations are related. Intuitively large variations in the mesoscale stretching, compression or shearing should be reflected in the local measurements as well. However, reality is more intricate as one can see in Figs. 4.23 and 4.25. For example, during the ZIP-97 experiment the large event that appeared in the mesoscale deformation record on 16th March did not produce an immediate response in the local deformation observations (Fig. 4.23). It is believed that the answer to this non-linear behaviour is in granular type dynamics of the floe assemblage on the mesoscale and in formation of supporting columns and force chains. The data were available only on two spatial scales, nevertheless some scaling relationships can be derived for the both ZIP-97 and SIMI experiments and incorporated into the analysis.

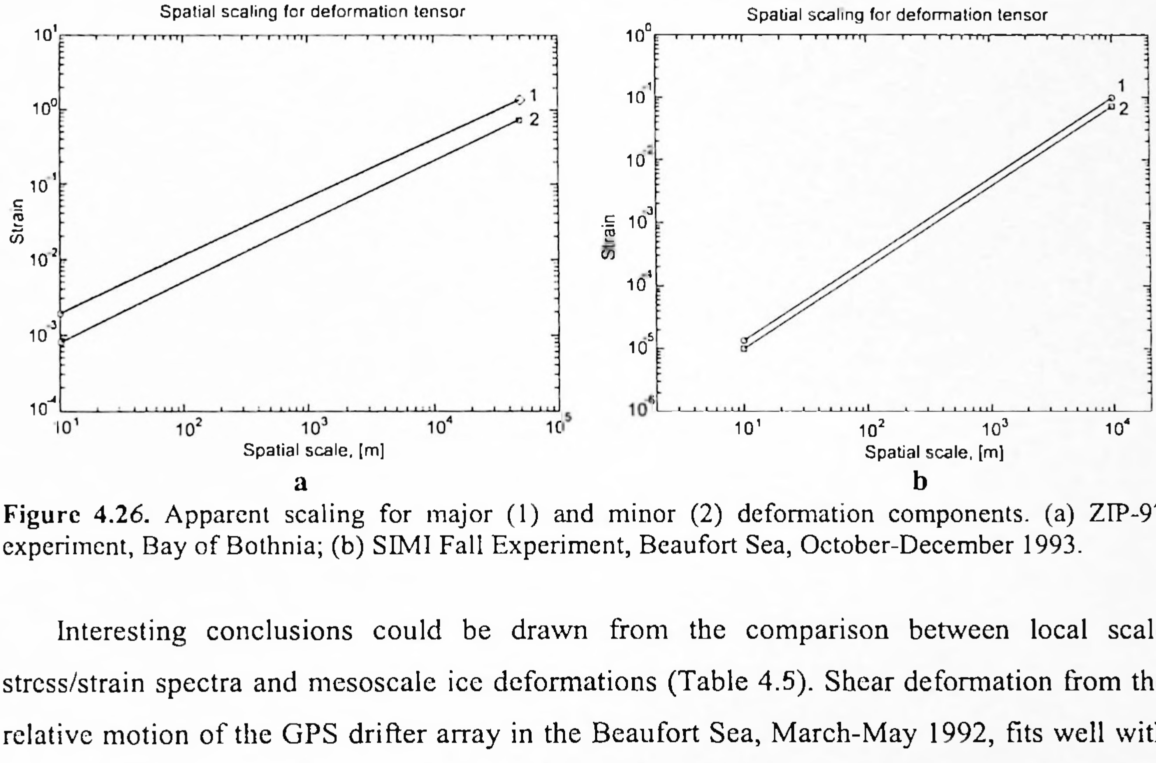


**Figure 4.26.** Apparent scaling for major (1) and minor (2) deformation components. (a) ZIP-97 experiment, Bay of Bothnia; (b) SIMI Fall Experiment, Beaufort Sea, October-December 1993.

Interesting conclusions could be drawn from the comparison between local scale stress/strain spectra and mesoscale ice deformations (Table 4.5). Shear deformation from the relative motion of the GPS drifter array in the Beaufort Sea, March-May 1992, fits well with the power law model spectrum, with an exponent of -0.7 in the frequency band ranging between $10^{-6}$ to $10^{-3}$ Hz. On the other hand, the shear of the wind flow calculated from anemometers mounted on the buoys with a 130 km separation produces a red-type spectrum with the slope of about -1.6 (Overland et al., 1995). Therefore, the ice cover under wind forcing generates its own spectrum. Other GPS drifter observations show evidence that the buoy distance change rates have a power law spectrum with exponents from -1.5 to -1.7 (Leppäranta and Hibler, 1987), being reasonably close to the exponents obtained for local

[illegible]

[illegible]

[illegible]

[illegible]

[illegible]

stresses. However, simple dimensional analysis shows that the spectral exponents for deformations $s_d$ and deformation rates $s_{dr}$ are related as $s_{def} = s_{defr} - 2$:

$$
\begin{gathered}
S(f) \propto y(t)^2 \propto (f)^{s_{def}} \propto (1/t)^{s_{def}} \propto (t)^{-s_{def}} \propto [Y]^2 \propto [T]^{-s_{def}} \\
S'(f) \propto \dot{y}(t)^2 \propto (f)^{s_{defr}} \propto (1/t)^{s_{defr}} \propto (t)^{-s_{defr}} \propto [\dot{Y}]^2 \propto \frac{[Y]^2}{[T]^2} \propto [T]^{-s_{def}-2} \propto [T]^{-s_{defr}}
\end{gathered}
\tag{4.17}
$$

where, $s_{def}$, and $s_{defr}$ - are spectral exponents, variables $t$ and $f$ - period and frequency, $T$ and $Y$ - dimensions of the time and deformation.

This fact is not in agreement with spectra observed for the ice cover mesoscale motion and requires further study.

# Chapter 5. Analysis of the wave-like deformation

In this chapter different types of waves and oscillations observed in the ice-covered regions, including both ice deformations caused by periodic forcing and wave emission initiated by aperiodic processes are considered. The goal of the analysis is to identify "signatures" of the oscillations generated by different type of processes and estimate their contribution into the overall ice deformation. The vibration of the ice cover associated with the ridge building, ice shearing and crack propagation represent a significant part of the energy loss during the deformation process. Therefore, this type of oscillation is of special interest.

## 5.1 Propagation of swell

Flexural gravity waves with a frequency of 0.036 Hz and a relatively small variability of 0.014 Hz were extensively monitored during the SIMI experiment (Fig. 5.1). It is believed that they are caused by long period swell penetrating from the open water area of the Greenland or Chukchi Seas. The ZIP experiment showed that most commonly encountered waves have a frequency of 0.08-0.1 Hz (Fig.5.2).

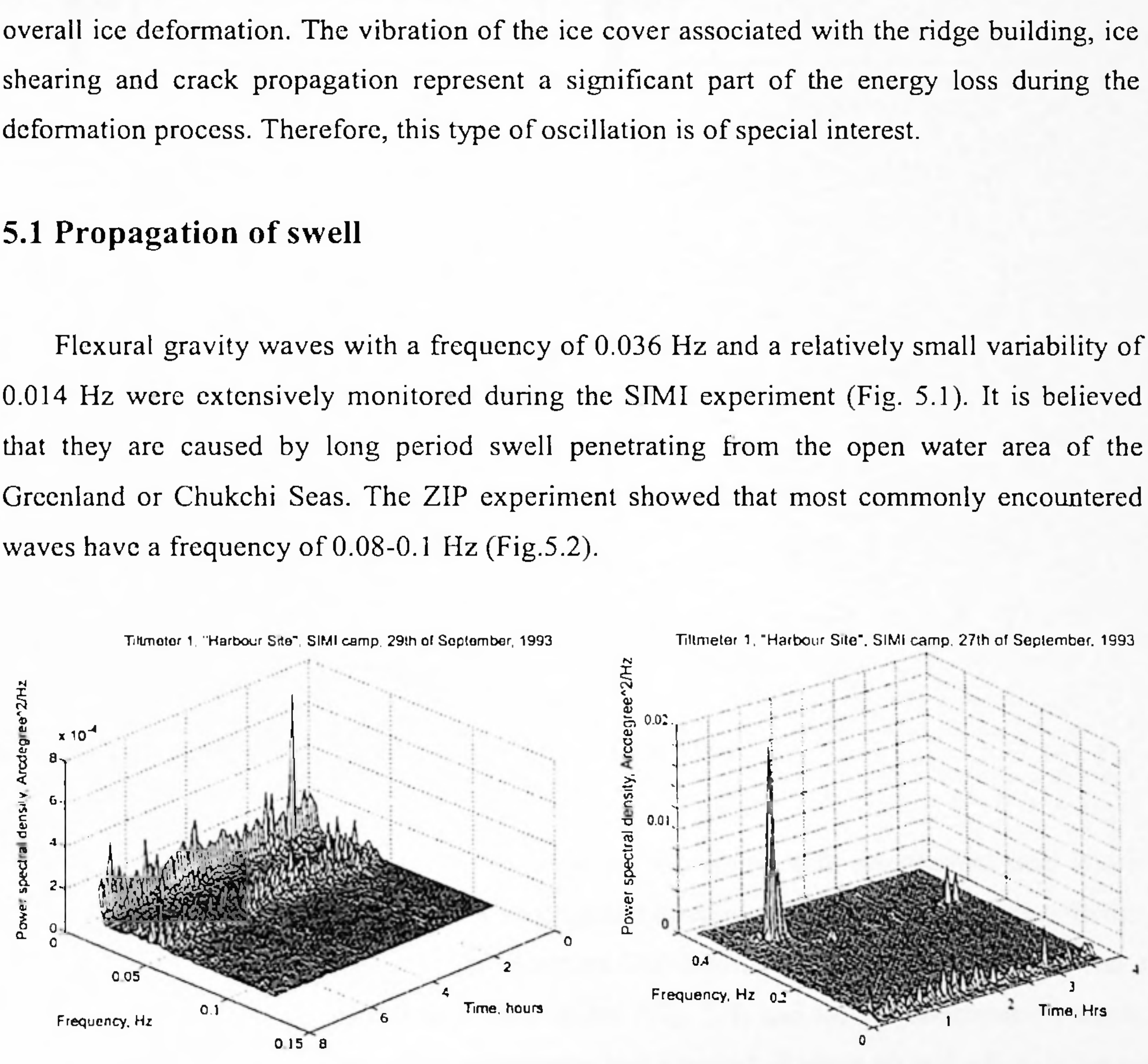


a b

**Figure 5.1.** Time structure of ice tilt spectrum. (a) flexural gravity waves caused by swell; (b) flexural gravity waves along with short-period oscillations.

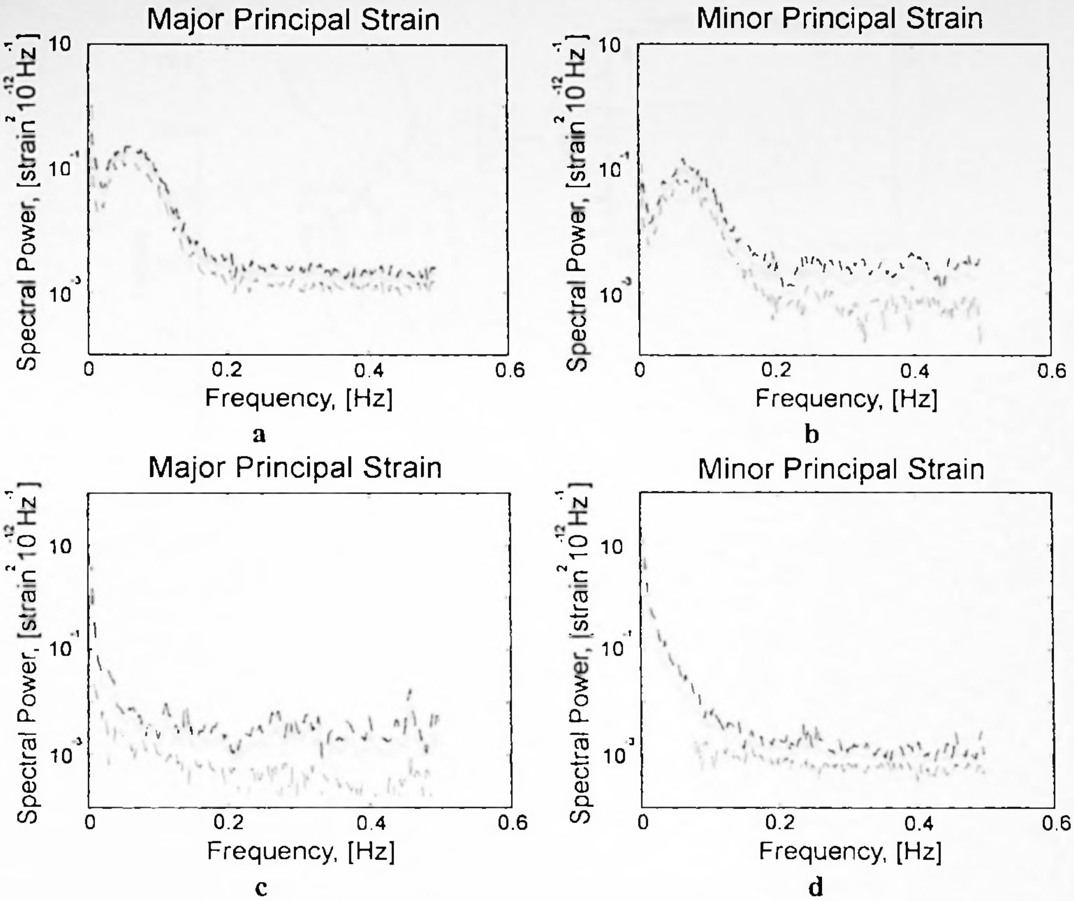


**Figure 5.2.** Spectral structure of strain time series. Examples of swell-like waves (a, b) and predominantly aperiodic deformations (c, d) are presented. Confidence limits (95 %) are shown.

## 5.2 Tidal, inertial oscillations and internal waves

Oscillations with a period of 11-12 hrs were associated with semidiurnal tidal waves responsible for tilting of ice floes. Their propagation direction was found to coincide with that of the tidal waves in this region of the Beaufort Sea. Inertial oscillations of ice drift with a period of 12 hrs were detected from a GPS drifter (Fig. 5.3) and tilt and strainmeter records. Internal waves observed in the SIMI experiment had a period of about 40 min which is longer than that from CEAREX, being 20-30 min long (Czipott et al., 1991). In both cases, the maximal tilt of the ice floe was about 10 arc-seconds.

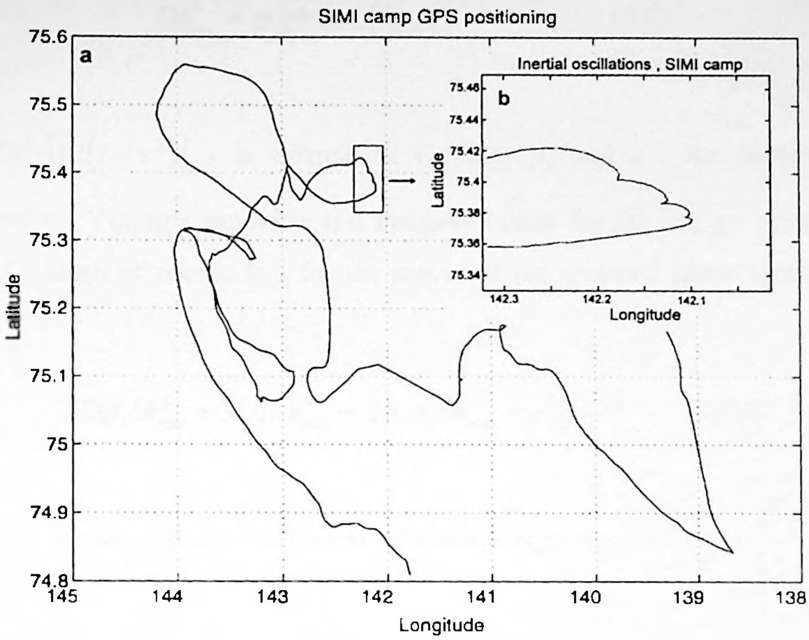


**Figure 5.3.** Location of SIMI camp during autumn/winter 1993 (a) and inertial oscillations of ice floe (b).

## 5.3 Resonant waves

Sporadic oscillations with a frequency of 0.14-0.16 Hz and an average duration of 10-20 min, locally generated by turbulent atmospheric pressure microfluctuations, were observed during the SIMI experiment. The mechanism has resonant characteristics, and favourable conditions occur when the mean wind speed is nearly equal to or higher than the minimum phase speed of flexural gravity waves (Squire et al., 1995; Wadhams, 1986).

Nagurny et al. (1994) put forward another mechanism for ice-ocean coupled wave generation, suggesting that atmospheric turbulence disturbs the continuous ice sheet covered ocean, causing vibration of the ice and underlying water column at two frequencies: $F_{res}$ and $F_{min}$. $F_{res}$ corresponds to a free transverse surface long wave propagating in the wave-guide mode where the hydrodynamic pressure is completely balanced with buoyancy forces. $F_{min}$ is a frequency of vibrations locally caused by turbulent atmospheric pressure microfluctuations. A solution of the equations for elastic vibrations in the infinite ice-plate lying on the water surface for the low-amplitude case (linear approximation) gives the resonant wave number $k_{res}$:

$$Dk_{res}^3 = \rho_1 gh \tanh(k_{res} H) \qquad (5.1)$$

where, $D = Eh^3 / [12(1-\nu^2)]$ - is cylindrical rigidity, $\rho_1$ and $h$ - ice density and average thickness, $E$ and $\nu$ - Young's modulus and Poisson's ratio for the ice, $g$ - acceleration due to gravity, and $H$ - depth of ocean. $k_{min}$ for the waves at the minimal phase speed can be found from:

$$2D\rho_1 hk_{min}^5 + 3D\rho_2 k_{min}^4 - 2\rho_1\rho_2 hk_{min} - \rho_2^2 g = 0 \qquad (5.2)$$

where, $\rho_2$ - water density, other variables are the same as in equation (5.1).

In equations (5.1) and (5.2), $F_{min}$ is always less than $F_{res}$. In addition, the model gives a method for estimating the average ice thickness in the region under study.

From the observations made in the central Arctic, it is evident that the frequencies of the resonant and minimal phase speed waves are about 0.04 and 0.06 Hz respectively. Tiltmeter observations during the autumn stage of the SIMI camp gave different figures for the swell and minimal phase speed waves: 0.035 Hz and 0.15 Hz. According to Nagurny, this leads to an unrealistic average ice thickness in the region (<0.5 m). We speculate that the error was introduced by using the continuous ice sheet assumption. In reality, the conditions were different. We studied the ice area close to the camp, which had several wide leads with very thin ice and an ice cover constantly subjected to cracking. Thus, Nagurny's theory requires to be substantiated.

Infra-gravity waves with a period of about 1 minute having a duration of about 2 hrs and an irregular occurrence pattern were seen in the Beaufort Sea. For the deep ocean, the dispersion relation of freely propagating gravity waves is:

$$\varpi^2 = gk \qquad (5.3)$$

where, $g$ - acceleration due to gravity, $k$ - wave number, $\varpi$ - angular frequency. It gives a wavelength of about 600 m for the 50 s period waves observed.

The mechanism responsible for infragravity wave generation is not yet understood. Let us consider two hypotheses. According to the first of these, the ice picks out the oscillations near its resonant frequency (Wadhams and Wells, 1995) while the second hypothesis suggests that such oscillations are caused by non-linear interactions between swell and waves of shorter periods.

### 5.4 Short-period waves

The propagation of short-period waves in the ice was recorded during several field experiments: MIZEX-84, CEAREX-88/89, SIMI-93/94, drifting stations North Pole 23 and 28, etc. (Bogorodsky and Smirnov, 1982; Czipott and Podney, 1989; Martin and Drucker, 1991; Smirnov and Shuslebin, 1990; Squire et al., 1995; Wadhams and Wells, 1995). This type of wave was found in tiltmeter and accelerometer records. The period of these oscillations is about 0.3-1 Hz. There is a narrow peak in the spectrum with variations in frequency of about $\pm$ 0.01 Hz. This type of wave was reported as frequent and with a significant level of power. A typical amplitude of the vertical component is about 10-20 mm, whereas for the swell it is smaller, 0.5-3 mm.

In the SIMI experiment, the short waves were observed at two rather distant sites A and B (1200 m apart), near the forming ridge (Fig. 3.36, Chapter 3, Part II). They occurred in several separate wave packets with a frequency of 0.32 - 0.5 Hz (variations in frequency of about $\pm$ 0.01 Hz) and each having a duration of 5-20 min, amounting to 50 min altogether (Fig. 5.1b; 5.4a). Their power spectral density was significantly greater than that of flexural gravity waves (for the tilt the order is $1\text{-}2 \cdot 10^{-2}$ arc degree $^2$/Hz). They were found to be vertically polarized, propagating from the 20 m wide source, beside the ridge. The ice cover bobbing induced by the unbalanced pushing upwards or downwards of newly fractured ice blocks adding to the growing ridge was considered to be the cause of these oscillations (Wadhams and Wells, 1995).

The simplest model of bobbing oscillations of an ice floe with a draft $h$, which comprises a free non-damped oscillation under the hydrostatic vertical restoring force, gives a resonant frequency:

$$\omega \cong \sqrt{g\rho_w / h\rho_I} \qquad (5.4)$$

where, $g$ - acceleration due to gravity, $h$ - mean draft of ice floe, $\rho_w$ and $\rho_I$ - water and ice density respectively. It gives an estimate of the bobbing frequency of about 0.33 Hz for a 2.5 m ice draft. Estimation of wavelength and phase velocity from the dispersion equation gave figures of 135 m and 54 m/s respectively.

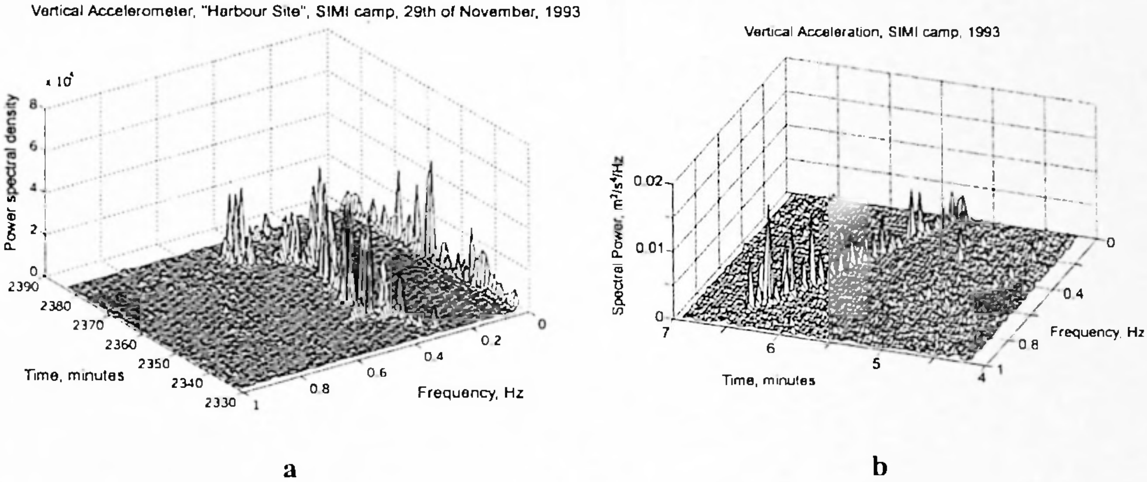


**Figure 5.4.** Time structure of spectrum for waves emitted during ice ridging (a) and variable frequency oscillations of an ice cover (b).

In addition to the vertical shear waves, predominantly horizontal shear waves (i.e. horizontally polarized) with a small vertical component were observed during the SIMI experiment. The waves were also observed at sites A and B (Fig. 3.36, Chapter 3, Part II). We speculate that they are initiated by ice stick-slip motion at the edges of the floes (Smirnov et al., 1993).

Ridge building laboratory experiments show periodic oscillations of the ice sheet with a well-pronounced peak of 9 Hz (Fig. 5.5). A light vertical accelerometer was installed on the top surface of the model ice sheet (Tuhkuri and Lensu, 1997). Taking into account the properties of the model ice the same mechanism may be responsible for the oscillations with frequency 0.3-0.5 Hz observed in the field. After detailed checking of the time series it was discovered that the signal was not amplified enough and so experiments should be repeated. Later tests included an amplifier and an antialias filter in the recording chain but did not show any stable oscillations, only a narrow band noise. However, it does not mean that these

oscillations do not exist. During the second set of the tests performed in August 1997, when the antialias filter was turned off, the oscillations with a variation in frequency similar to those observed in the field appeared. Thus, it is evident that ice motion during lab ridging tests has a high frequency component appearing in the working band as an alias effect.

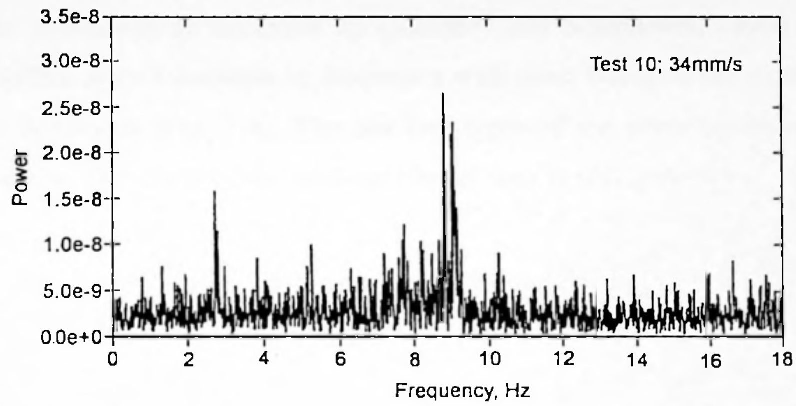


**Figure 5.5.** Spectrum for short-period waves monitored during ice ridging in the Ice Tank at the Helsinki University of Technology.

## 5.5 Events with variation in the frequency

Ice cover oscillations with regular variations in frequency were noticed both near the border of the floe and in the central area. The Doppler shift of frequency due to motion of the wave source relative to the point of observation can be an explanation of the phenomenon. A theoretical prediction of wave emission from the tip of a crack penetrating through the ice floe was made by Slepyan (1993):

$$k_{kelv} = \left(\frac{\rho g}{3D}\right)^{1/4} \approx 0.0438h^{-3/4}$$

$$c_g = c_{ph} = 17.3h^{3/8} \qquad (5.5)$$

where, $k_{kelv}$ - wave number for Kelvin's phase, $c_g$ and $c_{ph}$ - group and phase speeds of the emitted waves, $h$ - ice thickness [m].

[illegible]

[illegible]



[illegible]

## [illegible]

[illegible]

$$[illegible]$$

[illegible]

The asymptotic solution (5.5) corresponds to the emission of shear bending waves with a frequency of about 0.59 Hz, wave length of 38.4 m and phase velocity of 22.5 m/s for the crack moving faster than Kelvin's phase. If the crack tip emitting the waves moves towards the sensor indirectly, the Doppler shift produces frequency variation similar to that in Fig. 5.4b. Smirnov and Shushlebin observed variations in frequency of seismic ice waves, related, they assume, to movement of the crack tip (Smirnov and Shushlebin, 1990). The suggested hypothesis describes only a decrease in frequency with time, but does not explain its increase and oscillatory behaviour (Fig. 5.4). The last two types of ice cover oscillations are also of frequent occurrence. The explanation of these phenomena is still underway.

## 5.6 Overall spectrum of the local periodic ice motion

Figure 5.6 shows the model spectra for ice floe vertical velocity caused by different ice/ocean dynamic processes (Squire et al., 1995). Not all the processes represented occur simultaneously and their intensity can also differ significantly. For example, the signature of the internal waves can be buried under vibrations due to wind or swell. But despite its schematic character, the figure gives an idea on what type of periodic local ice deformations one can expect.

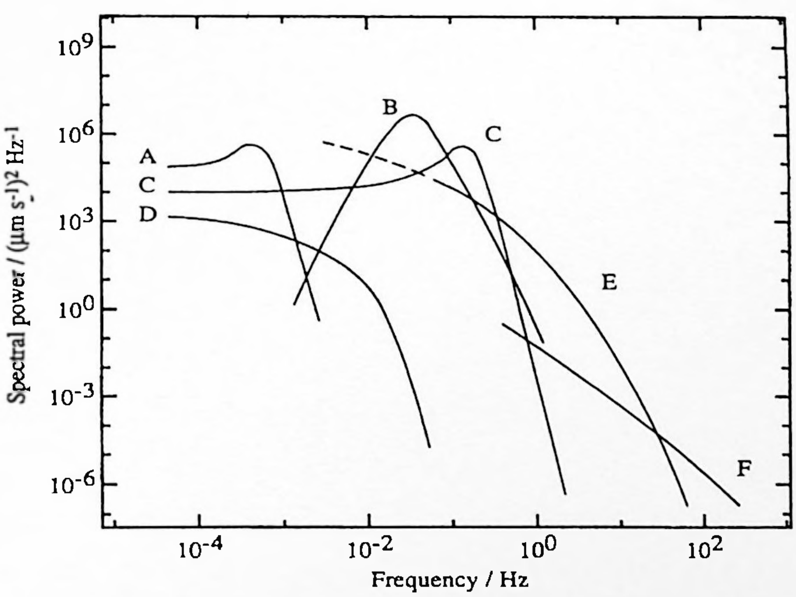


**Figure 5.6.** Model spectrum for vertical velocity of ice oscillations: (A) - internal ocean waves; (B) - surface gravity waves; (C) - motion generated by turbulent atmosphere pressure fluctuations; (D) - theoretical prediction for water turbulence; (E) - deformation waves caused by ridging process; (F) - acoustic waves (after Squire et al., 1995).

The figure also shows that the amplitude of the oscillations decreases rapidly, and practically in accordance with a power law for frequencies greater than $10^{-1}$ Hz. However, this is not the case for the observations lasting only several hours (Figs. 5.1 and 5.4), yet for the long period averaging it is still a reasonable assumption.

Based on the analysis performed, a redefinition of the general spectrum of local ice deformations was suggested where the main alteration is in the high frequency band (0.2-1 Hz). The temporal variability in the ice oscillations was studied with the help of time-frequency analysis enabling us to find additional vital details on the short-period wave spectrum. The existence of events with varying frequency or so-called "chirp oscillations" is considered to be an important feature of the spectrum.

# Chapter 6. Synthesis: Sea ice deformation from mesoscale to geophysical scale

The scope of this chapter is to present the essential features of sea ice cover deformations, their spatial variability and temporal evolution with the ultimate goal of formulating a hypothesis which describes some important relationships between ice deformations on different spatial-temporal scales. We will combine the overall picture of the sea ice deformation starting from floe scale ice deformation and failure events such as ice ridging and rafting, throughout the regional scale up to the large-scale fractures. We will relate deformations to the natural forces exerted on ice.

To study deformations on such a wide range of spatial and temporal scales data from as many sources as possible are used. Observations on ice deformations carried out from different platforms employing different methods and results from ice dynamics models are included in the analysis.

## 6.1 Methods to observe ice deformation

In previous chapters we discussed in detail methods enabling us to measure ice deformation and stress on the local and floe scale. These included the use of deformation and stress gauges, as well as a method to derive deformation on regional and mesoscale from the relative motion of ice drifters. These methods are very accurate and useful in obtaining time series of the deformation and stress in a limited region of the sea, however they are unable to define fine spatial structure of the deformation field. For example, to monitor local the ice strain field in the vicinity of the slip line we have to install an enormous number of strain gauges. To study spatial structure of the sea ice deformation field other approaches should be explored. There are several methods to observe or to estimate deformations of the sea ice cover indirectly. We start this section with a description of laboratory experiments in large-scale ice facilities, measurements of ice loads on offshore structures, and remote sensing techniques.

[illegible]

[illegible]

[illegible]

[illegible]

[illegible]

### 6.1.1 Large scale laboratory tests

Experiments carried out in large-scale ice facilities or simply "large ice tanks" should be considered as a useful tool for ice deformation studies in controlled conditions. With the help of these tests the complicated ice deformation can be "dissected" and the basic components of the overall deformation process (i.e. compaction of ice floes, rafting, ridging, etc.) can be studied separately making them easier to analyse. This approach was successfully implemented during ice rafting and ridging experiments performed in the ice tank, Helsinki University of Technology, Finland.

The tank is a large 40 × 40 m indoor basin filled with water, and equipped with a cooling system and a loading device attached to a bi-directional carriage (Tuhkuri and Lensu, 1998). Model fine-grained ice of non-uniform thickness was produced for the experiments by spraying a mixture of water with small amounts of ethanol added (about 0.4 percent) over the surface (Tuhkuri et al., 1999). Because of the ethanol component the model ice stiffness is significantly reduced (flexural strengths: 30-50 kPa, Young's modulus: 5-60 MPa) and therefore the model ice could be crushed more easily than ordinary ice. For the ridging and rafting experiments the ice was cut into strips of about 6 × 26 m with a pre-cut across the middle (Fig. 6.1). To create a ridge the ice was compressed at a constant velocity, and an ice rupture started developing in the zone of the pre-cut. First the ice rafted (Fig. 6.1a) with an ice ridge developing later as a second stage of rafting (Fig. 6.1b). The total loading force was estimated from transducers mounted on the pusher plates (Fig. 6.2).

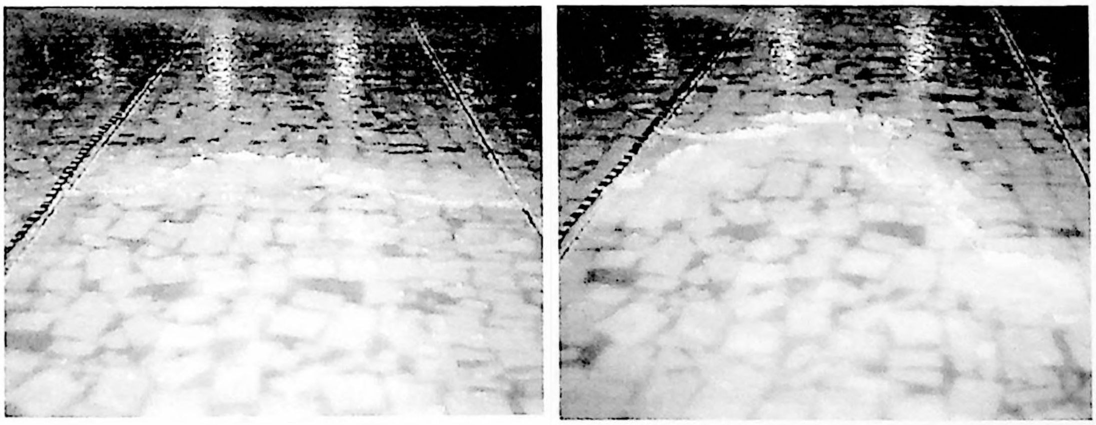

a b

**Figure 6.1.** Ridge formation during the experiment in the Large Scale Tank, Helsinki University of Technology. Displacement of pusher plate is about 1.9 m (a) and about 6.5 m (b) (from Tuhkuri et al., 1999).

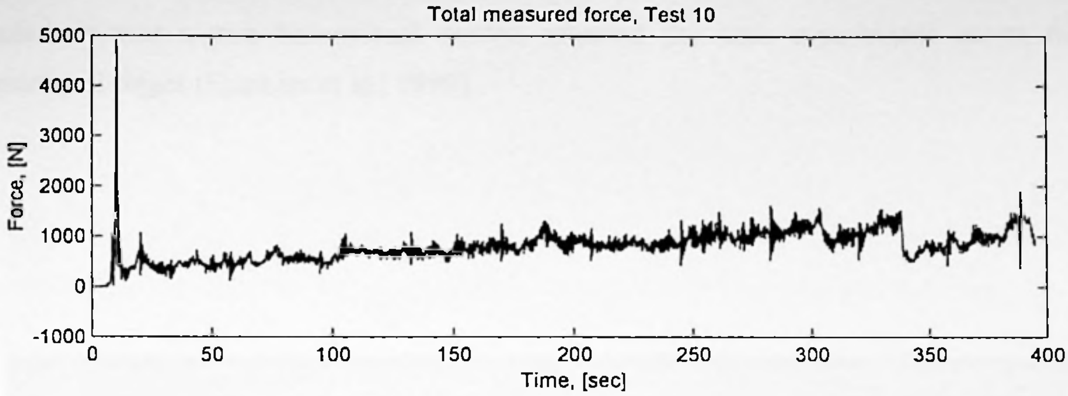


**Figure 6.2.** An example of the total ridging force measured during Experiment 10. Width of the model scale ridge was 6 m (data were obtained courtesy of Dr. J. Tuhkuri).

These tests have two main goals: to mimic the shape of the real ridge scaled accordingly to the mechanical properties of the model ice, and to compare the measured loading force occurring during the ridge formation process with the force calculated from the simulations (Hopkins et al., 1999). In trying to attribute the ridging tests to some real spatial scale one can say that the experiments should fall into the range between the single floe scale and the scale of floe assemblage, i.e. somewhat between tens of metres and several kilometres.

The discrete element model (DEM) employed for these simulations has been developed by Dr. M. Hopkins (CRREL) and describes the ice cover as a large set of interacting two-dimensional discrete particles (blocks). The motion of each particle follows Newtonian dynamics whereas the inter-particle interaction force has an elastic component proportional to the area of overlap between neighbouring particles, a viscous component proportional to the rate of change of the overlapping area, and Coulombic friction force. Initially the intact ice sheet consists of a single row of blocks, whereas each block is attached to its neighbours via viscous-elastic joints. To initiate deformation of the ice sheet strain-controlled or stress-controlled boundary conditions are applied to the ice blocks on the closed boundary. When the tensile stress in a joint exceeds a certain level the joint is broken and the separated block is added to the ridge (Hopkins, 1992 and 1994).

The model simulates a "virtual" ridge structure that resembles both ridges observed in the field and those created during experiments in ice tanks (Fig. 6.3). However, the level of the measured ridging forces was about twice as high as simulated ones (Fig. 6.4). The

[illegible]

[illegible]

[illegible]

[illegible]

[illegible]

[illegible]

discrepancy is thought to be due to the fact that the discrete element model used in the simulations was a two-dimensional model, whereas the tank experiments create three-dimensional ridges (Hopkins et al., 1999).

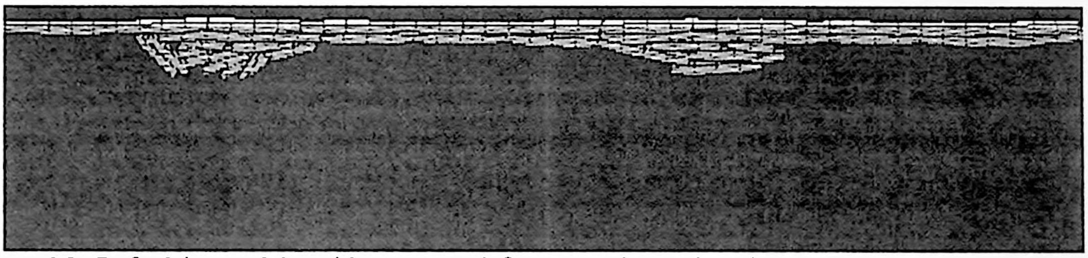

**Figure 6.3.** Rafted ice and ice ridges created from two intact ice sheets. A snapshot from discrete element simulation (from Tuhkuri et al., 1998).

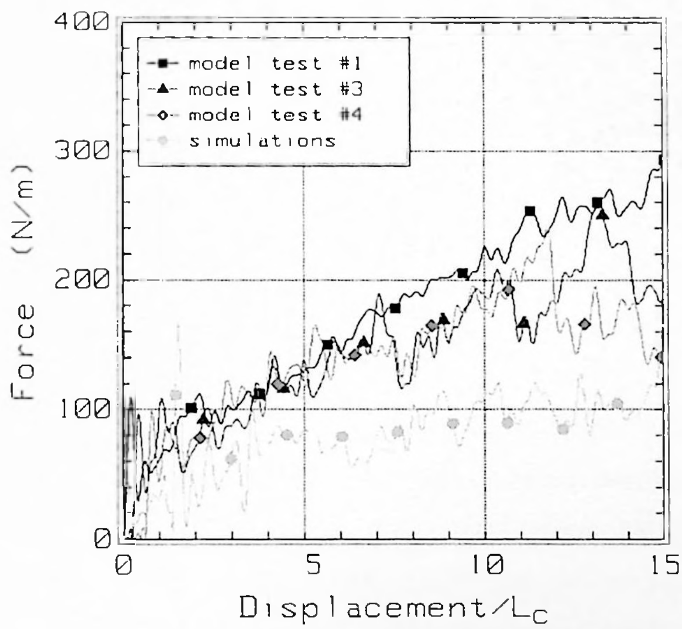


**Figure 6.4.** Measured and simulated ice forces. Tests 3 and 4 give examples of ice ridging whereas ice rafting occurred during Test 1. Simulated force is the average from eight runs of the DEM (after Tuhkuri et al., 1999).

Because the experiments use model ice with lower stiffness a direct comparison between the ice forces measured during the tank tests and those observed in the field experiments is impossible. Nevertheless, several important conclusions have been made from the analysis of

the non-dimensional parameters and ratios instead of absolute values. Here we describe only some of them bearing in mind that only one type of ridging structure, namely the pressure ridge, was studied.

The experiments showed that the force required for ice rafting is the upper limit for the interaction force that is generated during the ridging events. In other words, when the frictional force between two rafted ice sheets exceeds a certain level the deformation process "switches" to the ridging mode in a manner somewhat similar to the laminar flow of a fluid becoming a turbulent one. In this light the ridging process is considered to be a second phase of the rafting process with the ice elastic modulus, thickness of parental ice sheet and its roughness being the control parameters of ridging to rafting transition (Hopkins et al., 1999). In contrast to Parmerter's formulation (Parmerter, 1975) the ice roughness, meaning the ratio of thin ice thickness to thick ice thickness, plays an important role in this transition (Tuhkuri et al., 1999). Ridging of the rough ice sheets is more likely to happen whereas the "smoother" ice sheet is more likely to be rafted. Generally speaking, the ridging to rafting transition often exhibits an intermittent behaviour with both types of the processes co-existing for the same experimental set up (Fig. 6.3).

Finally a brief note should be made about the energetics of the deformation process. The ratio of the total deformation work to the potential energy gained by the ice cover due to deformation is a very important parameter for full-scale sea ice models because it affects the compressive strength of the ice cover (Flato and Hibler, 1995). Different authors estimate the range of this parameter as between 2 and 17 for the ice ridging process (Flato and Hibler, 1995; Hopkins, 1998). However, recent results have demonstrated that whereas for the ridging process the ratio of the total deformation work to the potential energy is in a range between 5 and 20, its upper limit for the rafting is far greater, about 100 (Hopkins et al., 1999). Therefore, on the one hand, the rafting requires more work and results in a smaller gain of the potential energy than ridging. This makes ridging more energetically stable than rafting. On the other hand, even during ridging events about 80 percent or more of the total ice deformation work is spent on ice fracturing, friction losses, and other energy sinks such as rotation of ice blocks and floes, and energy emission via ice cover oscillations (sections 5.4 and 5.5, Chapter 5). These facts are extremely important and lead us to a better understanding of the energy redistribution during the ice deformation processes.

[illegible]

[illegible]

[illegible]

[illegible]

[illegible]

For some ridging tests a light accelerometer was deployed on ice to measure vertical acceleration of the surface and to register short period vibrations (Tuhkuri and Lensu, 1997). The results from these tests and the ones from the field experiments were discussed earlier in section 5.4, Chapter 5.

### 6.1.2 Measurements of ice loads on offshore structures and artificial islands

In the 1970s, when oil and gas exploration on the Beaufort Sea Shelf began, more than a dozen offshore structures were constructed near the Canadian coast (Figs. 6.5 and 6.6). Since that time a large number of measurements of the ice loads exerted on the offshore structures has been made. The loads have been monitored by the use of three methods: interfacial measurements, monitoring of the structural response, and local ice stress and strain measurements (Sanderson 1988). The first method employs flat stress panels (so-called "flatjacks") affixed to the structure at the waterline (Fig. 6.7). The panels usually have dimensions 1 × 1 m or 2 × 2 m. They are in fact soft sensors with an overall stiffness of 1-5 GPa which is close to the stiffness of ice (Metge et al., 1983). The second method involves monitoring the movement of the whole structure under the ice load with the help of strain gauges installed on the different components of the structure (Fig. 6.7). The measured deformation is converted to stress by applying finite-element analysis of the structure. This is the most reliable method in measuring total ice load on the structure. Comparison between the interfacial stress measurements and the stress calculated from the structural response demonstrates satisfactory agreement between these two methods (Sanderson, 1988). The third approach estimates the loads on the structure by measuring local ice deformation, stresses, and ice deceleration in the vicinity of the structure (Fig. 6.7). The method of measuring local ice deformation with the help of stainmeters, stress gauges and accelerometers is described in Chapter 3 of the current thesis in detail and only one additional comment should be made. Because the deformed state of ice far from the structure can be very different from that near the structure the sensors should be installed as close as possible to the leading ice edge. Often this task can not be accomplished due to intensive ice fracture in the contact zone between ice and structure, therefore this type of data has to be treated with a certain caution.

[illegible]

[illegible]

[illegible]

[illegible]

[illegible]

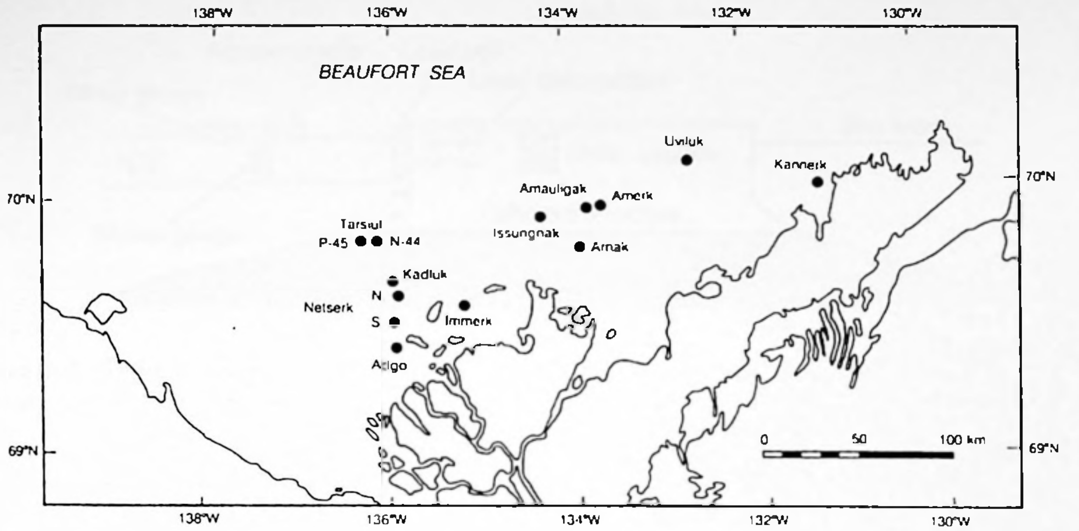


**Figure 6.5.** Locations of the offshore structures and artificial islands in the Beaufort Sea (after Sanderson, 1988).

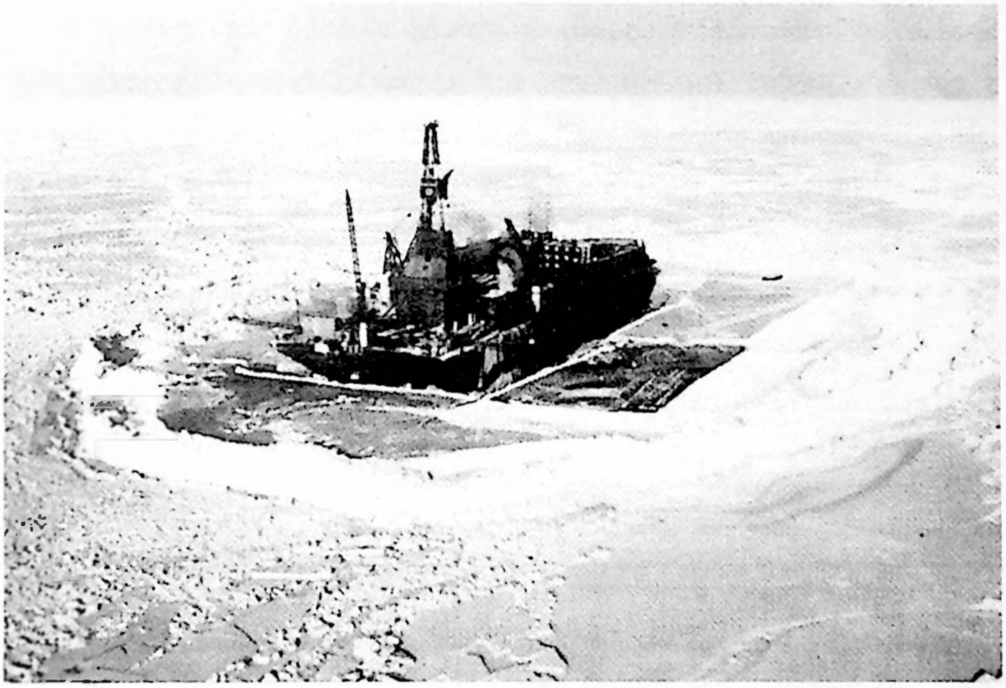

**Figure 6.6.** CANMAR Drilling Caisson, Uviluk artificial island, Beaufort Sea. The severe ice load is evident from the presence of the ice rubble around the structure (from Sanderson, 1988).

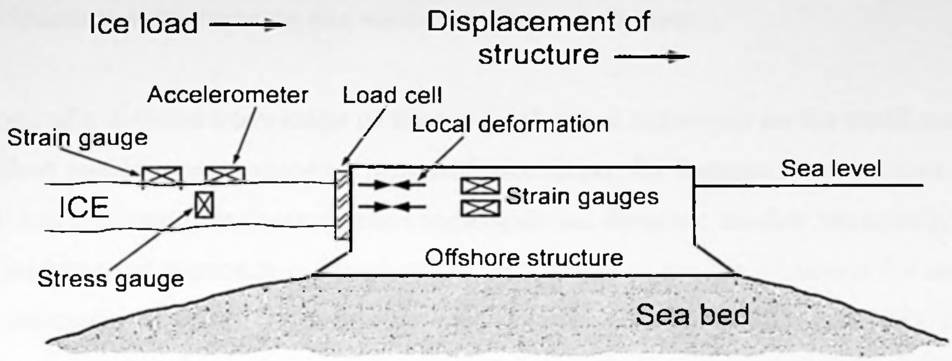


**Figure 6.7.** Typical layout of the sensors installed to measure ice loads exerted on an offshore structure. Three types of sensors can be used: load cells, strain gauges installed on the structure itself to monitor its motion and deformation, and a set of sensors deployed on ice to measure local ice deformation and stress (after Sanderson, 1988).

Measurements of ice loads acting on an offshore structure have great significance for the study of ice deformation. Despite all disagreements between different researchers in their views on what type of ice failure (i.e. brittle or ductile) dominates in the contact zone, it is the only method enabling us to measure directly ice stresses and deformations on scales from several tens to several hundreds of metres. The "pressure–area" curve (Sanderson, 1988) is based to a large extent on the records of ice loads. This curve will be discussed in section 7.2 of Chapter 7. An example of the ice load record is given in Fig. 6.8. Because of the way in which the transducers are designed and installed on the structure, the temporal variability of only one component of the stress tensor, uniaxial compressive stress (ice pressure), can be derived from the records.

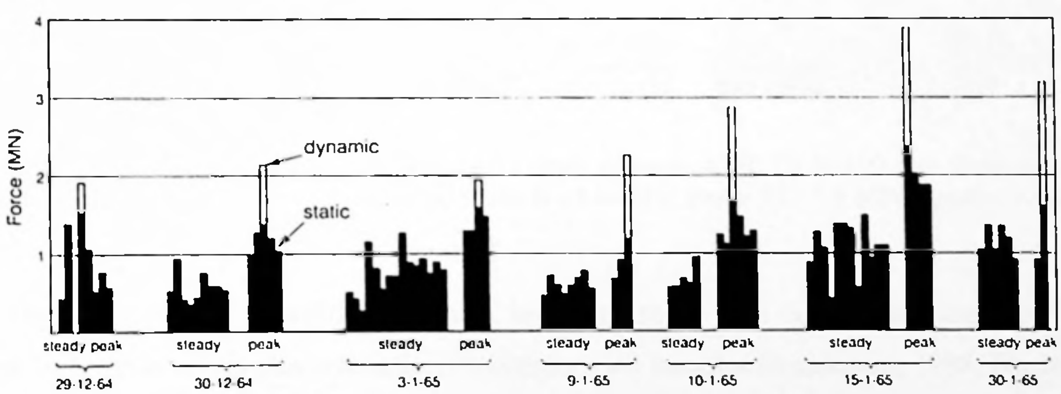


**Figure 6.8.** An example of the year-long ice load exerted on an oil rig. Cook Inlet, Beaufort Sea (from Sanderson, 1988).

### 6.1.3 Ice fracture signatures on the mesoscale and small scale

In spite of a detailed knowledge of the ice mechanical behaviour on the small scale, there is no method enabling us to measure mesoscale ice stress, for instance, over an area of about 100-1000 km$^2$. To estimate these stresses mesoscale ice dynamic models are usually applied. Another widely used approach is based on the calculation of the force balance for an ice area and the estimation of residual internal stresses (Lewis and Richter-Menge, 1998). It implies that calculations of deformations obtained by locating GPS or ARGOS drifters or assessing ice motion from SAR images have to be performed.

It is believed that the following indirect approach can also be applied. The method is based on the assessment of the stress needed to produce a particular type of ice deformation feature. In this section, we give an example of how the magnitude of ice stress can be derived from ice cracks and also from elastic buckling of thin ice in the lead. Let us consider this approach in detail.

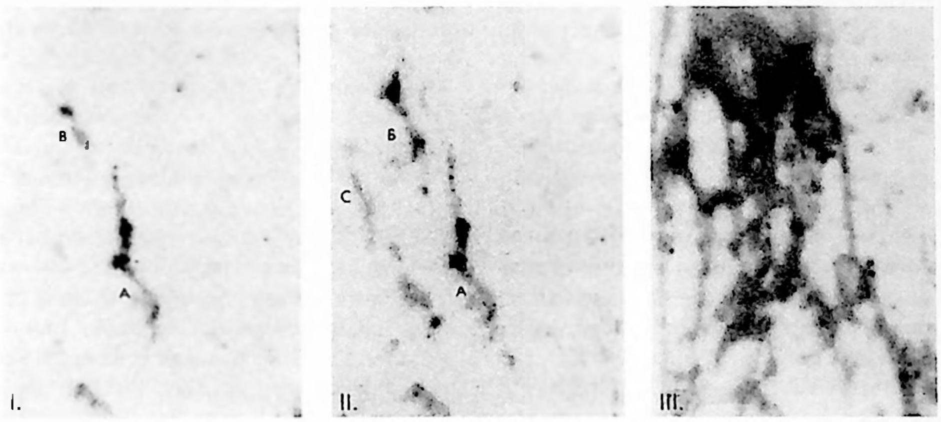


**Figure 6.9.** Development of wing-shaped cracks (dark features A, B, C) in 100 mm fresh-water ice specimen. Compression (frame I - 4.0 MPa; frame II - 4.8 MPa; frame III - 5.8 MPa) applied vertically (after Schulson and Hibler, 1991).

The formation of a specific pattern of in-plane cracks with out-of-plane extensions, so called "wing cracks", is characteristic of laboratory ice samples (Sanderson, 1988; Shulson et al., 1991), (Fig. 6.9), and the Arctic pack ice on a scale of several hundred kilometres (Shulson and Hibler, 1991), (Fig. 6.10). A typical wing crack is formed under low confined triaxial compression (whereas the compression applied along one of the directions is dominant, those along the other directions are nearly equal to each other and small, ~ 2

[illegible]

[illegible]

[illegible]

[illegible]

[illegible]

percent). The wing crack has an almost straight *primary crack* and curved *wings*. The primary crack is inclined with respect to the direction of the external load and formed by local shear deformation. The secondary wings are nucleated because of the shear sliding along the primary crack and an increase in local tensile stresses at the ends of the primary crack. The wings start to branch symmetrically at an angle between 40° and 90° to the primary crack and tend to curve towards the major compressive external load (Fig. 6.11).

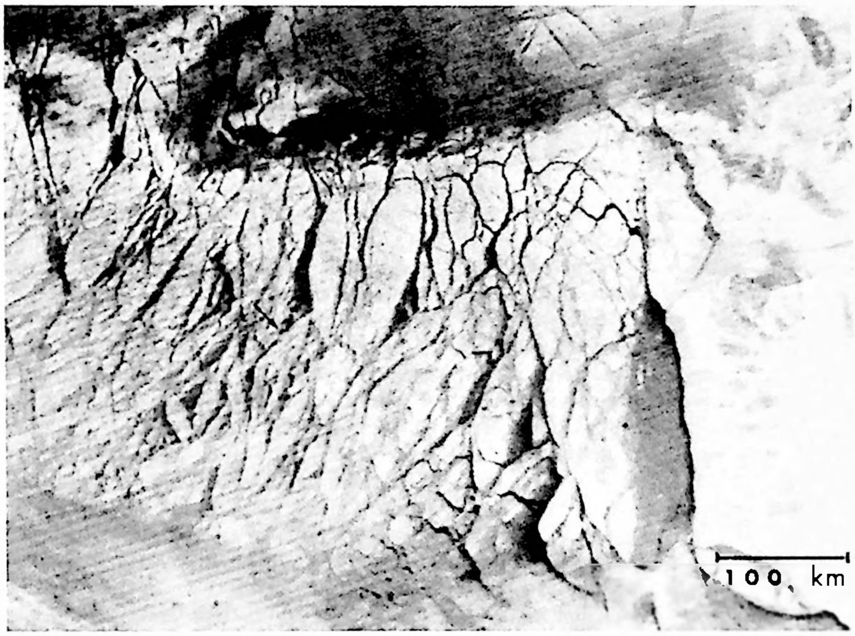


**Figure 6.10.** Image of first-year ice in the Beaufort Sea (infra-red band, 0.6 km resolution) obtained on 11 February 1983. Leads in the ice shown as dark features; the wing-shaped lead marked with the arrow. Banks Island is on the left-hand side (after Schulson and Hibler, 1991).

Similar features are found on SAR images of first-year ice in the Kara Sea (Fig. 6.12.), exhibiting the formation of the wing crack under west–east compression. Fig. 6.12b,c also shows the opening of compression cracks in the western part of the area. The direction of the compression is next rotated north-west to south-east, causing the closing of old leads and development of a new network (Fig. 6.12d). Later the wing crack starts to lose its shape, and becomes wider, practically disappearing.

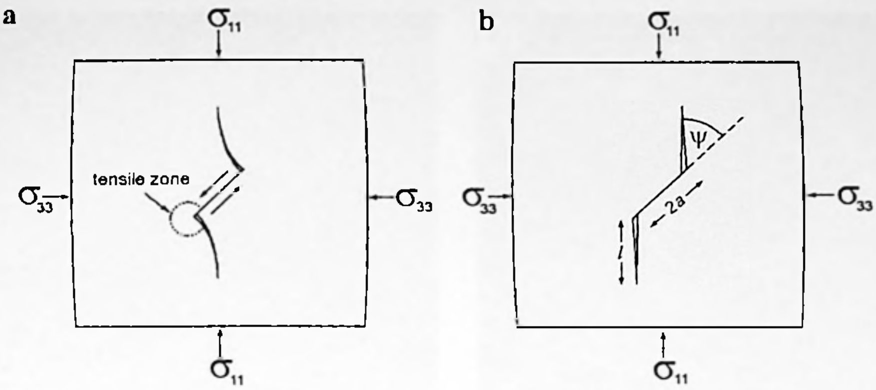


**Figure 6.11.** Formation of a wing crack in a brittle solid under compression (a) and an idealised model of wing crack formation (b) (after Sanderson, 1988).

The size of the primary crack is about 10 km with wings of about the same length. The external far-field stress activating the ice failure can be assessed employing fracture mechanics assuming that the loading is uniaxial (Ashby and Hallam, 1986; Shulson et al., 1991):

$$\sigma_{1c} = K_{1C} \frac{(1+l/a)^{3/2}}{\sqrt{\pi a}\cdot(1-\mu)\left[\frac{0.4\cdot(l/a)}{\sqrt{3}} + \frac{1}{\sqrt{3}\cdot(1+l/a)^{1/2}}\right]} \tag{6.1}$$

where: $\sigma_{lc}$ - critical stress, sufficient to generate a wing crack; $K_{IC}$ - fracture toughness (critical stress intensity factor); $a$ - half-length of the primary crack; $l$ - length of the wing; $\mu$ - friction coefficient of the primary crack interfaces.

To estimate the order of critical stress we can simplify equation (6.1) assuming that $l>>a$, i.e. it is a fully developed crack. After some algebra, we have:

$$\sigma_{1c} = K_{1C} \frac{\sqrt{3}\cdot(l/a^2)^{1/2}}{0.4\cdot\sqrt{\pi}\cdot(1-\mu)} \tag{6.2}$$

Using $K_{IC}$ = 0.1 MPa/m$^{1/2}$ suggested by Shulson et al. (1991), $\mu$ = 0.3, and parameters of the crack $a$ = 5 km, $l$ = 10 km, we estimate $\sigma_{lc}$ = 6.98 kPa. To check how our assumption "$l>>a$" affects the results we found $\sigma_{lc}$ from equation (6.1), which is 7.45 kPa. Both values appear to be reasonably close.

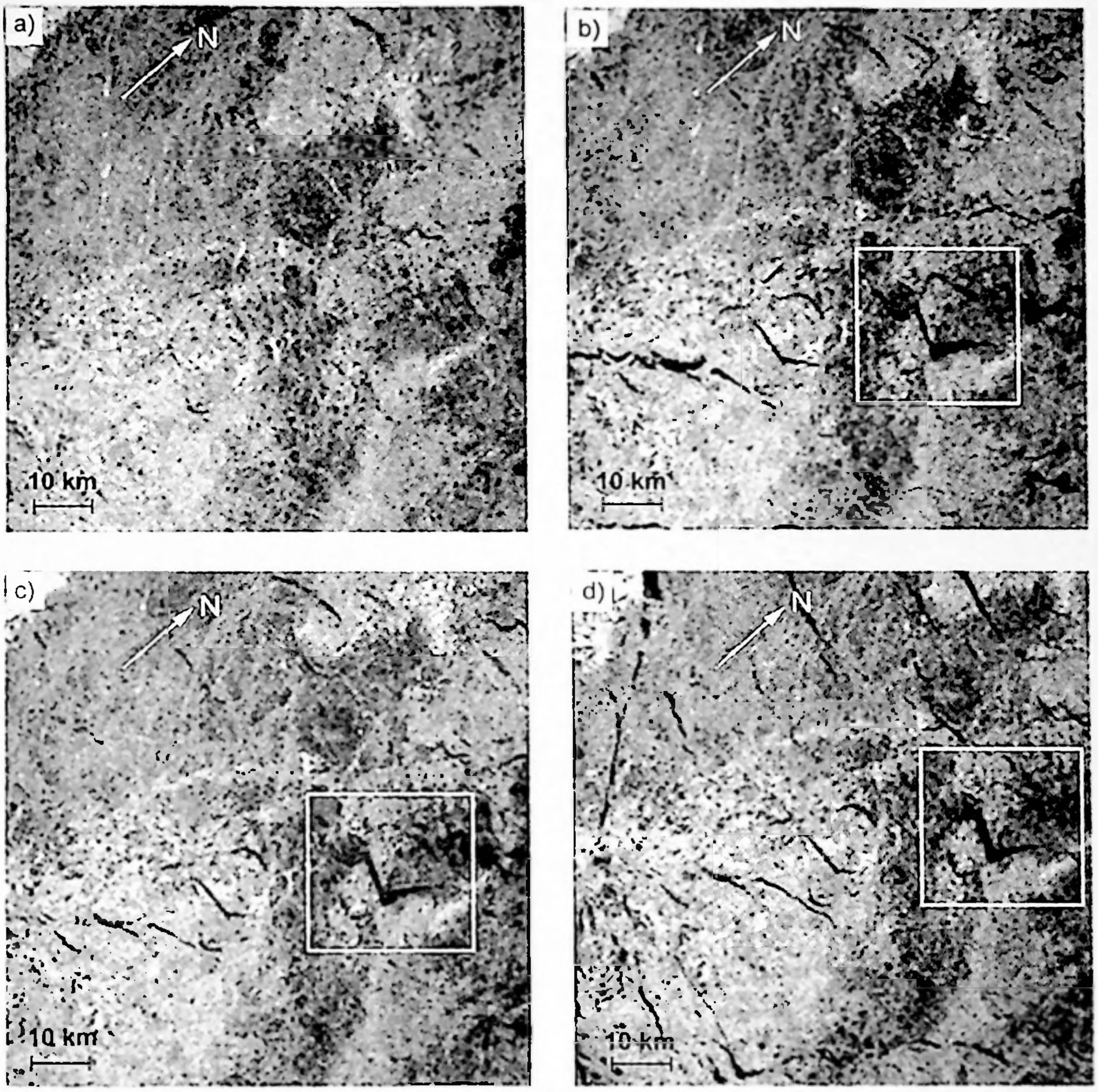


**Figure 6.12.** Formation of a wing-crack lead in first-year ice, on (a) - 15$^{th}$, (b) - 18$^{th}$, (c) - 21$^{st}$, (d) - 24$^{th}$ February 1994, Kara Sea, approx. 75° N and 70°E. SAR ERS-1 images Copyright European Space Agency - ESA) obtained from Earthnet Online Internet Server Catalogue.

Another example of possible wing crack formation on the geophysical scale was described in Schulson and Hibler (1991) (Fig. 6.10). The lead, presumably a wing crack, had a length of about 100 km with the wings extended for about 40 km. Following equations (6.1) and (6.2), the far field uniaxial stress needed to create the observed feature is about 2-3 kPa.

There are uncertainties in the method described above. For example, the critical stress intensity factor $K_{IC}$, is usually taken as 0.1 MPa, but it could be three times higher, up to 0.3 MPa (Dempsey, personal communication). It will increase the critical stress up to 21 kPa for the 10 km long crack shown in Fig. 6.12 and up to 10 kPa for the 100 km long wing crack

(Fig. 6.10). Nevertheless, the order of magnitude of the stress can be judged with reasonable accuracy. These results will be addressed later in Chapter 7 in the context of scaling analysis for the critical stress.

Dr. Max Coon (personal communication) suggested a hypothesis which explains the nucleation of a wing crack in sea ice in the following way. Initially, randomly oriented microscopic surface cracks are formed due to thermally induced deformations in the ice cover. Under external loading some of these microcracks start growing, penetrate through the whole ice thickness, expand horizontally and eventually become macrocracks. The new network of macrocracks is characteristic of two preferential directions with an intersection angle depending on the ratio of principal components of the local stress field. Finally the weakened ice fails along the directions of maximal shear. This is a sufficient explanation for the nucleation mechanism of the wing crack, and does explain why the primary crack is almost always inclined to the direction of the main far-field compression (Fig. 6.11).

Following the same argument we can apply the analysis to other types of ice deformation structures. A system of arch–shaped leads has been occasionally observed in the northern Baltic Sea (Fig.6.13). The fracture appears in winter when a northerly wind is prevalent and it is caused by the uniaxial tension developed in the ice pack under the wind stress with a restriction of ice movement at the lateral boundaries (Goldstein et al., 1999). The occurrence of a similar type of arching has been reported in arctic straits and thought to be a feature of granular media behaviour (Sodhi, 1977; Tremblay and Mysak, 1997). The structures also have been fairly successfully modelled with the help of continuum ice models with different rheologies (Appel and Gudkovich, 1992; Tremblay and Mysak, 1997).

However, the arch–shaped leads in the Baltic differ significantly from those in the Arctic. Instead of being a single arch, each lead consists of several arches and has a cycloid shape (Fig. 6.13). Such a shape suggests that the failure has been controlled by restriction near the coast only to a limited extent but is mainly governed by the local stress state and by

a

b

**Figure 6.13.** Arch-shaped lead in first-year ice, Bay of Bothnia, March, 1997. a – aerial view (photograph by author); b – RADARSAT image (courtesy of Prof. Leppäranta).

mechanical properties of the ice. Presumably the arch begins to develop as a tensile fault oriented perpendicularly to the wind stress. It then undergoes further curving parallel to the tensile component of the regional stress field, adjusting the local stress to the global stress somewhat in the same manner as during the development of a wing crack. As one could guess the curvature of the arches and their size should depend on the ice strength and principal

[illegible]

[illegible]

components of the local stress in the vicinity of the lead. Another important fact about the arch–shaped leads in the Baltic is that they form echelons of parallel faults with nearly uniform spacing between each other (Fig. 6.13). This phenomenon cannot be explained from fracture mechanics alone. Introduction of the hydraulic resistance allows stopping the expansion of the crack, which in turn creates the possibility for the next parallel fault to develop. A solution of the momentum balance model combined with the kinetic theory of crack propagation on the assumption of the quasi-static regime in a viscous medium, gives a crack propagation velocity according to Goldstein et al. (1999) that is proportional to the crack length *l* as:

$$V \propto l^{-1/3} \qquad (6.3)$$

From equation (6.3) it is evident that as the crack grows longer its velocity decreases towards zero creating the conditions for the next fault to grow.

The next example came from a different spatial scale. The development of so-called "wave-like" buckling of thin ice under compression is a frequently observed feature during the deformation of newly-formed ice in a lead (Fig. 6.14).

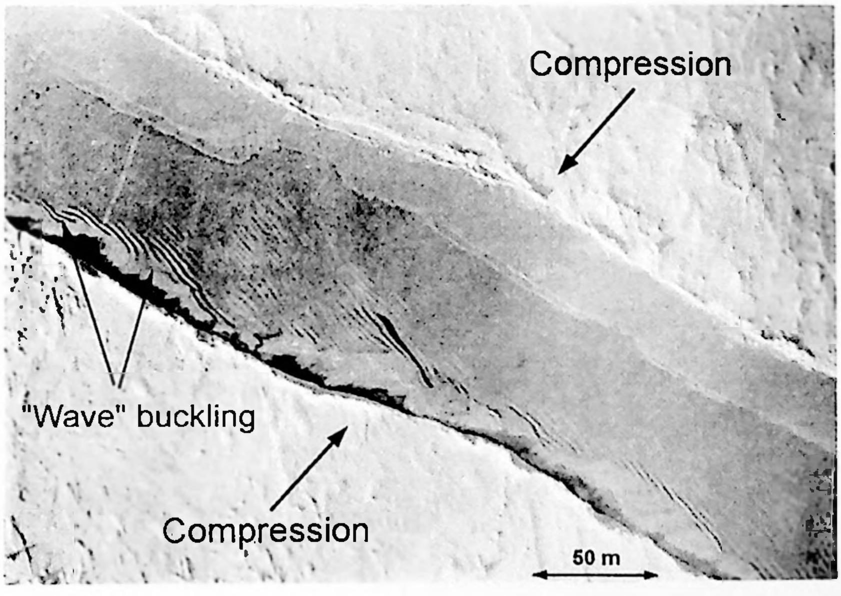


**Figure 6.14.** Buckling of grey ice in a lead (Borodachev et al., 1994, photograph 3)

From the picture the buckling wavelength $\lambda$ and width of deformation structure $W$ were estimated as 2-3 m and 40-50 m respectively. The mechanism of deformation implies that the buckling can start from elastic deformation or from creep. However, while buckling progresses the creep always overtakes elasticity. A typical strain rate for the transition between elastic and creep deformation is $3\times10^{-7}$ $s^{-1}$, which means that creep dominates when the loading time exceeds $10^5$ s (Sanderson, 1988). Because of the ambiguous rate and time of loading, both elastic (eq. 6.3a) and creep (eq. 6.3b) models describing the initial buckling of a finite width beam were applied (Kerr, 1978; Sanderson, 1988). The models consider lateral horizontal loading of an ice beam laying on an elastic foundation, resulting into out-of-plane (vertical) bending:

$$\frac{EI}{W\rho_w g}\cdot\frac{d^4w}{dx^4}+\frac{P}{W\rho_w g}\cdot\frac{d^2w}{dx^2}+w=0 \qquad (6.3a)$$

$$\frac{I}{WC\rho_w g}\cdot\frac{d^4\dot{w}}{dx^4}+\frac{P}{W\rho_w g}\cdot\frac{d^2w}{dx^2}+w=0 \qquad (6.3b)$$

where, $I=W\,h^3/12$ - second moment of inertia; $W$ - beam width; $h$ - ice thickness; $E$ - ice Young's modulus; $C$ - effective creep-rate compliance; $\rho_w$ - water density; $g$ - acceleration due to gravity; $P$ - external horizontal load; $w$ - vertical beam deflection; $x$ - horizontal co-ordinate.

The eigenvalue method applied to equations (6.3a,b) gives the following relation between the wavelength $\lambda_b$ and applied load $P$ for the both models:

$$\lambda_b = 2\pi\cdot\sqrt{\frac{P/W}{2\rho_w g}} \qquad (6.4)$$

where $\lambda_b$ can be calculated from:

$$\left(2\pi\lambda_b^{elast}\right)^4=\frac{EI}{\rho_w g} \qquad (6.5a)$$

[illegible]

$$\left(2\pi\lambda^{creep}{}_b\right)^4 = \frac{I}{C\rho_w g} \qquad (6.5b)$$

Taking an observed buckling width $W$=50 m, equation (6.5a) gives $\lambda_b^{elast}$≈5.6 m. Here, $E$=2 MPa, $\nu$=0.3, $g$=9.81 m/s$^2$, $\rho_w$=1028 kg/m$^3$. This leads to a loading force $P$=0.64 MPa (eq. 6.4) and stress $\sigma$=160 kPa for ice thickness $h$=0.1 m. The creep model gives almost the same values.

Because the calculated buckling wavelength appears to be higher than the observed value, the following model describing the buckling of a semi-infinite elastic plate was used to estimate the typical buckling stresses $\sigma$ (eq. 6.6):

$$\frac{Eh^3}{12(1-\nu^2)\rho_w g}\cdot\frac{d^4w}{dx^4}+\frac{P}{\rho_w g}\cdot\frac{d^2w}{dx^2}+w=0 \qquad (6.6)$$

where, $\nu$ - is Poisson's ratio.

The solution gives:

$$\sigma = 2\rho_w gh\left(\frac{\lambda_p}{2\pi}\right)^2 \qquad (6.7)$$

where,

$$\left(2\pi\lambda_p\right)^4 = \frac{Eh^3}{3\left(1-\nu^2\right)\rho_w g} \qquad (6.8)$$

and $\sigma$ - typical stress during buckling; $h$ - ice thickness.

Here, $\lambda_p$= 2.3 m, and it is closer to the observed value. For this wavelength typical stress $\sigma$ is 32 kPa.

### 6.1.4 Large scale ice fracture

As we saw from the examples described in the last section, the method based on the analysis of ice fracture signatures, although very useful, has one serious shortcoming. This method deals with ice deformation features when the ice failure has already occurred and does not allow us to see the dynamics of fracture, with exceptions in a few clear cases (Fig. 6.12). Another approach based on the automated analysis of Synthetic Aperture Radar (SAR) images has been developed in the Jet Propulsion Laboratory (Kwok and Cunningham, 1993) and initially implemented for the SEASAT and ERS-1 satellites at the Alaska SAR Facility (Kwok et al., 1990). The method is based on the earlier techniques of sea ice motion detection from SAR imagery (Curlander et al., 1985; Leberl et al., 1983) and detects the detailed ice motion field by matching the common ice features in sequences of SAR images (Figs. 6.15-6.17). In contrast to earlier developments, in addition to feature tracking the method also incorporates an area correlation technique which enables it to process large volume of data in an automatic regime (Kwok et al., 1990). Such an integrated approach makes the detection universally applicable for the coastal and marginal ice zones where the rotation of the ice floes is significant and the area correlation analysis can lead to erroneous results, as well as for the central ice pack areas where the translation component prevails in the ice motion and area-based tracking performs fairly well.

The image processing consists of several stages. At the first stage the reference image is chosen from a designated geographical location and the pair image to the reference one is selected with the help of a linear geostrophic ice drift model (Thorndike and Colony, 1982). In the next stage of processing the correspondence between common features in the reference and paired image is established and feature matching and area-based matching procedures are applied. For the internal ice pack area two-dimensional cross correlation between the intensities of the images is computed. Fast Fourier transformation is used in order to find the maxima in the correlation hypersurface and to derive translational and rotational parameters of the each sub–region of the image frame (Kwok et al., 1990). For the coastal regions and marginal ice zone an additional step which incorporates feature extraction and feature tracking is introduced. The extraction of the common features is based on the analysis of the image texture and image intensity and identification of the connected image areas (image regions). The boundaries of the regions are used for the feature matching and tracking. The

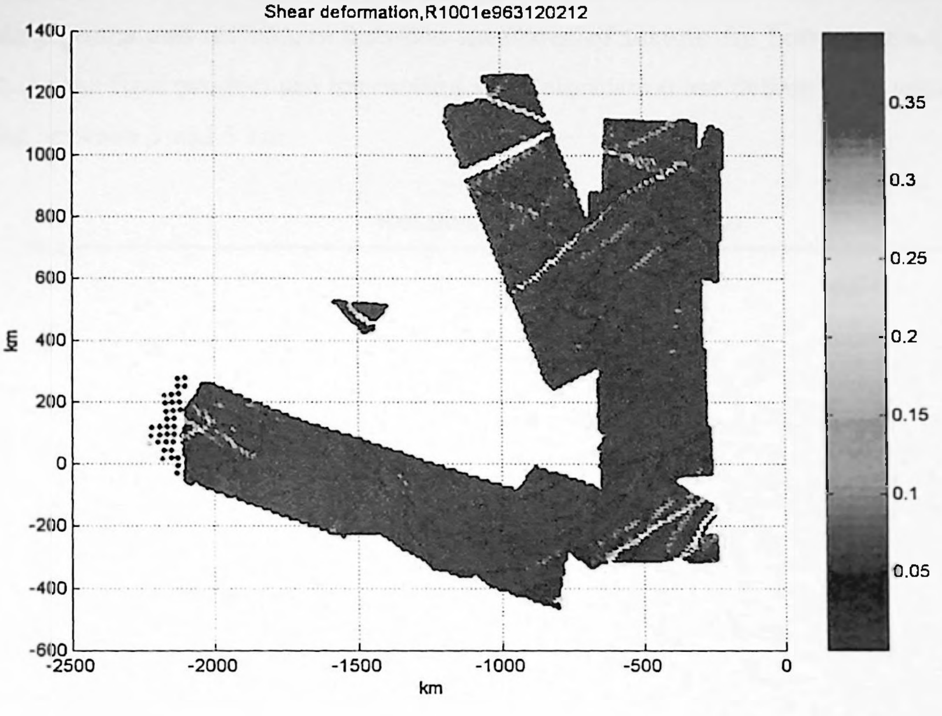


**Figure 6.15.** Ice shear in the central Arctic, November 1996. Initial data were obtained from RADARSAT Geophysical Processing System.

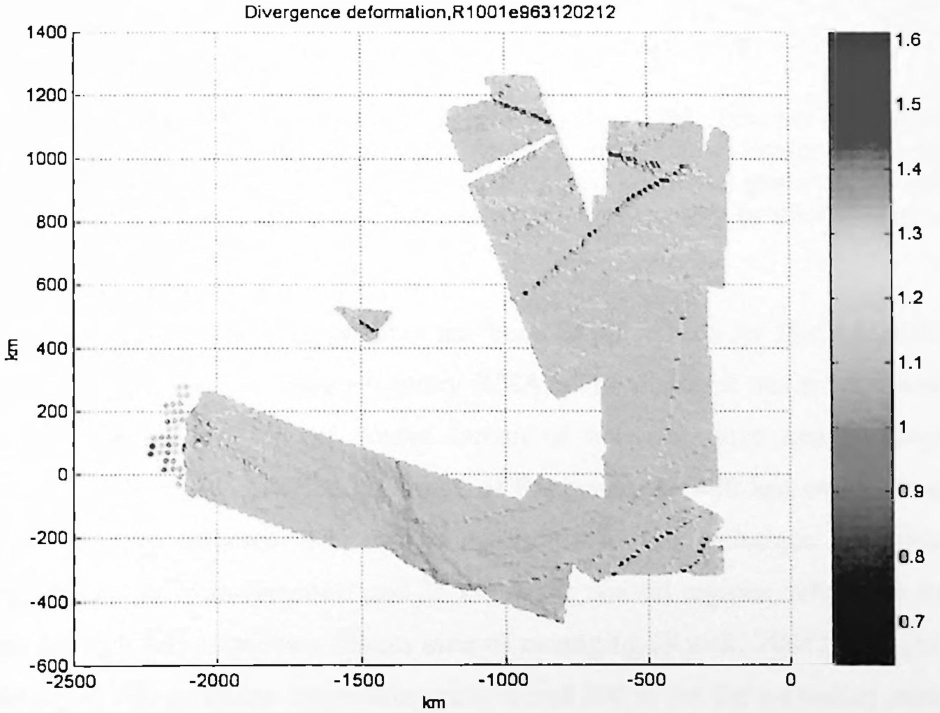


**Figure 6.16.** Ice divergence in the central Arctic, November 1996. Initial data were obtained from RADARSAT Geophysical Processing System.

tracking is performed via calculation of the displacement and rotation from the matched boundary points and difference between measures of texture for both images (Kwok et al., 1990). As the final product sea ice motion and deformation are defined on a regular grid with spacing between 3 and 5 km.

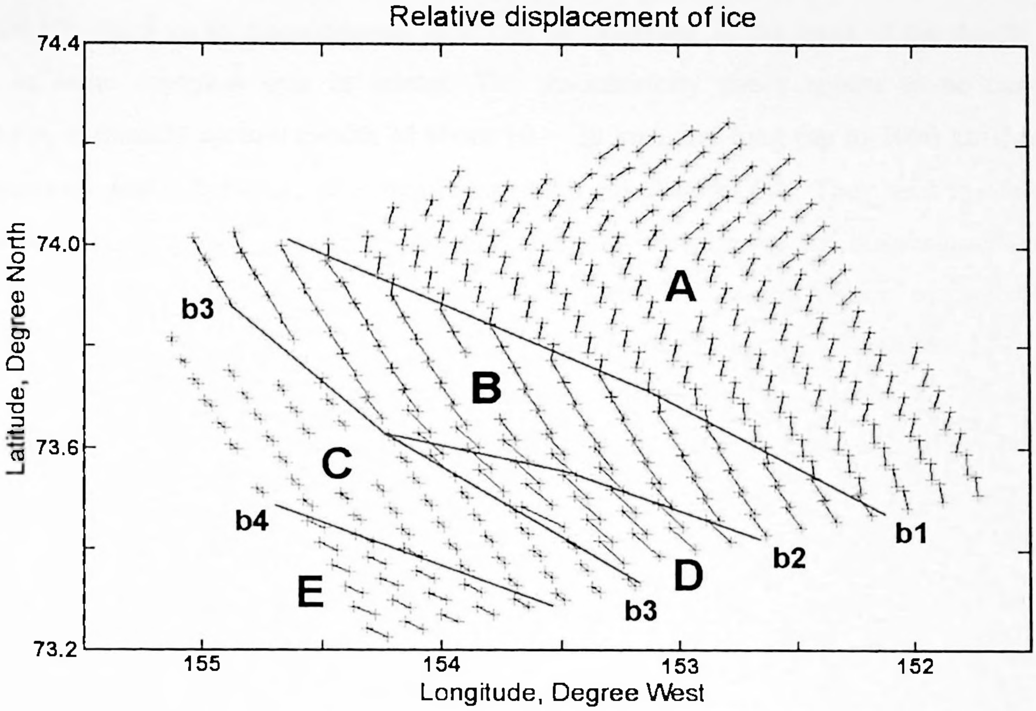


**Figure 6.17.** Relative displacement of ice in November 1993, Beaufort Sea. Displacement was calculated by the author using ice motion detected from ERS-1 imagery analysis (Geophysical Processor System). Light blue crosses depict starting points whereas green crosses correspond to the end points. Areas of the quasi-rigid ice motion (A – E) are separated by discontinuity zones (red lines b1 – b4).

The next generation of algorithms has been implemented for the RADARSAT platform managed by the Canadian Space Agency (CSA). The platform has a SAR sensor and has a repeat coverage period for the Arctic Ocean of between three and six days (Kwok and Cunningham, 1998). To provide coverage of the ocean the 460 km swath ScanSAR Wide B mode (SWB) was selected. The spatial resolution of this technique is limited by the grid spacing: 10 km far from the coast and 25 km in the coastal regions, where ice feature tracking is more difficult and requires a bigger area of averaging (Kwok, 2001). The absolute location uncertainty is 100 m for the descending passes and 200 m for the ascending ones. The random positioning error is approximately 50 m (Kwok and Cunningham, 1998).

[illegible]

[illegible]

[illegible]

[illegible]

As became evident from the early analysis of the ERS-1 and RADARSAT images the actual ice deformation fields are significantly different from what they were thought to be on the basis of observations and modelling (Overland et al., 1998). Instead of moving as a continuum with a smooth velocity field, the ice pack consists of areas which move as nearly rigid plates, separated by a kind of "boundary zone" where the ice drift is discontinuous (Figs. 6.15-6.17). Such rigid-discontinuous drift can be observed in the most of the Arctic Ocean and in some marginal seas in winter. The discontinuity zones appear to be curvilinear features, extremely narrow (width of about 10 – 20 km) and long (up to 1000 km), with the intersection angles between them nearly constant and close to 60°. They tend to cluster and apparently have a substructure. Figure 6.17 portrays the relative ice displacement (i.e. ice motion with subtracted average displacement of ice in the image frame) calculated from a SAR ERS-1 image. Because ice drift from the ERS-1 images has higher spatial resolution, the fine structure of the rigid plates (A, B, C, D, and E) and discontinuity zones (b1, b2, b3, b4) is clearly seen. The discontinuity zones shown in Fig. 6.17 are the discontinuities with lower spacing between each other depicted in Fig. 6.15. The components of the deformation tensor such as shear and divergence have significantly higher values in the discontinuity zones compare to the interior of the rigid plates (Figs. 6.15 and 6.16).

Comparison between the large scale deformations from RADARSAT and signatures of open leads from AVHRR and SSM/I sensors demonstrates that these structures coincide well (Overland et al., 1998). Rigid ice drift and zones of the drift discontinuity (sometime they are called "shear lines") derived from satellite imagery have been analysed along with concurrent observations on ice motion with the help of ice drifters. This cross-analysis showed that the majority of the deformation events are reflected in both type of measurements: deformation of buoy array and deformation obtained from the imagery (Goldstein et al., 1999; Sandven et al., 1999).

## 6.2 Modelling of ice deformation

Because of sparse data and complex relationships between deformation and ice stress on different spatial scales, modelling becomes a very powerful tool to investigate and reveal the underlying physical background of the ice deformation. The nature of the deformation field observed with the help of remote rensing or direct "on ice" measurements leads to the

conclusion that models which show a highly inhomogeneous and anisotropic deformation field are more suitable for the cross-scale analysis. We considered that the test modelling of the ice deformation process mainly on meso- and geophysical scales is aimed at a better understanding of the interaction of intermediate and large scale deformations (lead opening and closing, appearance of slip lines, dynamics of ice cover in general). Such a "simplified" modelling approach included the simulation of selected cases of ice pack deformations (for example rectangular or other simple domain), focusing on the spatial and temporal variability of the internal stress field. The results of the described approach could in future be included in a complex high-resolution coupled ice/ocean model. Originally the author intended to test several types of ice models which were based on different rheologies: a continuum model with viscous-plastic rheology, a continuum model with granular type rheology and a discrete element model (DEM), where the ice pack is represented by a set of floes. Unfortunately the granular type model with DEM architecture was not available for the project, and therefore our efforts were concentrated on analysis of two available models: a viscous-plastic anisotropic continuum model (Hibler and Schulson, 2000) and a granular model with dilatation rheology (Tremblay and Mysak, 1997).

### 6.2.1 Anisotropic continuum model

The main part of the modelling efforts was focused on numerical experiments with the help of an anisotropic continuum model (Hibler and Schulson, 2000). The recent version of the code developed by W. D. Hibler was in use with some alterations (Aksenov and Hibler, 2001). Conceptually following Coon et al. (1998) the model simulates two categories the ice: isotropic ice pack and anisotropic thin ice – lead with the orientation $\vartheta$ (Fig. 6.18a). The thin and thick ice are taken to follow an isotropic viscous-plastic rheology with a modified Coulombic rheology (Fig. 6.18b). The viscous portion of this rheology is adjusted (see Hibler and Schulson, 2000) so that for all strain rates the mechanical energy is dissipative.

The stress strain relationship for this composite may be derived from conservation of the overall strain field and stress continuity across the common thin ice/thick ice surface. The thin ice is considered to have an area A, and the strain rates and stresses are denoted by primed values $\dot{\varepsilon}'_{x'x'}$, $\dot{\varepsilon}'_{y'y'}$, $\dot{\varepsilon}'_{x'y'}$, $\sigma'_{x'x'}$, $\sigma'_{x'y'}$ in the thin ice and unprimed values $\dot{\varepsilon}_{x'x'}$, $\dot{\varepsilon}_{y'y'}$, $\dot{\varepsilon}_{x'y'}$, $\sigma_{x'x'}$, $\sigma_{x'y'}$ in the thick ice. Assuming uniform displacement at the boundaries, the strain rate

[illegible]

[illegible]

[illegible]

[illegible]

[illegible]

component $\dot{\varepsilon}_{y'y'}$ is taken to have the same value in both the lead and thick ice. The other strain rate components are in general different in the thin and thick ice but according to Green's theorem have areal weighted sums equal to the composite values denoted by a superscript zero $\dot{\varepsilon}^{o}_{x'x'}$, $\dot{\varepsilon}^{o}_{x'y'}$, $\dot{\varepsilon}^{o}_{y'y'}$, (eqs. 6.9a and 6.9b). Equations (6.9c) and (6.9d) describe the continuity of the stresses at the interface between the thick and thin ice.

$$\dot{\varepsilon}'_{x'x'}A+(1-A)\dot{\varepsilon}_{x'x'}=\dot{\varepsilon}^{o}_{x'x'} \quad (6.9a) \qquad \sigma'_{x'x'}=\sigma_{x'x'} \quad (6.9c)$$

$$\dot{\varepsilon}'_{x'y'}A+(1-A)\dot{\varepsilon}_{x'y'}=\dot{\varepsilon}^{o}_{x'y'} \quad (6.9b) \qquad \sigma'_{x'y'}=\sigma_{x'y'} \quad (6.9d)$$

These equations may be expressed in terms of the thin or thick ice strain rates using the viscous plastic constitutive equation for the yield surface in Fig. 6.18b. This gives us four nonlinear equations with four unknowns: the shear and compressive strain rates in the thick and thin ice. The equations may be solved numerically (Hibler and Schulson, 2000) by specifying an external strain rate for the whole composite system and then iterating the system until a plastic equilibrium is obtained.

In order to obtain deformation and stress fields similar to the ones observed for the Arctic pack ice 54 numerical experiments were performed. Some results of the experiments can be found in Aksenov and Hibler (2001) but here we give a more detailed analysis. The basic concept of the experiments was to study the structure of the deformation field depending on key model parameters such as domain size, ice strength and viscosity, number and orientation of leads. The second task was to investigate the response of the deformation and stresses to the different external forcing. Table 6.1 lists the set of experiments.

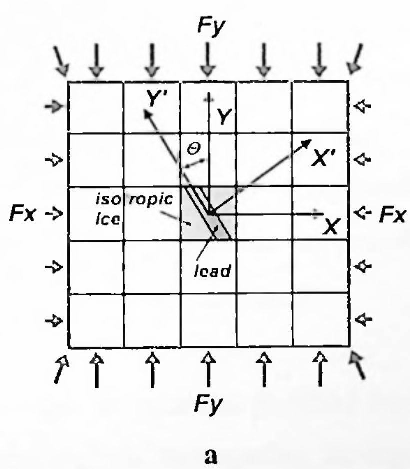


a

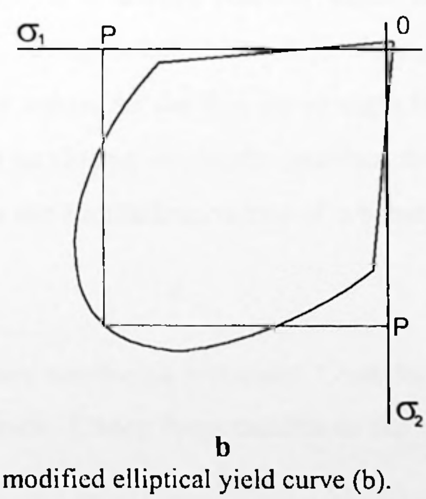


b

**Figure 6.18.** Model geometry (a) and a modified elliptical yield curve (b).

The tests fell into three major groups. The first one contains the tests, which have several layouts of leads. During these test we simulated the four following configurations of leads:

- Isolated leads (from one to four), when the distance between neighbouring leads is large enough not to distort the stress field in their vicinity;
- Grid of leads, when they are close enough to distort the stress field;
- A random positioning of leads in the domain, a large number of leads were placed as a rule;
- Leads located in every domain cell.

The second group of simulations included a test with the secondary bulk viscosity of ice cover. The parameterisation for the secondary bulk viscosity (eq. 6.10) was suggested by Hibler (personal communication). This approach allowed the model to be stable during the viscous/plastic transition when the sharp decrease of the viscosity occurs.

$$\zeta = \frac{P_{lead}}{\left(2\cdot\sqrt{\Delta}+2\cdot 10^{-6}\right)} + P_{lead}\cdot 4\cdot 10^{-7} \tag{6.10}$$

The third group of tests dealt with the decrease/increase of thin ice strength due to opening/closing of the lead. The following relationship between lead opening $\varepsilon_{xx}^{lead}$ and its strength $P_{lead}^{t}$ was introduced via a time iterative procedure:

$$P_{lead}^{t=1} = P_{lead}^{t} \cdot \left(1 + b - \frac{a \cdot \dot{\varepsilon}_{xx}^{lead} \cdot \Delta t}{4 \cdot 10^{5}}\right) \tag{6.11}$$

Here coefficients $a$ and $b$ are empirical constants; $a$ is always positive which reflects the weakening of the lead when it is opening and strengthening when it is closing; when $b$ introduces the offset. $P_{lead}^{t}$ and $P_{lead}^{t+1}$ – are the values for the thin ice strength for the time $t$ and $t+1$ respectively. Lead strengthening during its closing implicitly describes the cohesion of the lead because of the thin ice growth. During the simulations values of $a$ between $1.1\cdot 10^{6}$ and $1.1\cdot 10^{8}$ with $b$ =0 were used.

The value for $a$ can be justified from a fracture mechanics argument. Consider a lead (or crack) opening and propagating through the domain. Under these conditions the strength of

[illegible]

[illegible]
[illegible]

[illegible]
[illegible]
[illegible]
[illegible]
[illegible]
[illegible]

[illegible]
[illegible]
[illegible]
[illegible]

[illegible]
[illegible]
[illegible]

$$[illegible]$$

[illegible]
[illegible]
[illegible]
[illegible]
[illegible]
[illegible]

[illegible]
[illegible]

the crack $P^*$ is order of the critical stress $\sigma_{Ic}$ sufficient to expand the crack. Similarly to equation (6.1) the strength of the crack can be expressed in the following way:

$$P^* \propto \sigma_{1c} = K_{1C} \frac{\sqrt{3} \cdot \left(l/a^2\right)^{1/2}}{0.4 \cdot \sqrt{\pi} \cdot (1-\mu)} \qquad (6.12)$$

where: $K_{IC}$ - critical stress intensity factor; $a$ - half-length of the primary crack; $l$ - length of the crack expansion ( $l>>a$); $\mu$ - friction coefficient of crack interfaces. Choice of the parameters $K_{IC} = 0.1$ MPa/m$^{1/2}$ (Shulson et. al., 1991), $\mu = 0.3$, $l/a \sim 10^2$, and $\chi = l/\varepsilon \sim 10^4$ ($\varepsilon$ - crack opening) leads to $P^* \sim 3.4 \cdot 10^5 \cdot \sqrt[-2]{\varepsilon}$ which is in its turn gives $P^* \sim 1\text{-}1.7 \cdot 10^5 \cdot \varepsilon$ using the first two components of the Taylor's expansion. One can find that this figure is reasonably close to the upper limit of the empirical proportionality coefficient $k = a \cdot P_{lead}^{0} / 4 \cdot 10^5 = 2.5 \cdot 10^5$ in equation (6.11).

For each combination of the parameters simulations with model domains 40x40 cells and 100x100 cells were performed.

The main result is that the model as well as the observations exhibit a highly non-uniform character of the deformation field. Because the model was forced with constant stress on the boundaries it was impossible to estimate the temporal evolution of the deformation field, therefore only the spatial variability was under consideration.

Depending on the experimental layout the simulation produces several patterns of fracture. A few leads separate in such a way that they do not produce a serious stress field distortion but generate a regular pattern of leads (Figs. 6.19 and 6.20; Table 6.1: Tests 14, 22). The intersection angle between leads is consistent with an analytical solution of the generalised friction model (Hibler and Schulson, 2000). In the case shown in Fig. 6.19 the angle is about 60°. The pattern was frequently observed on both the geophysical and laboratory scale (Kwok, 2001; Schulson, 2001; Sodhi, 1977). Figure 6.19 portrays the bulk viscosity which becomes low when the stress state lies on the yield curve and the flow is plastic. Therefore this parameter is a good indicator of damage development inside the domain.

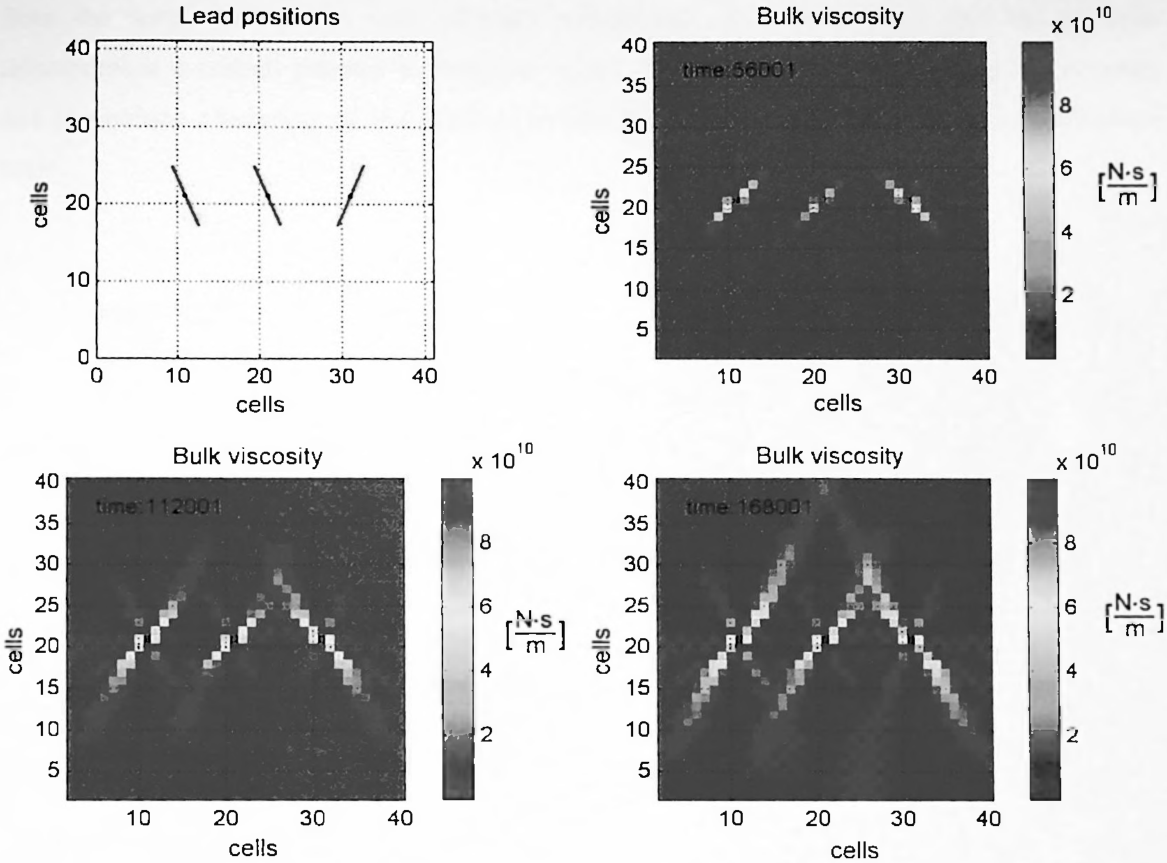


**Figure 6.19.** Formation of leads in pack ice on geophysical scale. Positions of leads (upper left) and evolution of bulk viscosity field are shown. (Table 1, Test 22).

The second type of damage pattern occurs when there are several closely located leads. Such a layout results in interaction of the stress fields generated by neighbouring leads and initiates the propagation of damage towards the nearest lead (Fig. 6.20, Test 14 in Table 6.1). This process co-exists with propagation with the intersection angle depending on the confinement ratio. The leads which have a preferred orientation for a given confinement ratio start to develop first. It was found from the experiments that areas with high deformation rates coincide well with the fault lines. Maximal shear and tensile stresses form clusters: "stress chains", when compressive stress concentrates in the "supporting" columns aligned to the direction of main load. When the distance between adjacent leads reduces even more, the damage clusters become less pronounced but are nevertheless still recognisable.

Patterns of localised damage were produced when randomly oriented leads were placed in every cell of the model domain and weakening of the active leads together with accretion

[illegible]

[illegible]

[illegible]

of the closing leads were introduced in the code (Fig. 6.21). The results are quite different from the tests without the lead strength adjustment. It was revealed that the strength adjustment is a crucial process to suppress small in-active cracks, to propagate active ones, and to produce clustering of the damage in the sea ice "sample" on local and geophysical scale.

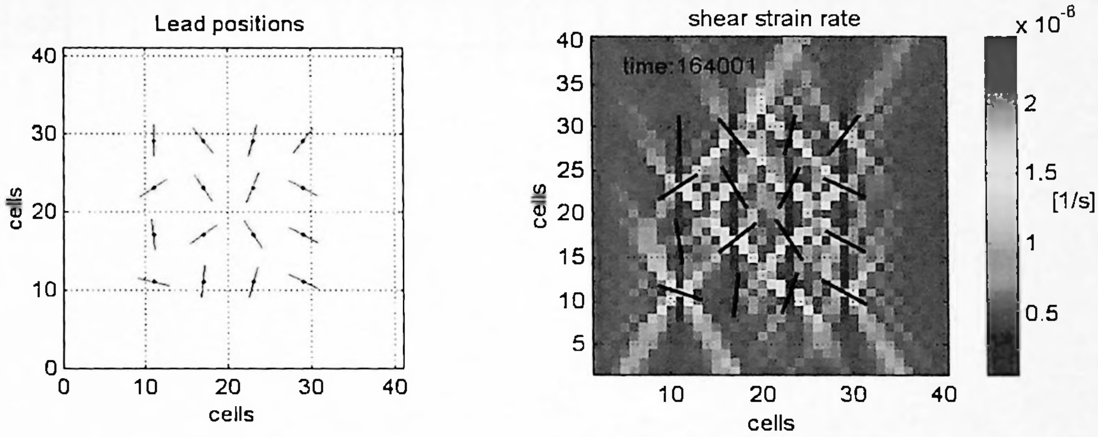


a b

**Figure 6.20.** Formation of leads in pack ice on geophysical scale. Positions of leads (a) and evolution of shear strain rate field (b) are shown. (Table 1, Test 14).

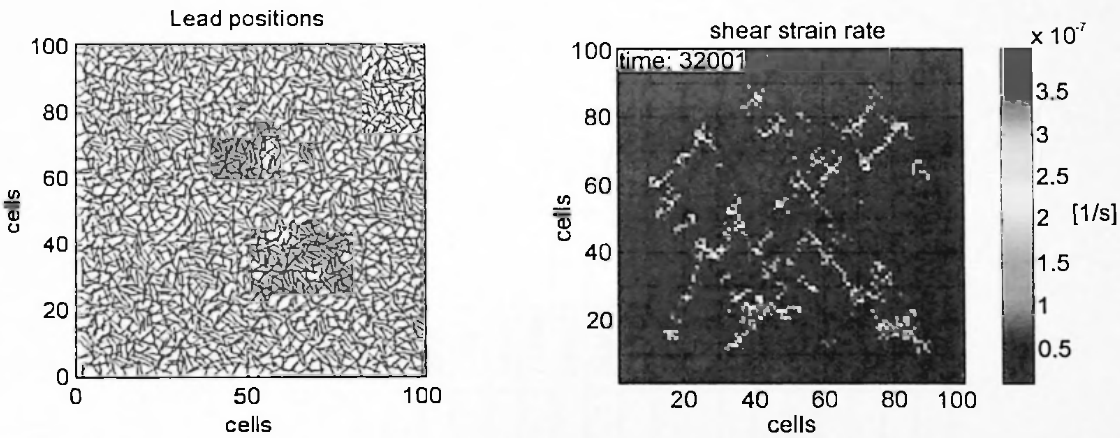


a b

**Figure 6.21.** Formation of leads in pack ice on geophysical scale. Positions of leads (a) and evolution of shear strain rate field (b) are shown. (Table 1, Test 55).

**Table 6.1.** List of numerical experiments performed for the fully anisotropic model.

| Test | Parameters of the simulation | | | | | | | | | |
|---|---|---|---|---|---|---|---|---|---|---|
| | Set up | | Leads | | | Boundary force | | Ice Strength | | |
| | Domain Size | Time [steps] | Numb | Located | Orientation [θ°] | Fby Along Y | Confin. Ratio | $p_1$ N/m | $p_2$ N/m | $P^*$ N/m |
| 1 | 100×100 | 174001 | 1 | Centre | +22 | 0.695 | 0.02 | 1e5 | — | 1e3 |
| 2 | 40×40 | 174001 | 1 | Centre | +22 | 0.695 | 0.02 | 1e5 | — | 1e3 |
| 3 | 100×100 | 174001 | 9801 | 99×99 Area | Random | 0.695/10 | 0.02 | 1e5 | — | 1e3 |
| 4 | 100×100 | 1312001 | 9801 | 99×99 Area | Random | 0.695/70 | 0.02 | 1e5 | — | 1e3 |
| 5 | 100×100 | 656001 | 9801 | 99×99 Area | Random | 0.695/100 | 0.02 | 1e5 | — | 1e3 |
| 6 | 100×100 | 348001 | 1 | Centre | +22 | 0.695 | 0.02 | 1e5 | — | 1e3 |
| 7 | 40×40 | 174001 | 1 | Centre | +22 | 0.695 | 0.02 | 1e5 | — | 1e3 |
| 8 | 40×40 | 174001 | 1 | Centre | +22 | 0.695 | 0.02 | 1e5 | — | 1e3 |
| 9 | 100×100 | 656001 | 1 | Centre | +22 | 0.695 | 0.02 | 1e5 | — | 1e3 |
| 10 | 40×40 | 100001 | 16 | 4x4 Grid | +22 | 0.695 | 0.02 | 1e5 | — | 1e3 |
| 11 | 40×40 | 80001 | 16 | 4x4 Grid | 0:1° random | 0.695 | 0.02 | 1e5 | — | 1e3 |
| 12 | 100×100 | 174001 | 16 | 4x4 Grid | +22 | 0.695 | 0.02 | 1e5 | — | 1e3 |
| 13 | 40×40 | 348001 | 16 | 4x4 Grid | 0:1° random | 0.695 | 0.02 | 1e5 | — | 1e3 |
| 14 | 40×40 | 174001 | 16 | 4x4 Grid | Random | 0.695 | 0.02 | 1e5 | — | 1e3 |
| 15 | 100×100 | 656001 | 1600 | 80×80Frame | Rand multpl | 0.695 | 0.02 | 1e5 | — | 1e3 |
| 16 | 100×100 | 348001 | 1398 | 80×80Frame | Random | 0.695/2 | 0.02 | 1e5 | — | 1e3 |
| 17 | 40×40 | 174001 | 16 | 4x4 Grid | +40 | 0.695 | 0.02 | 1e5 | — | 1e3 |
| 18 | 100×100 | 174001 | 6562 | 80×80 Area | Random | 0.695 | 0.02 | 1e5 | — | 1e3 |
| 19 | 100×100 | 16001 | 6562 | 80×80 Area | Random | 0.695 | 0.02 | 1e5 | — | 1e3 |
| 20 | 100×100 | 656001 | 6562 | 80×80 Area | Random | 0.695 | 0.02 | 1e5 | — | 1e3 |
| 21 | 40×40 | 174001 | 1 | Centre | +22 | 0.695 | 0.02 | 1e5 | — | 1e3 |
| 22 | 40×40 | 174001 | 3 | Central line | +22+22-22 | 0.695 | 0.02 | 1e5 | — | 1e3 |
| 23 | 100×100 | 174001 | 4 | Upper quart. | +22; −22 | 0.695 | 0.02 | 1e5 | — | 1e3 |
| 24 | 40×40 | 2624001 | 1521 | 39×39 Area | Random | 0.695/100 | 0.02 | 1e5 | — | 1e3 |
| 25 | 40×40 | 820001 | 1521 | 39×39 Area | Random | 0.695/50 | 0.02 | 1e5 | — | 1e3 |
| 26 | 40×40 | 2624001 | 1521 | 39×39 Area | Random | 0.695/70 | 0.02 | 1e5 | — | 1e3 |

**Table 6.1.** List of numerical experiments performed for the fully an-isotropic model (continued).

| | | | | | | | | | | |
|---|---|---|---|---|---|---|---|---|---|---|
| 27 | 100×100 | 174001 | 2 | Central line | +22; -22 | 0.695/10 | 0.02 | 1e5 | — | 1e3 |
| 28 | 100×100 | 174001 | 2 | Central line | +22; -22 | 0.695*10 | 0.02 | 1e5 | — | 1e3 |
| 29 | 100×100 | 174001 | 2 | Central line | +22; -22 | 0.695 | 0.02 | 1e5 | — | 1e3 |
| 30 | 100×100 | 656001 | 2 | Central line | +22; -22 | 0.695 | 0.02 | 1e5 | — | 1e3 |
| 31 | 100×100 | 174001 | 1 | Centre | +22 | 0.695 | 0.02 | 1e5 | — | 1e5 |
| 32 | 40x40 | 1312001 | 1521 | 39x39 Area | Random | 0.695/100 | 0.02 | 1e5 | — | 1e3 |
| 33 | 100×100 | 1312001 | 1 | Centre | +22 | 0.695 | 0.02 | 1e5 | — | 1e3 |
| 34 | 100×100 | 16001 | 1 | Centre | +22 | 0.695 | 0.02 | 1e5 | — | 1e5 |
| 35 | 40x40 | 174001 | 841 | 29x29Frame | Random | 0.695 | 0.02 | 1e5 | — | 1e3 |
| 36 | 40x40 | 1312001 | 1521 | 39x39 Area | Random +22 | 0.695/100 | 0.02 | 1e5 | 1e3 | $10^{+}$ |
| 37 | 40x40 | 1312001 | 1521 | 39x39 Area | Random +22 | 0.695/70 | 0.02 | 1e5 | 1e3 | $10^{+}$ |
| 38 | 40x40 | 2624001 | 1521 | 39x39 Area | Rand (Vis) | 0.695/50 | 0.02 | 1e5 | — | 1e3 |
| 39 | 40x40 | 1312001 | 1521 | 39x39Frame | Random +22 | 0.695/10 | 0.02 | 1e5 | 1e3 | $10^{+}$ |
| 40 | 40x40 | 1312001 | 1521 | 39x39 Area | Random +22 | 0.695/5 | 0.02 | 1e5 | 2e3 | $10^{+}$ |
| 41 | 40x40 | 348001 | 1521 | 39x39 Area | Random +22 | 0.695/50 | 0.02 | 1e5 | 1e3 | $10^{+}$ |
| 42 | 40x40 | 24000 | 1521 | 39x39 Area | Random +22 | 0.695/20 | 0.02 | 1e5 | 1e3 | $10^{+}$ |
| 43 | 40x40 | 348001 | 1521 | 39x39 Area | Random +22 | 0.695 | 0.02 | 1e5 | 1e5 | $10^{+}$ |
| 44 | 40x40 | 348001 | 1521 | 39x39 Area | Random +22 | 0.695 | 0.02 | 1e5 | 1e5 | $10^{+}$ |
| 45 | 40x40 | 348001 | 1521 | 39x39 Area | Random +22 | 0.695/60 | 0.02 | 1e5 | 1e5 | $10^{+}$ |
| 46 | 100×100 | 174001 | 2 | Central line | +22; -22 | 0.695/10 | 0.02 | 1e5 | — | 1e5 |
| 47 | 100×100 | 174001 | 2 | Central line | +22; -22 | 0.695*10 | 0.02 | 1e5 | — | 1e5 |
| 48 | 100×100 | 174001 | 2 | Central line | +22; -22 | 0.695 | 0.02 | 1e5 | — | 1e5 |
| 49 | 100×100 | 656001 | 2 | Central line | +22; -22 | 0.695 | 0.02 | 1e5 | — | 1e5 |
| 50 | 100×100 | 174001 | 1 | Centre | +22 | 0.695 | 0.02 | 1e5 | — | 1e5 |
| 51 | 40x40 | 1312001 | 1521 | 39x39Area | Random | 0.695/100 | 0.02 | 1e5 | 2e3 | — |
| 52 | 100×100 | 1312001 | 1 | Centre | +22 | 0.695 | 0.02 | 1e5 | — | 1e3 |
| 53 | 100×100 | 16001 | 1 | Centre | +22 | 0.695 | 0.02 | 1e5 | — | 1e5 |
| 54 | 40x40 | 174001 | 841 | 29x29Frame | Random | 0.695 | 0.02 | 1e5 | — | 1e5 |

The experiment carried out with the use of this anisotropic model can be associated with the ice deformation on the both laboratory and geophysical scales. A qualitative comparison between patterns of damage in laboratory samples, field experiments and from simulations demonstrated striking similarities (Kwok, 2001; Schulson, 2001). This presumes a universal behaviour of ice mechanics laws in the wide range of scales. This coincides well with the ideas introduced in section 7.2. However, there are some differences; for example, the experiment with a few cracks located close to each other (Fig. 6.20) gives a different pattern of cracks compared to those from the laboratory test performed by Nemat-Nasser and Horii (1982). The model results are somewhat closer to the lead patterns observed in the geophysical pack ice. The author believes that the dissimilarity is the result of the breaking down of universal scaling when the spatial scale approaches the size of ice grain (in the laboratory tests this scale is a distance between the neighbouring cracks). As was discussed previously, the weakening/hardening procedure of the geophysical ice is necessary to keep simulations stable and closer to the observed pattern. On the whole, it can be concluded that the inclusion of the anisotropic ice in to the model enables us to simulate intersecting damage patterns similar to those observed on the both laboratory and geophysical scales.

### 6.2.2 Granular model with the dilatation effect

By courtesy of Dr. B. Tremblay (Lamont Doherty Earth Observatory) we were able to use a version of the granular continuum model for the analysis as well. The model had a rectangular domain of 100x100 grid cells with the possibility of including "islands". The model employs a continuum viscous-plastic rheology with a dilatation effect, reflecting the tendency of the granular media to produce opening during shear deformation. The model uses Coulomb's friction law to derive a failure criterion (Tremblay and Mysak, 1997).

The model was forced by surface wind with a direction from the upper domain boundary towards the lower one. In order to derive the small-scale variability of the deformation field and the effect of the coastline seven numerical tests with different configuration of the model domain were performed (Table 6.2). The simulations showed that despite the fact that the deformation fields are still quite smooth the spatial structure of the simulated deformations is reasonably close to the average ones observed in nature (Fig. 6.22).

[illegible]

[illegible]

[illegible]

[illegible]

[illegible]

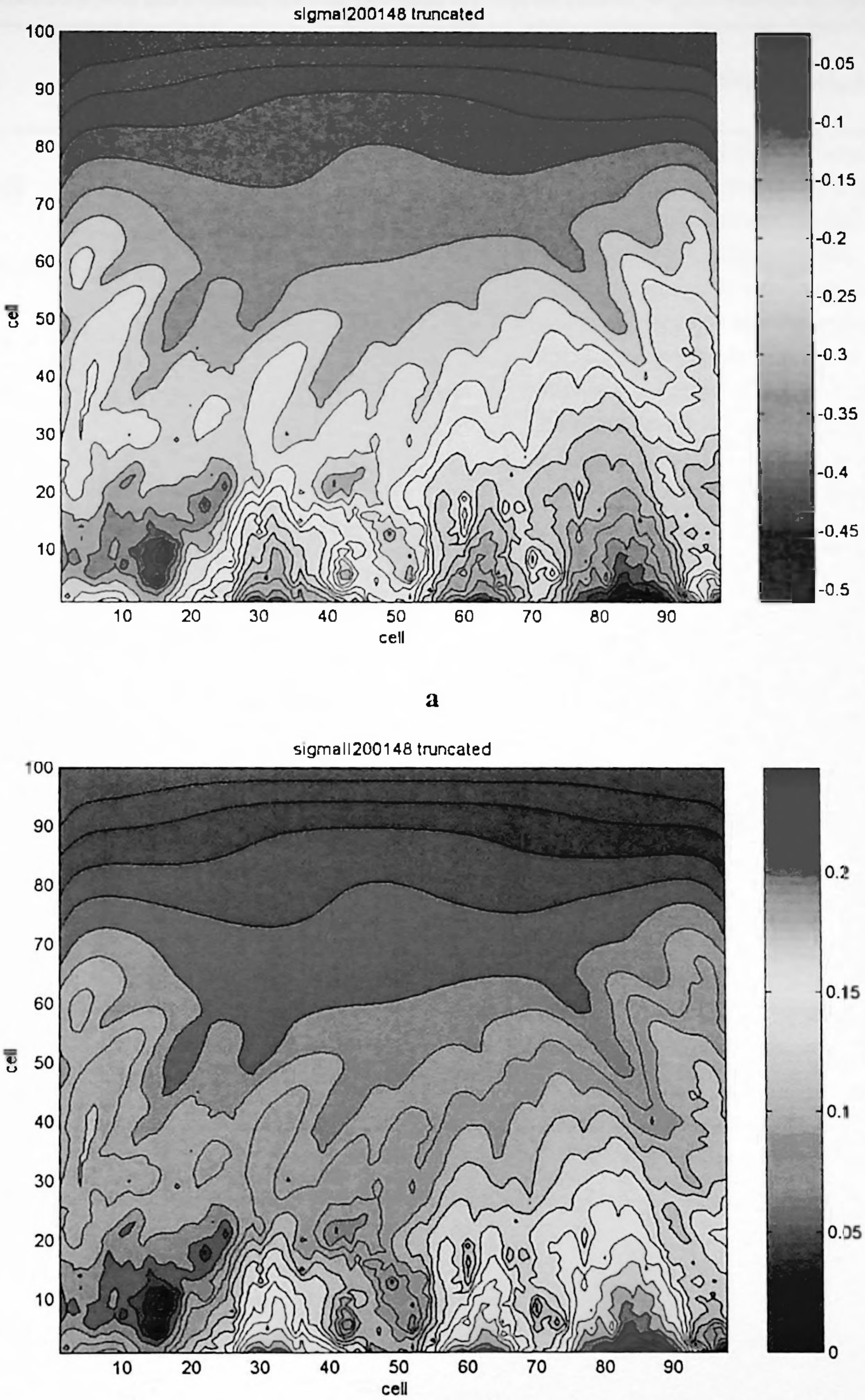


a

b

**Figure 6.22.** Principal components of the stress tensor from Test 5 (Well). (a) – major stress and (b) – minor stress. Negative sign corresponds to compression.

**Table 6.2.** Numerical test performed for the granular dilatation model with different model domains.

| Test | Domain configuration | Stress field structure |
|---|---|---|
| 1. Channel | Coasts at the side boundaries of the domain. | Smooth maximum of both tensile and compressive component with overall compression appears at the left boundary because of the Coriolis effect. |
| 2. Hopper | Coasts at the side boundaries. Narrowed section in the centre of channel. | Smooth large-scale maximum of both tensile and compressive component with overall compression appears at the left boundary because of the Coriolis effect. The large-scale variation is complemented by high fine-scale compression area upwind of the coastline indent. |
| 3. Well | Coasts at the side and lower boundaries. | Slight increase of the stress towards the right boundary of the domain. Compressive and tensile zones are concentrated in several areas near the lower boundary of the domain. They tend to cluster in the elongated features which grow upwind in a radial manner. |
| 4. Half-well | Coasts at the right side and lower boundaries. | Increase of the stress towards the right boundary of the domain. Compressive and tensile zones are concentrated in several areas near the lower boundary of the domain. They tend to cluster and propagate upwind. |
| 5. Islands | Coasts at the side and lower boundaries. Narrowed section in the centre of channel. Two islands: in the domain. | Compression zones appear upwind of the islands and coastal indentations. Same features produce tensile zones downwind. |

# Chapter 7. Discussion. Deformation of the sea ice cover across the range of scales

## 7.1 Ice stress and strain as non-stationary time series with scaling behaviour

### 7.1.1 Statistical moments

The majority of ice deformation data is collected as a time series. The reason for this is that it is expensive to cover a large area by deformation gauges installed close to each other. Arrays of drifting buoys give a better temporal than spatial resolution ($\Delta t_{min}$~ 20 min, $\Delta x_{min}$~ 10 km) (description of ice deformation measurements based on the analysis of tracks of ARGOS and GPS buoys can be found in several papers, for instance, Thorndike (1986)). Measurements of local deformations are usually carried out with a resolution of about 100 m, but the areal coverage is poor (Wadhams and Wells, 1995). Therefore, to study small-scale variations of sea ice deformations we need to establish relationships between temporal and spatial statistics of the deformation field.

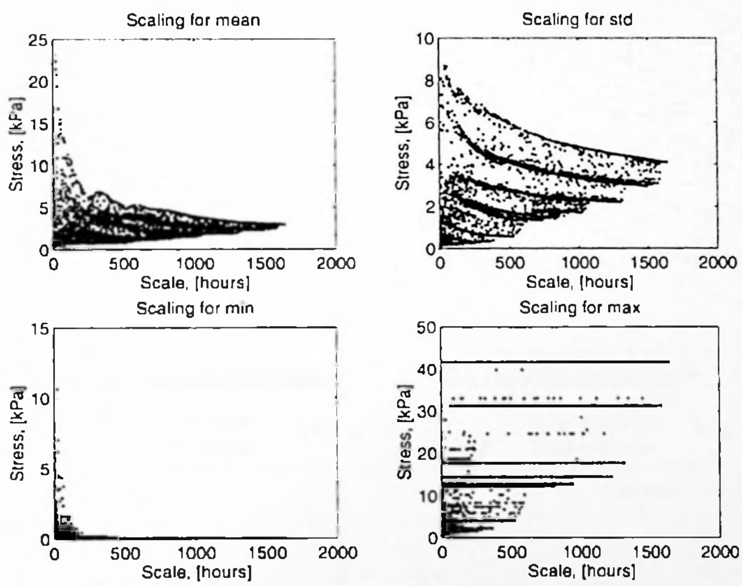


**Figure7.1.** Non-stationary behaviour of the shear stress statistics. Scatter plot for mean, standard deviation, minimum and maximum for the stress; Harbour Site, SIMI, Beaufort Sea, 1993.

The shear stresses exhibit non-stationary behaviour: their statistical moments vary for different subsections of the record (Fig. 7.1). These graphs were obtained in the following way: we calculated the mean, dispersion, maximum and minimum values ($M_0(T_0)$, $D_0(T_0)$, $Max_0(T_0)$, and $Min_0(T_0)$) for the stress time series with a length $T_0$. The subsection with a

## [illegible] 7. Discussion: Determination of the sex for [illegible] across the range of scales

[illegible]



[illegible]

length $T_1 < T_0$ was next chosen and the same statistics $M_1(T_1)$, $D_1(T_1)$, $Max_1(T_1)$, $Min_1(T_1)$ for the new length $T_1$ were re-computed. The process continues until the whole range of subsection lengths is covered. Figure 7.1 shows that the dispersion (scatter) of the mean and dispersion (scatter) of the dispersion increase as a subsection length (temporal scale) decreases. The upper and lower limits of the scatter of the mean are bounded by the power law envelope $\sim e^{\pm 0.5 \cdot T}$ (Fig. 7.2a). Hence, the extreme values of the average shear stress *scale* with time with exponents $k_{upper} \approx -0.5$ *and* $k_{lower} \approx 0.5$.

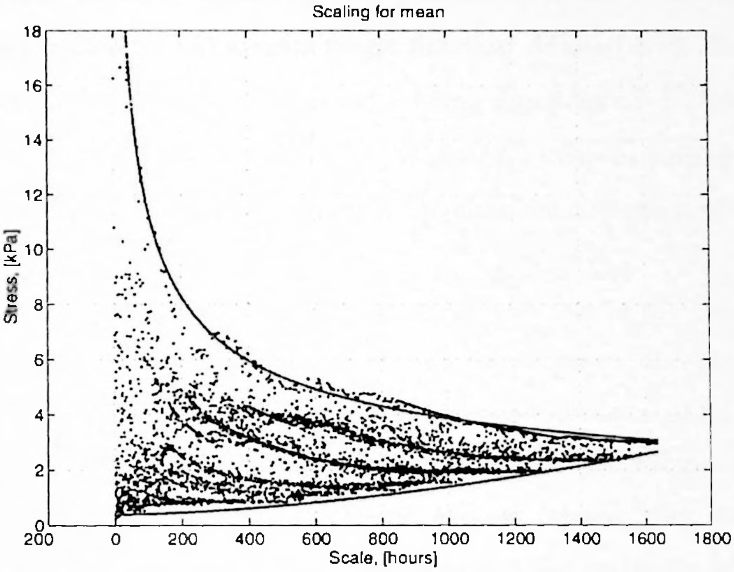


**a**

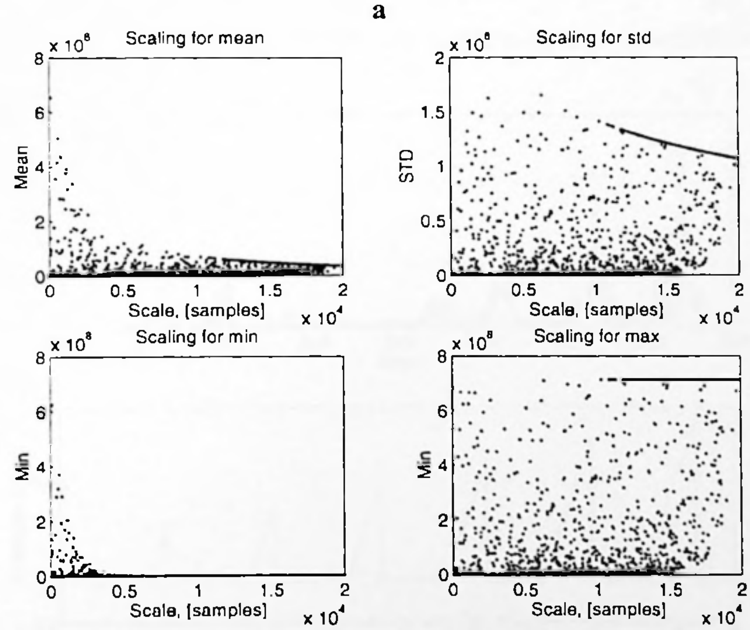


**b**

**Figure 7.2.** Scatter plot together with the scaling envelope $\sim e^{\pm 0.5 \cdot T}$ for the mean shear stress (a), Harbour Site, SIMI, Beaufort Sea, 1993. Scatter plot for mean, standard deviation, minimum and maximum of the exponential function (b).

Assuming that the shear stress has an exponential probability density function (eq. 4.14, Chapter 4) the mean shear stress $M'_{shear}$ for the section of different length $L'_t$ can be derived from equation (7.1).

$$M'_{shear}(L'_t) = \int_0^{L't} x \cdot be^{a \cdot x} dx = \frac{b}{a^2} \cdot \left(e^{a \cdot L't} \cdot (a \cdot L'_t - 1) + 1\right) \qquad (7.1)$$

where $a$ - slope of the exponent, $b$ - intersection.

If the time series exhibits ergodicity both parameters $a$ and $b$ are independent of the length $L'_t$ and thus equation (7.1) gives a single function $M'_{shear}(L'_t)$. However in our case the stress time series is not ergodic with $a$ and $b$ being functions of $L'_t$ (see Table 7.1, next section). Hence equation (7.1) produces set of $M'_{shear}(L'_t)$ curves similar to those depicted in Fig. 7.2. The same argument can be applied to calculate the dispersion of the time series.

By comparing the scaling law for the shear stress with that of the exponential functions (Fig. 7.2), it is possible to conclude that the stress series consists of a set of exponentially-shaped teeth (events) and some background noise. The approximation of the stress record by a saw-tooth function with variable amplitude is shown in Fig.7.3. This impulse-like stress series represents a stress build-up during compression and its release after ice ridging. On the average, there are two or three events per month. Impulse-like variations appeared with a rise in the peak stress level, probably related to the ice hardening due to accretion.

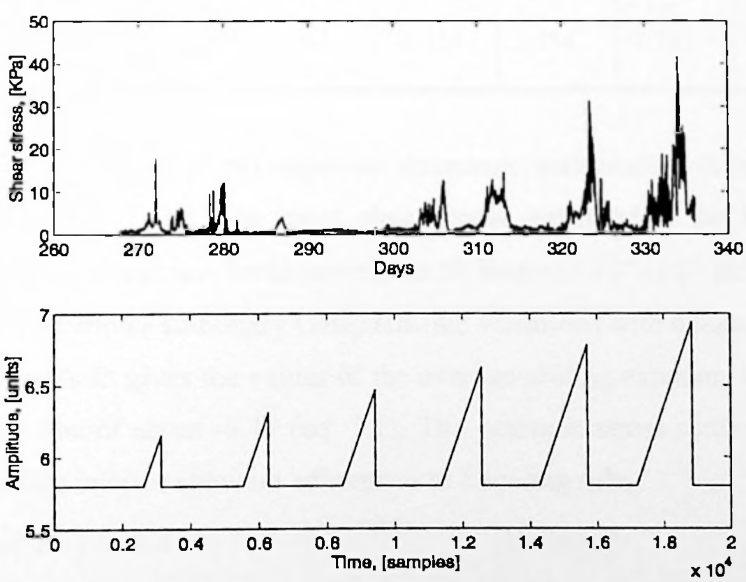


**Figure 7.3.** The shear component of stress (upper) and its approximation with a sawtooth-shaped series.

### 7.1.2 Probability Density Function

The probability density function (PDF) for the local ice stresses measured during the SIMI experiment was considered. In addition to the analysis discussed in Chapter 4 the author calculated probability density functions on the temporal scale from thousands to hundreds of hours (Fig. 7.4). The PDF was calculated for different lengths of time series where a shorter segment was inserted into the larger segment recurrently. The curves exhibit an exponential shape for the both Harbour and Frontier Sites on the temporal scale from thousands to hundreds of hours (eq. 4.14, Chapter 4).

**Table 7.1.** Parameters of the exponential approximation $f(\sigma)=b{\cdot}e^{a\sigma}$ for the ice stress probability density function, SIMI experiment, 1993.

| | Edge site 1 (Harbour) | | | Edge site 3 (Frontier) | | | Interior site (Center) | | |
|---|---|---|---|---|---|---|---|---|---|
| Scale [hrs] | Mean [kPa] | a | b | Mean [kPa] | a | b | Mean [kPa] | a | b |
| 1333 | 3.161 | -0.185 | 7.752 | 5.118* | -0.037* | 5.971* | 7.677 | -0.178 | 7.769 |
| 666 | 5.012 | -0.171 | 7.373 | 2.737 | -0.160 | 6.599 | 11.086 | -0.091 | 5.977 |
| 333 | 6.900 | -0.151 | 6.759 | 4.636 | -0.147 | 6.310 | 11.202 | -0.200 | 7.084 |
| 167 | 8.701 | -0.129 | 5.898 | 5.808 | -0.123 | 5.577 | 11.129 | -0.060 | 4.497 |
| 83 | 12.361 | -0.092 | 4.739 | 8.210 | -0.104 | 4.846 | 9.626 | -0.170 | 5.449 |
| 42 | 10.307 | -0.058 | 3.767 | 1.366 | -0.734 | 5.954 | 7.783 | -0.121 | 4.740 |

*- wild points.

As one can see the slope of the exponent decreases with scaling down when intersects increase (Table 7.1, Fig. 7.4b). The mean shear stress measured at the floe edge exhibits scaling behaviour with power law breakdown near 50 hours (~ $10^{-6}\div10^{-5}$ Hz), when the one in the interior of the floe shows stationary Gaussian-like variations with a mean of about 11 kPa. The mean least squares fit gives the values of the average scaling exponent for the shear stress at the edges of the floe of about -0.49 (eq. 7.2). The isotropic stress components for the floe edges, as well for floe interior show no adherence to a scaling rule.

$$M'_{shear}(L'_t) = 4.873 \cdot 10^6 \cdot L'^{\,-0.4727}_t \qquad \text{(Harbour)} \qquad (7.2a)$$

$$M'_{shear}(L'_t) = 5.064 \cdot 10^6 \cdot L'^{\,-0.5076}_t \qquad \text{(Frontier)} \qquad (7.2b)$$

where $L'_t$ - time scale [sec], $M'_{shear}$ - the mean of shear stress for a given scale [Pa];

[illegible]

[illegible]

[illegible]

[illegible]

The results of the analysis show the presence of scaling behaviour of principal PDF parameters such as mean and approximation coefficients, but do not lead us to a deep understanding of data structure. For instance, during down-scaling we decrease the length of the section and hence there is a chance to pick up a "big" single non-representative feature instead of several smaller features representing the character of the data.

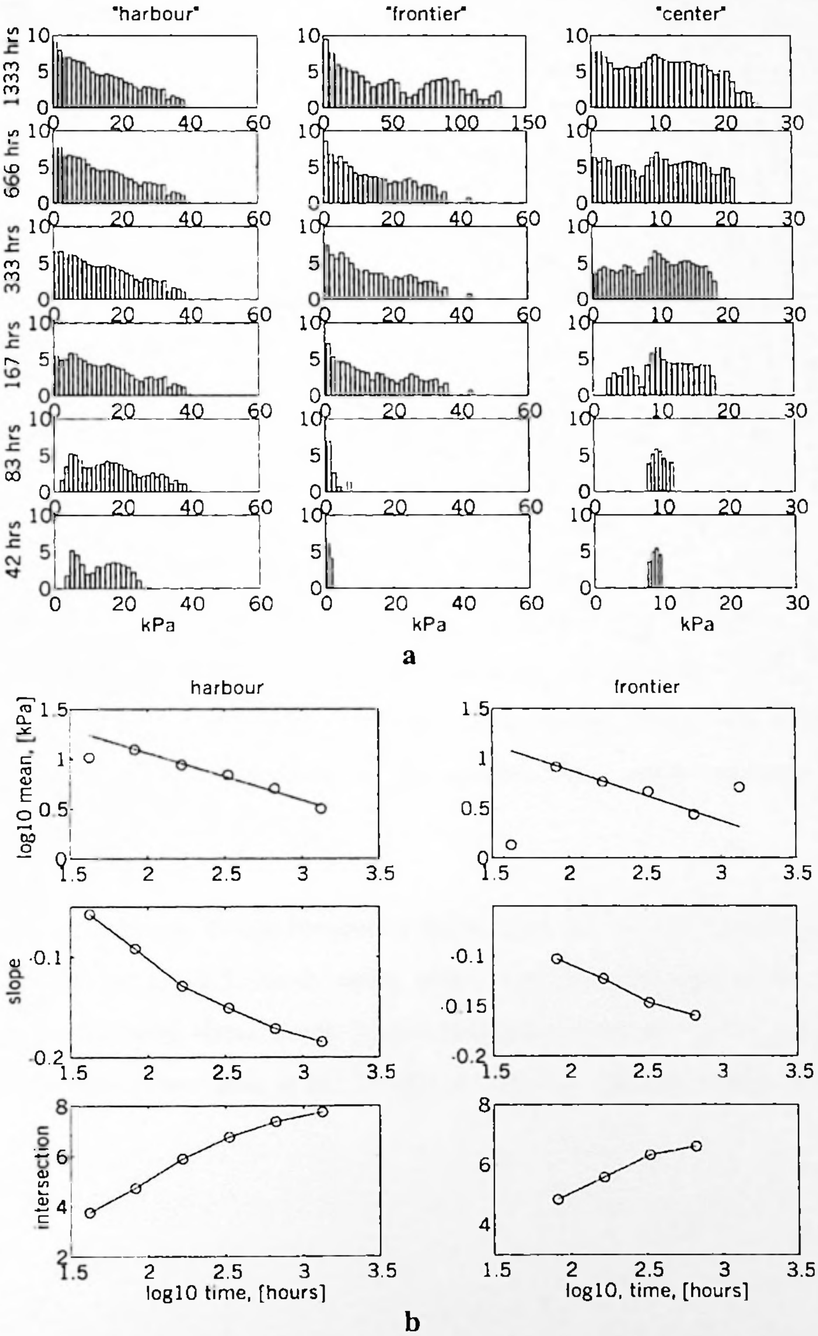


**Figure 7.4.** Shear stress distribution functions for the subsections of different lengths. Best linear fit is shown (a). Scaling behaviour of mean and distribution function approximation for shear stress (b). SIMI, West Camp, September-December 1993.

### 7.1.3 Spectrum and fractal dimension

The scaling structure of function *f(t)* can also be revealed via calculation of the fractal dimension from the power spectrum slope. Assuming that time series are rough continuous functions of a single variable they can be approximated by a Lipschitz-type function *f(x)* (Rothrock and Thorndike, 1980):

$$var(f(x+\Delta)-f(x)) \sim \Delta^{2\alpha} \quad \text{for } \Delta \to 0, \quad 0<\alpha\leq 1 \qquad (7.3)$$

where, $\Delta$ - small increment of the variable (time); $\alpha$ - Lipschitz-Höelder exponent. This in turn, implies the following relations between Hausdorff dimension $D$ and spectrum slope $p$ (Mandelbrot, 1977):

$$D = 2 - \alpha = \frac{p+5}{2} \qquad (7.4)$$

On comparing the spectra of ice local deformations and stresses (Aksenov, 1999b) to the spectra of mesoscale ice deformations (Leppäranta and Hibler, 1987), and to the spectrum of atmosphere forcing (Overland et al., 1995), the following important conclusion can be drawn. Spectra of all time series do not contain any significant energy peaks, and exhibit power law declining with the frequency. For most of the spectra three major sections with different slopes can be distinguished (Table 7.2).

The first one corresponds to the frequency band from $10^{-7}$ to $10^{-5}$ Hz. The spectral slopes of the stresses are close to -0.5. Both, wind shear and granular-type shear flow show the scaling similarity to the local shear stress. These processes dominate in the generation of large scale ice deformations (Overland, et al., 1998). A slightly positive slope in the mesoscale

**Table 7.2.** Spectral slopes and Hausdorff dimension for the ice deformations, stresses, and wind forcing.

| Frequency bands | $10^{-7}\div10^{-5}$ Hz 3 months÷1 day | | $10^{-5}\div10^{-4}$ Hz day÷hour | | $10^{-4}\div10^{-3}$ Hz hour÷minute | | $10^{-3}\div10^{-0}$ Hz minute÷second | |
|---|---|---|---|---|---|---|---|---|
| Spatial scale (from Table 7.1) | Large - meso (100 km÷10 km) | | Floe scale-local (1 km÷100 m) | | Small scale (10 m÷1 m) | | Microscale (10 cm÷1 m) | |
| Spectral slope $p$ Hausdorff dim. $D$ | $p$ | $D$ | $p$ | $D$ | $p$ | $D$ | $p$ | $D$ |
| Wind shear rate | -0.4 | 2.4(Δ) | -1.7 | 1.65 | – | – | – | – |
| Rate of mesoscale ice deformation | 0.2(JO) 0.3(LH) | 2.6(Δ) 2.7(Δ) | -0.7(JO) -1.9(LH) | 2.15(JO) 1.55(LH) | – -1.5(LH) | – 1.75(LH) | – | – |
| Mesoscale ice deformation | -1.9(SIM) | 1.55(SIM) | -1.9(SIM) | 1.55(SIM) | -0.4(SIM) | 2.3(Δ) | – | – |
| Granular shear flow stress (*) | -0.6 | 2.2(Δ) | -1.9 | 1.55 | -2.0 | 1.5 | -2.0 | 1.5 |
| Local shear stress | -0.8 | 2.1(Δ) | -1.7 | 1.65 | -0.9 | 2.05(Δ) | -0.8 | 2.1(Δ) |
| Local shear strain | – | – | – | – | – | – | -1.8(–) -0.8(++) | 1.6 2.1(Δ) |
| Ice temperature | -1.9 | 1.55 | -1.9 | 1.55 | -0.8 | 2.1(Δ) | -0.8 | 2.1(Δ) |

(*) - compressive stress obtained from the laboratory shear deforming of the granular medium (Miller et al., 1996). Frequency band for this small scale experiment was converted to the geophysical scale;
(Δ) - the value of the Hausdorff dimension is conventional, because spectral slope parameter exceeds one;
(–) - for the frequency < 0.3 Hz; (++) - for the frequency > 0.3 Hz;
(JO) - rate of the shear deformation (after Overland et al., 1995), spring, Beaufort Sea, 1992;
(LH) - rate of the dilatation (after Leppäranta and Hibler, 1987), summer, Greenland Sea, 1983;
(SIM) - dilatation deformation, SIMI experiment, autumn, Beaufort Sea, 1993.

deformation rate spectra appeared to be due to a rise of the spectra near the semi-diurnal period. It is related to inertial and tidal oscillations. The slopes of the mesoscale deformations $s_{def}$ and their rates $s_{defr}$ satisfy the following equation 7.5 (eq. 4.17, section 4.3, Chapter 4). Significantly steeper spectra were observed in the band of $10^{-5}\div10^{-4}$ Hz. Further, the spectra of wind forcing and granular flow resemble shear stress spectra, but the shear stress spectrum is closer to the spectrum of the shear than to that of granular flow. For summer conditions in

the MIZ the spectrum of the deformation rate is steeper than that for the arctic pack areas, slopes -1.9 and -0.7 respectively. The spectra of the dilatation deformation rate and local compressive component of the granular flow stress demonstrate high coherence, which implies viscous-type rheology. At the same time, the spectra of the mesoscale shear deformation rate and stress have different slopes, confirming that local shear stresses and mesoscale deformation rates are weakly related (Overland et al., 1998).

$$s_{def} = s_{defr} - 2 \qquad (7.5)$$

Besides the motion-induced deformations, the band with frequencies from $10^{-4}$ to 1 Hz contains thermally-induced deformations at a significant level. Most of the spectra are close to white noise. The granular flow spectrum diverges from the stress spectra. Local strain measured at the upper ice surface is affected more by variations of the air temperature than stress which was observed inside ice.

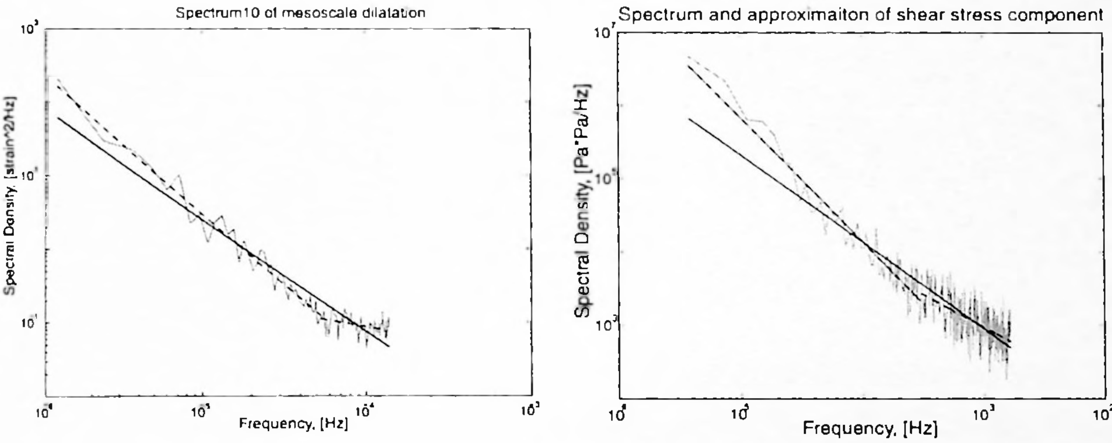


a b

**Figure 7.5.** Spectrum of: (a) mesoscale dilatation; (b) local shear stress. Linear fit is shown for each of the spectra. SIMI, autumn, 1993.

Because the slope of the spectrum characterises the ratio between stress fluctuations on different scales, the fractal behaviour of the data also should be reflected in its distribution function. Small scale experiments, for shear granular flow demonstrate that the probability distribution function for the time series of internal stress ($\sigma$) can be approximated by the function $\sigma^2 e^{-a\sigma}$, $a$= -1÷-0.3 (Miller et al., 1996). The field observations of ice local stress show a qualitatively similar probability distribution function: the stress follows a lognormal law (Tucker and Perovich, 1992) or exponential function for large stresses. The spatial distribution of static forces in the granular media follows the power law $\tau^{-0.5}$ and $\sigma^{-0.3}$ for large

shear ($\tau$) and compressive ($\sigma$) stresses respectively (Radjai et al., 1996). Palmer and Sanderson (1991) suggested that for crushed and broken materials the fragment size distribution follows the power law:

$$N(a)/N(b)=(a/b)^{-D} \qquad (7.6)$$

where $N(a)$, $N(b)$ - number of fragments larger than size $a$ and $b$; $D$ - Hausdorff dimension. Hence, the power law type PDF for fragmentation of a system presumes fractal behaviour with dimension equal to the minus power. This problem also seems to be very important for scaling analysis of ice morphology and dynamics, nevertheless a discussion about relation of the fragmentation and stresses has not yet been published.

### 7.1.4 Range–over–Standard analysis of the time series

The "Range–over–Standard Method" (R/S method) was developed by Hurst et al. (1965) to estimate the variation of the roughness function. It is based on the calculation of the ratio between range and dispersion of the function $R/S$ for different length of sequence:

$$\begin{aligned} R(N) &= max\left\{\sum_{i=1}^{N}(X_i-\overline{X})\right\} - min\left\{\sum_{i=1}^{N}(X_i-\overline{X})\right\} \\ S(N) &= \sigma(N) = \sqrt{\frac{1}{N}\sum_{i=1}^{N}(X_i-\overline{X})^2} \qquad (7.7) \\ R(N)/S(N) &= (a\cdot N/2)^H \end{aligned}$$

where, $\overline{X}$ - mean of sequence for given length of sequence $N$. For the Gaussian random sequence $R/S$ behaves as a power law with exponent equal to 1/2, but many natural time series such as volume of river discharges, rainfalls, depth of sediments layer, etc. give a value of exponent always higher than 1/2. This exponent, called the *Hurst exponent*, has a normal distribution with a mean of 0.73 and a standard deviation of 0.09 for many natural phenomena (Feder, 1988). The range of the Hurst exponent variation is from 0 to 1. Hurst suggested that such behaviour provides evidence about non random structure of natural events with power scaling law. Hastings and Sugihara (1993) showed that the Hurst exponent ($H$) is related to the box fractal dimension ($D$):

$$D = 2 - H \qquad (7.8)$$

The method was applied to the local stress series and demonstrated that all the stress data have $H$ close to 0.97 (Fig. 7.6). These values are rather high although not unusual and assume

[illegible]

[illegible]

[illegible]

[illegible]

[illegible]

the stress series to be a non–Gaussian process with the strong long-term dependence (Feder, 1988). The Hurst exponent $H \approx 0.97$ leads to the fractal dimension of stress series $D_H \approx 1.03$ which contradicts the calculation of the Hausdorff dimension obtained from the spectral slope, $D_s = 1.7 \div 2.1$. This disagreement, we assume, is related to the fact that the Hurst exponent gives the *global fractal dimension* of the series, when the spectral slope corresponds to the *local fractal dimension*. This proves that the stress time series have non-uniform fractal dimension and are multifractals.

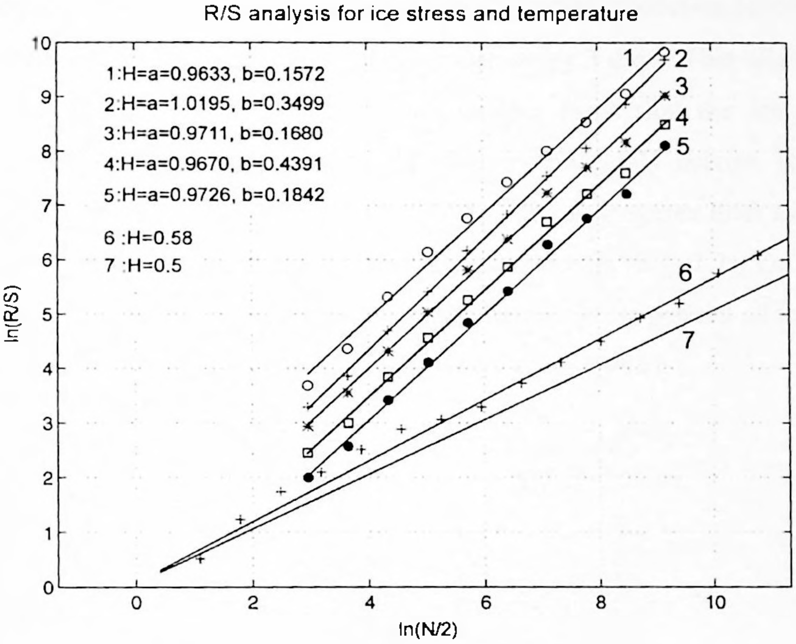


**Figure 7.6.** R/S analysis of data sets from the SIMI field experiment. Hurst scaling exponents H (see legend) for major (1) and minor (3) principal stresses, shear stress (4) and isotropic ice pressure (5) in ice cover, and also for ice temperature at a depth of 0.44 m (2) are shown. The Gaussian random sequence (6) is shown; 7 corresponds to H = 0.5. Constant offsets to curves (1-5) are introduced for clarity.

## 7.2 Ice mechanics on different spatial and temporal scales

### 7.2.1 Ice as a granular medium

At present, the most effective methods employed for ice dynamics simulation are based on numerical models considering the ice cover as a continuous medium with visco-elastic or visco-plastic behaviour (Hibler, 1986, Lemke et al., 1997). The ice characteristics are described by average values in a model grid cell and their local variations are smoothed out. On the one hand this method is restricted by the applicability of continuous representation on

the scales smaller 10 km, as the ice cover cannot be considered as a mixture of many small elements (floes). On the other hand the appearance of features smaller than the size of a grid cell, such as leads, shear zones, ridges, and elongated narrow coastal polynyas cannot be described precisely using continuous models either. To make further progress it will be necessary to find another approach to the ice dynamics.

On the one hand, satellite imagery (Overland et al., 1998) gives us a chance to obtain a picture of the sea ice dynamics with an extremely high spatial resolution (covering area ~500 km×100 km, resolution ~25 m) and temporal coverage every 3 days. This allows us to see the ice motion and deformation in great detail. The images show that the ice pack moves in aggregates of 20-200 km separated from each other by relatively narrow shear strips with widths of about 10 km or less (Overland et al., 1998). The aggregates drift as rigid granules, so that the velocity field across the shear zones is discontinuous (Fig. 7.7). On the other hand, lead patterns observed look extremely similar to the internal stress pattern of the granular flow in laboratory tests (Lindsay and Rothrock, 1995; Miller et al., 1996).

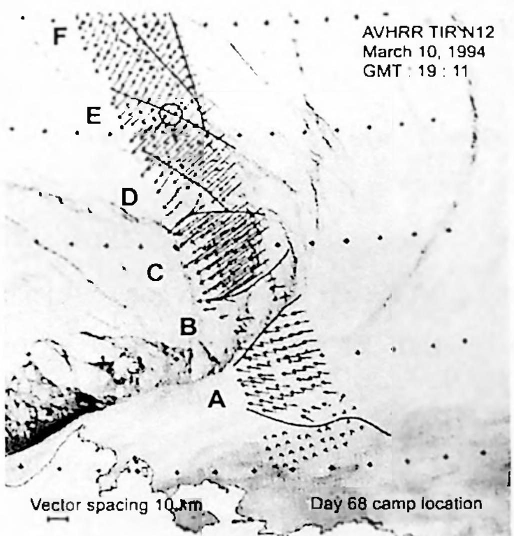


**Figure 7.7.** Ice displacement vectors from SAR image, combined with AVHRR image, Beaufort Sea. Ice pack moves in several aggregates (**A-F**). Leads (dark lines) are well correlated with discontinuity of displacement vectors (after Overland et al., 1998).

The most probable fracturing of the granular medium occurs in the areas of high stress and results in the formation of a set of cracks, correlated with the so-called "force chain": a dendrite-like distribution of the maximal stresses (Fig. 7.8). Despite the spatial scales of the ice pack dynamics and laboratory flow differing by a factor of $10^6$, the basic proportions, i.e.

"area of region/grain size" and "fracture width /grain size", are still approximately the same for both (~$10^2$ and ~$10^1$ accordingly).

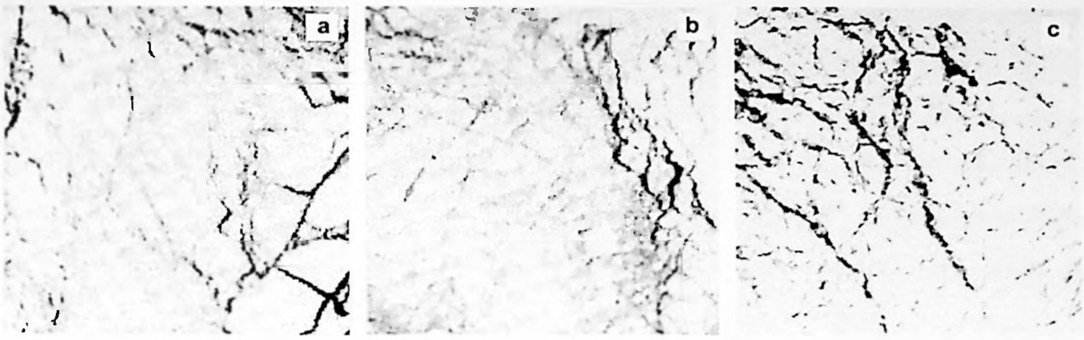


**Figure 7.8.** Leads patterns and stress chains. (a, b) Lead distributions from AVHRR imagery in Barents Sea and Central Arctic for area of 200 km × 200 km. Dark regions represent thin ice in lead (after Lindsay and Rothrock, 1995). (c) Stress distribution from laboratory tests employing visualisation of photoelasticity effect. Darker areas correspond to higher stresses (after Liu et al., 1995).

Based on experimental results, for shear granular flow with a constant shear rate, the normalized probability distribution function for the time series of internal stress in a fixed point can be approximated by the function $P(\sigma) \propto \sigma^2 e^{-\sigma}$ (Miller et al., 1996). The field measurements of the ice internal stresses exhibit a qualitatively similar probability distribution function: the stress follows a lognormal law (Aksenov, 1998a, 1999a,b; Tucker and Perovich, 1992). The spectrum of the temporal stress variations demonstrates the independence of the grain size and shear rate, and decreases as $S(\omega) \propto \omega^{-p}$ with $p$=2 for the laboratory tests (Miller et al., 1996) and $p$=1.6–1.7 for the field observations (this thesis). The spatial distribution of static forces in the granular media follows the superposition of the negative exponential and power laws (Radjai et al., 1996):

$$
\begin{aligned}
&P(\sigma) \propto e^{\beta(1-\sigma/<\sigma>)}, \text{ for } \sigma < <\sigma> \\
&P(\tau) \propto e^{b(1-\tau/<\tau>)}, \text{ for } \tau < <\tau> \\
&P(\sigma) \propto (\sigma/<\sigma>)^{\alpha}, \text{ for } \sigma > <\sigma> \\
&P(\tau) \propto (\tau/<\tau>)^{a}, \text{ for } \tau > <\tau>
\end{aligned}
\qquad (7.9)
$$

where, $\sigma$, $\tau$, $<\sigma>$, $<\tau>$ are normal and tangential stress components and their means;

[illegible]

[illegible]

[illegible]

$$[illegible]$$

$$[illegible]$$

$$[illegible]$$

$$[illegible]$$

[illegible]

$\alpha$ = -0.3, $a$ = -0.5, $\beta$ = 1.4, $b$ = 1 are parameters of the approximation.

The examples given show that granular-type dynamics may govern the ice deformation on a scale of 10-200 km. In addition, they revealed that the internal ice stress field has a highly inhomogeneous spatial structure. When the local ice stresses inside the ice floe reach 100-400 kPa during ridge building events, the maximal ice stress derived from the meso-scale ice models does not exceed 50 kPa (Lewis and Richter-Menge, 1998; Tucker and Perovich, 1992). One of the stress components is always about 100 times larger than the other (Hibler and Schulson, 1999). This fact also proves the existence of stress "chains".

### 7.2.2 Discrete medium or continuum?

The results both of the data analysis and modelling demonstrate that the structure of the deformation and stress fields of the Arctic pack ice have non-uniform and anisotropic structure. This is true for a wide range of spatial and temporal scales. The presence of discontinuities such as shear lines and stress chains makes the analysis and prognosis of the ice deformation very difficult. On the spatial scales larger than floe size pack ice appears to have a "dual" nature. It behaves as an isotropic continuum with embedded anisotripic structures on the longer time scales and demonstrates granular type dynamics for the shorter periods. The conventional isotropic continuum models produce reasonable results in terms of averaged ice drift and deformation. However, as was demonstrated in Chapter 6, these models are not able to simulate detailed structure of the deformation field. A plausible way to improve the simulations is to employ anisotropic continuum models, as was discussed in Chapter 6, or use granular media approach. The important feature for the both types of dynamics is the cohesion related to the ice growth between the floes. The cohesion which is introduced in the continuum models via the dependence of the strength of leads on the opening rate reflects the fact that when the lead does not open it start to freeze up whereas the active lead tends to become weaker (Chapter 6). In the granular model the neighbouring ice floes can freeze together and support tensile force (Hopkins, 2001). These two approaches seem to converge and in a sense describe the ice deformation from a different but consistent point of view.

[illegible]

[illegible]

[illegible]

[illegible]

[illegible]

### 7.2.3 Spatial and temporal scaling laws for ice stress

The indentation pressure/area curve shows that the ice failure pressure, calculated as a ratio of maximal applied load before ice failure to the contact area, is not constant for different contact areas but decreases as a power law with contact area (Fig. 7.9).

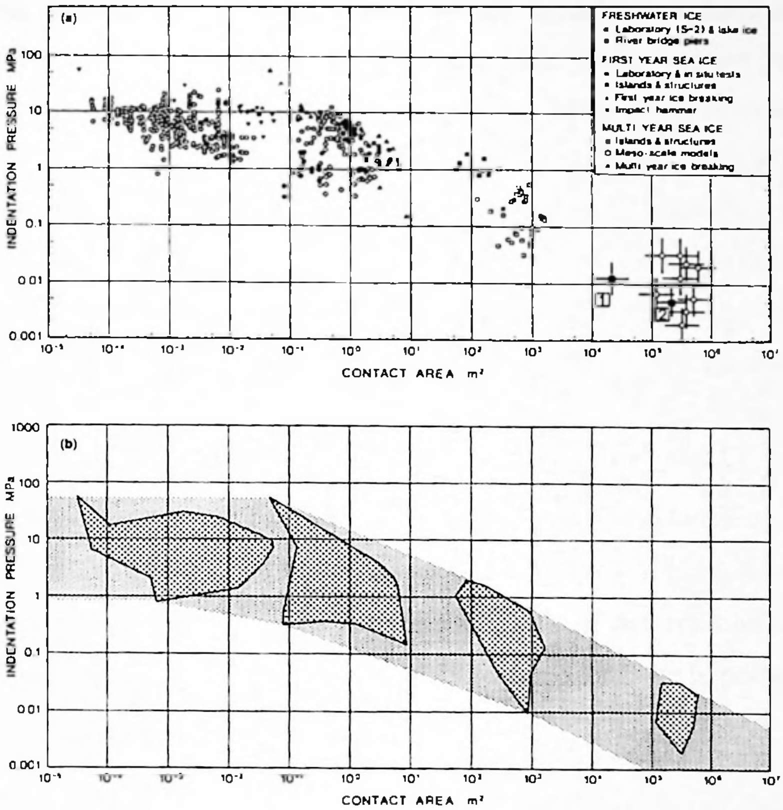


**Figure 7.9.** The apparent scale-dependence of ice failure pressure. Data points represent the maximum force per unit area sustained during ice indentation tests. Sources include laboratory experiments, icebreaker measurements, full-scale interaction with offshore islands and the results of mesoscale modelling of pack ice dynamics. (a) The full data set; (b) highlighted trend (after Sanderson, 1988). The curve was updated with the results on critical compressive stress required to form a wing-shaped crack in sea ice on 10 km (1) and 100 km (2) scales (section 6.1, Chapter 6).

This figure represents all ice indentation experimental data obtained from laboratory experiments, full-scale ice-island and ice-icebreaker interaction measurements and also results from mesoscale models (Sanderson, 1988). According to one contemporary hypothesis, the presence of weaknesses (microcracks) in the ice cover leads to non-simultaneous failure, and scale effects can appear. Observations of ice internal stresses collected from the ice pack on the local and meso-scales also support the suggested hypothesis.

Equations (6.1) and (6.2), Chapter 6, show evidence that there is a scaling effect $\sim L^{-1/2}$ for the stress which is required to form wing cracks on the scale $L$. For example, the typical compressive external stress required to form the wing-shaped crack in a small sample of about $10^3$ cm$^3$ can reach 7-17 MPa, and the failure far-field stresses for the ice cover on the scales 10 km and $10^2$ km are 7 kPa and 2-3 kPa respectively. The values of the stresses obtained are in good agreement with Sanderson's Indentation pressure–area plot (Fig. 7.9), but it is not yet clear whether this correspondence is generated by the model or a physical process. The applicability of the suggested model on the meso- and large scales has not yet been proved. For instance, the stress intensity factor, usually taken as 0.1 MPa, could be three times higher, up to 0.3 MPa (Dempsey, personal communication). It will increase critical stress up to 21 kPa for the 10 km scale and up to 10 kPa for the 100 km scale, and alter the scaling exponent. Due to insufficient information it is hardy possible to make a final judgement. But it can be concluded that if the scaling effect for ice critical stresses on local and mesoscales occurs, ice failure structures of certain sizes should be detectable from aerial photos or remote sensing images.

The calculated local stress appears to be consistent with the Sanderson's scaling curve ($\sigma$=160 kPa on the scale 50 m and $\sigma$=32 kPa on the scale 140 m). It gives further evidence of the negative power-law type relationships between the scale of deformation structures in sea ice cover and the load causing the deformation. This fact supports the hypothesis that there is a scaling effect for sea ice failure stress.

The approximation of the curve gives the following relation:

$$log_{10}[P_F] = -\frac{1}{4} \cdot log_{10}[S_{cont}] + 0.2 \qquad (7.10)$$

where $P_F$ - ice failure pressure [MPa], $S_{cont}$ - contact area [m$^2$].

Assuming that the contact area is proportional to the square of length which characterises the process, i.e. spatial scale $S_{cont} = L^2$ and using [Pa] and [m] as the basic units, we can

[illegible]

[illegible]

[illegible]

[illegible]

[illegible]

[illegible]

[illegible]

rewrite equation (7.10) as:

$$log_{10}[P'_F] = -\frac{1}{2} \cdot log_{10}[L] + 6.2 \qquad (7.11)$$

Dempsey (1996) also suggested a power law for the ice failure tensile stress on the scale of the solitary ice floe:

$$\frac{0.68}{\sqrt{1 + L/0.26}} \le \sigma_t \le 0.037 \cdot (1 + \frac{63.095}{L})^{1/2} \qquad (7.12)$$

where $L$ - size of specimen (length scale) [m], $\sigma_t$ - failure tensile stress [MPa].

These results suggest the existence of -1/2 scaling law for ice fracture. Here scaling implies spatial scaling. However, the important question arises: do similar relationships for the temporal scale exist, and how are they related to the spatial scaling laws? In other words, if we derive the spatial structure of some characteristics could we deduce their temporal variability at a given spatial point with considerable detail? To answer this question we assumed that the spatial scaling behaviour of ice failure pressure (eqs. 7.10 and 7.11) is related to maximal shear stress spatial scaling behaviour, i.e. damaging pressure equals maximal shear stress. As shown in section 7.1 the time series of the local shear stress exhibits scaling behaviour with a power scaling law for the mean. It is correct to compare scaling behaviour of the maximal shear and failure pressure. On the other hand, it is not clear whether the peaks in the shear record correspond to the ice failure and stress release or whether they appeared just because of the stopping of the ice cover loading. As a crude model for undertaking analysis the mean shear stress was taken as a failure stress.

To relate spatial and temporal scales of sea ice dynamics we use their estimations given by Overland et al. (1995) with some "characteristic" single values estimate suggested by the author (Table 2.1, Chapter 2).

The analysis presumes that spatial [*S*] and temporal [*T*] scales are related via the power law:

$$[S] = 5.3 \cdot 10^{-3} \cdot [T]^{0.9576} \qquad (7.13)$$

*S* is in metres and *T* is in seconds. Their relationship and its approximation are shown in Fig. 7.10. From equations (7.11) and (7.13) we can derive the temporal scaling law for ice failure pressure:

$$log_{10}[P'_F]=-0.4788\ log_{10}[T]+7.34 \qquad (7.14)$$

On comparing this result with the temporal scaling law for mean shear stress derived from equation (7.2) we notice remarkable agreement between parameters of approximation:

$$log_{10}[M'_{shear}]=-0.490\ log_{10}[L'_t]+6.697 \qquad (7.15)$$

where, $L'_t$ - is the time scale [sec], $M'_{shear}$ – is the mean of shear stress on a given scale [Pa]. Parameters for the shear stress law were chosen as the average for two cases. The fact that the ice failure pressure is about ten times greater than mean shear stress suggests that our approach is correct. The idea described bears some resemblance to the "frozen turbulence" method widely applied for the turbulence flows. This approach considers the turbulent flow as a mixture of turbulent vortices drifting down-stream with the main flow and made possible to relate spatial and temporal variations of the flow parameters easily. In our case, the drift velocity of the disturbances is not constant, which involves complication (Fig. 7.10).

The case described above has an example in the field. When the drifting station moves along for instance the Alaskan or Greenland coast it passes through zones with high and low deformations, which are stationary and related to the drifting ice – shore interaction. In this case the observer on the station "feels" that the "deformation wave" propagates from the shore towards him with the average speed of ice drift. This effect was observed during the SIMI experiment, when a deformation wave propagating with the speed of about 10-15 cm/s was spotted (Overland et. al., 1998).

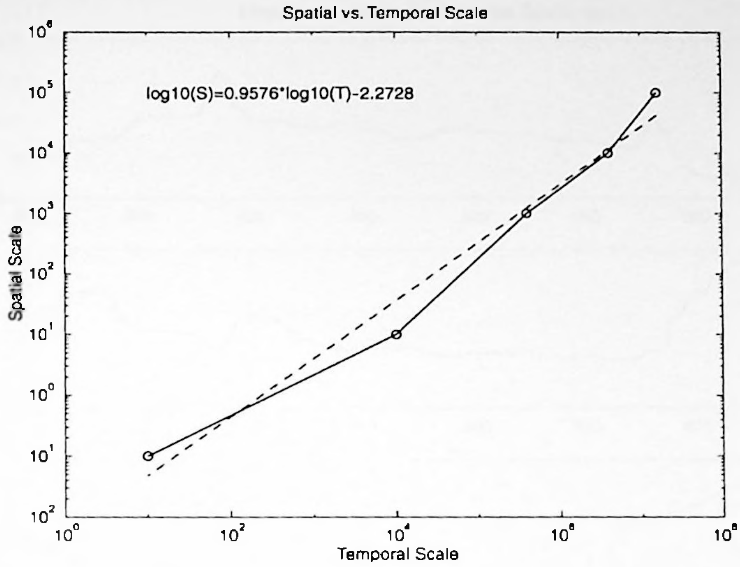


**Figure 7.10.** Relationship between spatial and temporal hierarchical scales and its power law approximation.

### 7.2.4 Scaling laws for ice deformation

To study the spatial structure of deformation field in greater detail we used the deformation fields calculated from the RADARSAT Geophysical Processor System differential ice motion analysis (Chapter 6). The techniques developed by the RADARSAT Geophysical Processor System (RGPS) allow us to obtain the deformation tensor in the 5×5 km grid with a total area of about 500×500 km. The main features of the deformation field such as slip lines are clearly seen (Figs. 6.15-6.17). The time series of the deformation field of the ice pack in the vicinity of the SHEBA station was our main interest. We calculated the time series of the areal averaged deformation tensor components. The averages were obtained for the areas 50×50 km, 100×100 km, 150×150 km and 200×200 km. The series for the different areas size correlate reasonably well but the mean and dispersion on different spatial scales are not equal. Mean values of shear deformation and shear deformation rate decrease with scale as a power law $L^a$ with $a = -0.23$ and $-0.27$ for shear and shear rate respectively (Fig. 7.15a). Here $L$ is the length of the box of averaging. At the same time divergence and dilatation do not follow the power law (Fig. 7.15b). The results imply that in terms of spatial variability the deformation field is highly non-stationary with areas of high and low deformation and deformation rate.

[illegible]

[illegible]

[illegible]

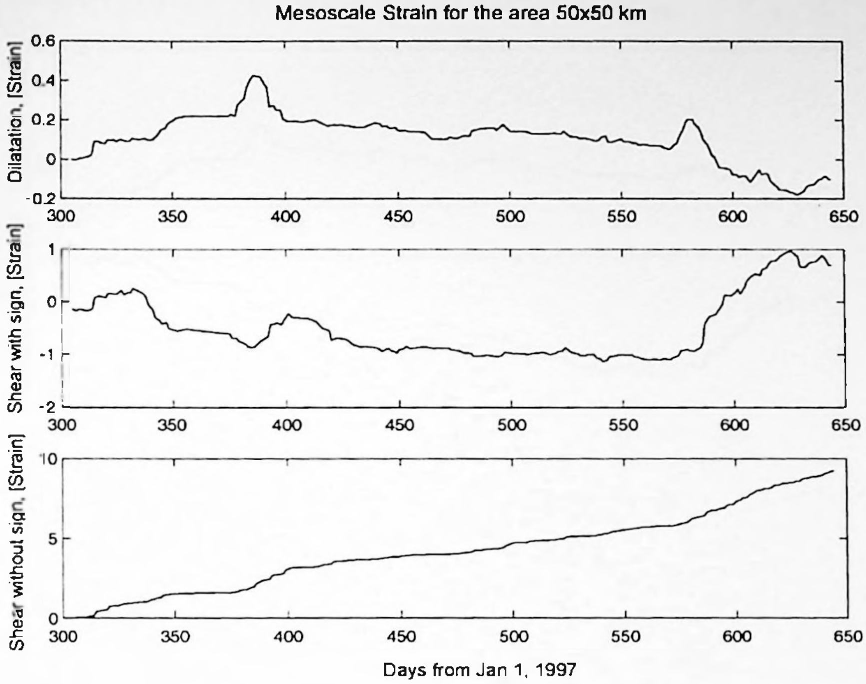


**Figure 7.11.** Ice deformation observed on spatial scales of 50 km×50 km in the vicinity of the SHEBA station computed from RGPS analysis. Ice deformation was calculated by the author using deformation rate time series obtained from the SHEBA Project Office website.

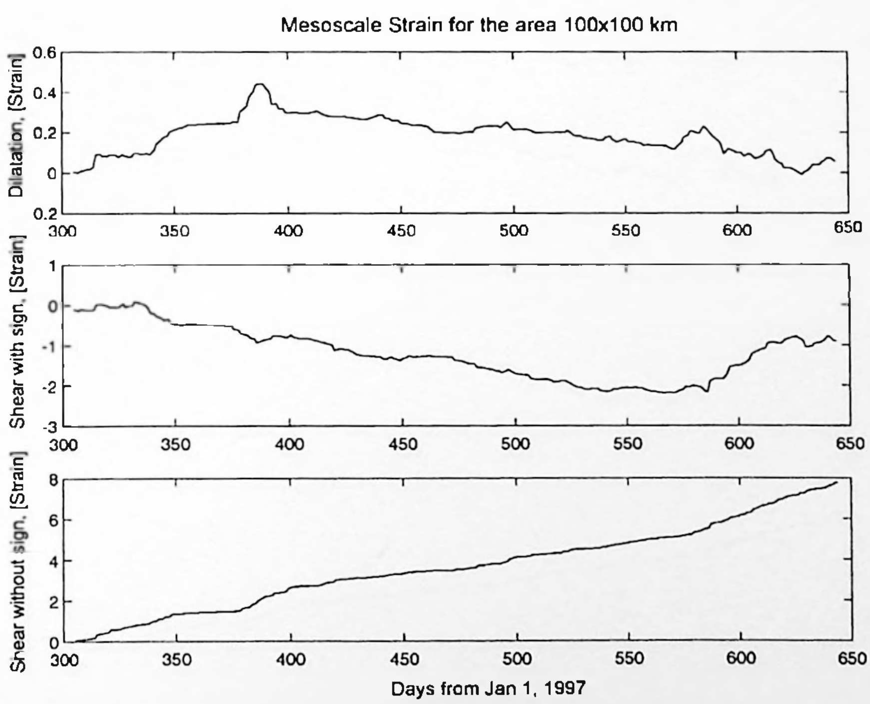


**Figure 7.12.** Ice deformation observed on spatial scales of 100 km×100 km in the vicinity of the SHEBA station computed from RGPS analysis. Ice deformation was calculated by the author using deformation rate time series obtained from the SHEBA Project Office website.

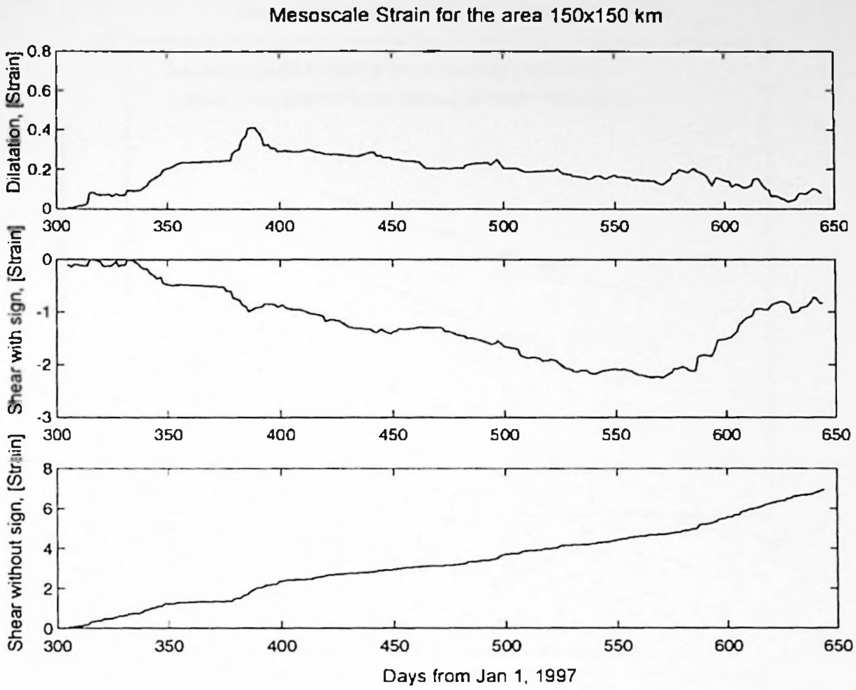


**Figure 7.13.** Ice deformation observed on spatial scales of 150 km×150 km in the vicinity of the SHEBA station computed from RGPS analysis. Ice deformation was calculated by the author using deformation rate time series obtained from the SHEBA Project Office website.

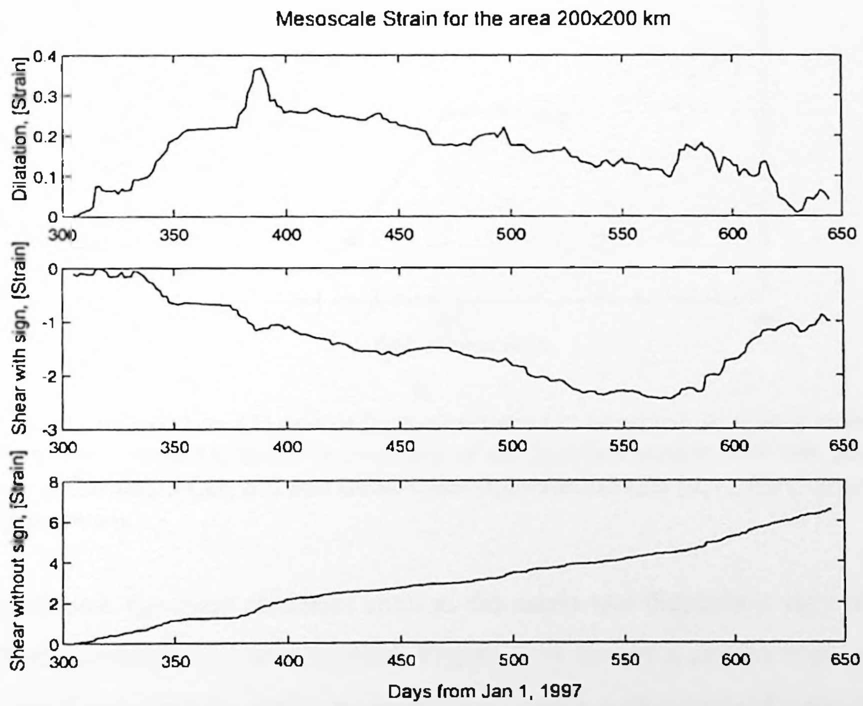


**Figure 7.14.** Ice deformation observed on spatial scales of 200 km×200 km in the vicinity of the SHEBA station computed from RGPS analysis. Ice deformation was calculated by the author using deformation rate time series obtained from the SHEBA Project Office website.

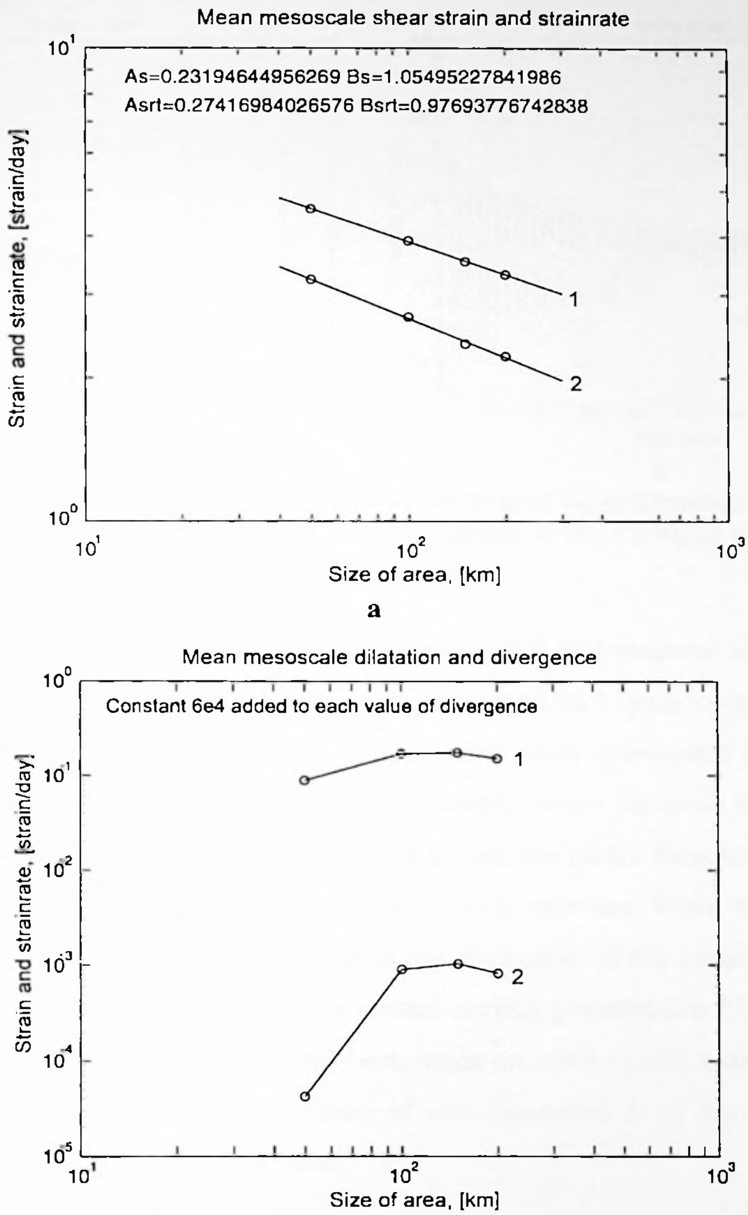


**Figure 7.15.** Mean ice deformation (1) and deformation rates (2) observed on spatial scales 50x50 km 100x100 km 150x150 km 200x200 km in the vicinity of the SHEBA station, 1997/98. Approximation for the mean shear deformation (*As*, *Bs*) and mean shear deformation rate (*Asrt*, *Bsrt*) depending on the area of averaging is shown.

To investigate how the main statistics such as the mean and dispersion vary with time the analysis described in section 7.1 was applied. Figure 7.16 shows a similar type of behaviour of the statistics as discovered for the local stress time series and discussed earlier. The upper and lower limits of the dispersion of the mean are bounded by the power law envelope $\sim T^{\pm 0.5 +- 0.2}$. Hence, the extreme values of the average shear and share rate *scale* with time with

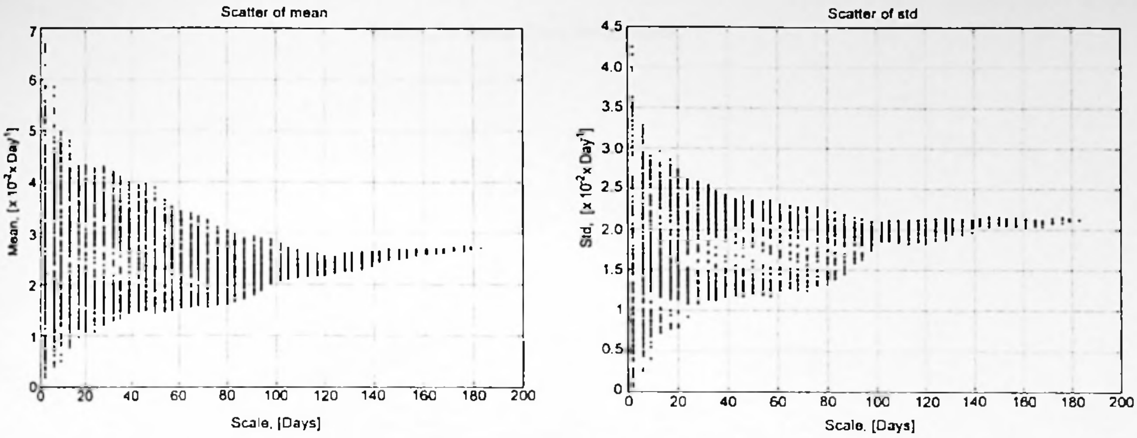


**Figure 7.16.** Spatial–temporal non-stationary structure (scaling) of ice deformation. The scatter of the mean (a) and dispersion (b) of shear declines with an increase in the averaging period. The area of averaging is 100x100 km.

exponents $k_{upper} \approx$ -0.5÷-0.2 *and* $k_{lower} \approx$ 0.2÷0.5. Both spatial and temporal scaling for the rate of the shear deformation complement each other and result in a quite complex 3-D picture (Fig. 7.17). The vertical "plates" violet, blue, green and black correspond to the scales 200 km, 150 km, 100 km and 50 km respectively. All possible values for mean observed on these scales lie on the plates. The power law envelopes bound the plates themselves, with scaling parameters decreasing with the temporal and spatial scale increase. When the period of time averaging reaches the whole length of the series the dispersion of the mean converges to the line (red one in Fig. 7.17), which represents spatial scaling portrayed in Fig. 7.15a. We can predict that if even more measurements had been made on other spatial scales besides 50 km and 200 km, all possible values of the mean $M$ and dispersion $D$ of the deformation rate would be limited by two power low surfaces:

$$M|D \propto c_l \cdot L^a + c_t \cdot T^b \qquad (7.16)$$

where, $a \approx$ -0.5÷-0.2 and $b \approx$ -0.5÷-0.2 – are the scaling parameters; $c_l$ and $c_t$ – are the empirical constants.

This intricate behaviour of the main deformation statistics are related to the fact that the ice deformation on the geophysical scale is not distributed evenly in the space, but has high and low activity zones, such as slip lines. Geometry of the slip lines, their location and spacing lead to the scaling of the statistics discussed above.

[illegible]

[illegible]

[illegible]

[illegible]

[illegible]

[illegible]

[illegible]

[illegible]

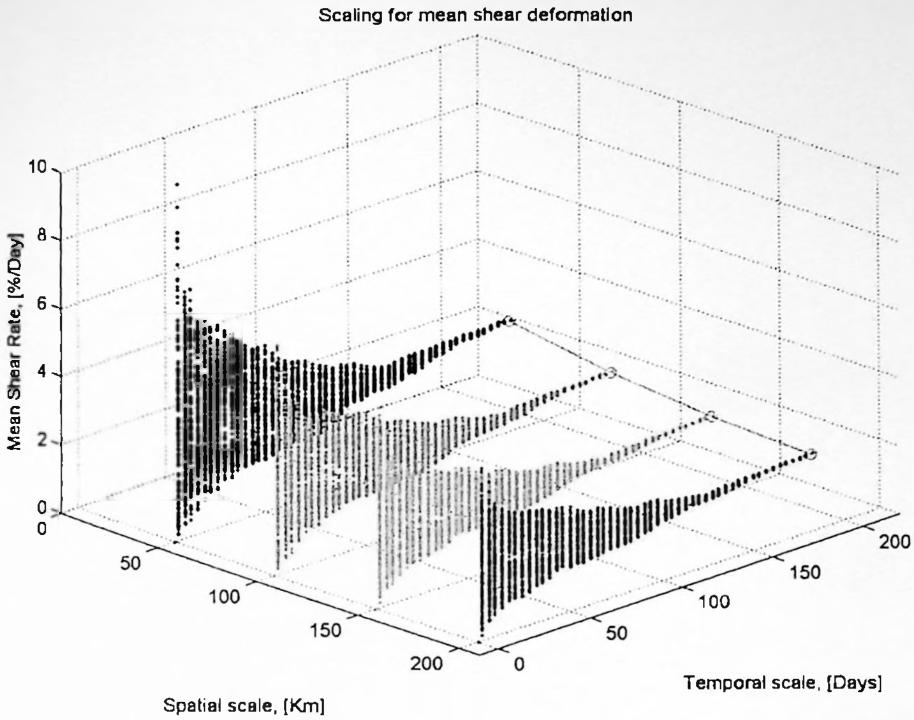


**Figure 7.17.** Spatial – temporal structure (scaling) of ice deformations, which is shown in Fig. 7.16. Non-stationary behaviour of the mean of shear deformation rate is presented. Red line with red circles shows the mean shear declining with increase of the area of averaging.

### 7.2.5 Spatial structure of the deformation field in the anisotropic ice model

Figures 7.18 and 7.19 show the spatial structure of the deformation and stress fields computed with the help of anisotropic model (Chapter 6). We applied the same scaling approach as was used for the observations. For all tests the mean and dispersion rapidly decline with the increase of the averaging area. For Test 55 the values of the mean shear strain rate are bounded by the envelope $L^{\pm 0.5}$, whereas the mean shear stress is limited by the $L^{\pm 0.3}$ scaling envelope for the spatial scale greater than 6 cells. The similarity between upper limit of the mean shear rate obtained from RADARSAT observations and the model is obvious (Fig. 7.15a). At present there is no possibility to measure *in situ* stress on the different spatial scales, so we can only hypothesise about spatial structure of the stresses. Nevertheless, extending the approach to relate spatial and temporal scaling, which was discussed earlier and comparing spatial structure of stresses simulated in the model to temporal structure of local stress observed in the field we can say the following with some degree of certainty. On the one hand the model gives a structure close to that observed. On the other hand, one can see the difference in the scatter plots obtained in tests 55 and 14 (Figs. 7.18 and 7.19). The author

attributes this dissimilarity to the number of slip lines generated in the model domain (Figs. 6.20 and 6.21).

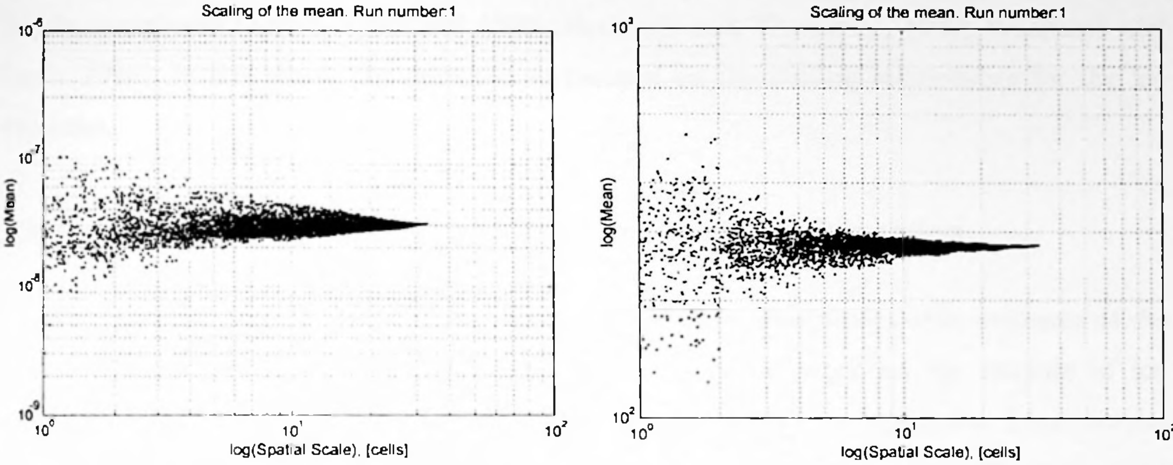


a b

**Figure 7.18.** Spatial structure of damage patterns. Rate of shear deformation (a) and shear stress (b) from test 55 (Table 6.1, Chapter 6).

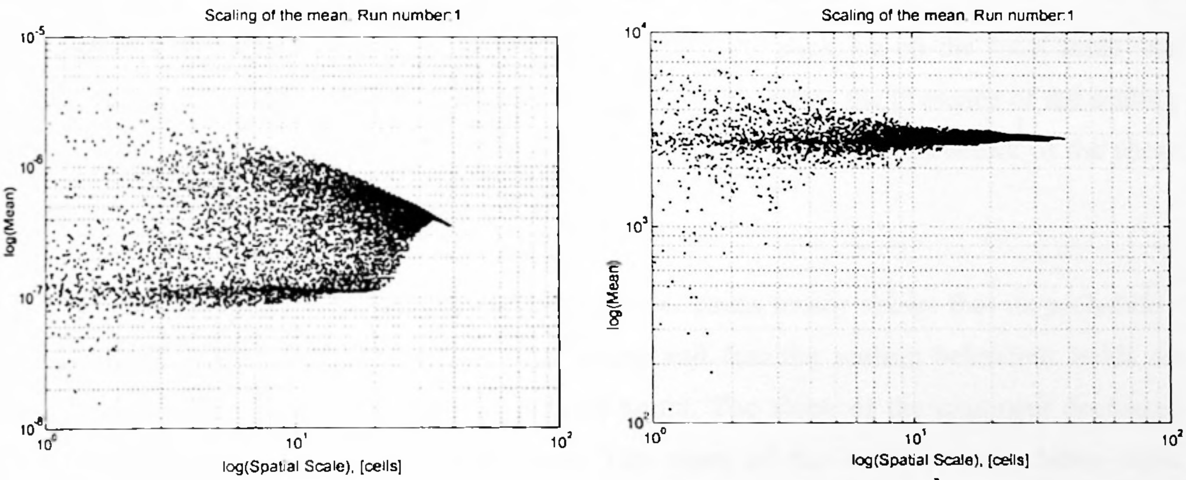


a b

**Figure 7.19.** Spatial structure of damage patterns. Shear stress (a), rate of shear deformation (b) from test 14 (Table 6.1, Chapter 6).

### 7.2.6 Scaling relationships between sea ice morphology and deformation

The morphology of ice cover and its dynamics are closely related. The appearance of deformed ice is the result of ice deformation and ridging, and in its turn, the fragmentation of an ice cover affects the distribution of ice internal stresses. Besides, the scaling laws in space should be reflected in scaling behaviour in the time domain, hence the complete set of scaling relations for sea ice cover should contain scaling laws for both forces (or energy) and ice

surface morphology in the time-space domain. However, at present there is no observational data to develop such a complicated formalism. Despite the fact that several attempts to apply scaling and fractal analyses to the ice morphology have been made this field continues to be largely unexplored (Lensu, 1998 and 1999; Rothrock and Thorndike, 1980; Wadhams and Davis, 1994). In this thesis our attention is focused on the scaling relationship for the ice dynamics.

## 7.3 Summarising the scaling hypothesis for sea ice deformation

The measurements of failure stress made on different spatial scales offer evidence of the scaling behaviour of internal ice stresses. The experimental work on the fracture of ice exhibits scaling behaviour with a power law for the size of ice specimen from several decimetres up to hundred of metres. According to one contemporary view, the presence of microcracks in the ice cover leads to non-simultaneous failure, and scale effects can appear.

Observations of ice internal stresses collected from the pack ice on the local scale and also measurements of ice loads on offshore structures demonstrate the presence of the scaling effect for the stress as well. There is a great similarity of the temporal structure of the shear stress observed in the central Arctic in different areas.

The analysis of the shear component of the local stress tensor shows that its probability density function has a negative exponential shape and that the scaling behaviour holds on temporal scales from thousands to hundreds of hours. The slope of the exponent decreases with scaling down when intersects increase. The mean of the shear stress exhibits scale dependent behaviour with breakdown near the 50 hours scale. The best fit gave the power law approximation. Stresses at the interior of the floe do not show scaling behaviour but rather stationary behaviour for the band of temporal scales from 100 to 1000 hours with near constant mean and a symmetrical shape of the distribution function. The analysis described above for compression stress shows no adherence to a scaling rule.

The spatial structure of the deformation and stress fields was investigated. As deformation and stress time series are non-stationary, their averages in time and space as well as their ensemble averages are not constant. Mesoscale ice deformations obtained on a spatial scale of 5-20 km from GPS drifters were compared with local ice deformations acting on an

area of about 100×100 m. The analysis of SAR images to derive ice deformation parameters using RGPS was also incorporated into the study. Ice deformations measured on different spatial scales were combined with the simultaneous local ice stresses in order to complete the inter-scale "picture". It was expected to prove the existence of power temporal/spatial scaling laws for the ice deformation field with an exponent between -0.4 and -0.6, spectrum decaying approximately as $\omega^{-2}$, and a probability distribution function equal to the product of the negative exponent and polynomial function. It is noteworthy that such a field should have a Hausdorff dimension near 1.5. Direct comparison between meso-scale and local scale ice stresses is not possible due to lack of direct meso-scale measurements. For this analysis, internal stresses obtained from ice dynamical models were used.

It was speculated that the failure stresses exhibit both spatial and temporal power law scaling for a wide range of scales: from $10^{-1}$ / $10^{1}$ sec to $10^{5}$ m / $10^{8}$ sec. This apparent scaling includes several mechanisms responsible for the failure stress that decrease with the scale. For the spatial scales less than floe size the presence of faults in ice can result in the reduction of ice plate strength and therefore lead to a scaling effect with a -1/2 exponent. For larger scales the floe aggregates behave as a granular medium and produce highly non-uniform non-stationary stress and deformation fields. The formation and decay of the force chains seem to be the main reason for the stress fluctuations. The analysis demonstrates that the stresses and deformations are affine multifractals with dimension varying from 1.1 for the large scale to 2 for the local scale. Comparison with data obtained from the laboratory tests and field experiments shows good agreement similarities in distribution functions and spectra.

A spectral analysis of the meso and local scale deformation together with local stress components was performed. The slope of the spectrum characterises the ratio between stress fluctuations on different scales. There are no identifiable peaks in the local stress spectra, and all the tensor components demonstrate a smooth spectral density decrease with frequency (spectral slopes between -1.2 and -1.7). It is possible to distinguish between two spectral slopes with a transition frequency of about $2\times10^{-4}$ Hz for the shear component, $4\times10^{-4}$ Hz for the major principal component, and near $7\times10^{-4}$ Hz for the isotropic and minor principal components. More detailed analysis shows that because the shear and major principal stress components, earlier attributed to motion-induced deformations, have higher dispersion for

[illegible]

[illegible]

[illegible]

[illegible]

[illegible]

short periods, they are characteristic of a more gentle spectral slope than the thermally-induced minor principal stress and isotropic pressure.

The co-analysis of spatial and temporal scales of ice dynamics processes gave their correlation as a power law with power close to 1. This fact suggests that the "characteristic velocity" for dynamical processes on different scales is nearly constant.

The ice ridging produces a power law function for the distribution of fragments. The approximation parameters can be obtained from the model of fractal crushing. This presumes a relationship between the temporal-spatial structure of forces and the fractal structure of broken ice.

# Concluding remarks

The aim of the present research has two aims: to investigate the variability of ice deformations and identify mechanisms responsible for their generation, and to explore the relationships of the ice deformation in the range of spatial scales. The research described in the thesis includes a field experiment, processing and analysis of experimental data, numerical and analytical modelling of ice deformation processes.

Two types of ice cover, the multi-year pack ice in the central Arctic and thin seasonal ice in the northern Baltic Sea, were studied. The main mechanisms identified as responsible for stress in the ice are as follows: non-uniform ice drift, ocean waves, turbulent atmospheric pressure fluctuations, and ice deformation due to ambient temperature variations.

On the assumption that thermal and motion-induced deformations of an ice floe are independent, a non-linear viscous-elastic thermo-mechanical model has been developed and coded. Verification of the model against *in situ* observations showed good agreement between theoretical prediction and measurements of internal ice stresses. The model allowed the author to separate thermal and motion-induced deformations and analyse them.

Cyclic deformations of significant amplitude were observed in field experiments. Along with the well-studied flexural-gravity waves, resonant behaviour of the ice cover in the infra-gravity band and at high frequencies was analysed. A comparison between field observations and laboratory tests in an ice tank together with modelling allowed us to identify mechanisms of wave emission accompanying ice failure. High frequency "chirp oscillations" emitted by propagating cracks were observed and discussed for the first time; in order to describe this phenomenon the asymptotic model of crack propagation was used.

Heuristic analysis of the observed local deformation and stress was carried out. The analysis included statistic characteristics of the ice deformation and stress, correlation and spectral analysis. The stress - strain curves were obtained from *in situ* local measurements, the result has never been discussed before.

Observations of ice cover mesoscale deformations obtained with the help of GPS drifters and ice motion detection from SAR imagery, along with local strain/stress measurements and modelling, were involved in the analysis. Both simulations and observations are indicative of the scale dependence of deformations and of stresses. Based on the analysis the scaling formalism for the ice deformation and stress was suggested.

An anisotropic continuum model was employed to refine the description of the deformations of an ice pack on a scale of several kilometres up to a hundred kilometres. The stress field generated by the model has a highly inhomogeneous spatial structure. The effect of the forcing and ice strength on the development of the deformation structures was investigated.

The results of the data analysis and modelling have been incorporated into a coherent scheme describing the spatial and temporal variability of the sea ice cover deformation from the local scale through the single floe scale to the mesoscale.

Spatial variability of stress and strain deformation fields is not yet well known. Several approaches to examine this problem were described in this thesis. The problem of scaling in sea ice mechanics is an extremely complex one and is not fully solved, but the author feels that the experiments and modelling results described in this thesis provide some basis for an improvement in our understanding. Much more remains to be done.

[illegible]

[illegible]

[illegible]

[illegible]

[illegible]

# Reference


Aagaard, K., and E.C. Carmack, The Arctic Ocean and climate: A perspective, in *The Polar Oceans and Their Role in Shaping the Global Environment*, Geophys. Monogr. 85, edited by O.M. Johannessen, R.D. Muench, and J.E. Overland, American Geophysical Union, Washington, DC, 5-20, 1994.

Adamson, R.M., J.P. Dempsey, S.J DeFranco, and Yu. Xie, Large-scale in-situ ice fracture experiments, Part I: Experimental aspects in *"Ice Mechanics-1995"*, edited by J.P. Dempsey and Y.D. Rajapakse, ASME, NY, 107-128, 1995.

Aksenov Ye., and S.P. Pozdnyshev, Modelling of the inertial oscillations of free ice drift (in Russian), 435, 104-111, 1995.

Aksenov Ye., Local deformations of sea ice cover. Analysis of Sea Ice Mechanics Initiative data, in *Local ice cover deformation and mesoscale ice dynamics, Ice State First year report,* edited by K. Riska, Helsinki Univ. of Technology, 1997.

Aksenov Ye., Ice mechanics studies, in *Local ice cover deformation and mesoscale ice dynamics, Ice State second year report,* edited by K. Riska, Helsinki Univ. of Technology, 1998(a).

Aksenov Ye., Fractal behaviour of ice. Scaling laws for dynamics and morphology, *Ice State project internal report,* Scott Polar Research Institute, Cambridge, UK, 1998(b).

Aksenov, Ye., and P. Wadhams, Ice deformations under the influence of natural forces. Field observation and analysis of cyclic oscillations, NATO ASI Series, I(56), *Ice Physics and the Natural Environment*, edited by J.S. Wettlaufer, J.G. Dash, and N. Untersteiner, Springer-Verlag Berlin Heidelberg, 281-284, 1999.

Aksenov Ye., Local deformation from field studies: Local scale deformation and stresses and their relationship to the mesoscale ice internal stress field, in *Local ice cover deformation and mesoscale ice dynamics, Part I: Final Report*, edited by K. Riska and J. Tuhkuri, Helsinki Univ. of Technology, Ship Laboratory, Espoo, 100-148, 1999a.

Aksenov Ye., Down-scaling: Scaling of local stresses and strains, in *Local ice cover deformation and mesoscale ice dynamics, Part II: Synthesis Report*, edited by K. Riska and J. Tuhkuri, Helsinki Univ. of Technology, Ship Laboratory, Espoo, 88-98, 1999b.

Aksenov Ye., Ice State Data report, Parts 1-4, Scott Polar Research Institute, Cambridge, UK, (Electronic version available through the ftp: pwd5-sig.spri.cam.ac.uk), 1999c.

Aksenov Ye., and W.D. Hibler, III, Failure propagation effects in an anisotropic sea ice dynamics model, in *Scaling Laws in Ice Mechanics and Ice Dynamics*, 94, Proc. of the IUTAM Symposium, Fairbanks 2000, edited by J.P. Dempsey and H.H. Shen, Kluwer Academic Publishers, 363-372, 2001.

# References

Allan, A.J., and W. Winsor, Industrial applications of ice strain measurements, in *Proc. of the International Conference on Port and Ocean Engineering under Arctic Conditions (POAC-1975)*, 2, 629-637, 1975.

Appel, I.L., and Z.M. Gudkovich, Numerical modelling and forecasting of the ice cover evolution in arctic seas during the melting season, in Russian (Chislennoe modelirovanie i prognoz evolucii ledianogo pokrova arkticheskikh morey v period tayaniya), 144 pages, Hydrometeoizdat, St.Petersburg, 1992.

Arakawa, K., and K. Higuchi, On the freezing process of aqueous solutions, *Low Temp. Sci.*, A12, 73-86, 1954.

Arctic Climate System Study, Proc. of the Conference on "Polar Processes and Global Climate", Rosario, Orcas Island, WA, USA, Dec. 1997, ACSYS Project Office, Oslo, Part I and II, 1997.

Ashby, M. F., and S. D. Hallam, The failure of brittle solids containing small cracks under compressive stress states, *Acta Metallurgica.*, 34(3), 497-510, 1986.

Assur, A., Composition of sea ice and its tensile strength, in *Arctic Sea Ice*, US National Academy of Science – National Research Council, 598, 106-138, 1958.

Bogorodsky, V.V., V.P. Gavrilo, A.V. Gusev, Z.M. Gudkovich, and A.P. Polyakov, Stressed ice cover state due to thermal wave and related underwater noise in the ocean, in *Proc. of the Ice Symposium*, Leningrad, AIRH translation, 28-33, 1972.

Bogorodsky, V.V., and V.N. Smirnov, Relaxation processes in Arctic ice fields, *Doklady Akademii Nauk SSSR*, 250, 24-26, 1982.

Borodachev, V.E., Laws of geometry for the ice floes breaking up (in Russian), *Trans. Arctic and Ant. Res. Inst.*, 316, 77-88, 1974.

Borodachev, V.E., N.A. Volkov, and V.D. Grischenko, Spatial structure of the ice cover in the Arctic Ocean and its seasonal variability (in Russian), *Trans. Arctic and Ant. Res. Inst.*, 372, 35-43, 1981.

Borodachev, V.E., V.P. Gavrilo, and M.M. Kazanskiy, The glossary of the ice marine terminology (Slovar morskikh ledovykh terminov), in Russian, St.Petersburg, Hydrometeoizdat, 1994.

Bragg, W.H., The crystal structure of ice, *Proc. Phys. Soc.*, 34, 98-103, 1922.

Bratchie, I., Rheology of an ice-floe field, *Ann. Glaciol.*, 5, 23-28, 1984.

Brigham, L.W.(ed.), The Soviet Maritime Arctic, Belhaven Press, London, 336pages, 1991.

Bryan, K., A numerical method for the study of the circulation of the world oceans, *J. Comput Phys.*, 4, 347-376, 1969.

Campbell, W.J., The wind-driven circulation of ice and water in a polar ocean, *J. Geophys. Res.*, 70, 3,279-3,301, 1965.

Cheng, B., J. Launiainen, T. Vihma, and J. Uotila, Modelling sea -ice thermodynamics in BALTEX-BASIS, *Ann. Glaciol.*, 33, 243-247, 2001.

References

[illegible]

[illegible]

[illegible]

[illegible]

[illegible]

[illegible]

[illegible]

[illegible]

[illegible]

[illegible]

[illegible]

[illegible]

[illegible]

[illegible]

[illegible]

Cherepanov, N.V., Using the methods of crystal optics for determining the age of drifting ice (in Russian), *Probl. of Arctic*, 2, 179-184, 1957.

Cherepanov, N.V., Structure of sea ice of great thickness (in Russian), *Trans. Arctic and Ant. Res. Inst.*, 267, 13-18, 1964.

Cherepanov, N.V., Spatial arrangement of sea ice crystal structure (in Russian), *Prob. Arctic and Ant. Res. Inst.*, 38, 179-184, 1971.

Cherepanov, N.V., Classification of ice in the natural water basins (translated from Russian), *Trans. Arctic and Ant. Res. Inst.*, 11(331), 77-99, 1976.

Child, A.J., and R. Duckworth, The use of ice strainmeters to measure the total load due to first year ice on Tarsuit artificial island in the Beaufort Sea, March, part of *BP Internal Report*, 1989.

Cole D.M., Field and laboratory experiments and modelling of the constitutive behaviour of sea ice, in *Proc. of the Sea Ice Mechanics and Arctic Modeling Workshop*, North West Research Assoc., Inc., Bellevue, WA, 1, 101-109, 1995.

Coon, M.D., G.A. Maykut, R.S. Pritchard, D.A. Rothrock, and A.S. Thorndike, Modelling the ice pack as an elastic-plastic material, *AIDJEX Bull.*, 24, 1-106, Univ. of Wash., Seattle, 1974.

Coon, M.D., A review of AIDJEX modeling, in *Sea Ice Processes and Models*, edited by R.S. Pritchard, Univ. Washington Press, Seattle, 12-27, 1980.

Coon, M.D., D.C. Echert, and G.S. Knoke, Force-displacement measurements of a first-year pressure ridge keel, in *"Ice Mechanics-1995"*, edited by J.P. Dempsey and Y.D. Rajapakse, ASME, NY, 239-254, 1995.

Coon M.D., G.S. Knoke, D.S. Echert, and R.S. Pritchard, The architecture of an anisotropic elastic-plastic sea ice mechanics constitutive law, *J. Geophys. Res.*, 103(C10), 21,915-21,925, 1998.

Cox, G.F.N., and W.F. Weeks, Salinity variations in sea ice, *J. Glaciol.*, 13(67), 109-120, 1974.

Cox, G.F.N., and W.F. Weeks, Brine drainage and initial salt entrapment in sodium chloride ice, USA Cold Regions Research and Engineering Laboratory (CRREL), *Cold Regions Environmental Engineering Laboratory Report*. 345, 46 pages, 1975.

Cox, G.F.N., and J.B. Johnson, Stress measurements in ice, USA Cold Regions Research and Engineering Laboratory (CRREL), *Cold Regions Environmental Engineering Laboratory Report*, 83-23, 1983.

Cox, G.F.N., A preliminary investigation of the thermal ice pressures, *Cold Regions Sci. Technol.*, 9, 221-229, 1984.

Crane, D., and P. Wadhams, Sea ice motion in Weddell Sea from drifting buoy and AVHRR data, *J. Glaciol.*, 42(141), 249-254, 1996.

Craze, A., FORTRAN programs for *SPRITel* and *SQUIRREL* data, Sea Ice Mechanics Initiative Preliminary Data Analysis, *SPRI Report*, Sea Ice Group, Scott Polar Research Institute, University of Cambridge, June 1995.

Croasdale, K.R., and R. Frederking, Field techniques for ice force measurement, Int. Assoc. for Hydraulics Res. Working Group on Ice Forces, US Army Cold Regions Res. and Eng. Lab., Hanover, NH, IAHR Spec. Rep. 87-17, Sept, 157-195, 1987.

Curlander, J.C., B. Holt, and K.J. Hussey, Determination of the ice motion using digital SAR imagery, *IEEE J. Oceanic Engineer.*, 10(10), 358-367, 1985.

Curtin, T.B. (ed.), Proceeding of Sea Ice Mechanics Workshop: 12-14 November 1990, Office of Naval Research, Washington DC, 51 pages, 1991.

Czipott, P.V., and W.N. Podney, Measurements of fluctuations in tilt of Arctic ice at the CEAREX Oceanography Camp, *Experiment Review, Data Catalog, and Preliminary results*, Physical Dynamics Inc., La Jolla, USA, 1989.

Czipott, P.V., M.D. Levine, C.A. Paulson, D. Menemenlis, D.M. Farmer, and R.G. Williams, Ice flexure forced by internal wave packets in the Arctic Ocean, *Science*, 254, 832-835, 1991.

Dempsey, J.P., and R. Adamson, Scale effects on the fracture and constitutive behavior of sea ice, in *Proc. of the Sea Ice Mechanics and Arctic Modeling Workshop*, North West Research Assoc., Inc., Bellevue, WA, 1, 84-99, 1995.

Dempsey, J.P., Scale effects on the fracture of ice, *The Johannes Weertman Symposium*, edited by R.J. Arsenault, D. Cole, T. Gross, G. Kostorz, P.K. Liaw, S. Parameswaran and H. Sizek, The Minerals, Metals and Material Soc., 1996.

Dempsey, J.P., and A.C. Palmer, Non-universal scaling of arctic fractures, in *Proc. of the International Conference on Port and Ocean Engineering under Arctic Conditions* (POAC 99), 1, 11-24, 1999.

Description of titmeter transducers, TILT Measurements Ltd., London, England, 1985.

Doronin, Yu.P., On a method of calculating the compactness and drift of ice floes, *AIDJEX Bull.*, 3, 22-39; Russian version in *Trudy Arkticheskogo and Antarkticheskogo NII*, 291, 5-17, Leningrad, 1970.

Doronin, Yu.P., and D.Ye. Kheysin, Morskoy led (Sea ice) (in Russian), Hydrometeoizdat, Leningrad, 320 pages, 1975.

Duckworth, R., and P.H. Westermann, Stress and strain instruments developed for field measurements of ice, *IEEE J. Oceanic Eng.*, 14(2), 159-165, 1989.

Duckworth, R., Notes on calibration of Delta strainmeters, *Personal communication between Marine and Field Measurement Ltd. and British Antarctic Survey*, Sept. 1995.

Dykins, J.E., Ice engineering-tensile properties of sea ice grown in a confined system, *Tech. Rep.*, R689, US Navy Civil Eng. Lab., California, 57 pages, 1970.

Eide, L., and S. Martin, The formation of brine drainage features in young sea ice, *J. Glaciol.*, 14(70), 137-154, 1975.

[illegible]

[illegible]

[illegible]

[illegible]

[illegible]

[illegible]

[illegible]

[illegible]

Farmer, D., and Yu. Xie, Acoustic and Seismic Studies of ice Mechanics, in *Proc. of the Sea Ice Mechanics and Arctic Modeling Workshop*, North West Research Assoc., Inc., Bellevue, WA, 1, 1-8, 1995.

Feder, J., Fractals, Plenum Press, New York and London, 283 pages, 1988.

Flato, G.M., and W.D. Hibler, III, On modelling ice pack as a cavitating fluid, *J. Phys. Oceanogr.*, 22, 626-651, 1992.

Flato, G.M., and W.D. Hibler, III, Ridging and strength in modeling the thickness distribution of Arctic sea ice, *J. Geophys. Res.*, 100(C9), 18,611-18,626, 1995.

Fletcher, N.H., The Chemical Physics of Ice, Cambridge Univ. Press, Cambridge, 1970.

Frederking, R., and M. Sayed, Numerical simulations of mesoscale rheology of broken ice fields, in *Proc. of the International Conference on Port and Ocean Engineering under Arctic Conditions (POAC 93),* 2, 789-798, 1993.

Geiger, C.A., and M.R. Drinkwater, Impact of temporal-spatial resolution on sea ice drift and deformation, in *Scaling Laws in Ice Mechanics and Ice Dynamics*, 94, Proc. of the IUTAM Symposium, Fairbanks 2000, edited by J.P. Dempsey and H.H. Shen, Kluwer Academic Publishers, 407-416, 2001.

Glen, J.W., The creep of polycrystalline ice, *Proc. Royal Soc. (London)*, Serie A, 228, 1175, 519-538, 1955.

Glen, J.W., Thoughts on a viscous model of sea ice, *AIDJEX Bull.*, 2, 18-27, 1970.

Goldstein, R.V., N.M. Osipenko, and M. Leppäranta, Remote sensing and sea ice mechanics, in *Local ice cover deformation and mesoscale ice dynamics, Part I: Final Report*, edited by K. Riska and J. Tuhkuri, Helsinki Univ. of Technology, Ship Laboratory, Espoo, 373-385, 1999.

Goldstein, R.V., N.M. Osipenko, and M. Leppäranta, On the formation of the large scale structural features, in *Scaling Laws in Ice Mechanics and Ice Dynamics*, 94, Proc. of the IUTAM Symposium, Fairbanks 2000, edited by J.P. Dempsey and H.H. Shen, Kluwer Academic Publishers, 323-334, 2001.

Goodman, D.J., A.J. Allan, and R.G. Bilham, Wire strain-meters on ice, *Nature*, 255, 45, 1975.

Goodman, D.J., Creep and fracture of ice and surface strain measurements on ice and on Erebus glacier tongue, McMurdo Sound, *Antarc. J. United States*, 13(4), 67-70, 1977.

Goodman, D.J., Surface strain measuring instruments for use on sea ice, in *Proc. of the Workshop on sea ice field measurements,* St. John's, Newfoundland, C-CORE Report 80-21, 75-96, 1980.

Haapala, J., and T. Stipa, GPS drifters, in *ZIP-97 data report, Report series in Geophysics N37*, edited by J. Haapala, and M. Leppäranta, Univ. of Helsinki, 59-67, 1997.

Hastings, H.M., and G. Sugihara, Fractals, A user's guide for the natural sciences, Oxford University Press, NY, 235 pages, 1993.

[illegible]

Herlevi, A., A. Blanco, M. Granskog, and Z. Zhang, Ground truth for the calibration line, in *ZIP-97 data report, Report series in Geophysics N37*, edited by J. Haapala, and M. Leppäranta, Univ. of Helsinki, 81-93, 1997.

Hibler, W.D., III, and W.B. Tucker III, Seasonal variations in apparent sea ice viscosity on the geophysical scale, *Geophys. Res. Lett.*, 4(2), 87-90, 1977.

Hibler, W.D., III, A viscous sea ice law as a stochastic average of plasticity, *J. Geophys. Res.*, 82, 3932-3938, 1977.

Hibler, W.D., III, A dynamic thermodynamic sea ice model, *J. Phys. Oceanogr.*, 9(4), 815-846, 1979.

Hibler, W.D., Modeling pack ice as viscous-plastic continuum: preliminary results, in *Sea Ice Processes and Models*, edited by R.S. Pritchard, Univ. Washington Press, Seattle, 163-176, 1980.

Hibler, W.D., III, Ice dynamics, in *The Geophysics of sea ice*, edited by N. Untersteiner, NATO ASI series B: Physics 146, Plenum Press, 577-640, 1986.

Hibler, W.D., III, and E.M. Schulson, On modeling the anisotropic failure and flow of flawed sea ice, *J. Geophys. Res.*, 105(C7), 17,105-17,120, 2000.

Hilling, W.B., The kinetics of freezing of ice in the direction perpendicular to the basal plane, in *Growth and Perfection of Crystals*, edited by R.H. Doremus, Willey, NY, 350-359, 1958.

Hobbs, P., Ice Physics, Oxford University Press, 837 pages, 1974.

Hopkins, M.A. and W.D. Hibler, III, Numerical simulations of a compact convergent system of ice floes, *Ann. Glaciol.*, 15, 26-30, 1991.

Hopkins, M.A., Numerical simulation of system of multitudinous polygonal blocks, *US Army Cold Regions Research and Engineering Laboratory, CRREL Report 92-22*, 69 pages, 1992.

Hopkins, M.A., On the ridging of intact lead ice, *J. Geophys. Res.*, 99(C8), 16,351-16,360, 1994.

Hopkins, M.A., On the mesoscale interaction of lead ice and floes, *J. Geophys. Res.*, 101(C8), 18,315-18,326, 1996.

Hopkins, M.A., Four stages of pressure ridging, *J. Geophys. Res.*, 103(C10), 21,883-21,891, 1998.

Hopkins, M.A., J. Tuhkuri, and M. Lensu, Rafting and ridging of thin ice sheets, *J. Geophys. Res.*, 104(C6), 13,605-13,613, 1999.

Hopkins, M.A., The effect of the tensile strength in the arctic ice pack, in *Scaling Laws in Ice Mechanics and Ice Dynamics*, 94, Proc. of the IUTAM Symposium, Fairbanks 2000, edited by J.P. Dempsey and H.H. Shen, Kluwer Academic Publishers, 373-386, 2001.

Hunke, E.C., and J.K. Dukowicz, An elastic-viscous-plastic model for sea-ice dynamics, *J. Phys. Ocean.*, 27, 1849-1867, 1997.

Hurst, H.E., R.P. Black, and Y.M. Simaika, Long-term storage, An experimental study, Constable, London, 1965.

Huppert, H.E., The fluid mechanics of solidification, *J. Fluid Mech.*, 212, 209-240, 1990.

Idso, S.B., and R.D. Jackson, Thermal radiation from the atmosphere, *J. Geophys. Res.*, 74, 5,397-5,403, 1969.

Johannessen, O.M., S. Sandven, W.P. Budgell, J.A. Johannessen and R.A. Suchman, Observation and Simulation of Ice Tongues and Vortex Pairs in the Marginal Ice Zone, in The Polar Oceans and their role in shaping the global environment, The Nansen's Centennial Volume, Geophysical Monograph 85, edited by O.M. Johannessen, R.D. Muench and J.E. Overland, AGU, 109-136, 1994.

Johnson, J.B., and G.F.N. Cox, The OSI ice stress sensor, in *Proc. of the Workshop on sea ice field measurements,* St. John's, Newfoundland, C-CORE Report 80-21, 193207, 1980.

Kamb, B., Crystallography of ice, in *Physics of Chemistry of Ice*, edited by E. Whalley, S.J. Jones, and L.W. Gold, Royal Soc. of Canada, Ottawa, 28-41, 1973.

Kawamura, T., K. Shirasawa, N. Ishikawa, A. Lindfors, K. Rasmus, M.A. Granskog, J. Ehn, M. Leppäranta, T. Martma, and R. Vaikmäe, Time-series observations of the structure and properties of brackish ice in the Gulf of Finland, *Ann. Glaciol.*, 33, 1-4, 2001.

Kerr, A.D., On determination of horizontal forces a floating ice plate exerts on a structure, *US Army Cold Regions Research and Engineering Laboratory, CRREL Report 78-15,* 1978.

Kowalik, Z., and J.B. Matthews, The $M_2$ tide in the Beaufort and Chukchi Seas, *J. Phys. Ocean.*, 12(7), 743-746, 1982.

Kwok, R, J.C. Curlander, R. McConnell, and S. Pang, An ice motion tracking system at the Alaska SAR Facility, *IEEE J. Oceanic Engineer.*, 15(1), 44-54, 1990.

Kwok, R, and G. Cunningham, Geophysical Processor System. Data User's Handbook. version 2.0, JPL D-9526, Jet Propulsion Laboratory, National Aeronautics and Space Administration, 1993.

Kwok, R., and G. Cunningham, RADARSAT Geophysical Processor System. Data User's Handbook. version 0.1, Draft, Jet Propulsion laboratory, National Aeronautics and Space Administration, 1998.

Kwok, R, Deformation of the Arctic ocean sea ice cover between November 1996 and April 1997: A qualitative survey, in *Scaling Laws in Ice Mechanics and Ice Dynamics*, 94, Proc. of the IUTAM Symposium, Fairbanks 2000, edited by J.P. Dempsey and H.H. Shen, Kluwer Academic Publishers, 315-322, 2001.

Laevastu, T., Factors affecting the temperature of the surface layer of the sea, *Comm. Phys. Math.*, 25(1), 8-134, 1960.

Lake, R.A., and E.L. Lewis, Salt rejection by sea ice during growth, *J. Geophys. Res.*, 75(3), 583-597, 1970.

Leberl, F., J. Raggam, C. Elachi, and W.J. Campbell, Sea ice measurements from SEASAT SAR images, *J.Geophys.Res.*, 88, 1915-1928, 1983.

[illegible]

[illegible]

[illegible]

[illegible]

[illegible]

[illegible]

[illegible]

[illegible]

[illegible]

[illegible]

[illegible]

[illegible]

[illegible]

Lemke, P., W.D. Hibler III, G. Flato, M. Harder, and M. Kreyscher, On the improvement of sea-ice models for climate simulations: the Sea Ice Model Intercomparison Project, *Ann. of Glaciol.*, 25, 183-187, 1997.

Lensu M., The *"Ice State"* of ridged, closed ice fields and its relation to SAR imagery, *Internal Report from the "Ice State" project,* Local ice cover deformation and mesoscale dynamics, Helsinki Univ. of Technology, Ship Laboratory, 1998a.

Lensu M., Distribution of the number of fragmentations in continuous fragmentation, *J. Phys.,* A: Math. Gen. 31, 5705-5715, 1998b.

Lensu M., Ridge field statistics, in *Local ice cover deformation and mesoscale ice dynamics, Part I: Final Report*, edited by K. Riska, and J. Tuhkuri, Helsinki Univ. of Technology, Ship Laboratory, Espoo, 358-372, 1999.

Leppäranta, M., and W.D. Hibler III, Mesoscale sea ice deformation in the East Greenland Marginal Ice Zone, , *J.Geophys.Res.*, 92(C7), 7,060-7,070, 1987.

Leppäranta, M. and A. Omstedt, Dynamic coupling of sea ice and water for an ice field with free boundaries, *Tellus,* 42A(4), 482-495, 1990.

Lewis, J.K., A model for thermally-induced stress in multi-year sea ice, *Cold Reg. Sci. Technol.*, 21, 337-348, 1993.

Lewis, J.K., W.B. Tucker III, and P.J. Stein, Observation and modeling of thermally induced stresses in first-year ice, *J. Geophys. Res.*, 99(C8), 16,361-16,371, 1994.

Lewis, J.K., A conceptual model of the impact of flaws on the stress state of sea ice, *J.Geophys.Res.*, 100(C5), 8,829-8,835, 1995.

Lewis, J., K., and J.A. Richter-Menge, Motion-induced stresses in pack ice, *J.Geophys.Res.*, 103(C10), 21,831-21,843, 1998.

Lewis, J.K., Thermomechanics of pack ice, *J. Geophys. Res.*, 103(C10), 21,869-21,882, 1998.

Lindsay, R.W., and D.A. Rothrock, Arctic sea ice leads from advanced very high resolution radiometer images, *J. Geophys. Res.,* 100(C3), 4,533-4,544, 1995.

Linear and angular servo accelerometrs. Users Manual, Schaevitz Engineering US, Pennsauke, New Jersey, 1982.

Liu, C.-h., S.R. Nagel, D.A. Schecter, S.N. Coppersmith, S. Majumdar, O. Narayan, and T.A. Witten, Force fluctuation in beads pack, *Science*, 269, 513-515, 1995.

Macklin, W.C., and B.F. Ryan, Habits of ice growth in supercooled water in aqueous solutions, *Phil. Mag.*, 14, 847-860, 1966.

Mader, H.M., The thermal behaviour of the water-vein system in polycrystalline ice, *J. Glaciol.*, 38, 359-374, 1992.

Mandelbrot, B.B., Fractals: form, chance, and dimension, W.H. Freeman, San Francisco, 1977.

Marco, J.R., and R.E. Tompson, Rectilinear leads and internal motions in the ice pack of the western Arctic Ocean, *J. Geoph. Res.*, 82(6), 979-987, 1977.

Marshunova, M.S., Principal characteristics of the radiation balance of the underlying surface and of the atmosphere in the Arctic, *Trans. Arctic and Ant. Res. Inst.* (Trudy Arkt. Antark. Nauch. Issled. Inst.), 229, in Russian, translated by the Rand Corp. Santa-Monica, CA (1966), 1961.

Martin, S., and R. Drucker, Observation of short-period ice floe accelerations during Leg-II of Polarbjorn drift, *J. Geophys. Res.*, 96(C6), 10,567-10,580, 1991.

Maykut, G.A., and N. Untersteiner, Some results from a time-dependent thermodynamic model of sea ice, *J. Geophys. Res.*, 76(6), 1,550-1,575, 1971.

McPhee, M.G., A simulation of inertial oscillation in drifting pack ice, *Dyn. of Atm. and Oceans*, 2, 107-122, 1978.

McPhee, M.G., Drift velocity during the drift-station phase of MIZEX 83, *MIZEX Bull IV*, 1-11, US CRREL, Hanover, N.H., 1984.

Meier, M.H.E., R. Döscher, A.C. Coward, J. Nycander, and K. Döös, Rossby Centre regional ocean climate model, model description and first results from the hindcast period 1992/93, Reports of Swedish Meteorological and Hydrological Institute, Oceanography, 26, 102 pages, 1999.

Mellor, M., Mechanical behavior of sea ice, in *The Geophysics of Sea Ice*, edited by N. Untersteiner, NATO ASI series B: Physics 146, Plenum Press, 165-281, 1986.

Mel'nichenko, N.A., V.I Mikhailov, and V.I. Chizhik, Studies of the temperature dependance of the brine content of sea ice by the pulse NMR method (in Russian), *Okeanologiya*, 19(5), 811-814, 1979.

Menemenlis, D., D.M. Farmer, and P.V. Czipott, A note on infragravity waves in the Arctic Ocean, *J. Geophys. Res.*, 100(C4), 7089-7093, 1995.

Metge M., G.R. Pilkington, A.G. Strandnerg, and D. Blanchet, A new sensor for measuring ice forces on structures: laboratory tests and field experience, in *Proc. of the International Conference on Port and Ocean Engineering under Arctic Conditions (POAC 83)*, 4, 790-801, 1983.

Miller, B., C. O'Hern, and R.P. Behringer, Stress fluctuations for continuously sheared granular materials, *Phys. Rev. Lett.*, 77(15), 3110-3113, 1996.

Millero, F.J., Freezing point of sea water, $8^{th}$ Report of the joint panel of oceanographic tables and standards, *UNESCO Technical Papers in Marine Science*, UNESCO, Paris, France, 1978.

Mollo-Christensen, E., Interaction between waves and mean drift in an ice pack, *J. Geophys. Res.*, 88(C5), 2,971-2,972, 1983.

Moor, S.C., and P. Wadhams, Recent developments in strainmeter design, presented at Workshop on Sea-Ice Field Measurements, St. Johns, NF, Can., 1981.

Mulmule, Sh.V., J.P. Dempsey, and R.M. Adamson, Large-scale in-situ ice fracture experiments, Part II: Modeling aspects in *"Ice Mechanics-1995"*, edited by J.P. Dempsey and Y.D. Rajapakse, ASME, NY, 129-145, 1995.

Murphy, G., A.H. Hausrath III, and P.W. Peterson, Response of resistance strain gauges to dynamic strains, *IX^e Congrès International de Méchanique Appliquée. Actes.*, 8, 448-456, 1957.

Nagurny, A.P., V.G. Korostelev, and V.P. Abaza, Wave method for evaluating the effective thickness of sea ice in climate monitoring, *Bull. Rus. Ac. Sci., Suppl., Phys. of Vibrations*, 58(3), 168-174, 1994.

Nakawo, M., and N.K. Sinha, Growth rate and salinity profile of first-year ice in the high Arctic, *J. Glaciol.*, 27(96), 315-330, 1981.

Nazintsev, Yu.L., Zh.A, Dmitrash, and V.I. Moiseev, Teplofizicheskiye svoy'stva morskogo l'da, Izdatel'stvo Leningradskogo Universiteta (in Russian), (Thermophysical properties of sea ice, published by Leningrad University Press), 260 pages, 1988.

Nemat-Nasser, S., and H. Horii, Compression-induced nonplanar crack extension with application to splitting, exfoliation, and rockburst, *J. Geophys. Res.*, 87(B8), 6,805-6,821, 1982.

Nikiforov, Ye.G., Z.M. Gudkovich, Yu.I. Yefimov, V.A. Romanov, Principles of a methods for computing ice redistribution under the influence of wind during the navigation period in arctic seas, *AIDJEX Bull.*, 3, 40-64, 1970; Russian version in *Trudy Arkticheskogo and Antarkticheskogo Instituta (Trans. Arctic and Ant. Res. Inst.)*, 275, 5-25, Leningrad, 1970.

Nye, J.F., Water-veins and lenses in polycrystalline ice, in *Physics and Chemistry of Ice*, edited by N. Maeno, and T. Hondoh, Hokkaido Univ. Press, 200-205, 1992.

Overland, J.E., B.A.Walter, Th.B. Curtin, and Ph. Turet, Hierarchy and sea ice mechanics: A case study from Beaufort Sea, *J. Geophys. Res.,* 100(C3), 4,559-4,571, 1995.

Overland J., S.L. McNutt, and S. Salo, Regional and floe-floe deformation, *Proc. of the Sea Ice Mechanics and Arctic Modeling Workshop*, North West Research Assoc., Inc., Bellevue, WA, 1, 168-177, 1995.

Overland, J.E., S.L. McNutt, S. Salo, J. Groves, and S. Li, Arctic sea ice as a granular plastic, *J. Geophys. Res.*, 103(C10), 21,845-21,867, 1998.

Overland, J.E., S. McNutt, J.A. Richter-Menge, B.C. Elder, S. Salo, and J. Groves, Regional atmosphere forcing and ice response during SHEBA, in press.

Parkinson, C.L., and W.M. Washington, A large-scale numerical model of sea ice, *J. Geophys. Res.*, 84(C1), 311-337, 1979.

Palmer, A.C., Ice forces and ice crushing, in *Proc. of the International Conference on Port and Ocean Engineering under Arctic Conditions (POAC 91),* 1, 43-64, 1991.

Palmer, A.C., and T.J.O. Sanderson, Fractal crushing of ice and brittle solids, *Proc. R. Soc. Lond. Series A*, 433, 469-477, 1991.

Parmerter, R.R., and M.D. Coon, Model of pressure ridge formation in the sea ice, *J. Geophys. Res.*, 77(33), 6565-6575, 1972.

Parmerter, R.R., A model of simple rafting in sea ice, *J. Geophys. Res.*, 80, 1,948-1,952, 1975.

Perey, F.G.J., and E.R. Pounder, Crystal orientation in ice sheets, *Can. J. Phys.*, 36, 494-502, 1958.

Perovich, D.K., B.C. Elder, and J.A. Richter-Menge, Observations of the annual cycle of sea ice temperature and mass balance, *Geophys. Res. Lett.*, 24(5), 555-558, 1997.

Pritchard, R.S., An elastic-plastic constitutive law for sea ice, *J. Appl. Mech.*, 42(E2), 379-384, 1975.

Pritchard R.S. et al., Acoustic Signatures of Falling Ice Blocks, in *Ice Mechanics-1995*, edited by J.P. Dempsey and Y.D. Rajapakse, ASME, NY, 219-229, 1995.

Pounder, E.R., Physics of ice, Pergamon Press, NY, 151 pages, 1965.

Radjai, F., M. Jean, J-J. Moreau, and S.Roux, Force distribution in dense two-dimensional granular systems, *Phys. Rev. Lett.*, 77(2), 274-277, 1996.

Rahmstorf, S.,and A. Ganopolski, Long-term global warming scenarios computed with an efficient coupled climate model, *Clim. Change,* 43(2), 352-367, 1999.

Richardson, C., and E.E. Keller, The brine content of sea ice measured with a nuclear magnetic resonance spectrometer, *J. Glaciol.,* 6(43), 89-100, 1966.

Richter-Menge, J.A., and G.F.N. Cox, Creep of saline ice at low stresses and high temperatures, in *5th Int. Offshore and Polar Engineering Conference,* Int. Soc. Offshore and Polar Eng., The Hague, Netherlands, June 11-16, 312-316, 1995.

Richter-Menge J.A. and B.C. Elder, Pack ice stresses and their relation to regional deformation, in *Proc. of the Sea Ice Mechanics and Arctic Modeling Workshop*, North West Research Assoc., Inc., Bellevue, WA, 1, 178-187, 1995.

Richter-Menge, J.A., and B.C. Elder, Characteristics of pack ice stress in the Alaskan Beaufort Sea, *J. Geophys. Res.*, 103(C10), 21,817-21,829, 1998.

Richter-Menge, J.A., S.L. McNutt, J.E. Overland, and R. Kwok, Relating Arctic pack ice stress and deformation under winter conditions, *J. Geophys. Res.*, in press.

Rothrock, D.A., The steady drift of an incompressible arctic ice cover, *AIDJEX Bull.*, 21, 49-78, 1973.

Rothrock, D.A., and A.S. Thorndike, Geometric properties of the underside of sea ice, *J. Geophys. Res.*, 85(C7), 3,955-3,963, 1980.

Rothrock, D.A., and O. Babko, Ice draft measurements from CIZEX-1999, 2000?.

Sanderson T.J.O., *Ice mechanics: risks to offshore structures.* London, Graham & Trotman, 253 pages, 1988.

Sandven, S., M. Lunhaug, Ø. Dallen, K. Kloster, and V. Alexandrov, Satellite observations, in *Local ice cover deformation and mesoscale ice dynamics, Part I: Final Report*, edited by K. Riska and J. Tuhkuri, Helsinki Univ. of Technology, Ship Laboratory, Espoo, 317-331, 1999.

[illegible]

Schmidt, H., and Yu. Dudko, Seismo-Acoustic Remote Sensing of ice fractures, in *Ice Mechanics-1995*, edited by J.P. Dempsey and Y.D. Rajapakse, ASME, NY, 231-237, 1995.

Schwarz, J., and W.F. Weeks, Engineering properties of sea ice, *J. Glaciol.*, 19(81), 499-531, 1977.

Schwarzacher, W., Pack-ice studies in the Arctic Ocean, *J. Geophys. Res.*, 64, 2,357-2,367, 1959.

Schwerdtfeger, P., The thermal properties of sea ice, *J. Glaciol.*, 4(36), 789-807, 1963.

Seidensticker, R.G., Comment on paper by P. Hoekstra, T.E. Osterkamp and W.F. Weeks, The migration of liquid inclusion in single ice crystal, *J. Geophys. Res.*, 71(8), 2,180-2,181, 1965.

Sinha, N.K., Rheology of columnar-grained ice, *Exp. Mechan.*, 18(12), 464-470, 1978.

Shreve, R.L., Migration of air bubbles, vapour figures, and brine pockets in ice under a temperature gradient, *J. Geophys. Res.*, 72(16), 4,093-4,100, 1967.

Schulson, E.M., and W.D. Hibler III, The fracture of ice on scales large and small: Arctic leads and wing cracks, *J. Glaciol.*, 37(127), 319-322, 1991.

Schulson, E.M., D.E. Jones, and G.A. Kuehn, The effect on the brittle compressive fracture of ice, *Ann. of Glaciol.*, 15, 216-221, 1991.

Schulson, E.M., Brittle failure of ice, *Engng. Fract. Mech.*, 68, 1839-1887, 2001.

Shine, K.P., Parameterization of the shortwave flux over high albedo surfaces as a function of the cloud thickness and a surface albedo, *Q. J. R. Meteorol. Soc.*, 110(465), 747-764, 1984.

Sinha, N.K., Technique for studying structure of sea ice, *J. Glaciol.*, 18(79), 315-323, 1977.

Slepyan, L.I., Crack dynamics in a plate under bending, in *Ice mechanics-1993*, edited by J.P. Dempsey, Z.P. Bazant, Y.D. Rajapakse, and S.S. Sunder, ASME, NY, 119-129, 1993.

Smirnov, V.N., and A.I. Shushlebin, The results of the studies of natural deformations of sea ice field, in *Proc. of the First European Offshore Mechanics Symposium*, Norway, 512-516, 1990.

Smirnov, V.N., V.G. Korostelev, and I.V. Stepanov, Physico-mechanical model of self-excited processes by sea ice compacting, in *Proc. of the 3rd International Offshore Polar Engineering Conference (ISOPE'93)*, Golden Co, 589-595, 1993.

Squire, V. A., An investigation into the use of strain rosettes for the measurements of propagating cyclic strains, *J. Glaciol.*, 29(83), 425-431, 1978.

Squire, V.A., J.P. Dugan, P. Wadhams, P.J. Rottier, and A.K. Liu, Of ocean waves and sea ice, *Annl. Rev. Fluid Mech.*, 27, 115-68, 1995.

Sodhi, D.S., Ice arching and the drift of pack ice through restricted channels, *US Army Cold Regions Research and Engineering Laboratory, CRREL Report 77-18*, 11 pages, 1977.

Sodhi, D.S., Absence of size effect in brittle crushing and breakthrough loads of floating ice sheets, in *Scaling Laws in Ice Mechanics and Ice Dynamics*, 94, Proc. of the IUTAM Symposium, Fairbanks 2000, edited by J.P. Dempsey and H.H. Shen, Kluwer Academic Publishers, 55-66, 2001.

[illegible]

[illegible]

[illegible]

[illegible]

[illegible]

[illegible]

[illegible]

[illegible]

[illegible]

[illegible]

[illegible]

[illegible]

[illegible]

[illegible]

[illegible]

[illegible]

[illegible]

[illegible]

[illegible]

[illegible]

Stefan, J., Uver die Theorie der Eisbildung, insbesondere uber die Eisbildung im Polarmeere: Sitzungsberichte Wien. Akad. Wiss. A, 98, 965 pages, 1890.

Templeton, J.S., On measurements of sea ice pressure, in *Proc. of the International Conference on Port and Ocean Engineering under Arctic Conditions (POAC-79),* 1, 73-88, 1979.

Thorndike, A.S., D.A. Rothrock, G.A. Maykut, and R. Colony, The thickness distribution of sea ice, *J. Geophys. Res.*, 80, 4,501-4,513, 1975.

Thorndike, A.S., and R. Colony, Sea-ice motion in response to geostrophic wind, *J. Geophys. Res.*, 87, 5,845-5,852, 1982.

Thorndike, A.S., Kinematics of sea ice, in *The Geophysics of sea ice*, edited by N. Untersteiner, NATO ASI series B: Physics 146, Plenum Press, 165-281, 1986.

Timco, G.W., and S. O'Brien, Flexural strength equation for seas ice, *Cold Regions Sci. Technol.*, 22(3), 285-298, 1994.

Timokhov, L.A., and D.E. Kheysin, Dynamics of Sea Ice. Mathematical models (in Russian), Hydrometeoizdat, Leningrad, 272 pages, 1987.

Tremblay, L.-B. and L.A. Mysak, Modeling sea ice as a granular material, including the dilatancy effect, *J. Phys. Oceanogr.*, 27(11), 2342-2360, 1997.

Tsurikov, V.L., The formation and composition of the gas content of sea ice, *J. Glaciol.*, 22(86), 67-81, 1979.

Tucker, W.B., III, D.K. Perovich, M.A. Hopkins, and W.D. Hibler, III, On the relationship between local stresses and strains in Arctic pack ice, *Ann. of Glaciol.*, 15, 265-270, 1991.

Tucker, W.B., III, and D.K. Perovich, Stress measurements in drifting pack ice, *Cold Reg. Sci. Technol.*, 20, 119-139, 1992.

Tuhkuri, J., and M. Lensu, Ice tank tests on ridging of an ice sheet, A preliminary report, Helsinki Univ. of Technology, Ship Laboratory, Espoo, 1997.

Tuhkuri, J., and M. Lensu, Ice tank tests on rafting of a broken ice field, Report M-236, Helsinki Univ. of Technology, Ship Laboratory, Espoo, 130 pages, 1998.

Tuhkuri, J. and 10 others, Local ice cover deformation and mesoscale ice dynamics "Ice State" Project, *Third European Marine Science and Technology Conference*, EXPO-98, Lisbon, May 1998.

Tuhkuri, J., M. Lensu, and M. Hopkins, Local ice cover deformation – laboratory experiments, discrete element simulations, and field observations, in *Local ice cover deformation and mesoscale ice dynamics, Part I: Final Report*, edited by K. Riska, and J. Tuhkuri, Helsinki Univ. of Technology, Ship Laboratory, Espoo, 1999.

Untersteiner, N., Natural desalination and equilibrium salinity profile of perennial sea ice, *J. Geophys. Res.*,73(4), 1,251-1,257, 1968.

Walker, E.R., and P. Wadhams, Thick sea-ice floes, *Arctic*, 32(2), 140-147, 1979.

Wadhams, P., The seasonal ice zone, in *The Geophysics of Sea Ice*, edited by N. Untersteiner, NATO ASI series B: Physics 146, Plenum Press, 825-991, 1986.

Wadhans, P., C.B. Sear, D.R. Crane, M.A. Rowe, S.J. Morrison, and D.W.S. Limbert, Basin-scale ice motion and deformation in the Weddell Sea during winter, *Ann. Glaciol.,* 12, 178-186, 1989.

Wadhams, P., W.B. Tucker, W.B. Krabill, R.N. Swift, J.C. Comiso, and N.R. Davis, Relationship between sea ice freeboard and draft in the Arctic Basin, and implications for ice thickness monitoring, *J. Geophys. Res.*, 97(C12), 20,325-20,334, 1992.

Wadhams, P., and N. Davis, The fractal properties of the underside of Arctic sea ice, in *Marine, Offshore and Ice Technology,* edited by T.K.S. Murthy, P.A. Wilson and P. Wadhams, Computational Mechanics Publications, Southampton, Boston, 1994.

Wadhams, P., and S. Wells, Ice surface oscillation measurements on SIMI using strain, heave and tilt sensors, in *Proc. of the Sea Ice Mechanics and Arctic Modeling Workshop*, North West Research Assoc., Inc., Bellevue, WA, 2, 176-189, 1995.

Wadhams, P., Sea ice morphology, in *Physics of Ice Covered Seas*, Lecture notes from a summer school in Savonlinna, June 1994, edited by M. Leppäranta, Helsinki Univ. Printing House, Helsinki, 231-287, 1998.

Wadhams, P., Ice in the Ocean, Gordon and Breach Science Publishers, Netherlands, 351 pages, 2000.

Weeks, W.F., and A. Assur, The mechanical properties of sea ice, Cold Regions Research and Engineering Laboratory Monograph, II-C3, 1967.

Weeks, W.F., and A.J. Gow, Crystal alignments in the fast ice of arctic Alaska, *J. Geophys. Res.*, 84(C10), 1,137-1,146, 1980.

Weeks, W.F., and S.F. Ackley, The growth, structure and properties of sea ice, in *The Geophysics of Sea Ice*, edited by N. Untersteiner, NATO ASI series B: Physics 146, Plenum Press, 9-164, 1986.

Weeks, W.F., Growth conditions and the Structure and Properties of Sea Ice, in *Physics of Ice Covered Seas*, Lecture notes from a summer school in Savonlinna, June 1994, edited by M. Leppäranta, Helsinki Univ. Printing House, Helsinki, 25-104, 1998.

Wells, S.C.S., A. Craze, and C. Shipman, Sea Ice Mechanics Initiative Fall/Winter 1993 Data report 1, Sea Ice Group Internal Report, Scott Polar Research Institute, University of Cambridge, January 1995.

Westerman P.H., and R. Duckworth, Calibration of Delta strainmeters, in *Total Ice Load Programme*, Tarsuit Island, BP Research Centre, BP, 1984.

Wettlaufer, J.S., M.G. Worster, and H.E. Huppert, The phase evolution of young sea ice, *Geophys. Res. Lett.*, 24(10), 1251-1254, 1997.

Wettlaufer, J.S., Introduction to crystallisation phenomena in natural and artificial sea ice, in *Physics of Ice Covered Seas*, Lecture notes from a summer school in Savonlinna, June 1994, edited by M. Leppäranta, Helsinki Univ. Printing House, Helsinki, 105-194, 1998.

WMO sea ice nomenclature, World Meteorological Organization, Rep. 259, T.P. 145, Geneva, 147 pages and 8 suppl., 1970.

Wood, R.A., A.B. Keen, J.F.B. Mitchell, and J.M. Gregory, Changing spatial structure of the thermohaline circulation in response to atmospheric $CO_2$ forcing in a climate model, *Nature,* 399, 572-575, 1999.

Worster, M.G., Instabilities of the liquid and mushy regions during solidification of alloys, *J. Fluid Mech.*, 237, 649-669, 1992.

Yen, Yi-C., Review of thermal properties of snow, ice and sea ice, USA Cold Regions Research and Engineering Laboratory, Cold Regions Environmental Engineering Laboratory Report, 81-10, 1981.

Yershov, E.D., General geocryology, Cambridge University Press, 580 pages, 1998.

Zhang, Yu., W. Maslowski, and A.J. Semtner, Impact of mesoscale ocean currents on sea ice in high-resolution Arctic ice and ocean simulations, *J. Geophys. Res.*, 104(C8), 18,409-18,429, 1999.

ZIP-97 data report, *Report series in Geophysics N37*, edited by J. Haapala and M. Leppäranta, Department of Geophysics, Univ. of Helsinki, 1997.

# Appendix

**Table A1.** BP Delta strainmeter characteristics.

| **Type of sensor** | **BP-Delta** |
|---|---|
| Manufacturer | British Petroleum |
| Type of transducer | Sangamo AC/AC LVDT |
| Length of gauge | 0.30 m |
| Maximal range of measurements | $3 \cdot 10^{-2}$ m·m$^{-1}$ |
| Lowest detectable deformation limited by electronics | $1 \cdot 10^{-9}$ m |
| Lowest detectable strain-rate | $1 \cdot 10^{-9}$ m· m$^{-1}$ s$^{-1}$ |
| Resolution of strain measurements | |
| with 16-bit digital card | $2 \cdot 10^{-9}$ m·m$^{-1}$ |
| with 12-bit digital card | $3 \cdot 10^{-8}$ m·m$^{-1}$ |
| Thermal expansion coefficient of the carbon fibre rod | $+1.5 \cdot 10^{-6}$ °C$^{-1}$ |
| Overall thermal expansion coefficient of the gauges | $-2.33 \cdot 10^{-6}$ °C$^{-1}$ |
| Residual sensor drift, probably due to thermal effect | $< 5 \cdot 10^{-9}$ m·m$^{-1}$·s$^{-1}$ |
| Total noise level with 12-bit card | $1 \cdot 10^{-8}$ m·m$^{-1}$ |
| Total power average consumption | 50 mA |
| Each leg power consumption | |
| average | 15 mA |
| during re-zero | 500 mA |
| Working temperature range | -40°C – -1°C |

**Source:** Child and Duckworth (1982).

**Table A2.** Characteristics of stress gauges.

| **Type of sensor** | **CRREL stress sensor** |
|---|---|
| Manufacturer | CRREL in house |
| Linear temperature relation | 5kPa °C$^{-1}$ |
| Resolution | 20kPa |
| Maximal stress | up to 2.5 MPa |
| Zero datum accurracy | ± 20 kPa |
| Maximal instrument drift in the sensors | 30 kPa over 6 months |

**Source:** Cox and Johnson (1983).

**Table A3.** Characteristics of tiltmeter.

| **Type of sensor** | **Tiltmeter ELH-46/47** |
|---|---|
| Manufacturer | TILT Measurements Ltd. |
| Limits of tiltmeter measurements | ±0.5° |
| Discrimination for tilt | 0.5 microrad |
| Datum temperature drift | 1.5 microrad $°C^{-1}$ |
| Datum change for ±5 arcdegree tilt about cross axis | 60 arcsec |
| Temperature coefficient (-10°C to +25°C) | max +0.2 % |

**Source:** Description of tiltmeter transducers (1985).

**Table A4.** Characteristics of linear accelerometer.

| **Type of sensor** | **Linear accelerometers LSM** |
|---|---|
| Manufacturer | Schaevitz Eng. Corp. |
| Maximal range of measurements for nominal natural frequency <=70 Hz | $\pm 4.9\ m \cdot s^{-2}$ |
| Resolution | $5 \cdot 10^{-5} m \cdot s^{-2}$ |
| Thermal coefficient of sensitivity | $1 \cdot 10^{-3} m \cdot s^{-2}$ |
| Cross-axis sensitivity | ±0.002 *g* per *g* |

**Source:** Linear and angular servo accelerometers (1982).

# Tables

## Calibration coefficients

**Table T1.** Calibration coefficients for strainmeter STM-1.

| | Arm A | Arm B | Arm C |
|---|---|---|---|
| p1 [volt·°C$^{-1}$] | 0.10258065 | 0.10774194 | 0.10897436 |
| p2 [volt·°C$^{-1}$] | 0.10601093 | 0.11195652 | 0.11483516 |
| p3 [volt·°C$^{-1}$] | 0.10000000 | 0.11022727 | 0.10786517 |
| p4 [volt·°C$^{-1}$] | 0.10081967 | 0.10406504 | 0.10406504 |
| p14 [volt·°C$^{-1}$] | 0.10235281 | 0.10849769 | 0.10893493 |
| std(p14) [volt·°C$^{-1}$] | 0.0026658313 | 0.0034241553 | 0.0044599902 |
| k6 high [μm m$^{-1}$ volt$^{-1}$] | 24.049675 | 22.667938 | 22.692764 |
| std of k6 high [μm m$^{-1}$ volt$^{-1}$] | 0.61745569 | 0.72363644 | 0.91804529 |
| ε of k6 high [%] | 2.5674181 | 3.1923347 | 4.0455420 |
| k5 low [μm m$^{-1}$ volt$^{-1}$] | 242.42072 | 232.34636 | 230.33155 |
| std of k5 low [μm m$^{-1}$ volt$^{-1}$] | 6.2239534 | 7.4172735 | 9.3181597 |
| ε of k5 low [%] | 2.5674181 | 3.1923347 | 4.0455420 |

**Table T2.** Calibration coefficients for strainmeter STM-2.

| | Arm A | Arm B | Arm C |
|---|---|---|---|
| p1 [volt·°C$^{-1}$] | 0.11013216 | 0.11674009 | 0.10572687 |
| p2 [volt·°C$^{-1}$] | 0.10445364 | 0.10820783 | 0.098765763 |
| p12 [volt·°C$^{-1}$] | 0.10729290 | 0.11247396 | 0.10224632 |
| std(p12) [volt·°C$^{-1}$] | 0.0040153192 | 0.0060332163 | 0.0049222473 |
| k6 high [μm m$^{-1}$ volt$^{-1}$] | 22.966022 | 21.690880 | 23.939389 |
| std of k6 high [μm m$^{-1}$ volt$^{-1}$] | 0.85947824 | 1.1635206 | 1.1524679 |
| ε of k6 high [%] | 3.7423905 | 5.3641005 | 4.8141072 |
| k5 low [μm m$^{-1}$ volt$^{-1}$] | 234.94241 | 220.81316 | 245.37874 |
| std of k5 low [μm m$^{-1}$ volt$^{-1}$] | 8.7924623 | 11.844640 | 11.812796 |
| ε of k5 low [%] | 3.7423905 | 5.3641005 | 4.8141072 |

**Table T3**. Calibration coefficients for strainmeter STM-11.

| | Arm A | Arm B | Arm C |
|---|---|---|---|
| p1 [volt·°C$^{-1}$] | 0.10288462 | 0.10788462 | 0.10915978 |
| p2 [volt·°C$^{-1}$] | 0.10580514 | 0.11161027 | 0.11502165 |
| p3 [volt·°C$^{-1}$] | 0.11065574 | 0.10406504 | 0.10406504 |
| p13 [volt·°C$^{-1}$] | 0.10644850 | 0.10785331 | 0.10941549 |
| std(p13) [volt·°C$^{-1}$] | 0.0039253051 | 0.0037727126 | 0.0054827773 |
| k6 high [μm m$^{-1}$ volt$^{-1}$] | 23.133545 | 22.804762 | 22.602782 |
| std of k6 high [μm m$^{-1}$ volt$^{-1}$] | 0.84607230 | 0.79854690 | 1.1300712 |
| ε of k6 high [%] | 3.6573396 | 3.5016673 | 4.9996997 |
| k5 low [μm m$^{-1}$ volt$^{-1}$] | 233.18614 | 233.74881 | 229.41824 |
| std of k5 low [μm m$^{-1}$ volt$^{-1}$] | 8.5284088 | 8.1851057 | 11.470223 |
| ε of k5 low [%] | 3.6573396 | 3.5016673 | 4.9996997 |

**Table T4**. Calibration coefficients for strainmeter STM-15.

| | Arm A | Arm B | Arm C |
|---|---|---|---|
| p1 [volt·°C$^{-1}$] | 0.10296296 | 0.10888889 | 0.11029412 |
| p2 [volt·°C$^{-1}$] | 0.10572917 | 0.11191710 | 0.11458333 |
| p3 [volt·°C$^{-1}$] | 0.097849462 | 0.10989011 | 0.10760870 |
| p4 [volt·°C$^{-1}$] | 0.10149636 | 0.10453396 | 0.10449892 |
| p14 [volt·°C$^{-1}$] | 0.10200949 | 0.10880752 | 0.10924627 |
| std(p14) [volt·°C$^{-1}$] | 0.0032819831 | 0.0031150917 | 0.0042740004 |
| k6 high [μm m$^{-1}$ volt$^{-1}$] | 23.947322 | 22.936073 | 22.625813 |
| std of k6 high [μm m$^{-1}$ volt$^{-1}$] | 0.77587627 | 0.66688470 | 0.88014257 |
| ε of k6 high [%] | 3.2399291 | 2.9075801 | 3.8899930 |
| k5 low [μm m$^{-1}$ volt$^{-1}$] | 243.30479 | 231.65434 | 229.65201 |
| std of k5 low [μm m$^{-1}$ volt$^{-1}$] | 7.8829029 | 6.7355354 | 8.9334471 |
| ε of k5 low [%] | 3.2399291 | 2.9075801 | 3.8899930 |

**Table T5.** Calibration coefficients for strainmeter STM-17.

| | Arm A | Arm B | Arm C |
|---|---|---|---|
| p1 [volt·°C$^{-1}$] | 0.09588218 | 0.10733979 | 0.10473835 |
| p2 [volt·°C$^{-1}$] | 0.10126582 | 0.10365854 | 0.11234568 |
| p12 [v/°C] | 0.09857400 | 0.10549916 | 0.10854201 |
| std(p12) [volt·°C$^{-1}$] | 0.00380681 | 0.00260304 | 0.00537919 |
| k6 high [μm m$^{-1}$ volt$^{-1}$] | 25.121293 | 23.386787 | 22.405865 |
| std of k6 high [μm m$^{-1}$ volt$^{-1}$] | 0.97015480 | 0.57703535 | 1.1104040 |
| ε of k6 high [%] | 3.8618825 | 2.4673562 | 4.9558631 |
| k5 low [μm m$^{-1}$ volt$^{-1}$] | 255.73476 | 237.60975 | 228.76388 |
| std of k5 low [μm m$^{-1}$ volt$^{-1}$] | 9.8761759 | 5.8626791 | 11.337225 |
| ε of k5 low [%] | 3.8618825 | 2.4673562 | 4.9558631 |

**Table T6.** Calibration coefficients for strainmeter STM-20.

| | Arm A | Arm B | Arm C |
|---|---|---|---|
| p1 [volt·°C$^{-1}$] | 0.10449536 | 0.11683435 | 0.10957403 |
| p2 [volt·°C$^{-1}$] | 0.11185463 | 0.12354250 | 0.11324513 |
| p12 [volt·°C$^{-1}$] | 0.10817499 | 0.12018843 | 0.11140958 |
| std(p12) [volt·°C$^{-1}$] | 0.0052037840 | 0.0047433823 | 0.0025958664 |
| k6 high [μm m$^{-1}$ volt$^{-1}$] | 22.524409 | 21.767418 | 22.189038 |
| std of k6 high [μm m$^{-1}$ volt$^{-1}$] | 1.0835421 | 0.81961138 | 0.51700921 |
| ε of k6 high [%] | 4.8105240 | 3.9466215 | 2.3300208 |
| k5 low [μm m$^{-1}$ volt$^{-1}$] | 229.52373 | 219.75092 | 224.99685 |
| std of k5 low [μm m$^{-1}$ volt$^{-1}$] | 11.041294 | 8.2780749 | 5.2424734 |
| ε of k5 low [%] | 4.8105240 | 3.9466215 | 2.3300208 |

**Table T7.** Calibration coefficients for strainmeter STM-28.

| | Arm A | Arm B | Arm C |
|---|---|---|---|
| p1 [volt·°C$^{-1}$] | 0.10314216 | 0.10668286 | 0.11804881 |
| p2 [volt·°C$^{-1}$] | 0.10651163 | 0.10837209 | 0.11064815 |
| p3 [volt·°C$^{-1}$] | 0.10964912 | 0.11578947 | 0.11739130 |
| p13 [volt·°C$^{-1}$] | 0.10643430 | 0.11028148 | 0.11536275 |
| std(p13) [volt·°C$^{-1}$] | 0.0032541706 | 0.0048442642 | 0.0040961830 |
| k6 high [μm m$^{-1}$ volt$^{-1}$] | 22.903054 | 21.864573 | 21.526166 |
| std of k6 high [μm m$^{-1}$ volt$^{-1}$] | 0.70133809 | 0.94004743 | 0.77988161 |
| ε of k6 high [%] | 3.0622034 | 4.2994090 | 3.6229472 |
| k5 low [μm m$^{-1}$ volt$^{-1}$] | 233.15309 | 228.70344 | 217.41427 |
| std of k5 low [μm m$^{-1}$ volt$^{-1}$] | 7.1396218 | 9.8328961 | 7.8768043 |
| ε of k5 low [%] | 3.0622034 | 4.2994090 | 3.6229472 |

**Table T8.** Thermal expansion coefficients of the calibration jig.

| | Arm A | Arm B | Arm C |
|---|---|---|---|
| E [μm·°C$^{-1}$] | 6.740 | 6.857 | 6.818 |
| $L_{jig}$ [m] | 0.29750 | 0.29975 | 0.3000 |
| β [°C$^{-1}$] | 22.660 | 22.876 | 22.730 |

[illegible]

| [illegible] | [illegible] | [illegible] |
|---|---|---|
| [illegible] | [illegible] | [illegible] |
| | [illegible] | [illegible] |
| | [illegible] | [illegible] |
| | | [illegible] |
| | | [illegible] |
| | | [illegible] |
| | | [illegible] |

[illegible]

| [illegible] | [illegible] | [illegible] | |
|---|---|---|---|
| [illegible] | [illegible] | [illegible] | |
| [illegible] | [illegible] | [illegible] | |
| [illegible] | [illegible] | [illegible] | |

**Table T9.** Parameters of BP-delta strainmeters (Westerman and Duckworth, 1984).

| Gauge | Arm | Length [m] | k [volt·$\mu m^{-1}$] | High/Low gain ratio |
|---|---|---|---|---|
| STM-1 | A | 0.30 | 0.0140 | 10.08 |
| | B | 0.30 | 0.0145 | 10.25 |
| | C | 0.30 | 0.0143 | 10.15 |
| STM-2 | A | 0.30 | 0.0140 | 10.23 |
| | B | 0.30 | 0.0146 | 10.18 |
| | C | 0.30 | 0.0143 | 10.25 |
| STM-4 | A | 0.30 | 0.0135 | 10.17 |
| | B | 0.30 | 0.0149 | 10.31 |
| | C | 0.30 | 0.0139 | 10.31 |
| STM-5 | A | 0.30 | 0.0134 | 10.20 |
| | B | 0.30 | 0.0147 | 10.27 |
| | C | 0.30 | 0.0149 | 10.22 |
| STM-8 | A | 0.30 | 0.0145 | 10.15 |
| | B | 0.30 | 0.0146 | 10.23 |
| | C | 0.30 | 0.0150 | 10.13 |
| STM-11 | A | 0.30 | 0.0144 | 10.16 |
| | B | 0.30 | 0.0142 | 10.16 |
| | C | 0.30 | 0.0150 | 10.25 |
| STM-15 | A | 0.30 | 0.0135 | 10.16 |
| | B | 0.30 | 0.0140 | 10.10 |
| | C | 0.30 | 0.0143 | 10.15 |
| STM-16 | A | 0.30 | 0.0144 | 10.20 |
| | B | 0.30 | 0.0153 | 10.16 |
| | C | 0.30 | 0.0154 | 10.30 |
| STM-17 | A | 0.30 | 0.0128 | 10.18 |
| | B | 0.30 | 0.0138 | 10.16 |
| | C | 0.30 | 0.0148 | 10.21 |
| STM-20 | A | 0.30 | 0.0139 | 10.19 |
| | B | 0.30 | 0.0152 | 10.10 |
| | C | 0.30 | 0.0146 | 10.14 |
| STM-26 | A | 0.30 | 0.0137 | 10.17 |
| | B | 0.30 | 0.0145 | 10.25 |
| | C | 0.30 | 0.0160 | 10.20 |
| STM-28 | A | 0.30 | 0.0142 | 10.18 |
| | B | 0.30 | 0.0147 | 10.46 |
| | C | 0.30 | 0.0155 | 10.10 |
| STM-30 | A | 0.30 | 0.0140 | 10.16 |
| | B | 0.30 | 0.0150 | 10.17 |
| | C | 0.30 | 0.0154 | 10.20 |

**Table T10.** Strainmeter calibrations performed by manufacturer (BP), by Marine & Field Measurement (MFM) and at SPRI.

| Gauge | Arm | k1 BP low gain [μm m$^{-1}$ volt$^{-1}$] | k2 BP high gain [μm m$^{-1}$ volt$^{-1}$] | k3 MFM low gain [μm m$^{-1}$ volt$^{-1}$] | k4 MFM high gain [μm m$^{-1}$ volt$^{-1}$] | k5 SPRI low gain [μm m$^{-1}$ volt$^{-1}$] | k6 SPRI high gain [μm m$^{-1}$ volt$^{-1}$] |
|---|---|---|---|---|---|---|---|
| STM-1 | A | 238.1 | 23.62 | 189.07 | 18.27 | 242.42072 | 24.049675 |
| | B | 229.9 | 22.43 | 191.73 | 18.58 | 232.34636 | 22.667938 |
| | C | 233.1 | 22.96 | 191.60 | 18.75 | 230.33155 | 22.692764 |
| STM-2 | A | 239.8 | 23.44 | – | – | 234.94241 | 22.966022 |
| | B | 228.3 | 22.43 | – | – | 220.81316 | 21.690880 |
| | C | 250.6 | 24.45 | – | – | 245.37874 | 23.939389 |
| STM-4 | A | 245.1 | 24.10 | 197.20 | 19.22 | $245.1^{S+}$ | $24.10^{S+}$ |
| | B | 226.7 | 22.08 | 192.80 | 18.94 | $226.7^{S+}$ | $22.08^{S+}$ |
| | C | 223.7 | 21.89 | 185.87 | 18.15 | $223.7^{S+}$ | $21.89^{S+}$ |
| STM-5 | A | 234.7 | 23.13 | – | – | $234.7^{S}$ | $23.13^{S}$ |
| | B | 229.9 | 23.01 | – | – | $229.9^{S}$ | $23.01^{S}$ |
| | C | 233.1 | 21.89 | – | – | $233.1^{S}$ | $21.89^{S}$ |
| STM-8 | A | 229.8 | 22.78 | – | – | $229.8^{S}$ | $22.78^{S}$ |
| | B | 238.1 | 23.43 | – | – | $238.1^{S}$ | $23.43^{S}$ |
| | C | 222.2 | 21.98 | – | – | $222.2^{S}$ | $21.98^{S}$ |
| STM-11 | A | 231.5 | 22.80 | 189.47 | 18.54 | 233.18614 | 23.133545 |
| | B | 234.7 | 23.10 | 189.07 | 18.66 | 233.74881 | 22.804762 |
| | C | 222.2 | 22.00 | 194.40 | 19.12 | 229.41824 | 22.602782 |
| STM-15 | A | 246.9 | 24.30 | – | – | 243.30479 | 23.947322 |
| | B | 238.1 | 23.57 | – | – | 231.65434 | 22.936073 |
| | C | 233.1 | 22.96 | – | – | 229.65201 | 22.625813 |

**Table T10.** Strainmeter calibrations (continued).

| Gauge | Arm | k1 BP low gain [μm $m^{-1}$ $volt^{-1}$] | k2 BP high gain [μm $m^{-1}$ $volt^{-1}$] | k3 BAS low gain [μm $m^{-1}$ $volt^{-1}$] | k4 BAS high gain [μm $m^{-1}$ $volt^{-1}$] | k5 SPRI low gain [μm $m^{-1}$ $volt^{-1}$] | k6 SPRI high gain [μm $m^{-1}$ $volt^{-1}$] |
|---|---|---|---|---|---|---|---|
| STM-16 | A | 231.5 | 22.69 | – | – | $231.5^{S}$ | $22.69^{S}$ |
| | B | 217.8 | 21.44 | – | – | $217.8^{S}$ | $21.44^{S}$ |
| | C | 216.4 | 21.01 | – | – | $216.4^{S}$ | $21.01^{S}$ |
| STM-17 | A | 260.4 | 25.58 | – | – | $255.73476^{+}$ | $25.121293^{+}$ |
| | B | 241.5 | 23.77 | – | – | $237.60975^{+}$ | $23.386787^{+}$ |
| | C | 225.2 | 22.06 | – | – | $228.76388^{+}$ | $22.405865^{+}$ |
| STM-20 | A | 239.8 | 23.53 | – | – | 229.52373 | 22.524409 |
| | B | 219.3 | 21.71 | – | – | 219.75092 | 21.767418 |
| | C | 228.3 | 22.51 | – | – | 224.99685 | 22.189038 |
| STM-26 | A | 243.3 | 23.92 | – | – | $243.3^{S}$ | $23.92^{S}$ |
| | B | 229.9 | 22.42 | – | – | $229.9^{S}$ | $22.42^{S}$ |
| | C | 208.3 | 20.42 | – | – | $208.3^{S}$ | $20.42^{S}$ |
| STM-28 | A | 234.7 | 23.08 | – | – | 233.15309 | 22.903054 |
| | B | 226.7 | 22.12 | – | – | 228.70344 | 21.864573 |
| | C | 215.0 | 21.08 | – | – | 217.41427 | 21.526166 |
| STM-30 | A | 238.1 | 23.43 | – | – | $238.1^{S}$ | $23.43^{S}$ |
| | B | 222.2 | 21.85 | – | – | $222.2^{S}$ | $21.85^{S}$ |
| | C | 216.4 | 21.20 | – | – | $216.4^{S}$ | $21.20^{S}$ |

**Notes:** $^{S}$ – calibration performed at SPRI for the SIMI experiment only;
$^{+}$ – post-experiment calibration was not possible as sensor was destroyed.

**Table T11.** Estimated accuracy of the strainmeter measurements.

| Parameter | Units | Value |
|---|---|---|
| klow_BP_max | [volt$^{-1}$] | $260.4 \cdot 10^{-6}$ |
| klow_BP_min | [volt$^{-1}$] | $215.0 \cdot 10^{-6}$ |
| delta_klow_BP | [volt$^{-1}$] | $1.470 \cdot 10^{-6}$ |
| eps_klow_BP | [%] | 0.562 |
| delta_khigh_BP | [volt$^{-1}$] | $1.586 \cdot 10^{-7}$ |
| eps_khigh_BP | [%] | 0.644 |
| klow_max | [volt$^{-1}$] | $262.72 \cdot 10^{-6}$ |
| klow_min | [volt$^{-1}$] | $220.75 \cdot 10^{-6}$ |
| delta_klow_max | [volt$^{-1}$] | $1.651 \cdot 10^{-5}$ |
| eps_klow_max | [%] | 6.285 |
| khigh_max | [volt$^{-1}$] | $25.807 \cdot 10^{-6}$ |
| khigh_min | [volt$^{-1}$] | $21.621 \cdot 10^{-6}$ |
| delta_khigh_max | [volt$^{-1}$] | $1.638 \cdot 10^{-6}$ |
| eps_khigh_max | [%] | 7.529 |
| delta_D_max | [m·m$^{-1}$] | $9.3 \cdot 10^{-7}$ |
| eps_D_max | [%] | 0.788 |

**Table T12.** Strainmeter calibration coefficients used during ZIP-97 experiment.

| Gauge | Calibration coefficients (high gain), [$10^{-6}$ volt$^{-1}$] | | |
|---|---|---|---|
| | Arm A | Arm B | Arm C |
| STM-1 | 23.62 | 22.43 | 22.96 |
| STM-2 | 23.44 | 22.43 | 24.45 |
| STM-4$^{+}$ | 24.10 | 22.08 | 21.89 |
| STM-11 | 22.80 | 23.10 | 22.00 |
| STM-17$^{+}$ | 25.58 | 23.77 | 22.06 |
| STM-28 | 23.08 | 22.12 | 21.08 |

**Note:** $^{+}$ – sensor was destroyed during the experiment.

**Table T13.** Strainmeter calibration coefficients used during SIMI experiment.

| Site | Gauge | Calibration coefficients (high gain), [$10^{-6}$ $volt^{-1}$] | | |
|---|---|---|---|---|
| | | Arm A | Arm B | Arm C |
| C1 | STM-5 | 23.13 | 23.01 | 21.89 |
| B | STM-8 | 22.78 | 23.43 | 21.98 |
| F | STM-16 | 22.69 | 21.44 | 21.01 |
| D1 | STM-17 | 25.58 | 23.77 | 22.06 |
| C2 | STM-20 | 23.53 | 21.71 | 22.51 |
| D2 | STM-26 | 23.92 | 22.42 | 20.42 |
| A | STM-30 | 23.43 | 21.85 | 21.20 |

**Table T14.** Calibration coefficients for tiltmeters.

| Gauge | Calibration coefficients, [$volt^{-1}$] | |
|---|---|---|
| | $\alpha$ | $\beta$ |
| ELH 46 | $1.0561 \cdot 10^{-1}$ | $3.7204 \cdot 10^{-4}$ |
| ELH 47 | $1.0561 \cdot 10^{-2}$ | $3.7204 \cdot 10^{-4}$ |

**Table T15.** Calibration coefficients for accelerometers.

| Gauge | Calibration coefficient, [volt $g^{-1}$] |
|---|---|
| Schaevitz S/N 3255 | 2.5293 |
| Schaevitz S/N 3256 | 2.5467 |
| Schaevitz S/N 3257 | 2.5575 |
| Schaevitz S/N 3258 | 2.5246 |
| Schaevitz S/N 3259 | 2.5782 |
| Schaevitz S/N 3260 | 2.4733 |
| Schaevitz S/N 2271 | 2.5502 |

## Measurements

**Table T16.** Observed ice, snow and near surface air temperatures, Crack Site, TMR-1 (near the shore).

| Depth [cm] | Time [days] | | | | | |
|---|---|---|---|---|---|---|
| | 15.4549 | 6.4583 | 17.75 | 18.375 | 19.7278 | 0.4028 |
| -150 | NaN | -6.8 | NaN | -8.2 | -2.9 | -5.6 |
| -2 | NaN | NaN | NaN | NaN | -3.1 | NaN |
| 10 | NaN | NaN | NaN | NaN | NaN | NaN |
| 20 | -6.8 | -6.8 | -5.4 | -8.0 | -4.5 | -4.7 |
| 30 | -6.0 | -7.4 | NaN | -7.8 | -4.4 | -4.7 |
| 40 | -4.1 | -6.1 | -4.3 | -6.2 | -4.5 | -4.1 |
| 50 | -2.2 | -4.4 | -3.6 | -4.8 | -4.1 | -3.4 |
| 60 | -1.6 | -3.0 | -3.0 | -3.7 | -3.7 | -2.8 |
| 70 | -1.4 | -1.5 | -2.2 | -2.3 | -2.5 | -2.0 |
| 80 | -1.0 | -0.9 | -0.9 | -0.9 | -1.2 | -0.8 |
| 90 | -1.4 | -1.3 | -1.2 | -1.2 | -1.7 | -1.2 |
| 100 | -1.2 | -1.1 | -1.0 | -0.9 | -1.4 | -0.9 |
| 110 | -1.1 | -1.0 | -0.8 | -0.7 | 1.2 | -0.8 |
| 120 | -1.1 | -1.0 | -0.8 | -0.7 | -1.2 | -0.8 |
| 130 | -1.1 | -0.9 | -0.6 | -0.6 | -1.2 | -0.8 |
| 140 | NaN | NaN | NaN | NaN | NaN | NaN |
| 150 | -0.7 | -0.5 | -0.5 | -0.5 | -0.9 | -0.6 |
| 160 | -0.7 | -0.5 | -0.5 | -0.4 | -0.8 | -0.5 |
| 170 | -0.8 | -0.7 | -0.6 | -0.5 | -1.0 | -0.6 |
| 180 | -0.8 | -0.7 | -0.8 | -0.6 | -0.9 | -0.6 |
| 190 | -0.9 | -0.9 | -1.0 | -0.8 | -1.2 | -0.8 |
| 200 | -1.2 | -1.1 | -1.2 | -1.0 | -1.3 | -1.1 |
| 210 | -0.6 | -0.6 | -0.7 | -0.5 | -0.8 | -0.6 |
| 220 | NaN | NaN | NaN | NaN | NaN | NaN |
| 230 | NaN | NaN | NaN | NaN | NaN | NaN |

**Note:** NaN - no observations. Ice temperature measurements were performed using thermistor chain, air and snow temperatures (rows 1 and 2) taken by portable thermistor probe; temperatures below 100 cm depth are rather conventional as thermistors were located in water. Bold lines show upper and lower ice surfaces.

[illegible]

**Table T17.** Observed ice, snow and near surface air temperatures, Crack Site, TMR-2 (far from the shore).

| Depth [cm] | Time [days] | | | | | |
|---|---|---|---|---|---|---|
| | 5.4653 | 16.4653 | 17.75 | 8.3681 | 19.7264 | 20.3958 |
| -150 | NaN | -6.8 | NaN | -8.2 | -2.9 | -5.6 |
| -2 | NaN | NaN | NaN | NaN | -3.1 | NaN |
| 10 | -5.6 | -5.5 | 4.9 | -7.1 | -4.0 | -2.6 |
| 20 | -6.2 | -7.6 | -5.6 | -7.7 | -4.4 | -3.8 |
| 30 | -6.1 | -8.3 | -5.8 | -8.2 | -5.1 | -4.8 |
| 40 | -3.7 | -6.4 | -4.8 | -6.3 | -4.9 | -4.3 |
| 50 | -1.9 | -4.6 | -4.3 | -5.0 | -4.5 | -3.6 |
| 60 | NaN | NaN | NaN | NaN | NaN | NaN |
| 70 | -1.2 | -1.2 | -2.0 | -2.0 | -2.4 | -1.9 |
| 80 | -1.3 | -1.1 | -1.2 | -1.2 | -1.5 | -1.2 |
| 90 | -0.9 | -0.8 | -0.7 | -0.6 | -1.0 | -0.7 |
| 100 | -1.0 | -0.9 | -0.8 | -0.7 | -1.1 | -0.8 |
| 110 | -1.1 | -1.2 | -0.9 | -0.8 | -1.3 | -1.0 |
| 120 | -0.6 | -1.0 | -0.8 | -0.6 | -1.0 | -0.8 |
| 130 | -0.9 | -1.1 | -0.9 | -0.8 | -1.2 | -0.9 |
| 140 | -0.8 | -1.0 | -0.8 | -0.7 | -1.1 | -0.8 |
| 150 | -0.5 | -0.7 | -0.6 | -0.5 | -1.1 | -0.6 |
| 160 | -0.8 | -0.8 | -0.7 | -0.6 | -1.1 | -0.8 |
| 170 | -0.8 | -0.8 | -0.7 | -0.5 | -1.1 | -0.7 |
| 180 | -0.8 | -0.8 | -0.8 | -0.6 | -1.1 | -0.7 |
| 190 | NaN | NaN | NaN | NaN | NaN | NaN |
| 200 | -1.4 | -1.3 | -1.2 | -1.1 | -1.4 | -1.2 |
| 210 | -1.2 | -1.1 | -1.0 | -0.9 | -1.2 | -0.9 |
| 220 | NaN | NaN | NaN | NaN | NaN | NaN |
| 230 | NaN | NaN | NaN | NaN | NaN | NaN |

**Note:** NaN - no observations. Ice temperature measurements were performed using thermistor chain, air and snow temperatures (rows 1 and 2) taken by portable thermistor probe; temperatures below 100 cm depth are rather conventional as thermistors were located in water. Bold lines show upper and lower ice surfaces.

[illegible]

**Table T18.** Observed ice, snow and near surface air temperatures, Hut Site, TMR-4 (near the ridge).

| Depth [cm] | Time [days] | | | | | |
|---|---|---|---|---|---|---|
| | 15.5312 | 16.4979 | 17.5208 | 18.5139 | 19.5 | 20.4431 |
| -150 | NaN | -6.1 | -5.6 | -5.7 | NaN | -6.4 |
| -2 | NaN | NaN | -5.2 | NaN | NaN | NaN |
| 10 | -4.7 | -4.8 | -2.5 | -2.7 | NaN | -2.7 |
| 20 | -5.5 | -5.8 | -3.9 | -4.4 | NaN | -3.9 |
| 30 | -6.0 | -6.2 | -4.9 | -5.4 | NaN | -3.8 |
| 40 | -2.0 | -3.6 | -3.5 | -4.1 | NaN | -2.9 |
| 50 | -1.4 | -1.8 | -2.1 | -3.7 | NaN | -2.3 |
| 60 | NaN | -1.6 | -1.7 | -2.3 | NaN | -2.3 |
| 70 | -1.2 | -1.2 | -1.2 | -1.6 | NaN | -1.4 |
| 80 | -1.1 | -1.1 | -1.0 | -1.2 | NaN | -1.1 |
| 90 | -1.3 | -1.2 | -1.2 | -1.0 | NaN | -1.2 |
| 100 | -1.3 | -1.2 | -1.1 | -0.9 | NaN | -1.2 |
| 110 | -1.1 | -1.1 | -0.9 | -0.8 | NaN | -1.0 |
| 120 | -1.1 | -0.9 | -0.8 | -0.7 | NaN | -0.8 |
| 130 | -1.2 | -1.1 | -1.0 | -1.2 | NaN | -1.1 |
| 140 | -1.3 | -1.2 | -1.1 | -1.2 | NaN | -1.1 |
| 150 | -1.0 | -0.8 | -0.7 | -0.8 | NaN | -0.7 |
| 160 | -0.8 | -0.7 | -0.6 | -0.8 | NaN | -0.7 |
| 170 | -1.1 | -1.0 | -0.9 | -0.8 | NaN | -1.0 |
| 180 | -0.9 | -0.7 | -0.6 | -0.8 | NaN | -0.8 |
| 190 | -1.2 | -1.1 | -1.0 | -0.9 | NaN | -1.0 |
| 200 | -1.3 | -1.2 | -1.2 | -0.8 | NaN | -1.2 |
| 210 | -1.1 | -1.0 | -0.9 | -0.7 | NaN | -0.9 |
| 220 | -1.1 | -1.0 | -0.9 | -0.8 | NaN | -0.9 |
| 230 | NaN | NaN | NaN | NaN | NaN | NaN |

**Note:** NaN - no observations. Ice temperature measurements were performed using thermistor chain, air and snow temperatures (rows 1 and 2) taken by portable thermistor probe; temperatures below 100 cm depth are rather conventional as thermistors were located in water. Bold lines show upper and lower ice surfaces.

**Table T19.** Observed ice, snow and near surface air temperatures, Hut Site, TMR-3 (far from the ridge).

| Depth [cm] | Time [days] | | | | | |
|---|---|---|---|---|---|---|
| | 5.5361 | 16.4931 | 17.5132 | 18.5208 | 19.5 | 20.4375 |
| -150 | NaN | -6.1 | -5.6 | -5.7 | NaN | -6.4 |
| -2 | NaN | NaN | -5.2 | NaN | NaN | NaN |
| 10 | -3.8 | -4.0 | -3.4 | -3.7 | NaN | -2.7 |
| 20 | -4.9 | -5.8 | -4.2 | -4.1 | NaN | -3.5 |
| 30 | -5.1 | -6.5 | -5.6 | -4.9 | NaN | -4.7 |
| 40 | -3.4 | -5.4 | NaN | NaN | NaN | -4.5 |
| 50 | -2.0 | -3.9 | -4.0 | -2.4 | NaN | -3.8 |
| 60 | -1.6 | -2.9 | -3.2 | -2.2 | NaN | -3.4 |
| 70 | -1.2 | -1.3 | -1.7 | -1.2 | NaN | -2.4 |
| 80 | -1.1 | -1.1 | -1.2 | -1.1 | NaN | -1.9 |
| 90 | -1.2 | -1.2 | -1.0 | -1.2 | NaN | -1.3 |
| 100 | -1.0 | -1.0 | -0.8 | -1.2 | NaN | -0.9 |
| 110 | -1.0 | -1.0 | -0.7 | -1.0 | NaN | -0.9 |
| 120 | -0.8 | -0.7 | -0.6 | -0.8 | NaN | -0.7 |
| 130 | -1.2 | -1.1 | -1.0 | -1.0 | NaN | -1.1 |
| 140 | -1.2 | -1.1 | -1.0 | -1.1 | NaN | -1.1 |
| 150 | -0.9 | -0.7 | -0.7 | -0.6 | NaN | -0.7 |
| 160 | -0.9 | -0.9 | -0.8 | -0.7 | NaN | -0.8 |
| 170 | -0.9 | -0.9 | -0.7 | -0.9 | NaN | -0.8 |
| 180 | -0.9 | -0.9 | -0.7 | -0.7 | NaN | -0.9 |
| 190 | -1.0 | -1.1 | -0.8 | -1.0 | NaN | -0.9 |
| 200 | -0.8 | -0.8 | -0.7 | -1.2 | NaN | -0.8 |
| 210 | -0.8 | -0.8 | -0.6 | -0.9 | NaN | -0.7 |
| 220 | -1.0 | -0.9 | -0.8 | -0.9 | NaN | -0.8 |
| 230 | -0.9 | -0.9 | -0.7 | -0.8 | NaN | -0.8 |

**Note:** NaN - no observations. Ice temperature measurements were performed using thermistor chain, air and snow temperatures (rows 1 and 2) taken by portable thermistor probe; temperatures below 100 cm depth are rather conventional as thermistors were located in water. Bold lines show the upper and lower ice surfaces.

**Table T20.** Observed ice salinity at experimental sites.

| Depth, [cm] | Salinity, [psu] | |
|---|---|---|
| | Crack Site | Hut Site |
| 0-10 | 0.3463 | 0.4676 |
| 10-20 | 0.7102 | 0.8922 |
| 20-30 | 0.7102 | 0.4676 |
| 30-40 | 0.5282 | 0.5889 |
| 40-50 | 0.3159 | 0.5889 |
| 50-60 | 0.4069 | 0.4069 |
| 60-70 | 0.4676 | 0.4069 |

**Table T21.** Ice thickness along calibration line between Marjaniemi and Hut Site. Data are taken from ZIP-97 Data Report.

| Distance along the calibration line [m] | Mean ice thickness [cm] | STD of ice thickness [cm] | Min ice thickness [cm] | Max ice thickness [cm] |
|---|---|---|---|---|
| 200-1050 | 70 | 6 | 59 | 91 |
| 1610-2000 | 69 | 6 | 60 | 80 |
| 4250-5740 | 64 | 7 | 51 | 85 |
| 6100-7840 | 72 | 7 | 65 | 111 |

**Note:** distance along the calibration line was measured from the Hut Site.

**Table T22.** Ice thickness at the Central Buoy Site.

| Section along the floe | | | Section across the floe | | |
|---|---|---|---|---|---|
| Flag N° | Distance from the floe edge [m] | Thickness [m] | Flag N° | Distance from the floe edge [m] | Thickness [m] |
| 1 | 7.8 | 5.50 | — | — | — |
| 2 | 9.4 | NaN | — | — | — |
| 3 | 10.9 | NaN | — | — | — |
| 4 | 12.6 | NaN | — | — | — |
| 5 | 14.5 | 3.60 | 1 | 0.5 | 1.55 |
| 6 | 16.1 | NaN | 2 | 2.5 | 1.83 |
| 7 | 17.9 | NaN | 3 | 4.0 | NaN |
| 8 | 19.3 | NaN | 4 | 5.8 | 2.62 |
| 9 | 20.7 | NaN | 5 | 7.6 | NaN |
| 10 | 21.9 | 3.64 | 6 | 9.8 | 3.60 |
| 11 | 23.3 | 3.94 | 7 | 11.4 | NaN |
| ✚ 12 | 25.6 | 3.99 | ✚ 8 | 13.4 | NaN |
| 13 | 27.6 | NaN | 9 | 15.6 | NaN |
| 14 | 29.6 | NaN | 10 | 17.6 | NaN |
| 15 | 31.8 | 0.90 | 11 | 19.6 | 0.39 |
| 16 | 34.5 | 0.30 | 12 | 21.6 | 0.36 |
| 17 | 36.8 | 0.30 | 13 | 23.3 | 0.36 |
| 18 | 38.8 | 0.29 | 14 | 25.3 | 0.36 |
| 19 | 41.6 | 0.27 | 15 | 27.0 | 0.35 |
| 20 | 44.0 | 0.26 | 16 | 29.0 | 0.36 |
| 21 | 46.3 | 0.29 | 17 | 31.0 | 0.37 |
| 22 | 49.0 | 0.31 | 18 | 33.0 | 0.35 |
| 23 | 50.5 | 0.55 | — | — | — |

**Note:** NaN - no ice thickness measurements were made; ✚ - crossing of drilling sections. Data were obtained via drilling. No information about number of ice layers is given. "Section along the floe" was drilled along the major floe dimension, whereas "section across the floe" was completed in perpendicular direction to the major floe dimension (see sketch in Fig. 3.24, Chapter 3).